

UNIVERSITY OF OKLAHOMA

GRADUATE COLLEGE

**CHEMOPOROELASTIC SOLUTION OF
TRANSVERSELY ISOTROPIC SATURATED
POROUS MEDIA**

A DISSERTATION

SUBMITTED TO THE GRADUATE FACULTY

in partial fulfillment of the requirements for the

degree of

DOCTOR OF PHILOSOPHY

BY

ARTURO DIAZ PEREZ

Norman, Oklahoma

2004

UMI Number: 3318583

INFORMATION TO USERS

The quality of this reproduction is dependent upon the quality of the copy submitted. Broken or indistinct print, colored or poor quality illustrations and photographs, print bleed-through, substandard margins, and improper alignment can adversely affect reproduction.

In the unlikely event that the author did not send a complete manuscript and there are missing pages, these will be noted. Also, if unauthorized copyright material had to be removed, a note will indicate the deletion.

UMI[®]

UMI Microform 3318583

Copyright 2008 by ProQuest LLC.

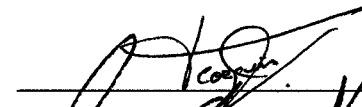
All rights reserved. This microform edition is protected against unauthorized copying under Title 17, United States Code.

ProQuest LLC
789 E. Eisenhower Parkway
PO Box 1346
Ann Arbor, MI 48106-1346

**CHEMOPOROELASTIC SOLUTION OF
TRANSVERSELY ISOTROPIC SATURATED
POROUS MEDIA**

A DISSERTATION APPROVED FOR THE MEWBOURNE SCHOOL OF
PETROLEUM AND GEOLOGICAL ENGINEERING

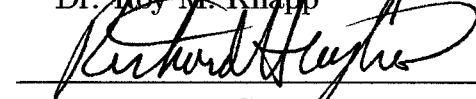
BY



Dr. Jean-Claude Roegiers



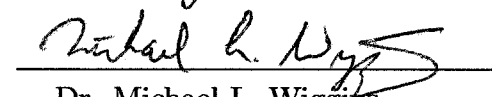
Dr. Roy M. Knapp



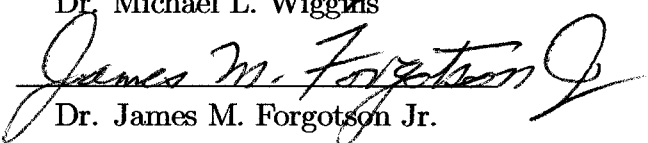
Dr. Richard G. Hughes



Dr. Daniel J. O'Meara



Dr. Michael L. Wiggins



Dr. James M. Forgotson Jr.

©Copyright by ARTURO DIAZ PEREZ 2004

All Rights Reserved.

Acknowledgments

I would like to express my sincere gratitude to Dr. Jean-Claude Roegiers for his support, patience, extensive guidance, teaching and supervision. Also for providing me the opportunity to conduct this research. I am thankful for his interest, generosity, and encouragement. Without his kindness, active help and understanding, this work would have never been possible.

Special thanks are also given to Dr. Adel Diek, for his invaluable contribution to this work, interest and generous investment of time in teaching me the fundamentals of shale behavior and sharing with me his ideas about swelling and fluid interactions.

My gratitude is extended to Dr. Roy Knapp, Dr. Richard Hughes, Dr. Daniel O'Meara, Dr. Michael Wiggins and Dr. James Forgotson for their teaching and kindly accepting to be member of my Doctoral's Advisory Committee and for revising this document. Important technical concepts were acquired during their courses and guidance. I will never forget their support and comprehension.

I am also particularly grateful to Ignacio Cortes Monroy, internal advisor from IMP for his efforts throughout this accomplishment.

Great appreciation also goes to Dr. Shubash Shah and Mr. Mike Shaw for their help and support. They invested great efforts in providing me access to the Rock Mechanics facilities.

I would like also to thank my friends Dr. Simón López Ramírez, Ivan Gil and Freddy H. Escobar for their honest friendship and support.

Finally, I do not forget to acknowledge The Instituto Mexicano del Petróleo (IMP) for the financial support to pursue this degree.

Table of Contents

Acknowledgments	iv
Abstract	vi
List of Figures	ix
List of Tables	x
1 Introduction	1
1.1 Introduction	1
1.2 Objective	4
1.3 Overview	4
2 General Review on Wellbore Stability	6
2.1 Fundamental concepts	6
2.1.1 Introduction	6
2.1.2 Rock failure	7
2.1.2.1 Failure criteria	8
2.1.2.1.1 Maximum tensile stress criterion	8
2.1.2.1.2 Maximum shear stress or Tresca's criterion	8
2.1.2.1.3 von Mises criterion	9
2.1.2.1.4 Drucker-Prager criterion	11
2.1.2.1.5 Coulomb's criterion	11
2.1.2.1.6 Mohr's criterion	12

2.2	Wellbore Stability	12
2.2.1	Borehole instability problems.	14
2.2.1.1	General review	14
2.2.1.2	Practical solution.	19
2.2.2	Wellbore stability models.	20
2.2.2.1	Analytical models	21
2.2.2.2	Numerical models	26
2.3	Poroelasticity	28
2.3.1	Introduction	28
2.3.2	Fundamental concepts of poroelasticity	29
2.4	Shale	34
2.4.1	Introduction	34
2.4.2	Clay-Water Interactions	35
2.4.2.1	Electrically charged surfaces of clay particles	36
2.4.2.2	Hydration of Clays	37
2.4.3	Swelling phenomenon while drilling	38
2.5	Summary	41
3	Theoretical Approach	43
3.1	Introduction	43
3.2	Transport processes.	45
3.3	Rock Constitutive Equations	48
3.3.1	Free Energy of Wetted Clay Matrix	48
3.3.2	Fundamental equations	51
3.3.3	Variations of the fluid content	53
3.3.4	Chemical Loading	54

3.3.4.1	Linearization of Chemical Loading	57
3.3.5	Complete Isotropy	58
3.3.6	Transverse Isotropy	59
3.4	Transport Equations	61
3.4.1	Isotropic Flows	61
3.4.2	Transversely Isotropic Flows	63
3.5	Field Equations	64
3.5.1	Navier-type Equations	65
3.5.1.1	Isotropic Media	65
3.5.1.2	Transversely Isotropic Media	66
3.5.2	Fluid Diffusion Equation	66
3.5.2.1	Isotropic Media	66
3.5.2.2	Transversely Isotropic Media	66
3.5.3	Solute Diffusion Equation	67
3.5.3.1	Isotropic Media	67
3.5.3.2	Transversely Isotropic Media	67
3.6	Swelling Parameter	67
3.6.1	Isotropic Media	67
3.6.2	Transversely Isotropic Media	69
4	Analytical solutions	72
4.1	Introduction	72
4.2	Diffusivity Equations for Irrotational Displacement Field	72
4.3	Solutions for Borehole Problems	77
4.3.1	Vertical Borehole	78
4.3.1.1	Mode 1	78

4.3.1.1.1	<i>Stresses</i>	78
4.3.1.2	Mode 2	79
4.3.1.2.1	<i>Solute mass fraction</i>	79
4.3.1.2.2	<i>Pore pressure</i>	79
4.3.1.2.3	<i>Stresses</i>	80
4.3.1.3	Mode 3	80
4.3.1.3.1	<i>Pore pressure</i>	81
4.3.1.3.2	<i>Stresses</i>	81
4.3.1.4	Final solution	82
4.3.2	Inclined Borehole	83
4.3.2.1	Problem I	84
4.3.2.2	Problem II	87
4.3.2.3	Problem III	88
4.3.2.4	Final Solution	89
5	Model Applications	90
5.1	Introduction	90
5.2	Isotropic Porous Media	91
5.3	Transversely Isotropic Porous Media	93
5.4	Discussion of Results	93
5.4.1	Solute Mass Fraction	95
5.4.2	Pore Pressure	97
5.4.3	Total Stresses	100
5.4.3.1	Radial Stress	100
5.4.3.2	Tangential Stress	100
5.4.3.3	Axial stress	101

5.4.4	Effective Stresses	102
5.4.4.1	Radial Stress	103
5.4.4.2	Tangential Stress	104
5.4.4.3	Axial stress	106
5.5	Failure analysis	107
5.5.1	Compressive failure	108
5.5.2	Tensile failure	110
5.5.2.1	Fracturing Failure	112
5.5.2.2	Spalling Failure	112
5.5.3	Shear failure	116
6	Conclusions and Recommendations	120
	References	123
	Appendix A: Free Energy of Fluid-saturated Porous Media	131
	Appendix B: Isotropic Thermodynamic Response Coefficients	134
B.1	Mechanical Loading	134
B.2	Chemical Loading	135
	Appendix C: Anisotropic Thermodynamic Response Coefficients	136
C.1	Mechanical Loading	137
C.2	Chemical Loading	137
	Appendix D: Mass Balance	138
	Appendix E: Solution for Loading Mode 2	140
E.1	Solute Mass Fraction	140
E.2	Pore Pressure	141
E.3	Stresses	142
	Appendix F: Nomenclature	144

Appendix G: Isotropic Porous Media Without Chemical Effect	147
Appendix H: Isotropic Porous Media With Chemical Effect	152
Appendix I: Transversely Isotropic Porous Media Without Chemical Effect (Anisotropic Factor Equal to two).	157
Appendix J: Transversely Isotropic Porous Media With Chemical Effect (Anisotropic Factor Equal to 1/2).	162
Appendix K: Transversely Isotropic Porous Media With Chemical Effect (Anisotropic Factor Equal to two).	167
Appendix L: Effect of the Mud's Solute Mass Fraction (Anisotropic Factor Equal to two).	172
Appendix M: Effect of the Swelling Coefficient of the Shale (Anisotropic Factor Equal to two).	177
Appendix N: Effect of the Shale's Reflection Coefficient (Anisotropic Factor Equal to two)	182
Appendix O: Effect of the Mud Pressure (Anisotropic Factor Equal to two)	187
Appendix P: Effect of the Normal Stress Field (Anisotropic Factor Equal to two)	192

Abstract

Wellbore stability, mainly in shales, is one of the major problems encountered during the drilling of wells, with an estimated cost exceeding hundreds of millions of dollars each year in remedial works. Presently, the design of improved water-base muds for shale stability is of primary concern for the drilling industry. A key factor in selecting the appropriate drilling fluid is a better understanding of the swelling phenomenon in shales; it is associated with the chemical composition and characteristics of the material. However, until now, the experimental data did not totally and effectively explain the observations.

Instability of shales involves fully coupled chemo-mechanical processes, in which fundamental intermolecular surface forces are acting between the clay layers. These forces are function of the composition, type, amount, and micro-fabric of the clay content in the rock which are responsible for the global shale behavior. Thus, for wellbore stability problems one needs to include the mechanical properties of these materials interacting with the pore fluid.

The purpose of this dissertation is to provide civil, petroleum and geological engineers, a model of chemical poroelasticity for fluid saturated argillaceous rocks, appropriate for laboratory and field applications. The theory couples mechanical, hydraulic and chemical processes in fluid-saturated transversely isotropic porous media. The model of hydration swelling is derived from non-equilibrium thermodynamics; it is a hybrid of an extended version of the theory of poroelasticity and Onsager's(1931) transport phenomenology. In particular, it is an extension of Heidug and Wong's model (1996) to accommodate compressibility of the fluid as well as anisotropy. The rock constitutive equations expressing the total stresses, the pore volume fraction per referential volume are constructed from the internal energy of the wetted clay matrix in terms of the solid strains, the pore pressure, and the fluid component chemical potentials. The total stresses, and the variation of fluid content are linearly related to these variables through anisotropic material

coefficients characterized via micro-homogeneity and micro-isotropy assumptions. The analysis incorporates four coupled transport processes of fluid, and solute in addition to mechanical deformation, and chemical swelling. The phenomenological equations relating the fluxes to their conjugate forces are constructed from the definition of the dissipation function and the generalized forces associated with it. Field equations for the linear chemical loading are derived and applied to vertical and inclined boreholes subjected to non-hydrostatic far-field loading.

The solution is closed-form in the Laplace domain; and is then inverted to the time domain by using Stehfest's (1970) algorithm. This solution simulates the chemoporoelastic process triggered by drilling a borehole in saturated porous media, and subject to a step constant mass fraction change together with mud pressure acting on the borehole wall. Results indicate that osmosis alters the pore pressure and effective stresses, which are function of the swelling coefficient and the reflection coefficient of the formation as well as the solute mass fraction of the mud.

Dedication

With great appreciation to my lovely family, my wife Irma and my two children Paulina and Eli, who have always been supporting and encouraging when difficult times happen. Also to my parents and professors, who have taught me valuable lessons of life, no matter how adverse would be the time that we are facing, never give up, challenge yourself, and build in a constructive way.

List of Figures

2.1	Compressive failure (break-out and borehole collapse) induced by insufficient wellbore pressure (after Bradley, 1979).	15
2.2	Tensile failure (hydraulic fracturing) induced by excessive wellbore pressure (after Bradley, 1979).	16
2.3	Lateral shift of borehole induced by shear release along preexisting fractures or faults (after Maury, 1994).	17
2.4	Characterization of reservoir critical properties in horizontal drilling (after Skopec, 1991).	20
2.5	Inclined borehole (local and global coordinate system).	23
2.6	Numerical method available to approximate the solution in simulation.	27
3.1	Pore model composed of a solid matrix with two kinds of connected pores of different scales.	44
4.1	Schematic diagram of an inclined borehole subjected to a non-hydrostatic stress field and wellbore pressure and solute mass concentration which are different from initial formation pore pressure and solute mass concentration.	83
4.2	Loading decomposition scheme for an inclined borehole problem (after Li, 1998)	85
4.3	Correspondence between the two local coordinate systems	86
5.1	Experimental lay-out	91
5.2	Solute mass fraction variation with time in a transversely isotropic saturated porous media using an anisotropy factor of two. Chemical effects are also considered.	96

5.3	Solute mass fraction variation when changing the solute concentration in the drilling mud at early and long times. The formation is a transversely isotropic, saturated, with an anisotropy factor of two. Chemical effects are also considered.	96
5.4	Pore pressure distribution along the radial direction ($\theta = 0$) at early and long times for different rock conditions (isotropic and anisotropic with and without chemical effects). The effect of the normal stress field in anisotropic conditions (AF=2) is also considered.	98
5.5	Radial stress variation along of radial ($\theta = 0$) direction for different rock conditions.	100
5.6	Tangential stress variation along the radial direction ($\theta = 0$) for different rock conditions, with and without chemical effects.	101
5.7	Axial stress distribution along the radial direction ($\theta = 0$) of the borehole at early and long times for different rock conditions.	102
5.8	Effective radial stress distribution along the radial direction ($\theta = 0$) at early and long times for different rock properties.	103
5.9	Effective stress distribution profile along the radial direction ($\theta = 0^0$) at early and long times for different rock properties	105
5.10	Effective tangential stress distribution along the radial direction ($\theta = 90^0$) for different mud salinities	109
5.11	Effective tangential stress distribution along the radial direction ($\theta = 90^0$) for different mud pressures.	110
5.12	Effective tangential stress distribution along the radial direction ($\theta = 90^0$) for different reflection coefficients.	111
5.13	Effective tangential stress distribution along the radial direction ($\theta = 90^0$) for different swelling coefficients.	111
5.14	Effective radial stress distribution along the radial direction ($\theta = 90^0$) for different mud salinities.	113
5.15	Effective radial stress distribution along the radial direction ($\theta = 90^0$) for different swelling coefficients.	114
5.16	Effective radial stress distribution along the radial direction ($\theta = 90^0$) for different reflection coefficients.	115

5.17	Effective radial stress distribution along the radial direction ($\theta = 90^\circ$) for different mud pressures.	115
5.18	Differential stress distribution along the radial direction at $\theta = 0^\circ$ for different swelling coefficients.	117
5.19	Differential stress distribution along the radial direction at $\theta = 0^\circ$ for different reflection coefficients.	117
5.20	Differential stress distribution along the radial direction at $\theta = 0^\circ$ for different solute mass fractions in the mud.	118
5.21	Differential stress distribution along the radial direction at $\theta = 0^\circ$ for different mud pressures.	119
5.22	Differential stress distribution along the radial direction $\theta = 0^\circ$ for different anisotropic conditions (porous media and stress field).	119
G.1	Pore pressure variation with the radial distance for different times in an isotropic saturated porous media (anisotropy ratio equal to one). No chemical effect is considered.	148
G.2	Radial stress variation with the radial distance for different times in an isotropic saturated porous media (anisotropy ratio equal to one). No chemical effect is considered.	148
G.3	Tangential stress variation with the radial distance for different times in an isotropic saturated porous media (anisotropy ratio equal to one). No chemical effect is considered.	149
G.4	Axial stress variation with the radial distance for different times in an isotropic saturated porous media (anisotropy ratio equal to one). No chemical effect is considered.	149
G.5	Effective radial stress variation with the radial distance for different times in an isotropic saturated porous media (anisotropy ratio equal to one). No chemical effect is considered.	150
G.6	Effective tangential stress variation with the radial distance for different times in an isotropic saturated porous media (anisotropy ratio equal to one). No chemical effect is considered.	150
G.7	Effective axial stress variation with the radial distance for different times in an isotropic saturated porous media (anisotropy ratio equal to one). No chemical effect is considered.	151

H.1	Solute mass fraction variation with the radial distance for different times in an isotropic saturated porous media (anisotropy ratio equal to one) and considering chemical effect.	153
H.2	Pore Pressure variation with the radial distance for different times in an isotropic saturated porous media (anisotropy ratio equal to one) and considering chemical effect.	153
H.3	Radial stress variation with the radial distance for different times in an isotropic saturated porous media (anisotropy ratio equal to one) and considering chemical effect.	154
H.4	Tangential stress variation with the radial distance for different times in an isotropic saturated porous media (anisotropy ratio equal to one) and considering chemical effect.	154
H.5	Axial stress variation with the radial distance for different times in an isotropic saturated porous media (anisotropy ratio equal to one) and considering chemical effect.	155
H.6	Effective radial stress variation with the radial distance for different times in an isotropic saturated porous media (anisotropy ratio equal to one) and considering chemical effect.	155
H.7	Effective tangential stress variation with the radial distance for different times in an isotropic saturated porous media (anisotropy ratio equal to one) and considering chemical effect.	156
H.8	Effective axial stress variation with the radial distance for different times in an isotropic saturated porous media (anisotropy ratio equal to one) and considering chemical effect.	156
I.1	Pore pressure variation with the radial distance for different times in a transversely isotropic saturated porous media (anisotropy ratio equal to two). No chemical effect is considered.	158
I.2	Radial stress variation with the radial distance for different times in a transversely isotropic saturated porous media (anisotropy ratio equal to two). No chemical effect is considered.	158
I.3	Tangential stress variation with the radial distance for different times in a transversely isotropic saturated porous media (anisotropy ratio equal to two). No chemical effect is considered.	159

I.4	Axial stress variation with the radial distance for different times in a transversely isotropic saturated porous media (anisotropy ratio equal to two). No chemical effect is considered.	159
I.5	Effective radial stress variation with the radial distance for different times in a transversely isotropic saturated porous media (anisotropy ratio equal to two). No chemical effect is considered.	160
I.6	Effective tangential stress variation with the radial distance for different times in a transversely isotropic saturated porous media (anisotropy ratio equal to two). No chemical effect is considered.	160
I.7	Effective axial stress variation with the radial distance for different times in a transversely isotropic saturated porous media (anisotropy ratio equal to two). No chemical effect is considered.	161
J.1	Solute mass fraction variation with radial distance for different times in a transversely isotropic saturated porous media (anisotropy ratio equal to 0.5). Chemical effect is considered.	163
J.2	Pore Pressure variation with radial distance for different times in a transversely isotropic saturated porous media (anisotropy ratio equal to 0.5). Chemical effect is considered.	163
J.3	Radial stress variation with radial distance for different times in a transversely isotropic saturated porous media (anisotropy ratio equal to 0.5). Chemical effect is considered.	164
J.4	Tangential stress variation with radial distance for different times in a transversely isotropic saturated porous media (anisotropy ratio equal to 0.5). Chemical effect is considered.	164
J.5	Axial stress variation with radial distance for different times in a transversely isotropic saturated porous media (anisotropy ratio equal to 0.5). Chemical effect is considered.	165
J.6	Effective radial stress variation with radial distance for different times in a transversely isotropic saturated porous media (anisotropy ratio equal to 0.5). Chemical effect is considered.	165
J.7	Effective tangential stress variation with radial distance for different times in a transversely isotropic saturated porous media (anisotropy ratio equal to 0.5). Chemical effect is considered.	166

J.8	Effective axial stress variation with radial distance for different times in a transversely isotropic saturated porous media (anisotropy ratio equal to 0.5). Chemical effect is considered.	166
K.1	Solute mass fraction variation with radial distance for different times in a transversely isotropic saturated porous media (anisotropy ratio equal to two) and taking into account the chemical effect.	168
K.2	Pore pressure variation with radial distance for different times in a transversely isotropic saturated porous media (anisotropy ratio equal to two) and taking into account the chemical effect.	168
K.3	Radial stress behavior with radial distance for different times in a transversely isotropic saturated porous media (anisotropy ratio equal to two) and taking into account the chemical effect.	169
K.4	Tangential stress variation with radial distance for different times in a transversely isotropic saturated porous media (anisotropy ratio equal to two) and taking into account the chemical effect.	169
K.5	Axial stress variation with radial distance for different times in a transversely isotropic saturated porous media (anisotropy ratio equal to two) and taking into account the chemical effect.	170
K.6	Effective radial stress variation with radial distance for different times in a transversely isotropic saturated porous media (anisotropy ratio equal to two) and taking into account the chemical effect.	170
K.7	Effective tangential stress variation with radial distance for different times in a transversely isotropic saturated porous media (anisotropy ratio equal to two) and taking into account the chemical effect.	171
K.8	Effective axial stress variation with radial distance for different times in a transversely isotropic saturated porous media (anisotropy ratio equal to two) and taking into account the chemical effect.	171
L.1	Solute mass fraction variation for different mud's solute mass fraction at early and long times, in a transversely isotropic saturated porous media (AF=2). Chemical effects are also considered.	173
L.2	Pore pressure variation for different mud's solute mass fraction at early and long times, in a transversely isotropic saturated porous media (AF=2). Chemical effects are also considered.	173

L.3	Radial stress variation for different mud's solute mass fraction at early and long times, in a transversely isotropic saturated porous media (AF=2). Chemical effects are also considered.	174
L.4	Tangential stress variation for different mud's solute mass fraction at early and long times, in a transversely isotropic saturated porous media (AF=2). Chemical effects are also considered.	174
L.5	Axial stress variation for different mud's solute mass fraction at early and long times, in a transversely isotropic saturated porous media (AF=2). Chemical effects are also considered.	175
L.6	Effective radial stress variation for different mud's solute mass fraction at early and long times, in a transversely isotropic saturated porous media (AF=2). Chemical effects are also considered.	175
L.7	Effective tangential stress variation for different mud's solute mass fraction at early and long times, in a transversely isotropic saturated porous media (AF=2). Chemical effects are also considered.	176
L.8	Effective axial stress variation for different mud's solute mass fraction at early and long times, in a transversely isotropic saturated porous media (AF=2). Chemical effects are also considered.	176
M.1	Solute mass fraction variation with radial distance at early and long times, for different swelling coefficients in a transversely isotropic saturated porous media (anisotropy factor equal to two).	178
M.2	Pore pressure variation with radial distance at early and long time, for different swelling coefficients in a transversely isotropic saturated porous media (anisotropy factor equal to two).	178
M.3	Radial stress variation with radial distance at early and long times, for different swelling coefficients in a transversely isotropic saturated porous media (anisotropy factor equal to two).	179
M.4	Tangential stress variation with radial distance at early and long times, for different swelling coefficients in a transversely isotropic saturated porous media (anisotropy factor equal to two).	179
M.5	Axial stress variation with radial distance at early and long times, for different swelling coefficients in a transversely isotropic saturated porous media (anisotropy factor equal to two).	180

M.6	Effective radial stress variation with radial distance at early and long times, for different swelling coefficients in a transversely isotropic saturated porous media (anisotropy factor equal to two).	180
M.7	Effective tangential stress variation with radial distance at early and long times, for different swelling coefficients in a transversely isotropic saturated porous media (anisotropy factor equal to two).	181
M.8	Effective axial stress variation with radial distance at early and long times, for different swelling coefficients in a transversely isotropic saturated porous media (anisotropy factor equal to two).	181
N.1	Solute mass fraction variation with radial distance at early and long times, for different reflection coefficients in a transversely isotropic saturated porous media (anisotropy factor equal to two).	183
N.2	Pore pressure variation with radial distance at early and long times, for different reflection coefficients in a transversely isotropic saturated porous media (anisotropy factor equal to two).	183
N.3	Radial stress variation with radial distance at early and long times, for different reflection coefficients in a transversely isotropic saturated porous media (anisotropy factor equal to two).	184
N.4	Tangential stress variation with radial distance at early and long times, for different reflection coefficients in a transversely isotropic saturated porous media (anisotropy factor equal to two).	184
N.5	Axial stress variation with radial distance at early and long times, for different reflection coefficients in a transversely isotropic saturated porous media (anisotropy factor equal to two).	185
N.6	Effective radial stress variation with radial distance at early and long times, for different reflection coefficients in a transversely isotropic saturated porous media (anisotropy factor equal to two).	185
N.7	Effective tangential stress variation with radial distance at early and long times, for different reflection coefficients in a transversely isotropic saturated porous media (anisotropy factor equal to two).	186
N.8	Effective axial stress variation with radial distance at early and long times, for different reflection coefficients in a transversely isotropic saturated porous media (anisotropy factor equal to two).	186

O.1	Solute mass fraction variation with radial distance, for different mud pressures in a transversely isotropic saturated porous media (anisotropy ratio equal to two)	188
O.2	Pore pressure variation with radial distance, for different mud pressures in a transversely isotropic saturated porous media (anisotropy ratio equal to two)	188
O.3	Radial stress variation with radial distance, for different mud pressures in a transversely isotropic saturated porous media (anisotropy ratio equal to two)	189
O.4	Tangential stress variation with radial distance, for different mud pressures in a transversely isotropic saturated porous media (anisotropy ratio equal to two)	189
O.5	Axial stress variation with radial distance, for different mud pressures in a transversely isotropic saturated porous media (anisotropy ratio equal to two)	190
O.6	Effective radial stress variation with radial distance, for different mud pressures in a transversely isotropic saturated porous media (anisotropy ratio equal to two)	190
O.7	Effective tangential stress variation with radial distance, for different mud pressures in a transversely isotropic saturated porous media (anisotropy ratio equal to two)	191
O.8	Effective axial stress variation with radial distance, for different mud pressures in a transversely isotropic saturated porous media (anisotropy ratio equal to two)	191
P.1	Pore pressure variation with radial distance, for different times in a transversely isotropic saturated porous media (anisotropy factor equal to two) at normal stress field.	193
P.2	Radial stress variation with radial distance, for different times in a transversely isotropic saturated porous media (anisotropy factor equal to two) at normal stress field.	193
P.3	Tangential stress variation with radial distance, for different times in a transversely isotropic saturated porous media (anisotropy factor equal to two) at normal stress field.	194

P.4	Axial stress variation with radial distance, for different times in a transversely isotropic saturated porous media (anisotropy factor equal to two) at normal stress field.	194
P.5	Effective radial stress variation with radial distance, for different times in a transversely isotropic saturated porous media (anisotropy factor equal to two) at normal stress field.	195
P.6	Effective tangential stress variation with radial distance, for different times in a transversely isotropic saturated porous media (anisotropy factor equal to two) at normal stress field.	195
P.7	Effective axial stress variation with radial distance, for different times in a transversely isotropic saturated porous media (anisotropy factor equal to two) at normal stress field.	196

List of Tables

3.1	Direct and Coupled Flow Phenomena	45
3.2	Values of parameters (after Cheng, 1997)	69
5.1	Entry data for isotropic saturated porous media	92
5.2	Entry data for transversely isotropic saturated porous media	94

1 Introduction

1.1 Introduction

Oil and gas wells represent the fundamental infrastructure in hydrocarbon exploitation. Drilling the wellbore is the first and, usually, the most expensive step in oil and gas production activities. As a consequence, designing a stable and safe well has become a critical issue in the industry, especially due to the recent and ever-increasing complexity of geological settings requiring continuous improvement in drilling technology.

Wellbore stability, mainly in shales, is one of the most difficult problems encountered during drilling; estimated to cost more than hundreds of millions of dollars each year in remedial works. These problems often depart from the classical mechanical failure mechanisms exhibiting time-dependent mud support changes and loss of strength according to physico-chemical processes. Swelling, dispersion, and deterioration of shale cause a great majority of wellbore instability problems. These problems range from hole tightening and shale adhesion to the drill bit to hole enlargement and /or even complete collapse of the borehole, as well as alteration of the rheological properties of the drilling fluid. Prior to drilling, a shale formation is in a state of mechanical, hydraulic, thermal, and chemical equilibrium. Drilling disturbs these natural equilibria, resulting in the modification of local stresses accompanied by deformation of the borehole, as well as the enforcement of hydraulic, temperature, and chemical potential gradients (Hale et al.,1993; Mody and Hale,1993; van Oort et al.,1996; and Diek et al.,1996). In the past, one solution has been to use oil-base muds, which can often eliminate the swelling problem associated with shales;

however, environmental concerns restrict their use, and in many cases water-base muds are now required. The development of improved water-base muds for shale stability is of primary concern in the drilling industry. Wellbore stability has occupied the attention of many researchers this last decade and some discrepancies have been reported, not only in their chemo-mechanical approach, but also in the understanding of their hydration behavior, and their characterization.

Shales are fine-grained detrital sedimentary rocks formed by the consolidation of clay, silt, or mud and are characterized by their finely laminated structure, cation exchange capacity, specific surface area, and water content. They contain wide ranges of clay minerals, and accessory minerals such as quartz, carbonates and feldspars. The chemical processes, responsible for this formation must be understood in terms of two mechanisms:

- 1) neoformation- actual precipitation from solution; and,
- 2) transformation- whereby a new clay mineral inherits a significant part of its silicate skeleton from preexisting minerals, usually also a phyllosilicate.

These processes include chemical weathering in soils, formation of authigenic minerals at the sediments depositional site, formation of diagenetic minerals after deposition, and clay minerals formed by hydrothermal alteration. Shales are, therefore, subject to phenomena such as hydration, swelling, shrinking, and strength reduction when exposed to water and ions. The mechanisms controlling these reactions are very complex and are not fully understood. These reactions result from the hydrophilic nature of the clay particles, which are somewhat altered by both the chemical and mechanical environments. The chemical effects are due to the intermolecular forces between the clay particles, the ionic pore fluid inside the shale, and the composition of the drilling fluid. However, it has been recognized that the type and amount of clay groups and clay subgroups play an important role in distinguishing different hydration behaviors, as a result of their charge deficiency location (silica tetrahedral or alumina octahedral sheet). These chemical effects result in a continuous change in shale pore pressure and composition.

It is believed (Diaz, 2000) that the shale stability involves fully coupled chemo-mechanical phenomena, in which fundamental intermolecular surface forces are acting between the clay surfaces. These forces are function of the composition, type, amount, and micro-fabric of the clay content in the rock which are responsible for the global shale behavior, where water content and water distribution are the partial result of these forces and are only one part of the picture.

A clay/water system is usually recognized as a four component system; clay particles (C), water molecules (W), counter-ions (I), and co-ions (A). So that a comprehensive model formulation has at least to consider all the pair interactions between these components (W-W; W-I; W-C; W-A; I-I; I-C; I-A; C-C; C-A; and A-A), which must be incorporated into the picture of the balance of forces. More terms have to be included in the above interactions if other components are added like polymers, surfactants, hydrocarbons, etc.

It is also well recognized (Diek et al, 1996) that the shale/swelling phenomena and their influence on the mechanical properties of the rock is a subject that involve two completely different scales, microscopic and macroscopic. At the microscopic level, which is ruled by Molecular Quantum Mechanics, molecular interactions induce changes in the structure of the rock which allow macroscopic driving forces to arise, which are unfortunately ruled by non-equilibrium thermodynamics. Both microscopic and macroscopic scales should, therefore, be connected using statistical thermodynamics. However, the specific linkage is not well known, and must be achieved when computing the phenomenological coefficients, which must then be considered as variables, using stochastic models. Computer simulations of clay-water interfaces have been attempted by Mulla et al. (1984) for two components (clay and water) and Skipper et al. (1991-a, and 1991-b); while Refson et al. (1991) assumed three components (clay, water, and counter-ion). Nevertheless, computer simulations need to be extended in the immediate future to clay/water systems with larger water contents and with full matrix of pair interactions in order to determine the configuration and dynamics of clay/water interfaces for various clays and dif-

ferent counter-ions. Also extensive experimental work on shale cores is needed to establish the mechanical properties of different types of shales subject to different ionic environments. Despite the fact that the knowledge of mechanical properties of shales is important, little research has been conducted on such materials. Even though the measurements of mineralogical and mechanical properties are complicated by the extremely fine grain size and the large clay content as well as the fact that they disintegrate in water, such effort should be undertaken. Correlation of chemical composition, physicochemical environment and mechanical properties of shale are extremely important in computer simulation of wellbore stability

1.2 Objective

The purpose of this research is to provide to civil, petroleum, and geological engineers a model of chemical-poroelasticity of fluid-saturated argillaceous rocks appropriate for laboratory and field applications. Such a theory will need to couple mechanical, hydraulic, and chemical processes in fluid-saturated transversely porous media. The model of hydration swelling is derived from non-equilibrium thermodynamics (Onsager's transport phenomenology) and is an extended version of the theory of poroelasticity. It is an extension of Heidug and Wong's model (1996) to accommodate for the compressibility of the fluid and inherent anisotropy of the porous media.

1.3 Overview

A critical review of the literature on wellbore stability, shale interaction and poroelasticity is presented in Chapter 2.

Chapter 3 contains the development of the theoretical approach of our chemoporoelasticity model.

Chapter 4 contains the analytical solutions for the general case of fully-coupled

chemoporoelasticity for axisymmetric mechanical and chemical loading conditions of vertical and inclined boreholes subjected to non-hydrostatic far field loading. The solution to the inclined situation is constructed via superposition of the plane strain solution (a vertical hole drilled in rock with far-field stress components P_0 and S_0) and the elastic anti-plane solution (a borehole subject to far field anti-plane shear stresses)

Chapter 5 presents the results of the application of our model to inclined borehole stability problems.

Finally the conclusions and recommendations are given in Chapter 6.

2 General Review on Wellbore Stability

2.1 Fundamental concepts

2.1.1 Introduction

Drilling the wellbore is the earliest and, usually, the most expensive step in oil and gas production activities. As a consequence, designing a drilling strategy has become a critical issue in petroleum engineering especially if one considers that geological settings of the new target become ever more complex.

Horizontal drilling, highly deviated wells, multilateral completions, extended-reach and slim holes are some examples of these technological advances. However, drilling in complex geological environments, such as faults, joints, fractures, layered formations, weak bedding planes, etc., usually leads to expensive borehole stability problems. Here, a deep understanding of the mechanics and mechanisms of rock fracture becomes a key element in solving such problems involving geotectonic structures.

Wellbore stabilization when drilling, should include preventing unwanted fluid or gas flow in or out of the wellbore, preventing the flow of particulates into the formation, and mitigating compressive or tensile failures. Solutions should involve the use of real-time drilling data obtained from measurement-while-drilling, wellbore image logs, a complete suit of logging, core samples, laboratory test data, advanced fluid chemistry, computer simulation models and a good file of case histories relating similar well problems to allow minimizing non-drilling rig time, eliminating emergency or unplanned casing strings and preventing unwanted gas or fluid flow

that causes environmental hazards.

2.1.2 Rock failure

In general, fractures initiate and propagate when, at a point, the stresses become equal to the strength of the rock. It is recognized (Aydin and Johnson, 1978) that the stresses in the earth's crust are generated by lithostatic changes, fluid pressure, tectonic events, thermal effects, volcanic activity, salt intrusion and, in some cases, from impact by extraterrestrial objects.

The basic concept of stress concentration and energy balance introduced by Griffith (1921) are fundamental to understanding rock fracture initiation as well as fracture propagation and distribution. Griffith originally defined the low tensile strength of brittle materials in terms of an inequality between the rate at which elastic energy is released and the rate at which surface energy is absorbed, as a flaw or crack extends within the material. The general basis of Griffith's theory is that elastic potential energy is converted into surface energy during rock failure. In this way, the excess energy, large in relation to the stored elastic strain energy, is dissipated during the rock failure. Thus, the macro-fracturing process is well recognized as originated by micro-fractures acting as 'strain concentrators'. Under a compressive stress state, the failure process starts with the creation of micro-cracks, due to localized tensile stresses, that eventually evolves into a damage zone turning towards the maximum principal stress direction. With the coalescence of those cracks, the specimen can not further sustain the applied load and failure of the specimen occurs (Roegiers, 1990, 1998).

Evidences of the fracturing process have been observed in laboratory experiments conducted in triaxial cells with acoustic sensors. An increase in acoustic emissions due to discrete events meant that the energy release mechanism is definitely fracturing. Besides fracture creation, heat is also exchanged with the surroundings, if the rock temperature is allowed to equilibrate with the ambient conditions. The rock does not completely lose its strength and with further energy

stored, more fractures are created until the internal energy level reaches a critical value and the specimen fails. This critical value is referred as ultimate strength which is the base for failure criteria.

2.1.2.1 Failure criteria

According to Jaeger and Cook (1969), a failure criterion is a relationship between the principal stresses such that, if it is satisfied, the material becomes ductile and should satisfy two requirements:

- any yield criterion must be independent of the choice of axes, and thus should be expressible in terms of the invariants of stresses or stress deviations; and,
- at hydrostatic conditions only stress deviation should appear in the yield criterion.

2.1.2.1.1 Maximum tensile stress criterion This criterion establish that failure is reached as soon as the minimum principal stress reaches the tensile strength of the material; i.e.

$$\sigma_3 = -T_o \quad (2.1)$$

2.1.2.1.2 Maximum shear stress or Tresca's criterion This criterion states that failure will occur when the maximum shear stress reaches a value $\frac{1}{2}\sigma_o$ characteristic of the material; i.e.

$$\sigma_1 - \sigma_3 = s_1 - s_3 = \sigma_0 \quad (2.2)$$

Where $s_{1,2,3}$ are the principal stresses deviation defined as:

$$s = \frac{1}{3} (\sigma_x + \sigma_y + \sigma_z) = \frac{1}{3} (\sigma_1 + \sigma_2 + \sigma_3) = \frac{1}{3} I_1 \quad (2.3)$$

and,

$$s_1 = \sigma_1 - s = \frac{(2\sigma_1 - \sigma_2 - \sigma_3)}{3} \quad (2.4)$$

$$s_2 = \sigma_2 - s = \frac{(2\sigma_2 - \sigma_1 - \sigma_3)}{3} \quad (2.5)$$

$$s_3 = \sigma_3 - s = \frac{(2\sigma_3 - \sigma_2 - \sigma_1)}{3} \quad (2.6)$$

$$s_x = \sigma_x - s; s_y = \sigma_y - s; s_z = \sigma_z - s; s_{yz} = \tau_{yz}; s_{zx} = \tau_{zx}; s_{xy} = \tau_{xy} \quad (2.7)$$

Also, in this particular case, the failure plane will occur at an angle bisecting the directions of maximum and minimum principal stresses.

2.1.2.1.3 von Mises criterion This criterion states that yield occurs when the octahedral shear stress, or strain energy associated with distortion, reaches a value characteristic of the material. This criterion is by far the most commonly used and is adequate for most problems on metals. It can be expressed in terms of the second invariant of stress deviation, which can be written in the alternative forms as:

$$J_2 = \frac{\sigma_0^2}{3} \quad (2.8)$$

$$s_1^2 + s_2^2 + s_3^2 = \frac{2\sigma_0^2}{3} \quad (2.9)$$

$$(\sigma_2 - \sigma_3)^2 + (\sigma_3 - \sigma_1)^2 + (\sigma_1 - \sigma_2)^2 = 2\sigma_0^2 \quad (2.10)$$

$$\tau_{oct} = \left(\frac{2}{9}\right)^{\frac{1}{2}} \sigma_0 \quad (2.11)$$

$$W_d = \frac{\sigma_0^2}{6G} \quad (2.12)$$

where,

$$J_2 = \frac{1}{2} (s_x^2 + s_y^2 + s_z^2) + s_{yz}^2 + s_{zx}^2 + s_{xy}^2 \quad (2.13)$$

$$J_2 = \frac{1}{6} ((\sigma_y - \sigma_z)^2 + (\sigma_z - \sigma_x)^2 + (\sigma_x - \sigma_y)^2) + s_{yz}^2 + s_{zx}^2 + s_{xy}^2 \quad (2.14)$$

$$J_2 = \frac{1}{6} ((\sigma_2 - \sigma_3)^2 + (\sigma_3 - \sigma_1)^2 + (\sigma_1 - \sigma_2)^2) \quad (2.15)$$

$$J_2 = \frac{1}{2} (s_1^2 + s_2^2 + s_3^2) \quad (2.16)$$

$$\tau_{oct} = \frac{1}{3} ((\sigma_2 - \sigma_3)^2 + (\sigma_3 - \sigma_1)^2 + (\sigma_1 - \sigma_2)^2)^{\frac{1}{2}} \quad (2.17)$$

$$W_d = \frac{1}{4G} (s_1^2 + s_2^2 + s_3^2) = G (e_1^2 + e_2^2 + e_3^2) = \frac{J_2}{2G} = \left(\frac{3}{4G}\right) \tau_{oct}^2 \quad (2.18)$$

where W_d is the strain energy of distortion.

The advantage of using this criterion is that it involves all three principal stress components.

2.1.2.1.4 Drücker-Prager criterion This criterion can be visualized as an extension of von Mises' criterion which can be expressed (Drücker and Prager, 1952) as:

$$\sqrt{J_2} = mJ_1^{eff} + \tau_o \quad (2.19)$$

where J_2 is the second invariant of the deviatoric stress tensor; J_1 is the first invariant of the stress tensor (mean stress); and, m and τ_o are material parameters measured in the laboratory. Note that J_1^{eff} is the effective mean stress. Also note that, in the case of $m = 0$, equation (2.19) becomes the original von Mises' criterion.

Here, failure takes place if the effective collapse stress, σ_d^{eff} , at a particular point around the wellbore, or at wellbore wall, is less than zero; i.e.

$$\sigma_d^{eff} = -\sqrt{J_2} + mJ_1^{eff} + \tau_o \leq 0 \quad (2.20)$$

Mc Lean and Addis (1990b) gave the relationships to calculate the material constants in the Drücker-Prager criterion knowing the material constants of Coulomb's criterion:

$$\tau_o = \frac{2\sqrt{3}c \cos \phi}{3 - \sin \phi} \quad (2.21)$$

$$m = \frac{2\sqrt{3} \sin \phi}{3 - \sin \phi} \quad (2.22)$$

2.1.2.1.5 Coulomb's criterion The simplest and most popular criterion was introduced by Coulomb (1773). He suggested that the shear stress tending to cause failure across a plane is resisted by the cohesion of the material and by a constant times the normal stress across the plane. This constant was called the *coefficient of internal friction* (μ) of the material. The criterion for shear failure in a plane is thus given by:

$$|\tau| = c + \mu\sigma \quad (2.23)$$

where σ and τ are the normal and shear stresses across the plane; c is the cohesion or inherent shear strength of the material; and, $\mu = \tan \phi$ where ϕ represent the angle of internal friction.

2.1.2.1.6 Mohr's criterion Mohr (Jaeger and Cook, 1969) proposed that the normal stress σ and the shear stress τ across the plane, where shear failure takes place, are related by a functional relation characteristic of the material; i.e.

$$|\tau| = f(\sigma) \quad (2.24)$$

Mohr's criterion is a generalized Coulomb's criterion derived from an experimental envelope of the Mohr circles corresponding to failure under a variety of conditions. It carries several important conclusions:

- the value of the intermediate principal stress σ_2 does not affect failure; and,
- the plane of shear failure passes through the direction of the intermediate principal stress, and its normal makes an angle β with the direction of maximum principal stress.

2.2 Wellbore Stability

Wellbore stability has been studied by the oil industry for a long time. The basic approach that has been applied is to compare the stresses induced in the rock with some selected failure criterion. Basically, two types of failure have been widely

investigated; borehole collapse and borehole fracturing. The first case is caused mainly by shear but also by active tensile failure (Aadnøy, 1987). The second case is when the stresses overcome the tensile strength and fracturing occurs either at or in the neighborhood of the wellbore.

While drilling (Bradley, 1979), a damage zone is created because the state of stress around the wellbore changed as a result of the removed rock, and the hydrostatic pressure exerted by the drilling fluid. Creating a hole produces an increase in the stresses around the borehole (a stress concentration) which induce cracks in weakened rock either by rock-fluid interaction or fluid pressure oscillations due to inadequate operational practices. In addition, in the case of inclined and/or horizontal boreholes, the stress tensor orientation also changes, so that in a normal stress field the inclination increases the local stress as well as stress differences while in a tectonic stress field the converse occurs.

In fractured zones, with random fracturing in all directions (which can be regarded as all planes were equally weak and the material was allowed to select its own plane of fracture), based on the Mohr and Coulomb theories, compressive shear fracturing will occur along one or a pair of conjugate planes which are parallel with the direction of the intermediate principal stress and are both oriented at an angle less than 45° to the direction of the maximum principal stress. Also shear fracturing is dependent on the relative values of the principal stresses. Thus, in a normal fault stress regime, a high-angle (with respect the horizontal plane) fracture zone occurs, whereas a low-angle fracture zone happens in a reverse fault stress regime, and vertical fractures in a strike-slip fault stress regime.

Tensile failure occurs when the pore pressure (P_p) in the rock formation is sufficiently high such that (Anderson, 1951); i.e.

$$P_p \geq \sigma_v + T \quad (2.25)$$

or, from the minimum tangential stress can be derived:

$$P_p > 3\sigma_h + T - \sigma_H \quad (2.26)$$

The plane of such tensile failure (open fracture) is perpendicular to the axis of σ_h so that in an extensional or strike-slip environment, tensile open fractures are vertical and parallel to the azimuth of σ_H ; in a compressional environment they are horizontal (Jaeger and Cook, 1969). The initiation and orientation of natural fractures need not to be related to the contemporary in-situ stress field. Natural fractures may have been created in a paleo-stress regime different to the contemporary stress field. However, if natural fractures are in an orientation inconsistent with the contemporary in situ stress field, they are not likely to remain open. Thus knowledge of the in-situ stresses field is a critical requirement for well design with regard to mechanical stability. The in-situ stress field also controls the orientation of open, natural and hydraulically induced fractures.

2.2.1 Borehole instability problems.

2.2.1.1 General review

Drilling problems frequently result from severe mechanical failures of the wellbore wall and thus depend on the interplay between magnitude and orientation of in-situ stresses, rock strength, wellbore and pore pressure, the orientation of the wellbore, and also the high borehole pressure fluctuations from surging. The stress-induced borehole failures (Aadnøy, 1987; Maury and Zurdo, 1996) can be summarized as:

- Compressive failure: i) hole size reduction due the plastic flow of the rock into the borehole (borehole collapse), which causes repeated requirements of reaming, difficulties to run in hole, pull out of hole or stuck pipe, ii) hole enlargement due to rock failing in a brittle manner and falling into the borehole (break-out), which results in poor directional control, poor cementing jobs, poor logging and formation evaluation.
- Tensile failure: fracturing due to tensile splitting of the rock as a result of excessive wellbore pressure. Severe loss of drilling fluid to the formation from

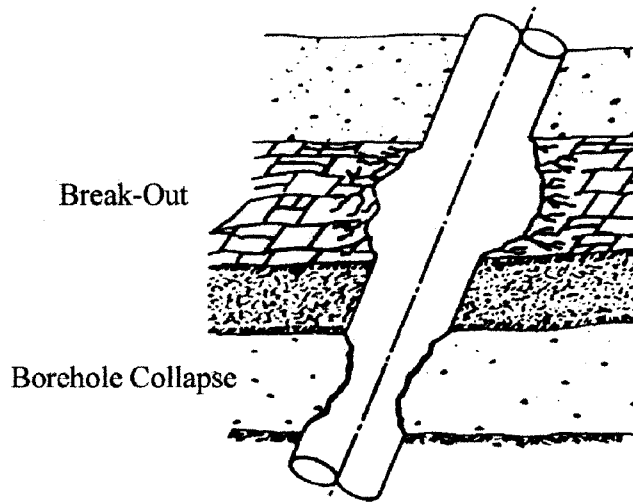


Figure 2.1: Compressive failure (break-out and borehole collapse) induced by insufficient wellbore pressure (after Bradley, 1979).

fracturing causes lost time as well as increased cost and often results in well control problems or blow-outs.

- Shear failure, when drilling through discontinuity and lateral shift of the wellbore trajectory occurs due to the slip of the fault.

The first two mechanisms (Figures 2.1 and 2.2) have been extensively studied and are usually related to the failure of the intact rock. According to Morita et al. (1990), drilling fluids not only stabilize the borehole, but also, seal off narrow natural or created fractures by laying down a low-permeable cake to prevent pore pressure build-up; maintaining high effective stresses acting on the formation. The mud solids build bridges in the fracture aperture, where minute cracks are consequently plugged. As a result, loss circulation pressures higher than predicted by the continuum theories develop. Thus lost circulation pressure depends on the Young's modulus, wellbore size, mud solid bridging at the narrow fracture tip and degree of dehydration, as well as the parameters which can be derived from conventional

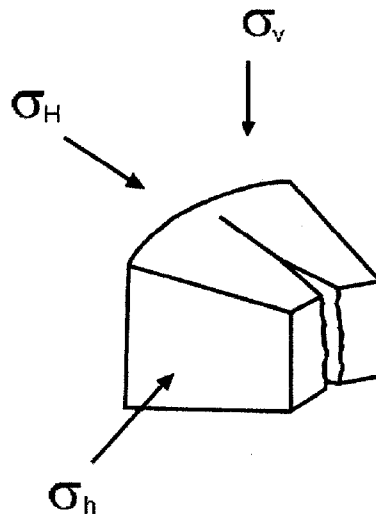


Figure 2.2: Tensile failure (hydraulic fracturing) induced by excessive wellbore pressure (after Bradley, 1979).

theories such as stress, pore pressure, temperature, borehole inclination, and pore pressure build-up.

On the other hand, in compressive failure, Zoback et al. (1985), among others, discussed the mechanism of break-out propagation. During drilling, borehole compressive stresses can decrease in some domains of the wall. As a result, crack growth can be observed in these areas due to the inherent pore pressure. These cracks will tend to grow in a plane perpendicular to the direction of smallest compression. Redistribution of these stresses in the borehole due to drilling and due to the formation of plastic zones around the borehole leads to sufficient increase of tangential compression stresses in a zone close to a plastic one; at the same time, the radial compression stresses decrease. This facilitates the growth of micro-cracks in the direction of the largest compression and, as a result, a system of circumferential cracks are formed in the vicinity of a plastic zone. Further increasing of radial stresses (or pressure inside a borehole) will lead to increasing of tangential stresses and to loss of stability of the system of concentric rings, breaking out rings into the

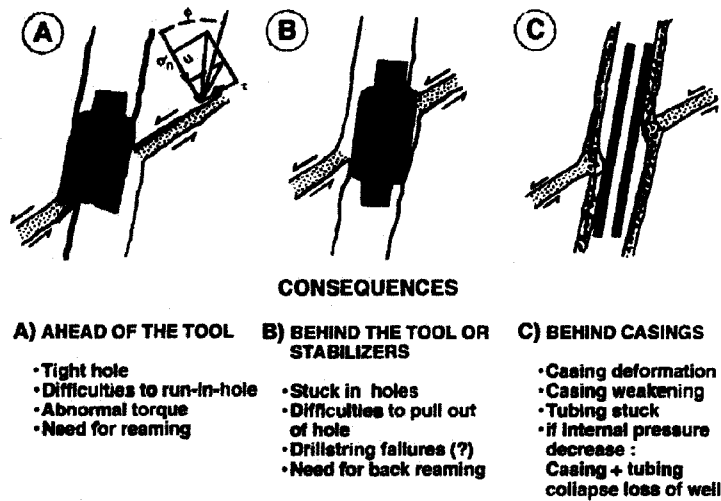


Figure 2.3: Lateral shift of borehole induced by shear release along preexisting fractures or faults (after Maury, 1994).

borehole.

To avoid this kind of instabilities, the classical remedy is to increase the mud density in order to help the wellbore to carry some of the load imposed on the borehole wall by the in-situ stresses. However, increasing the mud weight too far may result in the formation splitting in a tensile mode, causing lost circulation. Therefore, a balance is needed in the mud weight to prevent hole collapse without fracturing.

The third type of failure is related to drilling in a complex geological environment (faults, joints, natural fracture reservoir) where it is usually required to drill high inclined and horizontal wells. In this environment (Maury, 1994; Maury and Zurdo, 1996) drilling a deep well implies crossing all kind of discontinuities (fractures, faults bedding joints, etc.) present in all rock masses which can be stabilized by a simple mechanism. One needs to take special care to insure good mud sealing capabilities and effectiveness of the mud cake, because mud invasion into joints can increase the pore pressure in the discontinuity; at the same time decreasing the effective normal stress which previously stabilized it; the shear stress is not affected. A

shear release results in a lateral shift of the borehole (Figure 2.3). Initially such movement are responsible for minor incidents (tight hole, abnormal torque, overpull, etc.) occurring repeatedly at the same depth, resolved by reaming or back-reaming when possible. Later, when shifts become larger, problems become more serious, with stuck pipe, drillstring failures not resolved by classical drilling remedy (mud weight increase, jarring) which become even detrimental to stabilization. Highly fractured zones can be subjected to similar mechanisms. The stability then depends mainly on the effectiveness of the mud cake and condition of no filtration or mud invasion into the fractures. Mud weight increase is not always efficient and may sometimes cause worst instability problems.

Drilling highly deviated, extended reach and horizontal wells bring additional problems. Cutting transport, casing setting and cementing, and drillstring frictions are some examples. From the wellbore stability point of view the main concerns are the changes in stress concentrations as the inclination changes. As a consequence, the formation fracture gradient generally decreases as the borehole angle increases (Bradley, 1979). Many researchers (Skopec, 1991; Zhou and Sandiford, 1994; Maury, 1994; Last and McLean, 1996; Wilson et al., 1999; Moos et al., 1999 among others) studied the wellbore stability problems in high inclination and complex geological environments and the general conclusion is that the knowledge of the in-situ stress field is a critical requirement for well design, because it controls the orientation of open, natural and hydraulically induced fractures. Great efforts and much progress have been made towards the determination of the orientation and magnitude of the in-situ stresses in the crust, in particular by micro-hydraulic fracturing techniques, borehole break-out analyses, strain relaxation on oriented core expansion, and by measurements of passive acoustics during hydraulic fracturing. Once the orientation and magnitude of the in-situ stress field is constrained, the most stable inclined well trajectory can be designed.

2.2.1.2 Practical solution.

Wellbore stability requires a proper balance between the uncontrollable factors such as earth stresses, geological features, rock strength, and pore pressure; and the controllable factors such as wellbore fluids pressure, mud chemical composition, borehole orientation and good drilling practices.

In complex geological environments the following requirements should be emphasized: i) observing minimum fluid-rock interaction and maximum fracture sealing capacity (good filtration control) in the mud to delay invasion and pressure diffusion through discontinuities; ii) using fast but smooth drilling techniques to reduce exposure time and to minimize wellbore pressure fluctuations and mechanical shocks due to drilling string movements (tripping-in and -out of the hole, vibration, reaming and back-reaming, etc.); and, iii) designing the wellbore trajectory more appropriately to meet drilling and production goals.

An integrated solution of wellbore stability problems when drilling through a discontinuity, not only requires a systematic analysis of the information available of the history of the prospect field but also an adequate plan of gathering information and samples from the field in order to obtain a more complete formation evaluation. Nowadays the technological advances allow us to get formation evaluation data during drilling and an advanced set of well logging, together with lab characterization of rocks, give the information needed to run a wellbore stability analysis.

However, if information is not available and repeated drilling incidents have occurred (caving, stuck pipe, difficulties to run in hole, or to pull out of hole) the first step is to make an analysis of the field problems. A sensitive analysis, with given or assumed rock properties and in-situ state of stress, should be run in order to understand and resolve the wellbore stability problems, which most of the time require corrective actions (lower density and filtration properties and faster drilling speed) contrary to the traditional remedies (increase density).

Figure 2.4 shows the complete analytical scheme for the characterization of

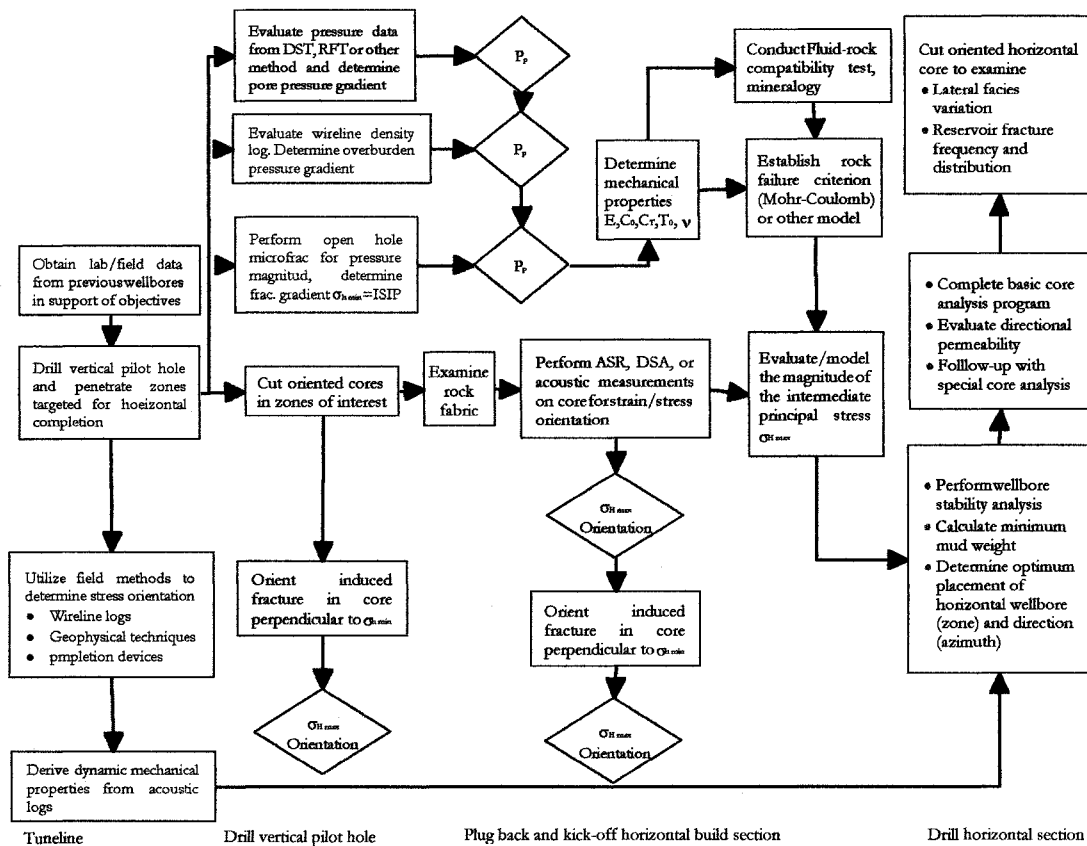


Figure 2.4: Characterization of reservoir critical properties in horizontal drilling (after Skopec, 1991).

reservoir properties critical in horizontal drilling (Skopec, 1991).

2.2.2 Wellbore stability models.

The high economic impact of the horizontal, extended reach and high inclined well drilling technology have been widely recognized through lower development costs, faster production rates, higher recovery factors and the potential exploitation of naturally fractured reservoir (Joshi, 1991). However, in a normal stress field, wellbore instability usually arise as the wellbore inclination increases, which impedes the realization of the benefits offered by the horizontal drilling technology. As a result, the understanding and modeling of inclined wellbores have intensified within

the oil industry.

Mathematical models describe material behavior in terms of equations which are used to find the distribution of displacements, stresses, and strains throughout a deforming body. In principle, these equations can be solved either analytically or numerically.

2.2.2.1 Analytical models

Analytical solutions are general solutions to the equations that express the values of the unknown quantities as a mathematical function of position and material properties. Thus the solution can be evaluated for a wide variety of specific conditions, and one can determine, from this general solution, how changes in conditions affect the specific solution. Analytic solutions, however, can be found only if the geometry of the body and the deformations are relatively simple; in addition, they generally apply only for small strain mathematical models.

In 1979, Bradley proposed a basic analytical model to account for the stress distribution around an inclined borehole which is based on Kirsch's solution, together with a solution by Fairhurst (1968). In this model, the formation around the borehole is considered as a linear elastic solid in plane strain condition along the axis of the borehole, the formation is considered to be normally stressed ($\sigma_H = \sigma_h < \sigma_1$) and no fluid flow into or out of the formation is taken into account. Also, the formation is assumed isotropic and no discontinuity planes are present. This model uses two failure criteria: i) tensile failure occurring at effective stresses less than or equal to zero (assume tensile strength equal to zero); and, ii) compressive failure occurring when the mean shear stress ($J_2^{\frac{1}{2}}$) vs the effective mean normal stress ($s - P_0$) is plotted and lies below the envelope of failure which is obtained experimentally (s is given by Equation 2.3). He also defined an effective borehole collapse stress which is positive for stable conditions:

$$J_{2eff}^{\frac{1}{2}} = J_{2rock\ failure}^{\frac{1}{2}} - J_{2borehole}^{\frac{1}{2}} \quad (2.27)$$

Later, Aadnøy and Chenevert (1987), following Bradley's approach, extended the model to take into account planes of weakness, incorporating the Mohr and Coulomb theories. They applied a simple algorithm as follow: first, the in-situ stresses are transformed to the direction of the borehole using Equation (2.30), then the stresses at the borehole wall are calculated using Equations (2.31) to (2.36). Finally, the principal stresses are calculated using Equations (2.42) to (2.44) and the shear and normal stresses acting on the rock are calculated using Equations (2.45) and (2.46). Zhou and Sandiford, (1994) extended the model to account for fracture intersection using an anisotropic stress field and introduced the concept of shear stress anisotropy to define and optimize both drilling direction and deviation angle. This parameter is given by Equation (2.28) which can be visualized as a normalized octahedral shear stress (Equation 2.17).

$$R_s = SSA = \frac{\tau_{oct}(\max) - \tau_{oct}(\min)}{\tau_{oct}(\min)} \quad (2.28)$$

The shear stress anisotropy (SSA) is a function of the effective principal stress ratios $n_h = \frac{\sigma_h}{\sigma_v}$ and $n_H = \frac{\sigma_H}{\sigma_v}$, the Poisson's ratio ν of the material, and the effective well pressure ΔP . The stable configuration is given by an optimum deviation angle β from the vertical and a drilling direction α with respect to the azimuth of the maximum horizontal principal stress.

Using the Mohr and Coulomb theories, Zhou and Sandiford, (1994) also proposed a measure of the wellbore stability by defining an effective failure stress as:

$$\sigma_{eff} = \sigma_{1rock\ failure} - \sigma_{1borehole} \quad (2.29)$$

where σ_{eff} is the effective failure stress, $\sigma_{1rock\ failure}$ is the rock strength evaluated using the Mohr and Coulomb theories (Equations 2.23 and 2.24) and the $\sigma_{1borehole}$ is

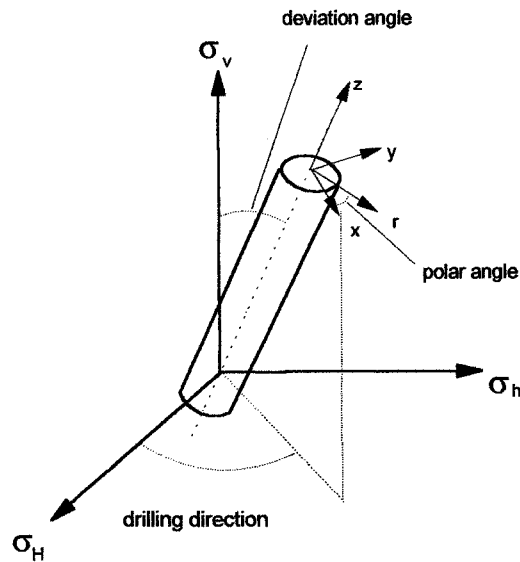


Figure 2.5: Inclined borehole (local and global coordinate system).

the maximum principal stress at the point on the borehole wall under consideration. A positive value of the effective failure stress indicates a stable condition. Also, using the concept of minimum SSA they showed that, contrary to intuitive expectation, in a highly anisotropic horizontal stress field (usually a strike-slip or tectonic environment) inclined wells may be more stable than vertical wells.

The octahedral shear stress, τ_{oct} , is considered the most useful parameter because the increasingly recognized fact that the octahedral shear stress is an important factor controlling the stress level at failure (Steiger and Leung, 1988, 1989). The conventional von Mises failure criterion for rocks (Woodland, 1990), in which the octahedral shear stress is considered to be the controlling rock stress at failure, and the effective strain energy failure criterion (Wiebols and Cook, 1968), which has been shown to be the most consistent with results of laboratory rock strength test (Hoek and Brown, 1980; Brady and Brown, 1985), and the elastic distortional strain energy is in fact directly proportional to the octahedral shear stress (Equation 2.18)

The in-situ stresses are transformed to the orientation of the borehole (Figure 2.5) using the following matrix operation:

$$\begin{pmatrix} \sigma_x \\ \sigma_y \\ \sigma_z \\ \tau_{yz} \\ \tau_{xz} \\ \tau_{xy} \end{pmatrix} = \begin{pmatrix} \sin^2 \beta & \cos^2 \beta \cos^2 \alpha & \cos^2 \beta \sin^2 \alpha \\ 0 & \sin^2 \alpha & \cos^2 \alpha \\ \cos^2 \beta & \sin^2 \beta \cos^2 \alpha & \sin^2 \beta \sin^2 \alpha \\ 0 & -\sin \alpha \cos \alpha \sin \beta & \sin \alpha \cos \alpha \sin \beta \\ -\sin \beta \cos \beta & \sin \beta \cos \beta \cos^2 \alpha & \sin \beta \cos \beta \sin^2 \alpha \\ 0 & -\sin \alpha \cos \alpha \cos \beta & \sin \alpha \cos \alpha \cos \beta \end{pmatrix} \cdot \begin{pmatrix} \sigma_v \\ \sigma_H \\ \sigma_h \end{pmatrix} \quad (2.30)$$

The stress field in radial coordinates is given by:

$$\begin{aligned} \sigma_r = \frac{1}{2} (\sigma_x + \sigma_y) \left(1 - \frac{a^2}{r^2}\right) + \frac{1}{2} (\sigma_x - \sigma_y) \left(1 + \frac{3a^4}{r^4} - \frac{4a^2}{r^2}\right) \cos 2\theta \\ + \tau_{xy} \left(1 + \frac{3a^4}{r^4} - \frac{4a^2}{r^2}\right) \sin 2\theta + \frac{a^2}{r^2} P_w \end{aligned} \quad (2.31)$$

$$\begin{aligned} \sigma_\theta = \frac{1}{2} (\sigma_x + \sigma_y) \left(1 + \frac{a^2}{r^2}\right) - \frac{1}{2} (\sigma_x - \sigma_y) \left(1 + \frac{3a^4}{r^4}\right) \cos 2\theta \\ - \tau_{xy} \left(1 + \frac{3a^4}{r^4}\right) \sin 2\theta - \frac{a^2}{r^2} P_w \end{aligned} \quad (2.32)$$

$$\sigma_z = \sigma_{zz} - 2\nu (\sigma_x - \sigma_y) \frac{a^2}{r^2} \cos 2\theta - 4\nu \tau_{xy} \frac{a^2}{r^2} \sin 2\theta \quad (2.33)$$

$$\tau_{r\theta} = \left[\frac{1}{2} (\sigma_x - \sigma_y) \sin 2\theta + \tau_{xy} \cos 2\theta \right] \left(1 - \frac{3a^4}{r^4} + \frac{2a^2}{r^2}\right) \quad (2.34)$$

$$\tau_{rz} = (\tau_{xz} \cos \theta + \tau_{yz} \sin \theta) \left(1 - \frac{a^2}{r^2}\right) \quad (2.35)$$

$$\tau_{\theta z} = (-\tau_{xz} \sin \theta + \tau_{yz} \cos \theta) \left(1 + \frac{a^2}{r^2}\right) \quad (2.36)$$

At the borehole wall ($r = a$) these equations reduce to:

$$\sigma_r = P_w \quad (2.37)$$

$$\sigma_\theta = \frac{1}{2}(\sigma_x + \sigma_y - P_w) - 2(\sigma_x - \sigma_y) \cos 2\theta - 4\tau_{xy} \sin 2\theta \quad (2.38)$$

$$\sigma_z = \sigma_{zz} - 2\nu(\sigma_x - \sigma_y) \cos 2\theta - 4\nu\tau_{xy} \sin 2\theta \quad (2.39)$$

$$\tau_{r\theta} = \tau_{rz} = 0 \quad (2.40)$$

$$\tau_{\theta z} = 2(-\tau_{xz} \sin \theta + \tau_{yz} \cos \theta) \quad (2.41)$$

the principal stresses are given by:

$$\sigma_1 = \sigma_r = P_w \quad (2.42)$$

$$\sigma_2 = \frac{1}{2}(\sigma_\theta + \sigma_z) + \frac{1}{2}\sqrt{((\sigma_\theta - \sigma_z)^2 + 4\tau_{\theta z}^2)} \quad (2.43)$$

$$\sigma_3 = \frac{1}{2}(\sigma_\theta + \sigma_z) - \frac{1}{2}\sqrt{((\sigma_\theta - \sigma_z)^2 + 4\tau_{\theta z}^2)} \quad (2.44)$$

and the normal and shear stresses are given by:

$$\sigma_s = \frac{1}{2}(\sigma_1 - \sigma_3) \sin 2\psi \quad (2.45)$$

$$\sigma_n = \frac{1}{2}(\sigma_1 + \sigma_3) + \frac{1}{2}(\sigma_1 - \sigma_3) \cos 2\psi \quad (2.46)$$

where ψ is the angle between the plane and σ_1

Other analytical models have been proposed, a complete review of them can be found in Charlez (1997).

2.2.2.2 Numerical models

Numerical solutions provide approximate values of the unknown quantities at specific points throughout the body (Figure 2.6) . These solutions are not general; however, they are specific to a particular set of conditions. Thus to investigate the effect of a change in a specific variable one must calculate another specific solution for the different variable value. The advantage of numerical solutions for investigating rock deformations, is that one can analyze geometrically complex geobodies and large and complex deformations. Problems in geomechanics involve considerably greater levels of data uncertainty and even lack of data. Geological heterogeneity, large-scale features (joints, faults, etc.) uncertainty of loading conditions (tectonic and gravitationally-induced), time-dependent changes of materials response, coupled interactions between fluids and solids, etc. Unfortunately, all may have an important influence on the behavior of the rock and all are often unknown in detail; so geomechanics problems are often data limited. However, “numerical experiments” using a computer can provide important insights into such variables that appear to be the most critical in controlling the overall behavior of the rock.

An appropriate methodology is necessary whatever numerical solution is used, but additional benefits are obtained if the numerical technique and solution procedures have been developed with the specific characteristics of geological materials (heterogeneity, non linear deformation behavior, large strain, coupled fluid/solid interactions, discontinuous displacement and slip along joints, faults, etc.) in mind.

In the market nowadays are basically two methodologies to apply numerical methods: i) continuum; and, ii) discrete models. Continuum models use either finite difference solutions or finite element procedures. Both methods translate a set of differential equations into matrix equations for each element, relating forces

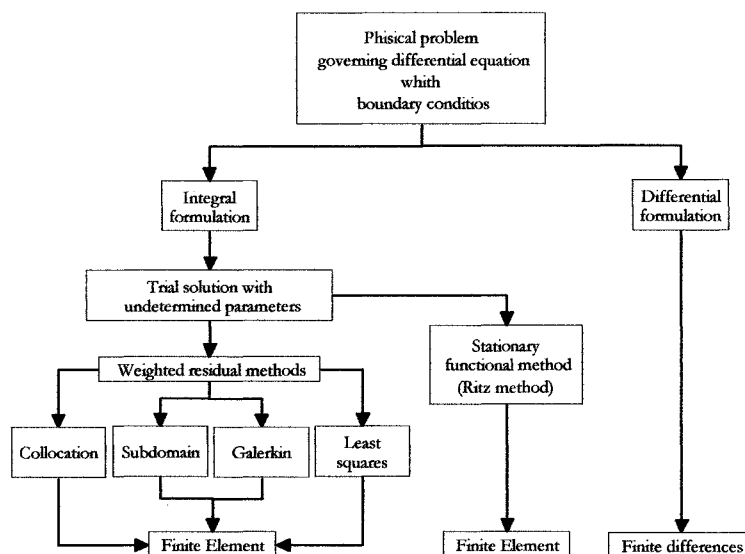


Figure 2.6: Numerical method available to approximate the solution in simulation.

at nodes to displacements of nodes. Although the equations are derived differently, for elastic material the resulting element matrix are the same between explicit finite difference simulators and finite element methods for constant strain triangles. However, both approaches differ in some aspects (Fairhurst and Lorig, 1999):

- “Mixed discretization” can be used for accurate modelling of plastic collapse loads in plastic flow which is physically more justifiable than the “reduced integration” scheme commonly used with finite elements.
- Dynamic equations of motion can be used even with modelling systems that are essentially static. This enables finite differences methods to follow physically unstable processes without numerical distress.
- Explicit schemes can follow arbitrary non-linear in stress/strain laws in almost the same computer time as a linear law, whereas implicit solutions can take significantly longer to solve non-linear problems. Furthermore, it is not necessary to store any matrices, so a large number of elements may be mod-

elled with less memory requirements, and large strain simulations are not more time consuming because there is no stiffness matrix to be updated.

Continuum methods attempt to account for the presence of discontinuity by an equivalent continuum representation. However, equivalent continuum models can only give a limited representation for the behavior of jointed rock.

Discontinuous methods are numerical techniques (explicit finite difference codes) formulated specifically to analyze the behavior of discontinuous or particulate systems. The best known and most advanced discontinuous method is the distinct element method, which was conceived as a mean to model the progressive failure of rock slopes (Cundall, 1971). The distinct element method is not very different from the other numerical methods, but has the following attributes associated with it:

- The rock mass is composed of individual blocks that can undergo large rotations and displacements relative to each another.
- Interaction forces between blocks arise from changes in their relative geometrical configuration.
- The solution scheme is explicit in time.

2.3 Poroelasticity

2.3.1 Introduction

The poroelasticity theory assumes pore-pressure dissipation according to Darcy's law (Detournay and Cheng, 1988). Based on this assumption the effect of an excess pore pressure generated by an external load or any other event can be estimated and quantified. The coupled diffusion-deformation mechanism generates a time-dependent effect in the response of the rock. In low permeability formations, the influence of excess pore pressure is more pronounced than in high permeability

formations, in which the dissipation takes place almost instantaneously. Rapid drainage of the rock near the borehole has direct impact on the stress concentration. Thus, at the borehole wall, the rock is characterized by the drained elastic modulus and beyond by a stiffer undrained modulus. As a result of this contrast, the borehole wall is partially shielded, at early times, from the stress concentration.

Poroelasticity is the basis of the theory of consolidation used in soil mechanics and is applicable to fundamental problems in the petroleum industry, such as the evaluation of stresses induced by the fluid flow through the elastic porous media, which could induce subsidence by fluid withdrawal or tensile failure by pressurization of a borehole.

2.3.2 Fundamental concepts of poroelasticity

Terzaghi (1948) was the first to develop a theory that takes into account the effect of pore fluid on the quasi-static deformation of soils in 1923. He introduced the concept of effective stress based on the assumption of incompressible fluid and solid material, which was defined as:

$$\sigma_{ij}^{eff} = \sigma_{ij} + p\delta_{ij} \quad (2.47)$$

However, it is Biot (1941) who first formulated the original poroelastic constitutive relations using the total stress tensor and pore pressure. He assumed a linear relationship between stress and strain, an isotropic material, and the reversibility of stress-strain relations under final equilibrium conditions. Later, Biot (1955) extended his isotropic theory to anisotropy, based on a generalization of Hooke's law. However, the anisotropic material coefficients remained unclear until Thomson and Willis (1991) reformulated the theory through micromechanical analyses. The identification of these coefficients and their relations to engineering constants led to the development of practical models for laboratory measurements (Cheng, 1997) and the extension of fundamental solutions of important problems to transversely isotropic media under non isothermal conditions (Ekbote et al., 2000).

Rice and Cleary (1976) linked the poroelastic parameters to physical concepts well understood in rock mechanics. They emphasized the limiting behaviors, drained ($p = cte.$) and undrained ($\zeta = 0$), of a saturated porous media which simplify the interpretation of asymptotic poroelastic phenomena. This basic state variables were the total stresses and the pore pressure.

Starting from the Biot's constitutive equation:

$$\varepsilon_{ij} = \frac{1 + \nu}{E} \sigma_{ij} - \frac{\nu}{E} \sigma_{kk} \delta_{ij} + \frac{p}{3H} \delta_{ij} \quad (2.48)$$

Rice and Cleary rearranged it as:

$$2G\varepsilon_{ij} = (\sigma_{ij} + p\delta_{ij}) - \frac{\nu}{1 + \nu} (\sigma_{kk} + 3p) \delta_{ij} - \frac{2G}{3K'_S} p \delta_{ij} \quad (2.49)$$

where E , ν , and G are Young's modulus, Poisson's ratio, and the shear modulus of the solid skeleton, respectively. H is a material constant and K'_S is given by:

$$\frac{1}{K'_S} = \frac{1}{K} - \frac{1}{H} \quad (2.50)$$

K being the drained bulk modulus, defined as:

$$K = \frac{2G(1 + \nu)}{3(1 - 2\nu)} \quad (2.51)$$

Also, Rice and Cleary represent the variation of fluid content as follow:

$$\zeta = V - V_o = \frac{1}{3H} (\sigma_{kk} + 3p) - \frac{V_o}{K''_S} p \quad (2.52)$$

where V_o is a reference volume fraction in the unstressed state.

The relationship between the constant proposed by Biot and the new constant K''_S is:

$$\frac{1}{R} = \frac{1}{H} - \frac{V_o}{K''_S} \quad (2.53)$$

According to Detournay and Cheng (1993), the bulk modulus of the solid constituent (K_S) can be related in special cases to the constants K'_S and K''_S .

The mass m of the pore fluid per unit volume can be expressed in a linearized form as:

$$\begin{aligned}\Delta m &= m - m_o = \rho_o \Delta V + V_o \Delta \rho \\ &= \frac{\rho_o V_o}{K_f} p + \frac{\rho_o}{3} \left(\frac{1}{K} - \frac{1}{K'_S} \right) (\sigma_{kk} + 3p) - \frac{\rho_o V_o}{K''_S} p\end{aligned}\quad (2.54)$$

where m_o and ρ_o are obtained in the reference state and K_f is bulk modulus of the fluid, which is given by:

$$K_f = \frac{\rho_o p}{\rho - \rho_o} \quad (2.55)$$

From Equation (2.54), it is clear that a pore pressure p , proportional to the total pressure $P = -\frac{\sigma_{kk}}{3}$, is induced under undrained conditions ($\zeta = 0$); i.e.

$$p = BP \quad (2.56)$$

where the coefficient B is known as the Skempton pore pressure coefficient ($B = \frac{R}{H}$), given by:

$$B = \frac{\frac{1}{K} - \frac{1}{K'_S}}{\frac{V_o}{K_f} + \frac{1}{K} - \frac{V_o}{K''_S} - \frac{1}{K'_S}}$$

On the other hand, Equation (2.49) can be separated into a deviatoric and a volumetric response; i.e.

$$e_{ij} = \frac{1}{2G} s_{ij} \quad (2.57)$$

$$\varepsilon = - \left(\frac{P}{K} - \frac{p}{H} \right) \quad (2.58)$$

where s_{ij} ($s_{ij} = \sigma_{ij} + P\delta_{ij}$) and e_{ij} ($e_{ij} = \varepsilon_{ij} - \frac{\varepsilon}{3}\delta_{ij}$) denote the deviatoric stresses and strains; P the mean or total pressure (isotropic compressive stress); and, ε (ε_{kk}) the volumetric strain.

Substituting the value of p given in Equation (2.56) into Equation (2.58) indicates that the volumetric strain is proportional to the total pressure P under the undrained conditions ($\zeta = 0$):

$$\varepsilon = -\frac{P}{K_u} \quad (2.59)$$

where,

$$K_u = \frac{KH^2}{H^2 - KR} \quad (2.60)$$

or,

$$K_u = K \left(1 + \frac{KR}{H^2 - KR} \right) \quad (2.61)$$

is the undrained bulk modulus of the material.

Under drained conditions ($p = 0$), the volumetric strain is also proportional to the total pressure (see Equation 2.58); i.e.

$$\varepsilon = -\frac{P}{K} \quad (2.62)$$

From Equations (2.59) and (2.62) it is clear that poroelastic material, in the limiting case, behaves as an elastic one. Also, using Equations (2.52) and (2.62) it can be shown that:

$$\zeta = \alpha\varepsilon \quad (2.63)$$

where $\alpha = \frac{K}{H}$. This equation gives a meaning to the constant α as the ratio of the fluid volume gained (or lost) in a material element to the volume change of that element, when the pore pressure is allowed to return to its initial state. Thus, the three volumetric constants, K , $K_u [K, \infty]$, and $\alpha [0, 1]$ have physical meanings that are associated with the drained and undrained responses of the material.

Alternative expressions for the volumetric response using the basic set of constants, K , K_u , and α , are given by:

$$\varepsilon = -\frac{1}{K} (P - \alpha p) \quad (2.64)$$

$$\zeta = -\frac{\alpha}{K} \left(P - \frac{p}{B} \right) \quad (2.65)$$

where,

$$B = \frac{K_u - K}{\alpha K_u} \quad (2.66)$$

Equations (2.64) and (2.65) can inversely be written as:

$$P = \alpha M \zeta - K_u \varepsilon \quad (2.67)$$

$$p = M (\zeta - \alpha \varepsilon) \quad (2.68)$$

where,

$$M = \frac{K_u - K}{\alpha^2} = \frac{H^2 R}{H^2 - KR} \quad (2.69)$$

The constant M is called the *Biot modulus* and is defined as the inverse of a storage coefficient or the increase of the amount of fluid (per unit volume of rock) as a result of a unit increase of pore pressure, under constant volumetric strain.

$$\frac{1}{M} = \left(\frac{\partial \zeta}{\partial p} \right)_\varepsilon \quad (2.70)$$

Detournay and Cheng (1988) rewrote the constitutive equations in a more elegant way, manipulating the Rice and Cleary equations as:

$$\begin{aligned} \sigma_{ij} &= 2G\varepsilon_{ij} + \frac{2G\nu}{1-2\nu} \varepsilon \delta_{ij} - \alpha p \delta_{ij} \\ p &= -\frac{2GB(1+\nu_u)}{3(1-2\nu_u)} \varepsilon + \frac{2GB^2(1+\nu_u)^2(1-2\nu_u)}{9(\nu_u-\nu)(1-2\nu_u)} \zeta \end{aligned} \quad (2.71)$$

where α can be defined as:

$$\alpha = \frac{3(\nu_u - \nu)}{B(1 + \nu_u)(1 - 2\nu)} \quad (2.72)$$

From Equation (2.71) it is clear that the Biot effective stress (Equation.2.47) is proportional to the solid strain in an identical elasticity relation.

Combining the constitutive equations (2.71), the equilibrium equations ($\sigma_{ij,j} = 0$), Darcy's law ($q_i = -\kappa p_{,i}$), and the continuity equation for the fluid phase ($\frac{\partial \zeta}{\partial t} + q_{i,i} = 0$), and neglecting body forces and fluid sources, they derived the borehole poroelastic response of isotropic porous media and presented numerical solutions of wellbore stress and pore pressure by superposing the three-mode loading aspects. The solutions were presented in the Laplace domain.

2.4 Shale

2.4.1 Introduction

Argillaceous rocks are fine-grained detrital sedimentary rocks formed by the consolidation of clay, silt, or mud and are characterized by their finely laminated structure, cation exchange capacity, specific surface area, and water content. They can contain a wide range of clay minerals, and accessory minerals such quartz, carbonates, and feldspars. The swelling of clay particles depends on the net effect of the intermolecular forces acting on the clay surfaces. For surface separations ranging from the scale of a water molecule (≈ 0.25 nm) to the scale of clay particles ($\approx 2 \mu\text{m}$), the operating forces and their respective ranges are (Israelachvili, 1991; Diek et al., 1996): attractive van der Waals forces (≤ 10 nm), attractive ion-ion correlation forces (≤ 4 nm), oscillatory hydration forces (≤ 2 nm), monotonic repulsive hydration forces (≤ 10 nm), and repulsive electric double-layer forces ($\leq 2 \mu\text{m}$). The attractive and oscillatory forces tend to limit the swelling to very small separation ($\approx 1, 2$ nm). This type of expansion is referred to as crystalline swelling, signifying that the overall crystal morphology is preserved. The monotonic repulsive hydra-

tion forces tend to extend this crystalline swelling, still limitedly, up to 10 nm with increasing electrolyte concentration. On the other hand, in the presence of diluted electrolytes, the repulsive electric double-layer forces dominate the interactions at larger surface separations ($> 10\text{nm}$), and tend to expand the interlayer unlimitedly up to the size of a particle. The change in the fluid chemistry alters the equilibrium of these forces, which could lead to the expansion of the surface separation and the hydration of the clay surface groups and interlayer cations. Thus, the hydration reaction influences the net result of these forces.

2.4.2 Clay-Water Interactions

Fundamental molecular concepts of clay-water interactions, are basic for understanding the hydration, swelling, and rheological behavior of clays. Of special importance are the colloidal characteristics of the clay particles, the hydration reactions of clays and ions, the inter-particle forces in aqueous media, the molecular configuration of the clay/water interface, and the stability of clay suspensions. These fundamental concepts of colloid chemistry are described in detail in numerous textbooks, like the monographs by Hunter (1987) and Everett (1988).

Aqueous clay suspensions could be considered as a system of four components: clay particles, water molecules, cations (counter-ions), and anions (co-ions). The contribution of each component is related to its intrinsic characteristics and to its interaction with the other three components, so that the hydration of clays and the behavior of aqueous clay suspensions could be treated as the total interaction between these components.

In general, primary clay particles consist of a coherent stack of silicate layers; they may range in thickness from a single to a few tens of layers. The properties of the clay particles that affect their rheological behavior are: morphology (size, shape) and flexibility of clay particles; surface area of clay particles and electrical charges on them; microstructure and micropores in clay aggregates; and modes of association of clay particles in suspensions.

Clay particles often occur as aggregates displaying various textures determined by the shape and arrangement of the constituent primary particles. The cluster of the clay aggregates may generate a micro-structure (fabric) often with large pores between the constituent clay aggregates. Thus, a clay may develop three kinds of pores: interlamellar pores within the primary particles; intra-aggregate pores between the primary particles within the aggregates; and inter-aggregate pores within the microstructure (fabric).

2.4.2.1 Electrically charged surfaces of clay particles

Clay particles may expose two types of basal surfaces that may be distinguished as "siloxane" and "hydroxide" surfaces. The siloxane surfaces consist of smooth planes of basal oxygen attached to the silica tetrahedra forming pseudo-hexagonal rings. A hydroxide surface consists of molecularly smooth planes of hydroxyl ions. Kaolinite and other 1:1 type layer silicates display a hydroxyl surface on one side of the layer, and a siloxane surface on the other side. Smectites and other 2:1 type layer silicates are bounded by siloxane surfaces on both sides.

The distribution of charge sites in the silicate layer is significant for the interlamellar hydration of 2:1 type clay minerals. Basal oxygen of the electrically neutral layers may act as weak Lewis bases (electron donors) and form weakly bounded aqueous complexes. Ionic substitutions within the silicate layer may generate excess negative charges on the basal oxygen and make stronger Lewis bases that can form stable aqueous complexes with water dipoles through H-bonds. Sposito (1982) pointed out that H-bonds between water molecules and the basal oxygen are considerably stronger when the charges are derived from tetrahedral substitutions than when they are derived from the octahedral substitutions.

Ionic substitutions in tetrahedral and octahedral sheets are assumed to be responsible for the creation of permanent charges on the basal surfaces of the layer silicates.

Bleam (1990a and 1990b) established the factors that define the electrostatic

potentials on clay surfaces.

The "localization of layer charge" on the certain basal oxygen is responsible for the development of a periodic electrostatic potential on the layer surface. However, there are no "localized" charges on the basal surfaces of smectites having octahedral excess charges. The latter reside on the octahedral cations which are about 0.5 nm away from the interlayer. The octahedral excess charges are, therefore, well shielded and generate weak fields at the basal surfaces.

2.4.2.2 Hydration of Clays

Clay hydration involves adsorption of water molecules on the clay surfaces that are exposed in different pore spaces of the clay. Three modes of clay hydration can be distinguished and may take place simultaneously with increasing water activity: interlamellar hydration which involves the adsorption of limited amounts of water molecules on the internal surfaces of primary clay particles; continuous (osmotic) hydration which is related to an unlimited adsorption of the water on the internal and external surfaces of primary particles; and capillary condensation of free water in micropores within the clay fabric (i.e., in the inter-aggregate and intra-aggregate pores).

The main elements of interlamellar clay hydration are: the hydration of interlayer cations; the interactions of clay surfaces with both water molecules and interlayer cations; and the activity of water (water content) in the system.

These interactions will be described first in the vapor phase; then in the liquid phase using "smectite hydration" as a model.

Just like the step-wise hydration of ions in the gas phase, clays may display a step-wise hydration in the vapor phase at low relative vapor pressures (P/P_0) by forming interlamellar hydration complexes. The interlamellar hydration of the clays has been well documented by Hendricks et al., (1940); Mooney et al., (1952a and 1952b); Norrish (1954); van Olphen (1965 and 1969); Suquet et al., (1975); MacEwan and Wilson (1980); Suquet and Pezerat (1987); Krachenbuechl et al.,

(1987); and Kahr et al., (1990). The interlamellar hydration complexes of clays are operationally distinguished by X-ray or neutron diffraction in terms of numbers of monomolecular water layers that are assumed to be intercalated between the silicate layers. The number of the water layers in well-defined interlamellar hydration complexes ranges from zero to three corresponding to zero-, one-, two-, and three-layer hydrates of clays.

Representative basal spacings for various n-layer hydrates of smectites and vermiculites were compiled by Suquet et al., (1977); MacEwan and Wilson (1980); and Suquet and Pezerat (1987). The main factors affecting interlamellar hydration of smectites and vermiculites may be summarized as: hydration energy of interlayer cations; polarization of water molecular by the interlayer cations; variation of electrostatic potential on the clay surface as determined by the magnitude and distribution of the charges in the silicate layers; activity of water (relative water vapor pressure); and size and morphology of smectite particles and the fabric of the clay.

2.4.3 Swelling phenomenon while drilling

Many different theories have been presented to explain the swelling phenomenon of shales, such as capillary suction, osmosis pressure, and hydraulic pore pressure imbalance. However, until now, the experimental data have not totally and effectively explained or even understood.

The pioneering work of Low and Anderson, (1958) suggests osmosis as the only mechanism responsible for swelling pressures generated by shales. They presented the osmotic pressure equations for determining the swelling properties of soil and gave the structural components of the swelling pressure of clays. Their theory is based on the principle that the shale itself acts as a semi-permeable membrane, allowing for the generation of osmotic pressures between the fluid in the shale and the drilling fluid. Chenevert et al., (1970 and 1993) used this osmotic pressure theory to propose shale control procedures, using the concept of "balanced activity".

Later Fritz et al. (1983) supported the osmotic theory as a basis to explain water and ion transport. They reported that clay membranes were not ideal and that the degree of "ideality" was a function of the membrane's cation exchange capacity, porosity, and concentration of pore fluid. They suggested that such "ideality" for a given shale-liquid system could be determined from the measurement of swelling pressures, which would then be used to calculate a "reflection coefficient," which is defined as the ratio of the measured swelling pressure divided by the theoretical swelling pressure for a perfect membrane. Mody and Hale, (1993) took a similar approach, postulating that *membrane efficiency* is a function of the confining pressure acting on the shale.

Pashley and Israelachvili (1984) and Pashley et al. (1989) described the hydration forces and chemical mechanisms behind the ion movements between mica surfaces. Their analysis takes into account the molecular interactions between the clay particles and the ions in the pores and drilling fluids. Barbour et al. (1989) presented a theoretical description of two potential mechanisms that could explain osmotic volume changes. The first one, *osmotic consolidation*, occurs as a result of changes in the electrostatic forces between the clay particles, whereas the second, *osmotically induced consolidation*, occurs because of fluid flow in response to osmotic gradients. However, Ballard et al. (1992) investigated water transport through shale and concluded that shales do not act as semi-permeable membranes and that ions can freely diffuse through them. Bol et al. (1992) came to the same conclusion after running a series of experiments, stating that "osmosis was not observed". Santarelli et al. (1995) discussed the swelling phenomenon and came to the conclusion that swelling pressures are caused by gas present in the pore structure of the rock, which induces capillary effects. They concluded that it is unlikely that swelling actually occurs under downhole conditions. Santos et al. (1996) concluded that rather than the gas contained in the pores driving the swelling process, the water content in shale and its distribution are controlling the changes that are occurring in the rock. However, both of these hypotheses neglect basic concepts of

surface chemistry and other phenomena at micro-scale levels that play a significant role in shale behavior. Also they can not explain the shale stability success usually achieved when balanced activity oil-base muds are used.

Diek et al. (1994 and 1996) have punctuated that mass transport into the formation leads to changes in the pore fluid chemistry, ion exchange, mineral dissolution, and maybe stress corrosion in certain fractured shale. The first two processes, mainly caused by solute diffusion, alter the equilibrium of the interlayer surface forces between clay platelets which may either contract, expelling bound water, or expand, uptaking free water. The last two processes, mainly caused by water invasion, produce weakened shale that become prone to erosion.

During the past decade, the extension of the classic poroelastic theory of Biot (1941) for coupling isothermal processes: mechanical, hydraulic, and chemical causing shale deterioration and borehole instability while drilling have been studied by a number of researchers. Sherwood (1993) and Sherwood and Bailey (1994) developed a coupled, Biot-like model in which the shale is an ideal ion exclusion membrane. The model neglects the diffusion of ions and limits the analysis to isotropic media under isothermal conditions; also, they assumed that the equilibrium state is independent of composition and only dependent on the pore pressure. Van Oort (1997) presented solutions for fluid pressure, filtrate invasion, and solute diffusion around a wellbore but the study did not consider transient effects, which play an important role and affect pressure transmission and solute diffusion. Ghassemi and Diek (2002) extended the model of Sherwood and Bailey to non-isothermal conditions to consider the influence of thermal osmosis on shale instability. They also proposed a linear chemo-poroelastic model for transversely isotropic shales including solute diffusion (Diek and Ghassemi, 2002). Using a non-equilibrium thermodynamics approach Heidung and Wong (1996) presented a fully-coupled Biot-like model for hydration swelling based on an extended version of the poroelastic model and Darcy's transport equation that considered ion diffusion. Nevertheless, the model is limited to isotropic porous media saturated by an incompressible fluid.

2.5 Summary

Drilling through thousands of meters increases the possibility of crossing all kinds of formation's features (swelling formation, weak layers, fractures, faults, etc.), which combined with a complex geological environment characterized by high horizontal stresses, steeply dipping beds and alternating sand/shale sequences lead to extremely severe instability problems not normally encountered in past common oilfield drilling. In addition, the very wide range of conditions under which clay minerals may form and the very large number of intervening factors, geological settings, physico-chemical parameters controlling the diagenetic process, etc. arise the complexity of genetic, structure and reactivity of clay minerals which are the outcome of a complex geological process. It is further complicated by the fact that, here, the interaction of matter and energy takes place in a mediating agency (water), as a result of which the parameters of the process become functions of time and, as the medium is in motion, also of place. These events also lead structural alteration and submineralic process, which are reflected in long-range interaction between particles and short-range interaction between structural layers. As a result, the swelling characteristic of shales changes. The surface of clay particles also alters the structure-sensitive properties of water to an appreciable distance and the swelling pressure of the clay is related to the degree of this alteration. The double layer contribution to the swelling pressure of the clay is insignificant because of lack of dissolution of the exchangeable cation; therefore, the swelling clays is due primarily to surface hydration.

On other hand, preexisting discontinuities present a basic mechanism of destabilization: mud invasion increases pore pressure in discontinuities, but at the same time decreases the effective normal stress which previously stabilized them. Then a shear release results in a lateral shift of the borehole which can be from a few millimeters to centimeters. All these mechanisms provoke abnormal torque, tight hole, difficulties in run-in-hole or pull out of hole, stuck pipe, drilling string failures,

etc. These situations are not always solved by using the classical drilling remedy: “mud weight increase and jarring”, which often worsens the instability problems, especially if shales are present. Here, special methods and remedies are necessary such as: avoiding high mud density wherever it is not strictly necessary for gas kick control; increasing the sealing capacity of the mud and reducing the filtrate at the maximum; avoiding swab and surge effect that increase the internal pressure; and foreseeing the possibility of back-reaming using special tools to avoid further damage. However, the identification and understanding of the basic rock failure mechanisms are fundamental to the choice of a solution.

Rock failure mechanisms that are responsible for wellbore instability problems have been extensively studied in the literature. They are related to the in-situ conditions of the rock masses, such as, geotectonic conditions, temperature, pore fluid interactions, composition, loading condition, etc., and can be classified as: i) compressive failure, where hole size reduction is observed, due to the plastic flow of the rock into the borehole (borehole collapse) or hole enlargement due to rock failing in a brittle manner and falling into the borehole (break-out); ii) tensile failure, where fracturing due to tensile splitting of the rock for excessive wellbore pressure is observed; and, iii) shear failure, when drilling through discontinuity and lateral shift of the wellbore trajectory occurs due to the slip of the fault. However, the changes of these in-situ conditions are often overlooked in wellbore stress analyses, neglecting thermal stresses and capillary effects in porous rocks with high and low permeability which is now possible thanks to the recent developments in thermoporoelasticity.

Finally, the phenomenological complexity of the wellbore stability problems in complex geotectonic environments require innovative and state-of-the-art wellbore-stabilization methods and numerical simulation to reduce the total cost associated to construction and productive life of the oil and gas wells; because a stable wellbore during the drilling, completion and production phases maximizes the well's economical potential.

3 Theoretical Approach

3.1 Introduction

This dissertation contains an extension of poroelasticity by fully coupling the three processes: mechanical, hydraulic, and chemical in transversely isotropic porous media saturated by a slightly compressible liquid consisting of a solvent and one or more solute. The results are valid for both neutral and electrolyte solutions. The theory generalizes Heidug and Wong's (1996) model by considering compressibility of the fluid and anisotropy. One will investigate an isothermal situation in which small disturbances occur to an equilibrium state, defined by an initial stress, pore pressure and solute mass fraction, at constant temperature, in a chemically active poroelastic medium. There are no body forces and volume fluid sources. The dissipation of energy is due to the relative motions between the fluid components and the solid. The fluid saturated porous medium is viewed as an open thermodynamic system. Under the actions of external forces, an element of the system deforms elastically as well as exchanges fluid mass with the surroundings. The model aims to describe the rock behavior under mechanical and chemical loading. It targets the chemical effects of electrolyte solutions causing hydration and swelling of the rock. The electrical effects are ignored based on the assumption that the influences of the electric field and resulting current are negligible. Therefore, the fluid is considered a solution composed of chemical components (a solvent and one or more solute) and not of ions. The fluid saturated porous medium is composed of a solid matrix which contains two kinds of connected voids of different scales: pore spaces filled with freely diffusing pore fluid, and interlayer spaces occupied by bound water



Figure 3.1: Pore model composed of a solid matrix with two kinds of connected pores of different scales.

between clay platelets (Figure 3.1). The model considers the hydration of the wetted clay minerals under the assumption that the hydration reaction rates are much faster than the rates at which macroscopic changes of hydraulic and chemical states are communicated through the rock, i.e. local physical and chemical equilibria are sustained (Heidug and Wong, 1996). The state equation for the fluid density is assumed linear. Similarly, the solute chemical potential is related to its mass fraction linearly. Field equations for linear chemical loading are obtained by implementing the derived rock constitutive equations and phenomenological transport equations into the momentum, mass and energy balance equations. The resulting Navier-type equations couple the three solid displacements to pore pressures and solute mass fractions. The driving forces of the flows are identified with the forces associated with the relative motions between the fluid components and the solid. The last derived field equations are the fully coupled fluid and solute diffusions, respectively. Finally, the swelling parameter and diffusivity are explored.

Flow/Gradient	Hydraulic	Chemical Potential
Fluid	Hydraulic Conduction ^{direct}	Chemical osmosis ^{Indirect}
Solute	Pressure diffusion ^{indirect}	Chemical Diffusion ^{direct}

Table 3.1: Direct and Coupled Flow Phenomena

3.2 Transport processes.

Various transport processes occur in fluid saturated chemoporoelastic media (e.g., shales) under isothermal conditions. The presence of hydraulic pressure and chemical potential gradients engender both direct and indirect or coupled flows. Direct flows are in the form of hydraulic conduction and chemical solute diffusion; whereas indirect or coupled flows are in the form of chemical osmosis and pressure solute diffusion, as depicted in Table 3.1. In summary, the solid deformations and stresses depend on changes in the hydraulic pressure and chemical potential components of the fluid.

A macroscopic thermodynamics theory of irreversible processes was developed by Onsager (1931) and refined by Casimir (1945) in which n independent forces \mathbf{X}^b are related to the n independent fluxes \mathbf{I}^a by the following linear relationships:

$$\mathbf{I}^a = \sum_{b=1}^n \mathcal{L}^{ab} \mathbf{X}^b \quad (a, b = 1, 2, \dots, n) \quad (3.1)$$

such that the tensor \mathcal{L} is symmetrical; i.e.

$$\mathcal{L}^{ab} = \mathcal{L}^{ba} \quad (a, b = 1, 2, \dots, n) \quad (3.2)$$

according to Onsager's theorem derived by means of general methods of statistical mechanics. The reciprocal relations in Equation (3.2) are an implication of the property of *microscopic reversibility*; i.e., the invariance of the equations of motion of individual microscopic particles under *time reversal*. Moreover, the phenomenological coefficients \mathcal{L}^{aa} express, for example, the coefficients of permeability, solute diffusion, thermal conductivity, etc.. The coefficients \mathcal{L}^{ab} ($a \neq b$) are connected to the cross or interference phenomena, they express, for example, the coefficients of

solute reflection, pressure diffusion, thermal diffusion, etc.. They are represented by scalars for isotropic flows, whereas they assume the role of the tensors for anisotropic flows. The occurrence of irreversible processes is represented by the local entropy production rate ϑ or Rayleigh's dissipation function \mathcal{D} which is expressed by the bilinear form:

$$T\vartheta \equiv 2\mathcal{D} = \sum_{a=1}^n \mathbf{I}^a \cdot \mathbf{X}^a \quad (3.3)$$

where T is the absolute temperature. Inserting (3.1) into (3.3), one gets:

$$2\mathcal{D} = \sum_{a,b=1}^n \mathcal{L}^{ab} (\mathbf{X}^a \cdot \mathbf{X}^b) \geq 0 \quad (3.4)$$

a positive definite quadratic expression according to the second law of thermodynamics, which vanishes for the reversible limiting case. The linear relations in (3.1) allow the construction of a reciprocal set of expressions in which the forces are represented as a linear functions of the fluxes such that:

$$\mathbf{X}^a = \frac{\partial \mathcal{D}}{\partial \mathbf{I}^a} = \sum_{b=1}^n R^{ab} \mathbf{I}^b \quad (3.5)$$

where the coefficients $R^{ab} = [\mathcal{L}^{-1}]^{ab}$ are elements of the inverse tensor $\mathbf{R} = \mathcal{L}^{-1}$, and represent generalized resistances or frictions. The determinant of \mathcal{L} is nonvanishing ($|\mathcal{L}| \neq 0$) since the fluxes \mathbf{I}^a are independent. Inserting (3.5) into (3.3) one gets:

$$2\mathcal{D} = \sum_{a,b=1}^n R^{ab} \mathbf{I}^a \cdot \mathbf{I}^b \quad (3.6)$$

For isothermal processes, the rate of dissipation energy $2\mathcal{D}$ can be expressed from (3.3) as:

$$T\vartheta \equiv 2\mathcal{D} = \sum_{\beta=1}^n \mathbf{I}^\beta \cdot \mathbf{X}^\beta \quad (3.7)$$

$$T\vartheta \equiv 2\mathcal{D} = - \sum_{\beta=1}^n \mathbf{I}^\beta \cdot \nabla \mu^\beta \quad (3.8)$$

where the right hand side (RHS) term in Equation (3.8) denotes the dissipation energy due to the relative motions between the fluid components and the solid matrix such that the fluxes \mathbf{I}^β measure the mass flow of the β^{th} fluid component relative to the solid velocity:

$$\mathbf{I}^\beta = \rho^\beta (\mathbf{v}^\beta - \mathbf{v}_s) \quad (3.9)$$

here μ^β , ρ^β , and \mathbf{v}^β denote the chemical potential, the mass density (per unit volume of the porous medium), and the velocity of the β^{th} fluid component, respectively, n denotes the total number of fluid components, and \mathbf{v}_s denotes the solid velocity. The independent diffusion fluxes, \mathbf{I}^β , can be decomposed into:

$$\mathbf{I}^\beta = \mathbf{J}^\beta + \check{\rho}^\beta \left(\frac{\mathbf{J}^f}{\rho_f} \right) \quad (3.10)$$

where,

$$\check{\rho}^\beta = \left(\frac{\rho^\beta}{\phi} \right); \quad \check{\rho}_f = \left(\frac{\rho_f}{\phi} \right) \quad (3.11)$$

are the intrinsic mass density of the β^{th} fluid component and total fluid mass density (per unit volume of the fluid), and ϕ denotes porosity. The dependent fluxes, \mathbf{J}^β , measure the mass flow of the β^{th} fluid component relative to the mixture's barycentric velocity $\mathbf{v}_f = \sum_\beta \left(\frac{\rho^\beta}{\rho_f} \right) \mathbf{v}^\beta$ and $\rho_f = \sum_\beta \rho^\beta$ is the total fluid mass density relative to the unit volume of the porous medium (solid-fluid mixture):

$$\mathbf{J}^\beta = \rho^\beta (\mathbf{v}^\beta - \mathbf{v}_f); \quad \sum_\beta \mathbf{J}^\beta = 0 \quad (3.12)$$

The mass flow \mathbf{J}^f of the fluid relative to the solid velocity is given by:

$$\mathbf{J}^f = \rho_f (\mathbf{v}_f - \mathbf{v}_s) = \check{\rho}_f \dot{\mathbf{w}} \quad (3.13)$$

where,

$$\dot{\mathbf{w}} = \phi (\mathbf{v}_f - \mathbf{v}_s) \quad (3.14)$$

is Darcy's filter velocity. Using (3.8), (3.10), (3.13), and Gibbs-Duhem relation:

$$\sum_{\beta} \check{\rho}^{\beta} \nabla \mu^{\beta} = \nabla p \quad (3.15)$$

the dissipation function (3.8) can be written as:

$$2\mathcal{D} = -\mathbf{J}^f \cdot \frac{\nabla p}{\check{\rho}_f} - \mathbf{J}^{\beta} \cdot \nabla \mu^{\beta} \quad (3.16)$$

where p is the pore pressure. For a binary solution, the dissipation function (3.16) becomes:

$$2\mathcal{D} = -\mathbf{J}^f \cdot \frac{\nabla p}{\check{\rho}_f} - \mathbf{J}^S \cdot \nabla (\mu^S - \mu^D) \quad (3.17)$$

in which the superscripts S and D refer to solute and diluent (solvent), respectively. From Equations (3.5) and (3.17), one could associate the independent fluxes \mathbf{J}^f and \mathbf{J}^S with their conjugated forces; i.e.

$$\mathbf{X}^f = \frac{\partial \mathcal{D}}{\partial \mathbf{J}^f} = -\frac{\nabla p}{\check{\rho}_f} \quad (3.18)$$

$$\mathbf{X}^S = \frac{\partial \mathcal{D}}{\partial \mathbf{J}^S} = -\nabla (\mu^S - \mu^D) \quad (3.19)$$

The rate of dissipation energy $-\mathbf{J}^S \cdot \nabla (\mu^S - \mu^D)$ applies to both neutral and binary electrolyte solutions (Heidug and Wong, 1996).

3.3 Rock Constitutive Equations

3.3.1 Free Energy of Wetted Clay Matrix

The fluid saturated porous medium is composed of a solid matrix which contains two kinds of connected voids of different scales: pore space filled with freely diffus-

ing pore fluid, and interlayer space occupied by bounded water between individual clay platelets. Bound water is defined, here, as the water that is subject to intermolecular surface forces (e.g., van der Waals, hydration, and electric double layer forces), which possesses physical properties that deviate from those of the bulk (Derjaguin et al., 1987; and Isrealachvili, 1991). On the other hand, pore water is not subject to these forces because it occupies voids with dimensions that are much larger than distances over which intermolecular surfaces forces are effective < 10 nm (Diek et al., 1994 and 1996). Consequently, one may divide the mass of the β^{th} fluid component per referential volume of the material into two parts (Heidug and Wong, 1996):

$$m^\beta = m_{pore}^\beta + m_{bound}^\beta \quad (3.20)$$

where m_{pore}^β and m_{bound}^β are the masses per referential volume of the β^{th} fluid component in the pore fluid and the bound water, respectively. The fundamental constitutive relations for the total stresses σ_{ij} , the pore volume fraction v or the variation of the pore fluid content ζ , and the fluid component masses in the bound water, m_{bound}^β , can be derived from the free energy \mathfrak{F}_{wm} of the wetted clay matrix containing bound water. This energy is obtained from the difference between the free energy of the fluid saturated porous medium \mathfrak{F} and that of the pore fluid \mathfrak{F}_{pore} , as illustrated below.

The following expression of the time evolution of the free energy \mathfrak{F} per referential volume of the fluid saturated porous material is obtained by combining the first and second laws of thermodynamics (refer to Appendix A.1):

$$\dot{\mathfrak{F}} = \sigma_{ij} \dot{\varepsilon}_{ij} + \sum_{\beta} \mu^\beta \dot{m}^\beta \quad (3.21)$$

where σ_{ij} and ε_{ij} are the components of the total stress and strain tensors and μ^β is the chemical potential of the β^{th} fluid component. This localized balance equation relates the time change of the free energy \mathfrak{F} per volume element in the reference

configuration to the deformation rate $\dot{\varepsilon}_{ij}$, and the rate of change of mass; i.e.

$$m^\beta = \mathcal{J} \rho^\beta = \mathcal{J} \phi \check{\rho}^\beta \quad (3.22)$$

of the β^{th} fluid component per unit referential volume. Note that \mathcal{J} is the determinant of the deformation gradient such that:

$$\mathcal{J} = \frac{dV}{dV_0}; \quad \dot{\mathcal{J}} = \mathcal{J} (\nabla \cdot \mathbf{v}_s) \quad (3.23)$$

where the volume element dV in the current configuration occupies the volume dV_0 in the reference configuration.

The pore volume fraction v is assumed to be a macroscopic state variable, such that the pore fluid free energy per unit volume of the porous medium is defined as:

$$\mathfrak{F}_{pore} = \sum_{\beta} m_{pore}^{\beta} f_{pore}^{\beta} = -pv + \sum_{\beta} \mu^{\beta} m_{pore}^{\beta} \quad (3.24)$$

where the mass per referential volume of the β^{th} component in the pore fluid is given by:

$$m_{pore}^{\beta} = \mathcal{J} \rho_{pore}^{\beta} = \mathcal{J} \phi \check{\rho}_{pore}^{\beta} = v \check{\rho}_{pore}^{\beta} \quad (3.25)$$

in which $v = \mathcal{J} \phi$ is the pore volume fraction per referential volume and $\check{\rho}_{pore}^{\beta}$ is the density of the β^{th} pore fluid component in the current configuration. The quantity f_{pore}^{β} denotes the specific free energy of the β^{th} pore fluid component; i.e.

$$f_{pore}^{\beta} = -\frac{p}{\check{\rho}_{pore}^{\beta}} + \mu^{\beta} \quad (3.26)$$

where $\check{\rho}_{pore} = \sum_{\beta} \check{\rho}_{pore}^{\beta}$. The assumption that the specific chemical potential μ^{β} of the β^{th} pore fluid component is the same for the pore fluid and bound water preserves the local chemical equilibrium. The evolution of the potential \mathfrak{F}_{wm} with time, then, obeys:

$$\mathfrak{F}_{wm} (\varepsilon, v, m_{bound}^{\beta}) = (\mathfrak{F} - \mathfrak{F}_{pore})$$

$$\mathfrak{F}_{wm}(\varepsilon, v, m_{bound}^\beta) = \sigma_{ij}\dot{\varepsilon}_{ij} + p\dot{v} + \sum_{\beta} \mu^\beta \dot{m}_{bound}^\beta \quad (3.27)$$

for which Gibbs-Duhem (relation 3.15) has been used.

Alternatively, the dual potential \mathcal{W} defined by:

$$\mathcal{W} = \mathfrak{F}_{wm} - pv - \sum_{\beta} m_{bound}^\beta \mu^\beta \quad (3.28)$$

satisfies the equation:

$$\dot{\mathcal{W}} = \sigma_{ij}\dot{\varepsilon}_{ij} - v\dot{p} - \sum_{\beta} m_{bound}^\beta \dot{\mu}^\beta \quad (3.29)$$

$$\sigma_{ij} = \left(\frac{\partial \mathcal{W}}{\partial \varepsilon_{ij}} \right)_{p, \mu^\beta}; \quad v = - \left(\frac{\partial \mathcal{W}}{\partial p} \right)_{\varepsilon_{ij}, \mu^\beta}; \quad (3.30)$$

$$m_{bound}^\beta = - \left(\frac{\partial \mathcal{W}}{\partial \mu^\beta} \right)_{p, \mu^\alpha (\neq \mu^\beta)}$$

in order for relation (3.29) to conform with the expression for $\dot{\mathcal{W}}$ derived from the differentiation chain rule:

$$\dot{\mathcal{W}} = \left(\frac{\partial \mathcal{W}}{\partial \varepsilon_{ij}} \right)_{p, \mu^\beta} \dot{\varepsilon}_{ij} + \left(\frac{\partial \mathcal{W}}{\partial p} \right)_{\varepsilon_{ij}, \mu^\beta} \dot{p} + \sum_{\beta} \left(\frac{\partial \mathcal{W}}{\partial \mu^\beta} \right)_{p, \mu^\alpha (\neq \mu^\beta)} \dot{\mu}^\beta \quad (3.31)$$

3.3.2 Fundamental equations

Differentiation of Equation (3.30) with respect to time, yield to the following constitutive equations for the time evolutions of total stress σ_{ij} , and pore volume fraction v :

$$\dot{\sigma}_{ij} = L_{ijkl}\dot{\varepsilon}_{kl} - \alpha_{ij}\dot{p} + \sum_{\beta} \omega_{ij}^\beta \dot{\mu}^\beta \quad (3.32)$$

$$\dot{v} = \alpha_{ij}\dot{\varepsilon}_{ij} + Q\dot{p} + \sum_{\beta} B^\beta \dot{\mu}^\beta \quad (3.33)$$

$$\dot{m}_{bound}^\beta = \omega_{ij}^\beta \dot{\varepsilon}_{ij} + B^\beta \dot{p} + \sum_{\beta} Z^{l\beta} \dot{\mu}^\beta \quad (3.34)$$

where tension is considered positive. The thermodynamic response coefficients are given by the following tensors ($i, j, k, l = 1, 2, 3$):

$$\begin{aligned} L_{ijkl} &= \left(\frac{\partial \sigma_{ij}}{\partial \varepsilon_{kl}} \right)_{p, \mu^\beta, T} = \left(\frac{\partial \sigma_{kl}}{\partial \varepsilon_{ij}} \right)_{p, \mu^\beta, T} \\ \alpha_{ij} &= - \left(\frac{\partial \sigma_{ij}}{\partial p} \right)_{\varepsilon_{ij}, \mu^\beta, T} = \left(\frac{\partial v}{\partial \varepsilon_{ij}} \right)_{p, \mu^\beta, T} \\ \omega_{ij}^\beta &= \left(\frac{\partial \sigma_{ij}}{\partial \mu^\beta} \right)_{\varepsilon_{ij}, p, T} = - \left(\frac{\partial m_{bound}^\beta}{\partial \varepsilon_{ij}} \right)_{p, \mu^\beta, T} \\ Z^{l\beta} &= \left(\frac{\partial m_{bound}^\beta}{\partial \mu^l} \right)_{p, \varepsilon_{ij}, T} = \left(\frac{\partial m_{bound}^l}{\partial \mu^\beta} \right)_{p, \varepsilon_{ij}, T} \\ B^\beta &= \left(\frac{\partial v}{\partial \mu^\beta} \right)_{\varepsilon_{ij}, p, T} = \left(\frac{\partial m_{bound}^\beta}{\partial p} \right)_{\varepsilon_{ij}, \mu^\beta, T} \end{aligned} \quad (3.35)$$

$$Q = \left(\frac{\partial v}{\partial p} \right)_{\varepsilon_{ij}, \mu^\beta, T}$$

where L_{ijkl} , α_{ij} , and ω_{ij}^β denote the elastic moduli, Biot effective stress coefficients, and the chemical swelling parameters of the β^{th} fluid component, respectively. For binary solutions, the constitutive relations (3.32) and (3.33) reduce to:

$$\dot{\sigma}_{ij} = L_{ijkl} \dot{\varepsilon}_{kl} - \alpha_{ij} \dot{p} + \omega_{ij}^S \dot{\mu}^S + \omega_{ij}^D \dot{\mu}^D \quad (3.36a)$$

$$\dot{v} = \alpha_{ij} \dot{\varepsilon}_{ij} + Q \dot{p} + B^S \dot{\mu}^S + B^D \dot{\mu}^D \quad (3.37)$$

$$\dot{m}_{bound}^D = \omega_{ij}^D \dot{\varepsilon}_{ij} + B^D \dot{p} + Z^{SD} (\dot{\mu}^D + \dot{\mu}^S) \quad (3.38)$$

$$\dot{m}_{bound}^S = \omega_{ij}^S \dot{\varepsilon}_{ij} + B^S \dot{p} + \mathcal{Z}^{DS} (\dot{\mu}^D + \dot{\mu}^S) \quad (3.39)$$

where the superscripts S and D denote solute and diluent, respectively. Note that the thermodynamic response coefficients L_{ijkl} , α_{ij} , ω_{ij}^S , and ω_{ij}^D are components of symmetric tensors.

3.3.3 Variations of the fluid content

Small variations of the ratio of the fluid densities $\check{\rho}_f$ and $\check{\rho}_{fo}$ in the current and reference configurations with respect to the fluid pressure at constant temperature, can be expressed by the following first order expansion or linear state equation:

$$\frac{\check{\rho}_f}{\check{\rho}_{fo}} \approx \left[1 + \left(\frac{p - p_o}{K_f} \right) \right] \quad (3.40)$$

where p_o refer to the initial fluid pressure, and K_f denotes the fluid bulk modulus. The linearization of the fluid state equation, relating its density response to its pressure (3.40) yields:

$$\frac{\dot{\check{\rho}}_f}{\check{\rho}_{fo}} \approx \frac{\dot{p}}{K_f} \quad (3.41)$$

The assumption that the porous medium is fully saturated with the fluid implies that the pore volume change is equal to the variation of the fluid volume in the pores. The latter results from the following two processes: i) fluid density change, and ii) fluid exchange between the porous media and the surroundings. The total fluid mass density m_f is defined by:

$$m_f = \mathcal{J} \rho_f = \mathcal{J} \phi \check{\rho}_f = v \check{\rho}_f \quad (3.42)$$

which reduces to the reference mass $m_{fo} = \phi \check{\rho}_{fo}$ with $v \rightarrow \phi$, and $\check{\rho}_f \rightarrow \check{\rho}_{fo}$. The variation of the fluid content ζ is related to the difference between the fluid mass densities in the current configuration m_f and the reference configuration m_{fo} by:

$$\zeta = \frac{m_f - m_{fo}}{\check{\rho}_{fo}} = v \frac{\check{\rho}_f}{\check{\rho}_{fo}} - \phi \quad (3.43)$$

such that its time evolution is given by:

$$\dot{\zeta} = \frac{\dot{m}_f}{\check{\rho}_{fo}} = \frac{\check{\rho}_f}{\check{\rho}_{fo}} \dot{v} + v \frac{\dot{\check{\rho}}_f}{\check{\rho}_{fo}} \quad (3.44)$$

If one chooses, as reference, the configuration at any instant, then for this selection $\mathcal{J} = 1$, but $\mathcal{J} \neq 0$, $\check{\rho}_f = \check{\rho}_{fo}$, but $\dot{\check{\rho}}_f \neq 0$, and $\zeta = 0$, but $\dot{\zeta} \neq 0$; hence, Equation (3.44) becomes:

$$\dot{\zeta} = \dot{v} + \frac{\phi \dot{p}}{K_f} \quad (3.45)$$

Substituting Equation (3.37) into (3.45), one gets the response of the rate of variation of the fluid content $\dot{\zeta}$ to the rates of strain components $\dot{\epsilon}_{ij}$, pore pressure \dot{p} , and the chemical potential of the β^{th} fluid component $\dot{\mu}^\beta$ as follows:

$$\dot{\zeta} = \alpha_{ij} \dot{\epsilon}_{ij} + \left(Q + \frac{\phi}{K_f} \right) \dot{p} + \sum_{\beta} B^{\beta} \dot{\mu}^{\beta} \quad (3.46)$$

or, in the case of binary solution:

$$\dot{\zeta} = \alpha_{ij} \dot{\epsilon}_{ij} + \left(Q + \frac{\phi}{K_f} \right) \dot{p} + B^S \dot{\mu}^S + B^D \dot{\mu}^D \quad (3.47)$$

Note that the storage coefficient, or the inverse of Biot Modulus M^{-1} , is defined by:

$$M^{-1} = \left(\frac{\partial \zeta}{\partial p} \right)_{\epsilon_{ij}, \mu^{\beta}} = \left(Q + \frac{\phi}{K_f} \right) \quad (3.48)$$

3.3.4 Chemical Loading

The solute chemical potential, μ^S , can be approximated such that any significant change is solely due to a change in the solute mass fraction C^S (Heidug and Wong, 1996):

$$\mu^S \approx \frac{RT}{M^S} \ln C^S \quad (3.49)$$

The solute and diluent mass fractions C^S and C^D are defined in terms of the reference solute and diluent mass densities $\check{\rho}_o^S$ and $\check{\rho}_o^D$, respectively, by:

$$C^S = \frac{\check{\rho}^S}{\check{\rho}_{fo}}; \quad C^D = (1 - C^S) = \frac{\check{\rho}^D}{\check{\rho}_{fo}}; \quad \check{\rho}_{fo} = \check{\rho}_o^S + \check{\rho}_o^D \quad (3.50)$$

The rate of change with time of the diluent chemical potential $\dot{\mu}^D$ can be expressed according to Gibbs-Duhem's relation with respect to $\check{\rho}_o^S$ and $\check{\rho}_o^D$ by:

$$\dot{\mu}^D = \frac{1}{C^D} \left[\frac{1}{\check{\rho}_{fo}} \dot{p} - C^S \dot{\mu}^S \right] \quad (3.51)$$

One could write the driving force $\nabla(\mu^S - \mu^D)$ as:

$$\nabla(\mu^S - \mu^D) = \left(\frac{\partial \mu^S}{\partial p} - \frac{\partial \mu^D}{\partial p} \right)_{C^S} \nabla p + \left(\frac{\partial \mu^S}{\partial C^S} - \frac{\partial \mu^D}{\partial C^S} \right)_p \nabla C^S \quad (3.52)$$

For dilute solutions, the first right hand side term¹ is negligible compared to the second term (Haase, 1990 and Heidug and Wong, 1996). This leads to the following simplification:

$$\nabla(\mu^S - \mu^D) \approx \left(\frac{\partial \mu^S}{\partial C^S} - \frac{\partial \mu^D}{\partial C^S} \right)_p \nabla C^S \approx \mathfrak{A} \nabla C^S \quad (3.53)$$

where,

$$\mathfrak{A} = \frac{RT}{M^S C^S C^D} \quad (3.54)$$

This follows from the Gibbs-Duhem's relation at constant pressure and temperature:

¹The partial specific volumes v^S and v^D of the solute and diluent, respectively, satisfy:

$$v^\beta = \frac{\partial(1/\rho^\beta)}{\partial C^\beta} = \frac{\partial \mu^\beta}{\partial p}; \quad \beta = S, D$$

$$C^S (d\mu^S)_{p,T} + C^D (d\mu^D)_{p,T} = 0 \quad (3.55)$$

Note that the chemical potentials represented in (3.49) and (3.51) satisfy Gibbs-Duhem's relation:

$$\sum_{\beta} \check{\rho}_o^{\beta} \dot{\mu}^{\beta} = \dot{p} \quad (3.56)$$

Furthermore, it is important to observe that the state equation (3.21) is valid for both neutral and electrolyte solutions, since if $\tilde{\mu}^b$ and z^b denote the electrochemical potential and the electric charge of the b^{th} ionic species:

$$\tilde{\mu}^b = \mu^b + z^b \varphi \quad (3.57)$$

where φ is the electric potential which vanishes at infinity (no charges), then the following expression is form invariant; i.e.

$$\sum_b \tilde{\mu}^b \dot{m}^b = \sum_{\beta} \mu^{\beta} \dot{m}^{\beta} \quad (3.58)$$

according to local electroneutrality and chemical equilibrium (Haase, 1990 and Heidug and Wong, 1996). Consequently, the derived constitutive equations (3.36a), (3.37), and (3.47) for a binary solution are valid for an electrolyte with the solute chemical potential μ^S related to the chemical potentials of the anions μ^A and cations μ^C , at the equilibrium of dissociation by:

$$\mu^S = N^A \mu^A + N^C \mu^C \quad (3.59)$$

where N^A and N^C are the numbers of anions and cations, respectively. Note that a binary electrolyte solution is composed of four species: water molecules, undissociated electrolyte molecules, cations and anions.

3.3.4.1 Linearization of Chemical Loading

Linearization of the rock-fluid constitutive equations in term of the above five independent variables is accomplished by assuming that the chemical disturbances to the system are small enough to induce linear responses of the total stress σ_{ij} , and the variation of the fluid content ζ with respect to the solute mass fraction C^S . This approximation is appropriate for laboratory and field applications (Diek and Ghassemi, 2002). The chemical potential can be linearized with respect to the solute mass fraction by approximating $\ln C^S$ by a linear relation for a particular range of values of C^S ; i.e.

$$\mu^S \approx \frac{RT}{M^S} (a^S C^S - b), \quad \text{for all } C^S \in [C_{\min}^S, C_{\max}^S], \text{ and } a^S, b > 0 \quad (3.60)$$

where $a^S \approx (\overline{C^S})^{-1}$, such that $\overline{C^S}$ denotes the mean value of the solute mass fraction and b is a reference constant. The time rate of change of the diluent chemical potential $\dot{\mu}^D$ satisfies the approximated Gibbs-Duhem's relation:

$$\dot{\mu}^D \approx \frac{1}{\overline{C^D}} \left(\frac{1}{\check{\rho}_{fo}} \dot{p} - \overline{C^S} \dot{\mu}^S \right) = a^D \left(\frac{1}{\check{\rho}_{fo}} \dot{p} - \frac{RT}{M^S} \dot{C}^S \right) \quad (3.61)$$

The constant $a^D = (\overline{C^D})^{-1}$ where $\overline{C^D}$ denotes the mean value of the diluent mass fraction.

Finally, the approximation in Equation (3.53) takes the form:

$$\nabla (\mu^S - \mu^D) \approx \left(\frac{\partial \mu^S}{\partial C^S} - \frac{\partial \mu^D}{\partial C^S} \right)_p \nabla C^S \approx \bar{\alpha} \nabla C^S \quad (3.62)$$

where,

$$\bar{\alpha} = \frac{a^S a^D RT}{M^S} \quad (3.63)$$

is a constant. The linearization leads to the following result:

$$\dot{\sigma}_{ij} = L_{ijkl} \dot{\epsilon}_{kl} - \left(\alpha_{ij} - \frac{a^D \omega_{ij}^D}{\check{\rho}_{fo}} \right) \dot{p} + \frac{RT}{M^S} (a^S \omega_{ij}^S - a^D \omega_{ij}^D) \dot{C}^S \quad (3.64a)$$

$$\dot{\zeta} = \alpha_{ij} \dot{\varepsilon}_{ij} + \left(Q + \frac{\phi}{K_f} + \frac{a^D B^D}{\check{\rho}_{of}} \right) \dot{p} + \frac{RT}{M^S} (a^S B^S - a^D B^D) \dot{C}^S \quad (3.65)$$

3.3.5 Complete Isotropy

In the case of complete isotropy, Equations (3.64a) and (3.65) reduce to:

$$\dot{\sigma}_{ij} = \left(K - \frac{2G}{3} \right) \dot{\varepsilon}_{kk} \delta_{ij} + 2G \dot{\varepsilon}_{ij} - \mathcal{B} \dot{p} \delta_{ij} + \chi \dot{C}^S \delta_{ij} \quad (3.66)$$

$$\dot{\zeta} = \alpha_{ij} \dot{\varepsilon}_{ij} + \Lambda \dot{p} + \Omega \dot{C}^S \quad (3.67)$$

where the chemical swelling parameters ω_{ij}^β reduce to $\omega_{ij}^\beta = \omega^\beta \delta_{ij}$, and the isotropic thermodynamic response coefficients are given by (see Appendix A.2):

$$\alpha = \left(1 - \frac{K}{K_s} \right); \quad Q = \left(\frac{\alpha - \phi}{K_s} \right); \quad B^\beta = \left(\frac{-\omega^\beta}{K_s} \right) \quad (3.68)$$

K and G denotes the rock's bulk and shear moduli, respectively. The poroelastic (Biot effective stress) coefficient α is a scalar, K_s denotes the bulk modulus of the solid matrix, and ρ_s is the mass density of the solid matrix. The other constant coefficients are given as follows:

$$\begin{aligned} \mathcal{B} &= \left(\alpha - \frac{a^D \omega^D}{\check{\rho}_{fo}} \right); \quad \Lambda = \left(Q + \frac{\phi}{K_f} + \frac{a^D B^D}{\check{\rho}_{fo}} \right) \\ \chi &= \frac{RT}{M^S} (a^S \omega^S - a^D \omega^D); \quad \Omega = \frac{(\alpha - 1)}{K} \chi \end{aligned} \quad (3.69)$$

Finally, the components of the total stress σ_{ij} are given (integration of 3.66) by:

$$\sigma_{ij} = \left(K - \frac{2G}{3} \right) \varepsilon_{kk} \delta_{ij} + 2G \varepsilon_{ij} - \mathcal{B} p \delta_{ij} + \chi \left(C^S - \frac{b}{a^S} \right) \delta_{ij} \quad (3.70)$$

In particular, one may represent the input swelling parameters ω^S and ω^D by:

$$\omega^S = \omega^D = \omega_0 \frac{M^S}{RT} \quad (3.71)$$

3.3.6 Transverse Isotropy

Argillaceous rocks are often transversely isotropic, in which there exist a rotational symmetry about the axis perpendicular to the bedding plane. In the case of transverse isotropy, the linear responses of total stresses σ_{ij} and the variation of the fluid content ζ to the strain components ε_{ij} , pore pressure p , and solute mass fraction C^S are as follows:

$$\dot{\sigma}_{ij} = L_{ijkl}\dot{\varepsilon}_{kl} - \mathcal{B}_{ij}\dot{p} + \chi_{ij}\dot{C}^S \quad (3.72)$$

$$\begin{pmatrix} \dot{\sigma}_{11} \\ \dot{\sigma}_{22} \\ \dot{\sigma}_{33} \\ \dot{\tau}_{12} \\ \dot{\tau}_{23} \\ \dot{\tau}_{31} \end{pmatrix} = \begin{bmatrix} L_{11} & L_{12} & L_{13} & 0 & 0 & 0 \\ L_{12} & L_{11} & L_{13} & 0 & 0 & 0 \\ L_{13} & L_{13} & L_{33} & 0 & 0 & 0 \\ 0 & 0 & 0 & G & 0 & 0 \\ 0 & 0 & 0 & 0 & G' & 0 \\ 0 & 0 & 0 & 0 & 0 & G' \end{bmatrix} \begin{pmatrix} \dot{\varepsilon}_{11} \\ \dot{\varepsilon}_{22} \\ \dot{\varepsilon}_{33} \\ \dot{\gamma}_{12} \\ \dot{\gamma}_{23} \\ \dot{\gamma}_{31} \end{pmatrix} - \begin{bmatrix} \mathcal{B} \\ \mathcal{B} \\ \mathcal{B}' \\ 0 \\ 0 \\ 0 \end{bmatrix} \dot{p} + \begin{bmatrix} \chi \\ \chi \\ \chi' \\ 0 \\ 0 \\ 0 \end{bmatrix} \dot{C}^S \quad (3.73)$$

$$\dot{\zeta} = \alpha(\dot{\varepsilon}_{11} + \dot{\varepsilon}_{22}) + \alpha'\dot{\varepsilon}_{33} + \Lambda\dot{p} + \Omega\dot{C}^S \quad (3.74)$$

where the five independent drained elastic moduli are:

$$L_{11} = \frac{E(E' - E(\nu')^2)}{(E' - E'\nu - 2E(\nu')^2)(1 + \nu)} \quad (3.75)$$

$$L_{12} = \frac{E (E' \nu + E (\nu')^2)}{(E' - E' \nu - 2E (\nu')^2) (1 + \nu)} \quad (3.76)$$

$$L_{13} = \frac{EE' \nu'}{(E' - E' \nu - 2E (\nu')^2)} \quad (3.77)$$

$$L_{33} = \frac{(1 - \nu) (E')^2}{(E' - E' \nu - 2E (\nu')^2)} \quad (3.78)$$

$$L_{55} = L_{66} = G_{yz} = G_{zx} = G' \quad (3.79)$$

and the dependent parameter:

$$G = L_{44} = \frac{L_{11} - L_{12}}{2} \quad (3.80)$$

The other thermodynamic response coefficients are given by (see Appendix C):

$$\alpha = 1 - \frac{(L_{11} + L_{12} + L_{13})}{3K_s} \quad (3.81)$$

$$\alpha' = 1 - \frac{(2L_{13} + L_{33})}{3K_s} \quad (3.82)$$

$$Q = \frac{(1 - \phi)}{K_s} - \frac{(2L_{11} + L_{33} + 2L_{12} + 4L_{13})}{9K_s^2} \quad (3.83)$$

$$B^S = -\frac{1}{3} \left(\frac{2\omega^S + \omega'^S}{K_s} \right); \quad \text{and} \quad B^D = -\frac{1}{3} \left(\frac{2\omega^D + \omega'^D}{K_s} \right) \quad (3.84)$$

The unprimed and primed parameters represent the material coefficients in the isotropic plane and in the direction normal to this plane (z -direction), respectively.

The remaining constant coefficients are as follow:

$$\mathcal{B} = \left(\alpha - \frac{a^D \omega^D}{\check{\rho}_{fo}} \right) \quad \text{and} \quad \mathcal{B}' = \left(\alpha' - \frac{a^D \omega'^D}{\check{\rho}_{fo}} \right) \quad (3.85)$$

$$\chi = \frac{RT}{M^S} (a^S \omega^S - a^D \omega^D) \quad \text{and} \quad \chi' = \frac{RT}{M^S} (a^S \omega'^S - a^D \omega'^D) \quad (3.86)$$

$$\Omega = \frac{RT}{M^S} (a^S B^S - a^D B^D) \quad (3.87)$$

$$\Lambda = \left(Q + \frac{\phi}{K_f} + \frac{a^D B^D}{\check{\rho}_{fo}} \right) \quad (3.88)$$

In particular, one may represent the input swelling parameters ω^S , ω^D , ω'^S , and ω'^D by:

$$\omega^S = \omega^D = \omega_0 \frac{M^S}{RT}; \quad \text{and} \quad \omega'^S = \omega'^D = \omega'_0 \frac{M^S}{RT} \quad (3.89)$$

3.4 Transport Equations

In this section, the phenomenological equations relating the fluxes to their driving forces are derived from the definition of Rayleigh's dissipation function and the generalized forces associated with it. Choosing, as reference, the configuration at any instant and writing the fluxes with respect to the reference fluid density $\check{\rho}_f \rightarrow \check{\rho}_{fo}^2$.

3.4.1 Isotropic Flows

The rate of dissipated energy or local entropy production rate results from the relative motions between the fluid components and the solid, as well as the dissipated heat from the total heat supplied by pure heat and by the flows of all fluid masses. Introducing Rayleigh's dissipation function \mathcal{D} (3.6) as a quadratic function of the

²In that way, one ignores the spacial variation of the total fluid mass density such that:

$$\nabla \check{\rho}^\beta = \nabla \left(\check{\rho}_f^\beta C^\beta \right) \rightarrow \check{\rho}_{of}^\beta \nabla C^\beta \quad \text{or} \quad \nabla \check{\rho}^\beta \rightarrow \nabla \check{\rho}_o^\beta = \check{\rho}_{of}^\beta \nabla C^\beta$$

This assumption is required for the linearization of the balance or conservation equations (see Appendix D).

independent fluxes \mathbf{J}^f associated with the flow, and \mathbf{J}^S associated with the solute flow, leads to:

$$2\mathcal{D} = R^{11} (\mathbf{J}^f \cdot \mathbf{J}^f) + R^{12} (\mathbf{J}^f \cdot \mathbf{J}^S) + R^{21} (\mathbf{J}^S \cdot \mathbf{J}^f) + R^{22} (\mathbf{J}^S \cdot \mathbf{J}^S) \quad (3.90)$$

where the phenomenological coefficients R^{ij} are components of a symmetric tensor. Substituting (3.90) into (3.18) and (3.19), one obtains the following set of flow equations:

$$-\left(\frac{\nabla p}{\check{\rho}_{fo}}\right) = R^{11} \mathbf{J}^f + R^{12} \mathbf{J}^S \quad (3.91)$$

$$-\nabla (\mu^S - \mu^D) = R^{21} \mathbf{J}^f + R^{22} \mathbf{J}^S \quad (3.92)$$

Solving for \mathbf{J}^f , and \mathbf{J}^S in Equations (3.91) and (3.92) one finds that, in the presence of hydraulic and chemical potential gradients, the fluid mass flux and solute mass flux can be related to the driving forces through experimentally measurable phenomenological coefficients, \mathcal{L}^{ij} ; i.e.

$$\mathbf{J}^f = -\mathcal{L}^{11} \frac{\nabla p}{\check{\rho}_{fo}} - \mathcal{L}^{12} \nabla (\mu^S - \mu^D) \quad (3.93)$$

$$\mathbf{J}^S = -\mathcal{L}^{21} \frac{\nabla p}{\check{\rho}_{fo}} - \mathcal{L}^{22} \nabla (\mu^S - \mu^D) \quad (3.94)$$

where the coefficients $\mathcal{L}^{ij} = [\mathbf{R}^{-1}]^{ij}$, elements of the inverse tensor $\mathcal{L} = \mathbf{R}^{-1}$, are independent of the driving forces but may depend on the pore pressure and the solute concentration. One assumes the following phenomenological coefficients for isotropic flows:

$$\mathcal{L}^{11} = \frac{\check{\rho}_{fo}^2 k}{\eta} \quad (3.95)$$

$$\mathcal{L}^{12} = -\mathcal{L}^{11} \mathfrak{R} \quad (3.96)$$

$$\mathcal{L}^{21} = \check{\rho}_{fo}^2 L_p \quad (3.97)$$

$$\mathcal{L}^{22} = \check{\rho}_{fo} \bar{\mathfrak{A}}^{-1} D^S \quad (3.98)$$

Nevertheless, with the approximation in Equation (3.62) and the definitions in Equations (3.95) to (3.98), the transport equations for isotropic flows reduce to:

$$\dot{\mathbf{w}} = -\frac{k}{\eta} (\nabla p - \check{\rho}_{fo} \mathfrak{R} \bar{\mathfrak{A}} \nabla C^S) \quad (3.99)$$

$$\mathbf{J}^S = -\check{\rho}_{fo} L_p \nabla p - \check{\rho}_{fo} D^S \nabla C^S \quad (3.100)$$

The constants are defined as follows: k is the intrinsic permeability; η is the viscosity of the fluid; \mathfrak{R} is the membrane reflection coefficient; L_p is the pressure solute diffusion coefficient; and, D^S is the chemical solute diffusion coefficient. If one abides by Onsager's reciprocity theorem then, L_p can be estimated by:

$$L_{12} = L_{21} = \check{\rho}_{fo}^2 L_p = -\frac{\check{\rho}_{fo}^2 k \mathfrak{R}}{\eta} \implies L_p = -\frac{k \mathfrak{R}}{\eta} \quad (3.101)$$

3.4.2 Transversely Isotropic Flows

The phenomenological equations may be written as:

$$\begin{aligned} \mathbf{J}^f &= -\frac{1}{\check{\rho}_{fo}} \left[\mathcal{L}^{11} (\nabla_x + \nabla_y) + \mathcal{L}'^{11} \nabla_z \right] p \\ &\quad - \left[\mathcal{L}^{12} (\nabla_x + \nabla_y) + \mathcal{L}'^{12} \nabla_z \right] (\mu^S - \mu^D) \end{aligned} \quad (3.102)$$

$$\begin{aligned} \mathbf{J}^S &= -\frac{1}{\check{\rho}_{fo}} \left[\mathcal{L}^{21} (\nabla_x + \nabla_y) + \mathcal{L}'^{21} \nabla_z \right] p \\ &\quad - \left[\mathcal{L}^{22} (\nabla_x + \nabla_y) + \mathcal{L}'^{22} \nabla_z \right] (\mu^S - \mu^D) \end{aligned} \quad (3.103)$$

As a first approximation, one assumes Equations (3.95) to (3.98), and the following phenomenological coefficients for transversely isotropic flows:

$$\mathcal{L}'_{11} = \frac{\check{\rho}_{fo}^2 k'}{\eta} \quad (3.104)$$

$$\mathcal{L}'_{12} = -\mathcal{L}'_{11} \mathfrak{R}' \quad (3.105)$$

$$\mathcal{L}'_{21} = \check{\rho}_{fo}^2 L'_p \quad (3.106)$$

$$\mathcal{L}'_{22} = \check{\rho}_{fo} \bar{\mathfrak{A}}^{-1} D'^S \quad (3.107)$$

The unprimed and primed parameters represent the phenomenological coefficients in the isotropic plane and in the direction normal to this plane (z -direction), respectively. The resulting transversely isotropic fluxes are:

$$\mathbf{J}^f = -\frac{\check{\rho}_{fo}}{\eta} [k(\nabla x + \nabla y) + k' \nabla z] p + \frac{\check{\rho}_{fo}^2 \bar{\mathfrak{A}}}{\eta} [k \mathfrak{R}(\nabla x + \nabla y) + k' \mathfrak{R}' \nabla z] C^S \quad (3.108)$$

$$\mathbf{J}^S = -\check{\rho}_{fo} [L_p(\nabla x + \nabla y) + L'_p \nabla z] p - \check{\rho}_{fo} [D^S(\nabla x + \nabla y) + D'^S \nabla z] C^S \quad (3.109)$$

Note that the fluxes are expressed in terms of the reference fluid density $\check{\rho}_{fo}$ to ensure the linearity of the theory.

3.5 Field Equations

The field equations are developed by substituting the suggested phenomenological and constitutive equations into the momentum, mass, and energy balance equations. In the absence of body forces, the momentum balance or the mechanical equilibrium condition states:

$$\sigma_{ij,j} = 0 \quad (3.110)$$

Conservation of the fluid mass in the absence of volume sources yields (see Appendix D):

$$\dot{\zeta} + \nabla \cdot \dot{\mathbf{w}} = 0 \quad (3.111)$$

Conservation of the solute mass states (see Appendix D):

$$\phi \check{\rho}_{fo} \dot{C}^S + \check{\rho}_{fo} (\dot{\mathbf{w}} \cdot \nabla C^S) + \nabla \cdot \mathbf{J}^S = 0 \quad (3.112)$$

However, in rocks with very low permeability as shales (nano-darcy), one can simplify the above equation by neglecting the convective term $(\dot{\mathbf{w}} \cdot \nabla C^S)$. This leads to the linearized diffusion equation:

$$\phi \check{\rho}_{fo} \dot{C}^S + \nabla \cdot \mathbf{J}^S = 0 \quad (3.113)$$

3.5.1 Navier-type Equations

3.5.1.1 Isotropic Media

The linear Navier-type field equations are obtained by substituting the constitutive Equations (3.66) into the mechanical equilibrium Equations (3.110), with constants given by (3.68), to (3.69):

$$\left(K + \frac{G}{3} \right) \nabla (\nabla \cdot \mathbf{u}) + G \nabla^2 \mathbf{u} = \mathcal{B} \nabla p - \chi \nabla C^S \quad (3.114)$$

where \mathbf{u} is the solid displacement vector. Note that the coupling terms may be viewed as *body forces* proportional to the gradients of the pore pressure, and the solute mass fraction.

3.5.1.2 Transversely Isotropic Media

The Navier-type field equations are obtained by substituting the constitutive equations (3.73) into the mechanical equilibrium equations (3.110), with the constant coefficients given by (3.75) to (3.79), (3.81) to (3.84), and (3.85) to (3.88). Assuming plane strain conditions, one gets the coupled Navier-type field equations in the isotropic plane ($i, j = 1, 2$):

$$\frac{1}{2}(L_{11} + L_{12})u_{j,ji} + \frac{1}{2}(L_{11} - L_{12})u_{i,jj} = \mathcal{B}p_{,i} - \chi C_{,i}^S \quad (3.115)$$

3.5.2 Fluid Diffusion Equation

3.5.2.1 Isotropic Media

The coupled diffusion equation is obtained by substituting the constitutive Equations (3.67), and flux (3.99) into (3.111) with the coefficients given by (3.63), and (3.68) to (3.69):

$$\alpha(\nabla \cdot \mathbf{u}) + \Lambda \dot{p} + \Omega \dot{C}^S = \frac{k}{\eta} [\nabla^2 p - \check{\rho}_{fo} \mathfrak{R} \bar{\mathfrak{A}} \nabla^2 C^S] \quad (3.116)$$

3.5.2.2 Transversely Isotropic Media

The fluid diffusion field equations are obtained by substituting the constitutive equations (3.74), and fluid flux (3.108) into (3.111), with the constant coefficients given by (3.63), and (3.81) to (3.88). Assuming the case of plane strain conditions, one gets the fluid diffusion equation in the isotropic plane as:

$$\alpha \dot{u}_{j,j} + \Lambda \dot{p} + \Omega \dot{C}^S = \frac{k}{\eta} [p_{,jj} - \check{\rho}_{fo} \mathfrak{R} \bar{\mathfrak{A}} C_{,jj}^S] \quad (3.117)$$

3.5.3 Solute Diffusion Equation

3.5.3.1 Isotropic Media

Substituting (3.100) into (3.113), one gets the coupled linear solute diffusion equation:

$$\phi \dot{C}^S - L_p \nabla^2 p - D^S \nabla^2 C^S = 0 \quad (3.118)$$

3.5.3.2 Transversely Isotropic Media

The general coupled solute diffusion equation is obtained by substituting the solute flux equation (3.109) into the balance equation (3.113). Assuming the case of plane strain conditions, the solute diffusion equation is given in the isotropic plain by:

$$\phi \dot{C}^S - L_p p_{,jj} - D^S C^S_{,jj} = 0 \quad (3.119)$$

3.6 Swelling Parameter

3.6.1 Isotropic Media

For isothermal processes, the isotropic rock constitutive equations expressing the time evolution of the total stresses $\dot{\sigma}_{ij}$ and the variation of the fluid content $\dot{\zeta}$ are given by Equations (3.66) and (3.67), and the transport fluxes are given by Equations (3.99) and (3.100), such that the field equations are expressed by (3.114), (3.116) and (3.118).

In the case of constant total stress and constant pore pressure ($\dot{\sigma}_{ij} = 0$, $\dot{p} = 0$, $\nabla p = 0$) such that the fluid flows solely by osmosis under the action of solute mass fraction or concentration gradient, and the deformation is solely due to the chemical loading or swelling, one may estimate the order of magnitude of the swelling parameter from an expression consisting of the drained elastic moduli, permeability, fluid viscosity, and solute diffusion and reflection coefficients, as follows.

From Equation (3.114):

$$\dot{\varepsilon}_{kk} = -\frac{\chi}{K} \dot{C}^S \quad (3.120)$$

If one substitutes $\dot{\varepsilon}_{kk}$ from (3.120) and $\nabla^2 C^S$ from (3.118), into (3.116), and equates the coefficients of \dot{C}^S , one gets:

$$-\frac{\alpha\chi}{K} + \Omega = -\frac{\check{\rho}_{fo}k\mathfrak{R}\bar{\mathfrak{A}}\phi}{\eta D^S} \quad (3.121)$$

from Equations (3.69) and (3.63) it follows that:

$$\Omega = \frac{(\alpha - 1)\chi}{K}$$

$$\chi = \frac{RT}{M^S} (\omega^S a^S - \omega^D a^D) \quad (3.122)$$

$$\bar{\mathfrak{A}} = \frac{a^S a^D RT}{M^S}$$

therefore:

$$\chi = \frac{RT}{M^S} (\omega^S a^S - \omega^D a^D) = \frac{K\check{\rho}_{fo}RTk\mathfrak{R}\phi a^S a^D}{\eta M^S D^S} \quad (3.123)$$

where χ is the coefficient associated with the chemical swelling or osmotic pressure.

Assuming the chemical swelling parameters satisfy:

$$\omega^S = \omega^D = \omega \quad (3.124)$$

it follows that:

$$\omega = \frac{\check{\rho}_{fo}k\mathfrak{R}\phi a^S a^D}{\eta D^S (a^S - a^D)} = \frac{\check{\rho}_{fo}k\mathfrak{R}\phi}{\eta D^S (1 - 2\bar{C}^S)} \quad (3.125)$$

or one may write:

$$\chi = \frac{\omega_0 (1 - 2\bar{C}^S)}{\bar{C}^S (1 - \bar{C}^S)} \quad (3.126)$$

Parameter	Value
Drained Young's Modulus, E	20.6 GPa ^(*)
Solid Bulk Modulus, K_s	48.2 GPa ^(*)
Biot Modulus, M	15.8 GPa ^(*)
Drained Poisson's ratio, ν	0.189 ^(*)
Fluid Bulk Modulus, K_f	3.30 GPa
Fluid mass density, $\check{\rho}_{of}$	1.11×10^3 Kg/m ³
Fluid viscosity, η	4.0×10^{-4} Pa·s
Permeability, k	10^{-9} darcy
Reflection coefficient, \mathfrak{R}	0.1
Molar mass of solute (KCl), M^S	0.0746 Kg/mole
Mean solute mass fraction, $\overline{C^S}$	0.15
Solute Diffusion coefficient, D^S	5×10^{-9} m ² /s

Table 3.2: Values of parameters (after Cheng, 1997)

where,

$$\omega_0 = \frac{RT}{M^S} \omega = \frac{K \check{\rho}_{fo} RT k \mathfrak{R} \phi}{\eta M^S D^S (1 - 2\overline{C^S})} \quad (3.127)$$

Consider, for example, a shale saturated with a KCl solution at $T = 338$ °K with the parameters given in Table 3.2

From the data given by Cheng (1997), the drained bulk modulus K and the porosity ϕ [see relation (3.48)] are calculated using:

$$K = \frac{E}{3(1 - 2\nu)}; \quad \phi = \left[\frac{(K_s/M) - \alpha}{(K_s/K_f) - 1} \right] \quad (3.128)$$

Relations (3.125), (3.126), and (3.127) give: $\omega \approx 145$ Kg/m³, $\omega_0 \approx 5.5$ MPa, and $\chi \approx 30$ MPa.

3.6.2 Transversely Isotropic Media

If one considers solely the isothermal chemical loading at constant total stress, pore pressure and temperature ($\dot{\sigma}_{ij} = 0$, $\dot{p} = 0$, $\nabla p = 0$), and assumes plane strain conditions, then it follows from (3.73) that to:

$$\dot{\epsilon}_{11} = \dot{\epsilon}_{22} = -\frac{\chi}{L_{11} + L_{12}} \dot{C}^S = -\frac{\chi'}{2L_{13}} \dot{C}^S; \quad \dot{\epsilon}_{33} = 0 \quad (3.129)$$

The additional assumptions $\omega^S = \omega^D = \omega$, and $\omega'^S = \omega'^D = \omega'$ yield:

$$\chi = \frac{\omega RT_o}{M^S} (a^S - a^D) \quad (3.130)$$

$$\chi' = \frac{\omega' RT_o}{M^S} (a^S - a^D)$$

The fluid and solute diffusion equations in the plane of isotropy ($i = 1, 2$) reduce to, respectively:

$$\alpha \dot{u}_{i,i} + \Omega \dot{C}^S = -\frac{k\check{\rho}_{fo}\mathfrak{R}\bar{\mathfrak{A}}}{\eta} C_{,ii}^S \quad (3.131)$$

$$\phi \dot{C}^S = D^S C_{,ii}^S \quad (3.132)$$

with α given by (3.81), and Ω given by (3.87) this last expression can be rewritten as:

$$\Omega = -\frac{1}{3} \left(\frac{2\chi + \chi'}{K_S} \right) \quad (3.133)$$

using (3.84) and (3.130). If one substitutes $\dot{\epsilon}_{ii}$ from (3.129) and $C_{,ii}^S$ from (3.132), into (3.131), then equates the coefficients of \dot{C}^S , one gets:

$$-\frac{2\alpha\chi}{L_{11} + L_{12}} - \frac{1}{3} \left(\frac{2\chi + \chi'}{K_S} \right) = -\frac{k\check{\rho}_{fo}\mathfrak{R}\bar{\mathfrak{A}}\phi}{\eta D^S} \quad (3.134)$$

which can be simplified using (3.81) and the constraint in (3.129):

$$\frac{\chi'}{\chi} = \frac{2L_{13}}{L_{11} + L_{12}} \quad (3.135)$$

to yield:

$$\chi = \frac{1}{2} (L_{11} + L_{12}) \frac{k\check{\rho}_{fo}\mathfrak{R}\bar{\mathfrak{A}}\phi}{\eta D^S} \quad (3.136)$$

therefore:

$$\omega = \frac{(L_{11} + L_{12}) k \check{\rho}_{f_0} \Re \phi a^S a^D}{2\eta D^S (a^S - a^D)} = \frac{(L_{11} + L_{12}) k \check{\rho}_{f_0} \Re \phi}{2\eta D^S (1 - 2\overline{C^S})} \quad (3.137)$$

or,

$$\omega_0 = \frac{RT_o}{M^S} \omega = \frac{(L_{11} + L_{12}) RT_o k \check{\rho}_{f_0} \Re \phi}{2M^S \eta D^S (1 - 2\overline{C^S})} \quad (3.138)$$

Note that according to Equation (3.135), the swelling parameters obey the constraint:

$$\frac{\omega'}{\omega} = \frac{\omega'_0}{\omega_0} = \frac{2L_{13}}{L_{11} + L_{12}} \quad (3.139)$$

Consider for example a shale saturated with KCl solution at $T = 338 \text{ }^\circ\text{K}$ with the parameters given in Table 3.2, and the following data calculated by Cheng (1997): $L_{11} = 24.1 \text{ GPa}$, $L_{12} = 6.80 \text{ GPa}$, $L_{13} = 7.62 \text{ GPa}$. Relations (3.135), (3.136), (3.137), (3.138), and (3.139) give: $\omega \approx 203 \text{ Kg/m}^3$, $\omega' \approx 100 \text{ Kg/m}^3$, $\omega_0 \approx 7.7 \text{ MPa}$, $\omega'_0 \approx 3.8 \text{ MPa}$, $\chi \approx 42 \text{ MPa}$, and $\chi' = 21 \text{ MPa}$.

4 Analytical solutions

4.1 Introduction

This chapter presents the analytical solutions obtained in this dissertation for the general case of fully-coupled chemoporoelasticity comprising the solution for axisymmetric mechanical and chemical loading conditions of vertical and inclined boreholes subjected to non-hydrostatic far-field loading.

4.2 Diffusivity Equations for Irrotational Displacement Field

The displacement field under the condition of axisymmetric loading is irrotational. This allows the decoupling of the displacement field from the pore pressure and the solute mass fraction fields. This decoupling significantly simplify the solution procedure of the borehole problem in which the displacement field exhibits rotational symmetry.

For an irrotational displacement field, the displacement can be expressed as the gradient of the scalar function Φ , such that:

$$\mathbf{u} = \nabla\Phi \tag{4.1}$$

$$\varepsilon_{ii} = \nabla \cdot \mathbf{u} = \nabla^2\Phi \tag{4.2}$$

$$\nabla^2 \mathbf{u} = \nabla^2 (\nabla \Phi) = \nabla (\nabla^2 \Phi) \quad (4.3)$$

$$\int \nabla^2 \mathbf{u} dx = \int \nabla (\nabla^2 \Phi) dx = \nabla^2 \Phi = \varepsilon_{ii} \quad (4.4)$$

Substituting Equations (4.2) and (4.3) into the Navier-type field equations (3.115) and rearranging, one gets:

$$L_{11} \nabla (\nabla^2 \Phi) = \mathcal{B} \nabla p - \chi \nabla C^S$$

$$L_{11} (\Phi_{,jj})_{,i} = \mathcal{B} p_{,i} - \chi C^S_{,i} \quad (4.5)$$

Integrating (4.5) on both sides and using (4.4), one obtains, after rearrangement:

$$\varepsilon_{ii} = \frac{\mathcal{B} p - \chi C^S}{L_{11}} + g(t) \quad (4.6)$$

where,

$$\mathcal{B} = (\alpha - \tilde{\alpha}^D) \quad (4.7)$$

$$\chi = \check{\mu}_o (\tilde{\alpha}^S - \tilde{\alpha}^D) \quad (4.8)$$

$$\check{\mu}_o = \frac{\check{\rho}_{fo} RT}{MS} \quad (4.9)$$

$$\tilde{\alpha}^v = \frac{a^v \omega^v}{\check{\rho}_{fo}}; \quad v = S, D \quad (4.10)$$

and $g(t)$ is an arbitrary function of time t that vanishes for infinite or semi-infinite domains.

Under isothermal conditions, the transversely isotropic rock constitutive equations expressing the time evolutions of the total stresses $\dot{\sigma}_{ij}$ and the variation of the

fluid content ζ are given by Equations (3.73) and (3.74). Assuming plane strain conditions, the field equations in the isotropic plane are expressed by (3.115), (3.117), and (3.119). Substituting (3.119) into (3.117) and rearranging, one gets:

$$\dot{p} - \Lambda^{-1} \kappa \left(1 + \tilde{L}_p \tilde{\mathcal{R}} \right) p_{,ii} = -\Lambda^{-1} \tilde{\Omega} \dot{C}^S - \Lambda^{-1} \alpha \dot{\epsilon}_{kk} \quad (4.11)$$

where Λ^{-1} is a parameter that reduces to Biot Modulus M in the absence of chemical effects $\omega^v, \omega'^v \rightarrow 0$, and:

$$\Lambda = \left(M^{-1} + \tilde{B}^D \right)$$

$$\tilde{\Omega} = \left(\Omega + \check{\mu}_o \kappa \tilde{\phi} \tilde{\mathcal{R}} \right)$$

$$\tilde{\phi} = \frac{\phi}{D^S}$$

$$\kappa = \frac{k}{\eta}$$

$$\tilde{\mathcal{R}} = \Re a^S a^D \quad (4.12)$$

$$\tilde{L}_p = \frac{L_p}{D^S}$$

$$\Omega = \check{\mu}_o \left(\tilde{B}^S - \tilde{B}^D \right)$$

$$\tilde{B}^v = \frac{-(2\tilde{\alpha}^v + \tilde{\alpha}'^v)}{3K_S}$$

$$\tilde{\alpha}'^v = \frac{a^v \omega'^v}{\check{\rho}_{fo}}; \quad v = S, D$$

Assuming the irrotational vector displacement property; i.e.

$$\dot{\varepsilon}_{kk} = \frac{\mathcal{B}\dot{p} - \chi\dot{C}^S}{L_{11}} \quad (4.13)$$

$$\nabla^2 \varepsilon_{kk} = \frac{\mathcal{B}\nabla^2 p - \chi\nabla^2 C^S}{L_{11}} \quad (4.14)$$

and substituting (4.13) into (4.11) and rearranging, one gets the pressure diffusion equation:

$$\dot{p} = \lambda_p^f p_{,ii} + \lambda_p^S \dot{C}^S \quad (4.15)$$

where,

$$\lambda_p^f = \frac{\kappa \left(1 + \check{\mu}_o \tilde{\mathcal{R}} \tilde{L}_p\right) L_{11}}{(\Lambda L_{11} + \alpha \mathcal{B})} = \frac{\kappa \left(1 + \check{\mu}_o \tilde{\mathcal{R}} \tilde{L}_p\right) L_{11} M}{\left[L_{11} \left(1 + M \tilde{B}^D\right) + M \left(\alpha^2 - \alpha \tilde{\alpha}^D\right) \right]} \quad (4.16)$$

$$\lambda_p^S = \frac{\left(\alpha \chi - L_{11} \tilde{\Omega}\right) L_{11}}{(\Lambda L_{11} + \alpha \mathcal{B})} \quad (4.17)$$

$$\lambda_p^S = \frac{\check{\mu}_o M \left[\alpha \left(\tilde{\alpha}^S - \tilde{\alpha}^D\right) - L_{11} \left(\tilde{B}^S - \tilde{B}^D\right) - \kappa \tilde{\phi} \tilde{\mathcal{R}} L_{11} \right]}{\left[L_{11} \left(1 + M \tilde{B}^D\right) + M \left(\alpha^2 - \alpha \tilde{\alpha}^D\right) \right]}$$

Substituting (4.13) and (3.119) into (3.117) and rearranging, one gets the solute mass fraction diffusion equation:

$$\dot{C}^S = \lambda_{Cs}^f \dot{p} + \lambda_{Cs}^S C_{,jj} \quad (4.18)$$

where,

$$\lambda_{Cs}^f = \frac{\alpha \mathcal{B} L_p + \Lambda L_p}{\frac{k\phi}{\eta} + \frac{\alpha \chi L_p}{L_{11}} - \Omega L_p} \quad (4.19)$$

$$\lambda_{Cs}^S = \frac{\frac{k}{\eta} \left(D^S + L_p \check{\rho}_{fo} \Re \bar{\mathcal{A}}\right)}{\frac{k\phi}{\eta} + \frac{\alpha \chi L_p}{L_{11}} - \Omega L_p} \quad (4.20)$$

Further simplification of Equation (4.18) can be made by assuming $L_p \rightarrow 0$ [see Equation (3.119)], such that:

$$\dot{C}^S = \lambda_{Cs}^S C_{,jj}^S \quad (4.21)$$

where,

$$\lambda_{Cs}^S = \frac{D^S}{\phi} \quad (4.22)$$

Also, Equation (4.16) becomes:

$$\lambda_p^f = \frac{\kappa L_{11}}{(\Lambda L_{11} + \alpha \mathcal{B})} = \frac{\kappa L_{11} M}{\left[L_{11} \left(1 + M \tilde{B}^D \right) + M \left(\alpha^2 - \alpha \tilde{\alpha}^D \right) \right]}$$

Similarly, the diffusion of the variation of the fluid content ζ can be rewritten as:

$$\dot{\zeta} = \lambda_{\zeta}^f \zeta_{,ii} + \lambda_{\zeta}^S C_{,ii}^S \quad (4.23)$$

where,

$$\lambda_{\zeta}^f = \frac{\kappa L_{11}}{(\Lambda L_{11} + \alpha \mathcal{B})} = \frac{\kappa M L_{11}}{\left[L_{11} \left(1 + M \tilde{B}^D \right) + M \left(\alpha^2 - \alpha \tilde{\alpha}^D \right) \right]} \quad (4.24)$$

$$\lambda_{\zeta}^S = \left[\frac{\kappa (\alpha \chi - L_{11} \Omega)}{(\Lambda L_{11} + \alpha \mathcal{B})} - \kappa \check{\mu}_o \tilde{\mathcal{R}} \right] \quad (4.25)$$

$$\lambda_{\zeta}^S = \kappa \check{\mu}_o \left\{ \frac{M \left[\alpha \left(\tilde{\alpha}^S - \tilde{\alpha}^D \right) - L_{11} \left(\tilde{B}^S - \tilde{B}^D \right) \right]}{\left[L_{11} \left(1 + M \tilde{B}^D \right) + M \left(\alpha^2 - \alpha \tilde{\alpha}^D \right) \right]} - \tilde{\mathcal{R}} \right\}$$

Note that if all the solute molecules diffuse through the membrane (none is reflected), $\mathfrak{R} \rightarrow 0$ ($\tilde{\mathcal{R}} \rightarrow 0$), no chemical osmosis, the diffusivities coefficients $\lambda_{\zeta}^f = \lambda_p^f$, and $\lambda_{\zeta}^S = \kappa \lambda_p^S$. In this case the fluid flows solely under the action of a hydraulic gradient. On other hand, in the absence of a pore pressure gradient, the case of no pressure diffusion, $M = 0$, $\lambda_{\zeta}^f = 0$, but $\lambda_{\zeta}^S = -\kappa \check{\mu}_o \tilde{\mathcal{R}}$ represents the coefficient

of chemical osmosis, which means that the fluid flows solely by chemical osmosis under the action of a solute concentration gradient. In the purely poroelastic limit (no chemical effects), the coefficients reduce to ($\omega^v, \omega'^v, \mathfrak{R} \rightarrow 0$):

$$c^f = \lambda_\zeta^f = \lambda_p^f = \frac{\kappa M L_{11}}{[L_{11} + M\alpha^2]}; \quad \lambda_\zeta^S = \lambda_p^S = 0 \quad (4.26)$$

where c^f is known as the diffusivity coefficient. Solutions of the isothermal field equations and their application to the borehole problem in transversely isotropic porous media were presented by Diek and Ghassemi, (2002).

4.3 Solutions for Borehole Problems

In the case of a borehole, it is more convenient to express the diffusion field equations in a cylindrical coordinate system. It is assumed that the material is homogeneous, the boundary conditions do not vary along the z -axis, and an infinitely long borehole is drilled in an infinite transversely isotropic saturated poroelastic medium, perpendicular to the isotropic plane. The borehole is subjected to non-hydrostatic far-field stresses, a borehole fluid pressure, and a constant solute mass fraction on the borehole wall; hence, plane strain conditions apply, which results in that all stresses, strain components, pore pressure, and solute mass fraction are independent of z . In addition, one can assume that the pore pressure and solute mass fraction only depend on the distance (r) and the time (t); so that it leads to the following system of equations:

$$\frac{\partial p}{\partial t} = \lambda_p^f \left[\frac{\partial^2 p}{\partial r^2} + \frac{1}{r} \frac{\partial p}{\partial r} \right] + \lambda_p^S \frac{\partial C^S}{\partial t} \quad (4.27)$$

$$\frac{\partial C^S}{\partial t} = \lambda_{C^S}^S \left[\frac{\partial^2 C^S}{\partial r^2} + \frac{1}{r} \frac{\partial C^S}{\partial r} \right] \quad (4.28)$$

$$\frac{\partial \zeta}{\partial t} = \lambda_\zeta^f \left[\frac{\partial^2 \zeta}{\partial r^2} + \frac{1}{r} \frac{\partial \zeta}{\partial r} \right] + \lambda_\zeta^S \left[\frac{\partial^2 C^S}{\partial r^2} + \frac{1}{r} \frac{\partial C^S}{\partial r} \right] \quad (4.29)$$

4.3.1 Vertical Borehole

The procedure for solving the field equations is similar to that for porothermoelasticity, details of which can be found elsewhere (Li, 1998; Ghassemi et al., 1999; Ekbote et al., 2000). However, for the sake of completeness, a brief description follows.

The solution to the borehole problem can be constructed, following Detournay and Cheng (1988), by considering three loading modes superimposing the results onto the virgin formation conditions. Assuming that the axis of the wellbore coincides with one of the in-situ principal stress directions, and that p_o , C_o^S , and $\sigma_2 \neq \sigma_3$ are the initial formation pore pressure, solute mass fraction, and in-situ principal stresses acting perpendicularly to the borehole axis, respectively; the following boundary conditions can be written for each of the loading modes:

4.3.1.1 Mode 1

Mode 1 considers a hole in an infinite space under hydrostatic stress with the following boundary conditions:

$$\begin{aligned}\sigma_{rr}^{(1)} &= H(t) (P_0 - p_m) \\ \sigma_{r\theta}^{(1)} &= 0 \\ p^{(1)} &= 0 \\ C^{(1)S} &= 0\end{aligned}\tag{4.30}$$

In mode 1, the solute mass fraction and pore pressure boundary condition are zero, so the solutions corresponding to the classical Lamé solutions in elasticity (Detournay and Cheng, 1988); i.e.

4.3.1.1.1 Stresses

$$\sigma_{rr}^{(1)} = H(t)(P_0 - p_m)\frac{a^2}{r^2}\tag{4.31}$$

$$\sigma_{\theta\theta}^{(1)} = -H(t)(P_0 - p_m) \frac{a^2}{r^2} \quad (4.32)$$

4.3.1.2 Mode 2

Mode 2 considers a virgin pore pressure and chemical loading at the wellbore wall with the following boundary conditions:

$$\begin{aligned} \sigma_{rr}^{(2)} &= 0 \\ \sigma_{r\theta}^{(2)} &= 0 \\ p^{(2)} &= H(t)(p_m - p_o) \\ C^{(2)S} &= H(t)(C_m^S - C_o^S) \end{aligned} \quad (4.33)$$

where $H(t)$ denotes the Heaviside unit step function; p_m , and C_m^S are the wellbore pressure and the mud solute mass fraction content:

$$\left\{ \begin{array}{ll} H(t) = 0 & \text{for } t \leq 0 \\ H(t) = 1 & \text{for } t > 0 \end{array} \right\} \quad (4.34)$$

The solution of mode 2 (see Appendix E) is obtained by using the Laplace transform technique and then inverted to the time domain using Stehfest's algorithm. In the Laplace domain the solution is:

4.3.1.2.1 Solute mass fraction

$$\tilde{C}^{(2)S} = \frac{H(t)(C_m^S - C_o^S)}{s} \frac{K_0(\lambda r)}{K_0(\lambda a)} \quad (4.35)$$

4.3.1.2.2 Pore pressure

$$\tilde{p} = \frac{H(t)}{s} \left[(p_m - p_o) - \frac{\lambda_p^S (\tilde{C}_m^S - \tilde{C}_o^S)}{1 - \frac{\lambda_p^f}{\lambda_C^S}} \right] \frac{K_0(\xi_1 r)}{K_0(\xi_1 a)} + \frac{\lambda_p^S (\tilde{C}_m^S - \tilde{C}_o^S) H(t)}{s} \frac{K_0(\lambda r)}{K_0(\lambda a)} \quad (4.36)$$

4.3.1.2.3 Stresses

$$s\tilde{\sigma}_{rr}^{(2)} = \frac{(1-2\nu)\alpha'}{(1-\nu)} \left\{ \begin{aligned} & \left[(p_m - p_0) - \frac{\lambda_p^S (\tilde{C}_m^S - \tilde{C}_o^S)}{1 - \frac{\lambda_p^f}{\lambda_C^S}} \right] \\ & \left[\frac{K_1(\xi_1 r)}{r\xi_1 K_0(\xi_1 a)} - \frac{aK_1(\xi_1 a)}{r^2 \xi_1 K_0(\xi_1 a)} \right] + \frac{\lambda_p^S (\tilde{C}_m^S - \tilde{C}_o^S)}{1 - \frac{\lambda_p^f}{\lambda_C^S}} \left[\frac{K_1(\lambda r)}{r\lambda K_0(\lambda a)} - \frac{aK_1(\lambda a)}{r^2 \lambda K_0(\lambda a)} \right] \end{aligned} \right\} \\ + \frac{2G\beta(1+\nu)}{3(1-\nu)} (\tilde{C}_m^S - \tilde{C}_o^S) \left[\frac{K_1(\lambda r)}{r\lambda K_0(\lambda a)} - \frac{aK_1(\lambda a)}{r^2 \lambda K_0(\lambda a)} \right] \quad (4.37)$$

$$s\tilde{\sigma}_{\theta\theta}^{(2)} = -\frac{(1-2\nu)\alpha'}{(1-\nu)} \left\{ \begin{aligned} & \left[(p_m - p_0) - \frac{\lambda_p^S (\tilde{C}_m^S - \tilde{C}_o^S)}{1 - \frac{\lambda_p^f}{\lambda_C^S}} \right] \left[\frac{K_1(\xi_1 r)}{r\xi_1 K_0(\xi_1 a)} - \frac{aK_1(\xi_1 a)}{r^2 \xi_1 K_0(\xi_1 a)} + \frac{K_0(\xi_1 r)}{K_0(\xi_1 a)} \right] \\ & + \frac{\lambda_p^S (\tilde{C}_m^S - \tilde{C}_o^S)}{1 - \frac{\lambda_p^f}{\lambda_C^S}} \left[\frac{K_1(\lambda r)}{r\lambda K_0(\lambda a)} - \frac{aK_1(\lambda a)}{r^2 \lambda K_0(\lambda a)} + \frac{K_0(\lambda r)}{K_0(\lambda a)} \right] \end{aligned} \right\} \\ - \frac{2G\beta(1+\nu)}{3(1-\nu)} (\tilde{C}_m^S - \tilde{C}_o^S) \left[\frac{K_1(\lambda r)}{r\lambda K_0(\lambda a)} - \frac{aK_1(\lambda a)}{r^2 \lambda K_0(\lambda a)} + \frac{K_0(\lambda r)}{K_0(\lambda a)} \right] \quad (4.38)$$

4.3.1.3 Mode 3

Mode 3 considers a far-field deviatoric loading with the following boundary conditions:

$$\begin{aligned} \sigma_{rr}^{(3)} &= -S_0 H(t) \cos 2\theta \\ \sigma_{r\theta}^{(3)} &= S_0 H(t) \sin 2\theta \\ p^{(3)} &= 0 \\ C^{(3)S} &= 0 \end{aligned} \quad (4.39)$$

where:

$$P_0 = \frac{\sigma_{xx}^0 + \sigma_{yy}^0}{2}, \quad S_0 = \frac{\sqrt{[(\sigma_{xx}^0 - \sigma_{yy}^0)^2 + 4(\sigma_{xy}^0)^2]}}{2} \quad (4.40)$$

P_0 is the isotropic part of the stress tensor and S_0 represents its deviatoric part acting in a plane normal to the hole axis; then the principal stresses in the plane can be written as:

$$S_1 = (P_0 + S_0) \quad (4.41)$$

$$S_2 = (P_0 - S_0)$$

with the orientation given by:

$$\gamma = \frac{\arctan(2\sigma_{xy}^0)}{\sigma_{xx}^0 + \sigma_{yy}^0} \quad (4.42)$$

In mode 3, the solution is also obtained using the Laplace transform technique which is then inverted to the time domain using Stehfest's algorithm. Due to the fact that in mode 3, the solute mass fraction boundary condition is zero, the solutions given by Detournay and Cheng (1988), can be applied; i.e.

4.3.1.3.1 Pore pressure

$$\frac{s\tilde{p}^{(3)}}{S_0 \cos 2\theta} = \frac{B^2(1-\nu)(1+\nu_u)}{9(1-\nu_u)(\nu_u-\nu)} C_1 K_2(\lambda r) + \frac{B(1+\nu_u)C_2 a^2}{3(1-\nu_u)r^2} \quad (4.43)$$

4.3.1.3.2 Stresses

$$\frac{s\tilde{\sigma}_{rr}^{(3)}}{S_0 \cos 2\theta} = \frac{B(1+\nu_u)}{3(1-\nu_u)} C_1 \left[\frac{1}{(\lambda r)} K_1(\lambda r) + \frac{6}{(\lambda r)^2} K_2(\lambda r) \right] - \frac{C_2 a^2}{(1-\nu_u)r^2} - 3C_3 \frac{a^4}{r^4} \quad (4.44)$$

$$\frac{s\tilde{\sigma}_{\theta\theta}^{(3)}}{S_0 \cos 2\theta} = \frac{B(1+\nu_u)}{3(1-\nu_u)} C_1 \left[\frac{1}{(\lambda r)} K_1(\lambda r) + \left(1 + \frac{6}{(\lambda r)^2}\right) K_2(\lambda r) \right] + 3C_3 \frac{a^4}{r^4} \quad (4.45)$$

$$\frac{s\tilde{\sigma}_{r\theta}^{(3)}}{S_0 \sin 2\theta} = \frac{2B(1+\nu_u)}{3(1-\nu_u)} C_1 \left[\frac{1}{(\lambda r)} K_1(\lambda r) + \frac{3}{(\lambda r)^2} K_2(\lambda r) \right] - \frac{C_2 a^2}{2(1-\nu_u)r^2} - 3C_3 \frac{a^4}{r^4} \quad (4.46)$$

where $\lambda^2 = \frac{s}{c_f}$, and C_1, C_2, C_3 , are constants obtained from boundary conditions:

$$C_1 = \frac{12\lambda a(1-\nu_u)(\nu_u-\nu)}{B(1+\nu_u)(D_2-D_1)} \quad (4.47)$$

$$C_2 = \frac{4(1 - \nu_u)D_2}{D_2 - D_1} \quad (4.48)$$

$$C_3 = \frac{\lambda a (D_2 - D_1) + 8(\nu_u - \nu) K_2(\lambda a)}{\lambda a (D_2 - D_1)} \quad (4.49)$$

$$D_1 = 2(\nu_u - \nu) K_1(\lambda a) \quad \text{and} \quad D_2 = \lambda a (1 - \nu) K_2(\lambda a) \quad (4.50)$$

4.3.1.4 Final solution

The final solution for the solute mass fraction, the pore pressure and the stress distributions can be obtained by superimposing solutions from modes 1 to 3 onto the original stress, solute mass fraction and pore pressure fields; i.e.

$$\sigma_{rr} = -P_0 + S_0 \cos 2\theta + \sigma_{rr}^{(1)} + \sigma_{rr}^{(2)} + \sigma_{rr}^{(3)} \quad (4.51)$$

$$\sigma_{\theta\theta} = -P_0 - S_0 \cos 2\theta + \sigma_{\theta\theta}^{(1)} + \sigma_{\theta\theta}^{(2)} + \sigma_{\theta\theta}^{(3)} \quad (4.52)$$

$$\sigma_{zz} = \sigma_z + \nu' \left(\sigma_{rr}^{(1)} + \sigma_{rr}^{(2)} + \sigma_{rr}^{(3)} + \sigma_{\theta\theta}^{(1)} + \sigma_{\theta\theta}^{(2)} + \sigma_{\theta\theta}^{(3)} \right) - (\alpha' - 2\nu'\alpha) (p_0 + p^{(2)} + p^{(3)}) \quad (4.53)$$

$$\sigma_{r\theta} = -S_0 \sin 2\theta + \sigma_{r\theta}^{(3)} \quad (4.54)$$

$$p = p_0 + p^{(2)} + p^{(3)} \quad (4.55)$$

$$C^S = C_o^S + C^{(2)S} \quad (4.56)$$

where the superscript ⁽ⁱ⁾ represent the solution for loading mode i.

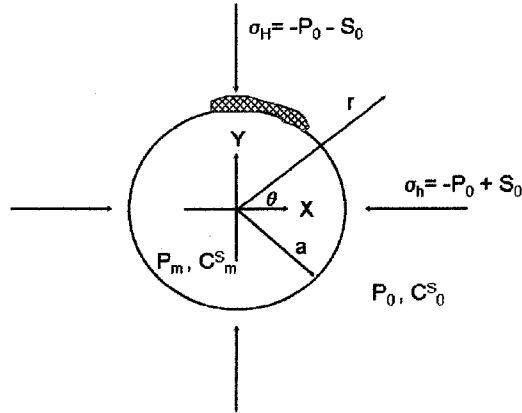


Figure 4.1: Schematic diagram of an inclined borehole subjected to a non-hydrostatic stress field and wellbore pressure and solute mass concentration which are different from initial formation pore pressure and solute mass concentration.

4.3.2 Inclined Borehole

An inclined borehole problem is solved by superposition of three fundamental problems (Cui et al., 1997); an chemoporoelastic plane-strain problem; an elastic uniaxial stress problem; and an elastic anti-plane shear problem.

It is also assumed that the borehole is drilled perpendicular to the isotropic plane; the borehole axis (Figure 4.1) is parallel to z -axis; subjected to in-situ principal compressive stresses denoted by $S_{x'}$, $S_{y'}$, and $S_{z'}$; the formation has a virgin pore pressure p_0 and an initial solute mass fraction C_0^S ; and a wellbore pressure p_m , and solute mass fraction C_m^S . The local borehole coordinate system, xyz , is related to the global coordinate system, $x'y'z'$, by an azimuth angle, $\varphi_{z'}$, formed by rotation about the z' -axis, and an inclination angle, φ_y , formed by further rotation about the y -axis. The in-situ principal stresses, $S_{x'}$, $S_{y'}$, $S_{z'}$, can be converted to the stress under borehole coordinate system, S_x , S_y , S_z , S_{xy} , S_{yz} , S_{zx} , using the method given by Fjær et al. (1992).

The boundary conditions at the instant of drilling are assumed to be:

$$\text{for } r \rightarrow \infty \quad \left\{ \begin{array}{ll} \sigma_{xx} = -S_x & \sigma_{yz} = -S_{yz} \\ \sigma_{yy} = -S_y & \sigma_{xz} = -S_{xz} \\ \sigma_{zz} = -S_z & p = p_0 \\ \sigma_{xy} = -S_{xy} & C^S = C_o^S \end{array} \right\} \quad (4.57)$$

$$\text{for } r = a \quad \left\{ \begin{array}{l} \sigma_{rr} = -S_r H(-t) \\ \sigma_{r\theta} = -S_{r\theta} H(-t) \\ \sigma_{rz} = -S_{rz} H(-t) \\ p = p_m H(t) - p_0 H(-t) \\ C^S = C_m^S H(t) - C_o^S \end{array} \right\} \quad (4.58)$$

where S_r , $S_{r\theta}$, and S_{rz} are the far-field compressive stress components in cylindrical coordinates. $H(-t)$ is defined as $1 - H(t)$ such that:

$$\left\{ \begin{array}{ll} H(-t) = 1 & \text{for } t \leq 0 \\ H(-t) = 0 & \text{for } t > 0 \end{array} \right\} \quad (4.59)$$

4.3.2.1 Problem I

Problem I (Figure 4.2) is a chemoporoelastic plane-strain problem. In elasticity, the plane strain solution for stresses in transverse isotropic material is the same as that for the isotropic case, if the plane of symmetry is perpendicular to the axis of symmetry. The boundary conditions for this problem are as follows:

$$r \rightarrow \infty \quad \left\{ \begin{array}{ll} \sigma_{xx} = -S_x & \sigma_{yz} = \sigma_{xz} = 0 \\ \sigma_{yy} = -S_y & p = p_0 \\ \sigma_{xy} = -S_{xy} & C^S = C_o^S \end{array} \right\} \quad (4.60)$$

$$\sigma_{zz} = -\nu'(S_x + S_y) - (\alpha' - 2\nu'\alpha)p_0 + (\chi' - 2\nu'\chi)C_o^S$$

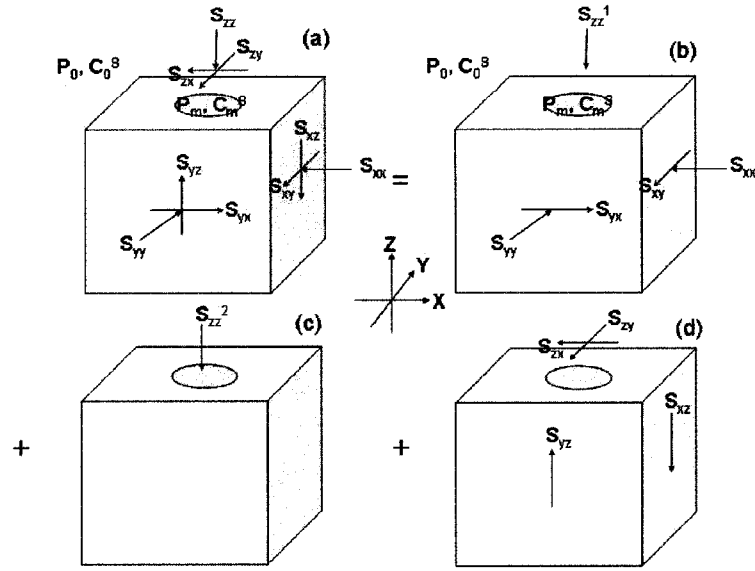


Figure 4.2: Loading decomposition scheme for an inclined borehole problem (after Li, 1998)

$$r = a \left\{ \begin{array}{l} \sigma_{rr} = -S_r H(-t) \\ \sigma_{r\theta} = -S_{r\theta} H(-t) \\ \sigma_{rz} = 0 \\ p = p_m H(t) - p_0 H(-t) \\ C^S = C_m^S H(t) - C_o^S \end{array} \right\} \quad (4.61)$$

The problem can be solved by further decomposing this situation into three loading modes, as derived in the last section (Equations 4.51 to 4.56). Because, the solutions(4.51 to 4.56) are given in a coordinate system, namely $x^*y^*z^*$, where the x^* -axis coincides with the in-plane minimum principal stress $\sigma_{x^*x^*}$ (Figure 4.3), there is an angular difference between the coordinate systems xyz and $x^*y^*z^*$, i.e.:

$$\theta_r = \theta - \theta^* \quad (4.62)$$

where θ and θ^* are the polar angles in the xyz - and $x^*y^*z^*$ -systems, respectively; and,

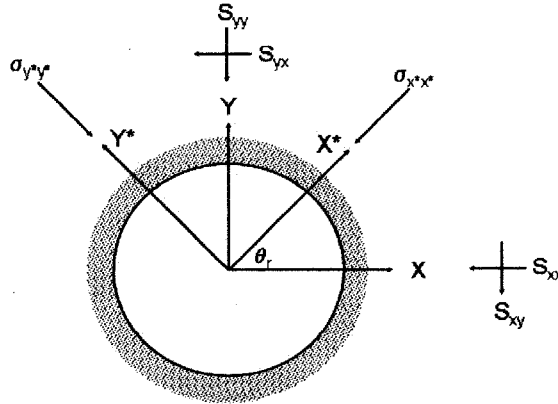


Figure 4.3: Correspondence between the two local coordinate systems

$$\theta_r = \frac{1}{2} \tan^{-1} \frac{2S_{xy}}{S_x - S_y} \quad (4.63)$$

The in-plane maximum and minimum principal stresses in $(x^*y^*z^*)$ -coordinates are:

$$\begin{aligned} \sigma_{y^*y^*} \\ \sigma_{x^*x^*} \end{aligned} = -\frac{S_x + S_y}{2} \pm \sqrt{\left(\frac{S_x - S_y}{2}\right)^2 + S_{xy}^2} \quad (4.64)$$

The final solution for problem I in a polar coordinate system, complying with the $(x^*y^*z^*)$ -coordinates, is given by the following equations:

$$C^{(I)S} = C_o^S + C^{(2)S} \quad (4.65)$$

$$p^{(I)} = p_0 + p^{(2)} + p^{(3)} \quad (4.66)$$

$$\sigma_{rr}^{(I)} = -P_0 + S_0 \cos 2\theta^* + \sigma_{rr}^{(1)} + \sigma_{rr}^{(2)} + \sigma_{rr}^{(3)} \quad (4.67)$$

$$\sigma_{\theta\theta}^{(I)} = -P_0 - S_0 \cos 2\theta^* + \sigma_{\theta\theta}^{(1)} + \sigma_{\theta\theta}^{(2)} + \sigma_{\theta\theta}^{(3)} \quad (4.68)$$

$$\sigma_{zz}^{(I)} = 2\nu'P_0 + \nu' \left(\sigma_{rr}^{(1,2,3)} + \sigma_{\theta\theta}^{(1,2,3)} \right) - (\alpha' - 2\nu'\alpha) p^{(I)} + (\chi' - 2\nu'\chi) C^S \quad (4.69)$$

$$\sigma_{r\theta}^{(I)} = -S_0 \sin 2\theta^* + \sigma_{r\theta}^{(3)} \quad (4.70)$$

$$\sigma_{rz}^{(I)} = \sigma_{\theta z}^{(I)} = 0 \quad (4.71)$$

where,

$$P_0 = -\frac{\sigma_{x^*x^*} + \sigma_{y^*y^*}}{2} \quad (4.72)$$

$$S_0 = \frac{\sigma_{x^*x^*} - \sigma_{y^*y^*}}{2} \quad (4.73)$$

4.3.2.2 Problem II

Problem II (Figure 4.2) is a uniaxial loading problem with the following boundary conditions:

$$\text{at } r \rightarrow \infty \quad \left\{ \begin{array}{l} \sigma_{zz} = -S_z + [\nu'(S_x + S_y) + (\alpha' - 2\nu'\alpha) p_0 + (\chi' - 2\nu'\chi) C_o^S] \\ \sigma_{xx} = \sigma_{yy} = \sigma_{xy} = \sigma_{yz} = \sigma_{xz} = p = C^S = 0 \end{array} \right\} \quad (4.74)$$

$$\text{at } r = a \quad \{ \sigma_{rr} = \sigma_{r\theta} = \sigma_{rz} = p = C^S = 0 \} \quad (4.75)$$

Since the boundary conditions at the borehole are zero, the drilling and pressurization of the borehole do not provoke any disturbances for this specific problem; that means no in-plane stresses are generated and it is a pure elastic problem (Cui et al., 1998). Its solution for stresses is the same as the one for the corresponding

isotropic problem; thus the solution is time-independent. In fact, it is given by a constant σ_{zz} prevailing everywhere:

$$\sigma_{zz}^{(II)} = -S_z + [\nu'(S_x + S_y) + (\alpha' - 2\nu'\alpha)p_0 + (\chi' - 2\nu'\chi)C_o^S] \quad (4.76)$$

$$\sigma_{rr}^{(II)} = \sigma_{\theta\theta}^{(II)} = \sigma_{r\theta}^{(II)} = \sigma_{rz}^{(II)} = \sigma_{\theta z}^{(II)} = p^{(II)} = C^{(II)}S = 0 \quad (4.77)$$

4.3.2.3 Problem III

Problem III (Figure 4.2) is an anti-plane shear problem with the following boundary conditions:

$$\text{at } r \rightarrow \infty \quad \left\{ \begin{array}{l} \sigma_{xx} = \sigma_{yy} = \sigma_{zz} = \sigma_{xy} = p = C^S = 0 \\ \sigma_{yz} = -S_{yz} \\ \sigma_{xz} = -S_{xz} \end{array} \right\} \quad (4.78)$$

$$\text{at } r = a \quad \left\{ \begin{array}{l} \sigma_{rr} = \sigma_{r\theta} = p = C^S = 0 \\ \sigma_{rz} = -S_{rz}H(-t) \end{array} \right\} \quad (4.79)$$

This problem is also purely elastic, where the shear deformation is uncoupled with the pore fluid and the solute mass fraction flow. The stress disturbance due to drilling is introduced by the sudden drop of surface traction σ_{rz} along the borehole wall from $-S_{rz}$ to zero. Therefore, the solution can be expressed as:

$$\sigma_{rz}^{(III)} = -(S_{xz} \cos \theta + S_{yz} \sin \theta) \left(1 - \frac{a^2}{r^2}\right) \quad (4.80)$$

$$\sigma_{\theta z}^{(III)} = -(S_{xz} \sin \theta - S_{yz} \cos \theta) \left(1 + \frac{a^2}{r^2}\right) \quad (4.81)$$

$$\sigma_{rr}^{(III)} = \sigma_{\theta\theta}^{(III)} = \sigma_{r\theta}^{(III)} = p^{(III)} = C^{(III)}S = 0 \quad (4.82)$$

4.3.2.4 Final Solution

Finally, superimposing the solution from problems I to III yields the following expressions (omitting the zero components):

$$\sigma_{rr} = \sigma_{rr}^{(I)} \quad (4.83)$$

$$\sigma_{\theta\theta} = \sigma_{\theta\theta}^{(I)} \quad (4.84)$$

$$\sigma_{zz} = \sigma_{zz}^{(I)} + \sigma_{zz}^{(II)} \quad (4.85)$$

$$\sigma_{r\theta} = \sigma_{r\theta}^{(I)} \quad (4.86)$$

$$\sigma_{rz} = \sigma_{rz}^{(III)} \quad (4.87)$$

$$\sigma_{\theta z} = \sigma_{\theta z}^{(III)} \quad (4.88)$$

$$p = p^{(I)} \quad (4.89)$$

$$C^S = C^{(I)S} \quad (4.90)$$

5 Model Applications

5.1 Introduction

Drilling a borehole results in a redistribution of the original stresses and pore pressure near the wellbore. In addition, the drilling fluid exerts a system of mechanical and chemical loads onto the rock; as a consequence, the response of the rock to imposed loads is deformation. The redistribution of stresses and pore pressure as well as the resulting deformations can be solved using the model developed in this dissertation. In this chapter, results will be given of the effect varying some parameters on the stress distribution around the borehole, solute mass fraction and pore pressure. Plots will be presented for different angles, times, solute concentrations, swelling coefficients, reflection coefficients, and degree of anisotropy. In order to study the impact of ion transfer on the pore pressure/stress field around the wellbore, an inclined well, drilled in a shale formation with material properties as well as relevant drilling fluid properties and geometrical well parameters, reported in Tables 5.1 and 5.2, will be considered. Eventhough, the theory was formulated using engineering sign conventions (tension positive), the results and the graphs will be given using the rock mechanics sign convention (compression positive). Figure 5.1 shows the experimental lay-out that was followed in getting the data. Finally, some failure analyses will be discussed.

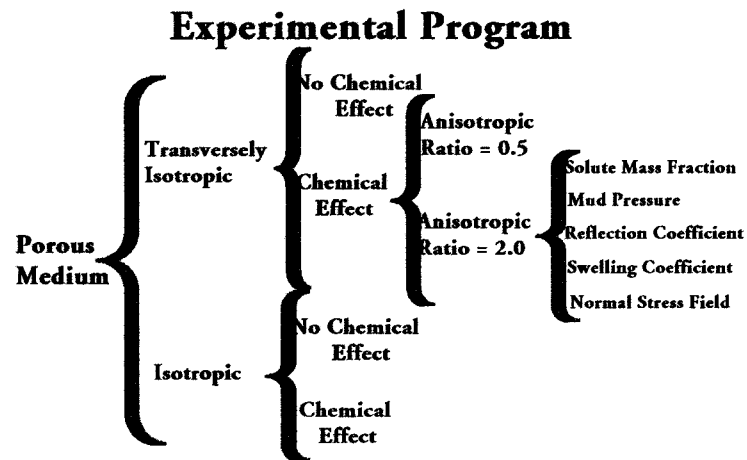


Figure 5.1: Experimental lay-out

5.2 Isotropic Porous Media

As pointed before, the model was used for inclined boreholes in shale; considering both an isotropic saturated porous media with and without chemical effects. The cases without chemical effects were used to simply simulate the poroelastic effect. Here, the solute mass fraction in the mud and the formation were equated. Also, the swelling coefficient, ω ; and reflection coefficient, \mathfrak{R} were set equal to zero¹. Other parameters for isotropic saturated porous media that were used as entry data are reported in Table (5.1).

Results at different times and polar angles (0 and 90 degrees) for the pore pressure, total stresses, and effective stresses are reported in Appendix G for the isotropic case without chemical effects in Figures (G.1) to (G.7); for the case where the chemical effects were considered the results are reported in Appendix H Figures (H.1) to (H.8).

¹If ω^β , ω'^β , and $\mathfrak{R} \rightarrow 0$ no chemical osmosis is involved. The phenomenon then falls under the purely poroelastic limit.

Parameters	Values
Poisson's ratio, ν	0.189
Undrained Poisson's ratio, ν_u	0.31
Young's Modulus, E	20.6 GPa
Solid Bulk Modulus, K_s	48.2 GPa
Fluid Bulk Modulus, K_f	2.5 GPa
Permeability, k	7.66 E-8 Darcy
Porosity, ϕ	0.143
Pore Fluid mass density, ρ_{of}	1111.11 Kg/m ³
Pore Fluid viscosity, η	3.0 E - 4 Pa-sec
Molar mass of solute (NaCl), M^S	58.5 kg/Kgmol
Pore solute mass fraction, C_0^S	0.1
Reflexion coefficient, \Re	0.0 and 0.4
Swelling Coefficient, ω_o	0.0 and 2.0 MPa
Solute Diffusion coefficient, D^S	1.0E-8 m ² /sec
Pore Pressure, p_0	10.0 MPa
Temperature, T	80 °C
Vertical Stress, σ_v	25 MPa
Maximum Horizontal Stress, σ_H	29 MPa
Minimum Horizontal Stress, σ_h	20 MPa
Mud Pressure, p_m	15 MPa
Mud solute mass fraction, C_m^S	0.20
Wellbore radius, r	0.10 m
Borehole Azimuth,	30°
Borehole Inclination,	60°
Polar Angle, θ	0° and 90°
Time, t	0.1; 0.5; 1; 10; and 100 hrs

Table 5.1: Entry data for isotropic saturated porous media

5.3 Transversely Isotropic Porous Media

The model was also used in the case of an inclined transversely isotropic saturated shale formation considering both cases: with and without chemical effects. The last one for the purpose of evaluating the difference between anisotropic and isotropic poroelastic effects.

In the anisotropic case with chemical effects two cases were explored: when the ratio between the mechanical and chemical properties in the isotropic plane and axial direction were 2 and 0.5, respectively. The results at different times and polar angles (0 and 90 degrees) with and without chemical effect for anisotropy ratio of 0.5 and 2.0 are reported in Appendixes I, J, and K respectively. For the anisotropic case without chemical effects the results are shown in Figures (I.1) to (I.7); the anisotropic case with chemical effects are represented in Figures (J.1) to (J.8) and (K.1) to (K.8) for $AR = 0.5$ and $AR = 2$ respectively for solute mass fraction diffusion, pore pressure, total stresses and effective stresses. In addition, for the anisotropic case with a ratio of two ($AR = 2$) the chemical effects at early and long times were considered varying the concentration of solute mass fraction in the mud, the swelling coefficient, the reflection coefficient, and the mud pressure. The results are also reported in Appendixes L, M, N, and O in Figures (L.1) to (L.8); (M.1) to (M.8); (N.1) to (N.8); and Figures (O.1) to (O.8), respectively.

Finally, the anisotropic case was explored with chemical effects in a normal stress field. These results too are reported in Appendix P in Figures (P.1) to (P.7). The entry data used for these cases are reported in Table 5.2.

5.4 Discussion of Results

It is wellknown, that when a borehole is drilled it is filled with drilling fluids which assists in keeping the stress concentration level within the limits of permissible

Parameters	Values
Poisson's ratio, ν	0.189 and 0.378
Undrained Poisson's ratio, ν_u	0.31
Poisson's ratio, ν'	0.189 and 0.378
Young's Modulus, E	20.6 and 41.2 GPa
Young's Modulus, E'	20.6 and 41.2 GPa
Solid Bulk Modulus, K_s	48.2 GPa
Fluid Bulk Modulus, K_f	2.5 GPa
Permeability, k	7.66 E-8 Darcy
Permeability, k'	7.66 E-8 Darcy
Porosity, ϕ	0.143
Pore Fluid mass density, ρ_{of}	1111.11 Kg/m ³
Pore Fluid viscosity, η	3.0 E - 4 Pa-sec
Molar mass of solute (NaCl), M^S	58.5 kg/Kgmol
Pore solute mass fraction, C_0^S	0.1
Reflexion coefficient, \Re	0.0; 0.25; 0.5; 0.75; and 1.00
Swelling Coefficient, ω_o	0.0; 0.4; 2.0; 4.0; 20.0; and 40.0 MPa
Swelling Coefficient, ω'_o	0.0; 0.2; 1.0; 2.0; 10; and 20.0 MPa
Solute Diffusion coefficient, D^S	1.0 E-8 m ² /sec
Pore Pressure, p_0	10.0 MPa
Temperature, T	80 °C
Vertical Stress, σ_v	25 and 29 MPa
Maximum Horizontal Stress, σ_H	29 and 25 MPa
Minimum Horizontal Stress, σ_h	20 MPa
Mud Pressure, p_m	15 MPa
Mud solute mass fraction, C_m^S	0.001; 0.05; 0.1; 0.15; 0.20; and 0.25
Wellbore radius, r	0.10 m
Borehole Azimuth,	30°
Borehole Inclination,	60°
Polar Angle, θ	0° and 90°
Time, t	0.1; 0.5; 1; 10; and 100 hrs

Table 5.2: Entry data for transversely isotropic saturated porous media

material strength. However, chemical composition of the drilling fluids leads to chemical gradients which act as driving forces for chemical processes which affect the stress and pore pressure distributions near the borehole. The level of these changes are discussed in the following sections, as well as the impact of the main variables related to wellbore stability problems.

Anisotropy was studied setting the ratio between the properties of the isotropic plane and the axial direction of the Young's modulus, Poisson's ratio and swelling coefficient to 1/2, 1/1, and 2/1, respectively. Other properties, such as solute mass fraction in the drilling mud, drilling mud pressure, swelling coefficient, reflection coefficient and stress field were varied in order to capture the predicted chemical effect.

5.4.1 Solute Mass Fraction

Because of the uncoupling of the solute mass concentration and pore pressure in Equation 4.18 (by assuming $L_p \rightarrow 0$), the diffusion of the solute mass fraction of the mud obeys the classical diffusion equation. This does not depend on the rock properties such as isotropy, anisotropy, reflection coefficient, swelling coefficient, etc. The diffusion of the solute mass fraction is only a function of time, diffusion coefficient, and the difference of concentration between the mud and the formation, as is shown in Figures 5.2 and 5.3. It can be observed that due to ion transfer, the solute mass fraction in the formation, increases with time. The variation of the solute mass fraction through the formation increases or decreases in a monotonic way according to the initial value of the solute in the mud. At early times they converge rather fast to the formation value with a small perturbation radius, just behind the borehole wall. This perturbation zone is increased as time increases beyond the borehole wall. When the concentration of the solute mass fraction is the same in the mud than in the formation, no ion transfer or perturbation occurs.

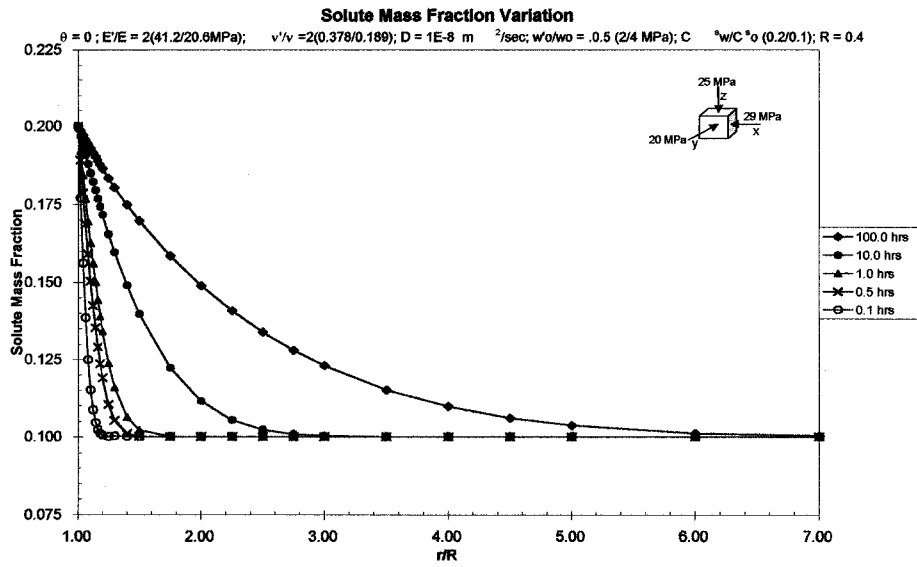


Figure 5.2: Solute mass fraction variation with time in a transversely isotropic saturated porous media using an anisotropy factor of two. Chemical effects are also considered.

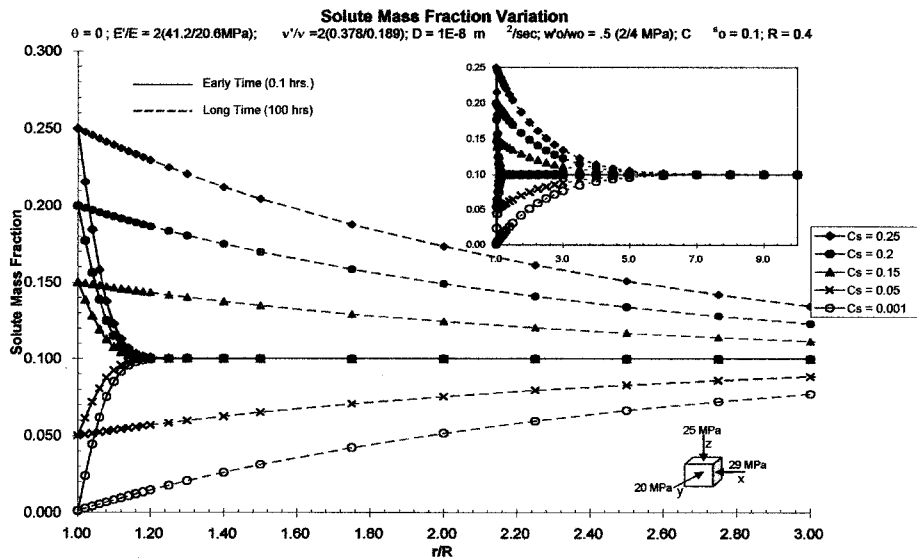


Figure 5.3: Solute mass fraction variation when changing the solute concentration in the drilling mud at early and long times. The formation is a transversely isotropic, saturated, with an anisotropy factor of two. Chemical effects are also considered.

5.4.2 Pore Pressure

When no chemical effects are considered, in both isotropic and transversely isotropic saturated porous media, the pore pressure distributions along the radial direction as a function of time, are monotonic and obey a diffusion-like law. At early times, the equilibrium value is reached faster within a few centimeters of the borehole wall. However, when the mud pressure is higher than the formation pressure, the isotropy case shows a slightly minimum in the pore pressure profile at very small times (0.1 Hr) mainly along $\theta = 0^\circ$, it also presents a difference between the pore pressure distribution at $\theta = 0^\circ$ and $\theta = 90^\circ$ which decreases as time increases (see Figures G.1 and I.1). For the case of anisotropy, the minimum of the pore pressure at early times does not exist and the values and perturbation zone slightly increases, converging to the formation pore pressure beyond the borehole wall. Also, the differences of the pore pressure at different polar angles diminishes. In both isotropy and anisotropy cases, at long times, the perturbation reaches beyond twenty times the radius of the well.

Figure 5.4 shows the early and long times behavior of the pore pressure for five different cases: i) isotropic with chemical effects; ii) isotropic without chemical effects; iii) transversely isotropic with chemical effects; iv) transversely isotropic without chemical effects; and v) variation of the stress field (normal).

When chemical effects are taken into account, the pore pressure distribution along the radial direction is not monotonic. In both isotropic and transversely isotropic cases, the pore pressure shows a pronounced minimum value near the borehole wall. At early times, this minimum value is located very near the borehole wall. The pore pressure increases quickly to converge to the initial pore pressure in less than three times the wellbore radius. As time increases, these minima are located far away from the wellbore wall, which indicates that the slope in pore pressure reduction is smaller and their minimum values also increase. In this zone, the perturbation radius is bigger as time increases (see Figures H.2 , J.2, K.2, and 5.4) due to the fact that the pore pressure increases after the minimum with a

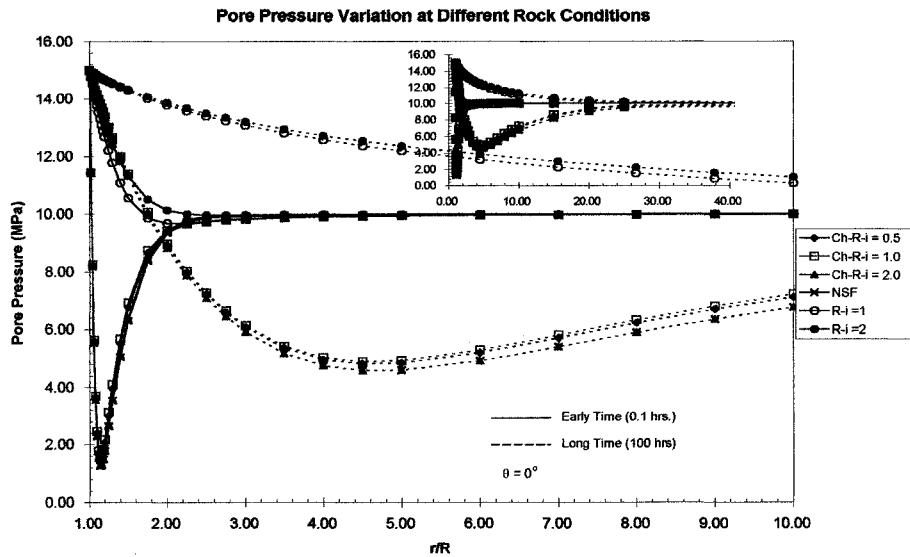


Figure 5.4: Pore pressure distribution along the radial direction ($\theta = 0$) at early and long times for different rock conditions (isotropic and anisotropic with and without chemical effects). The effect of the normal stress field in anisotropic conditions (AF=2) is also considered.

smaller slope, so that the convergence with the initial pore pressure takes place in more than 20 times the wellbore radius.

From these figures it is clear that chemical osmosis significantly modifies the pore pressure profile. Nevertheless, as time increases, the diffusion of ions dissipates the osmotic pressure by reducing the chemical potential gradient, which leads the reestablishment of a pore pressure regime, characteristic of hydraulic flow. This has significant implications on borehole stability because it affects the effective stresses and can cause delayed borehole failures. This behavior occurs when the solute mass fraction and mud pressure are higher than the values of the formation.

On the other hand, from the aforementioned figures one can observe small differences in the pore pressure profile between isotropy and anisotropy at early times along the radial direction at $\theta = 0$ and $\theta = 90$, that disappears when the time increases. The anisotropic case reaches smaller values of the pore pressure as the radial distance increases; and no changes in the pore pressure occurs when the

stress field was changed, at least within the order of magnitude considered in this dissertation.

In addition, pore pressure was not affected by the swelling coefficient as one can see in Figure (M.2) due to the fact of neglecting the pressure solute diffusion ($L_p \rightarrow 0$). In Figures (L.2), (O.2), and (N.2) the pore pressure distributions are plotted along the radial direction ($\theta = 0$) at early and long times, for a number of cases of solute mass concentration in the drilling fluids, mud pressure, and reflection coefficient, respectively. One observes negative values of the pore pressure for certain combinations of input data (high solute concentration in the mud, small mud pressure, and high values of the reflection coefficients), which may be due to the fact that the solute diffusion due to the hydraulic gradient was neglected (pressure solute diffusion $L_p = 0$). The assumption results in uncoupling the effect of osmosis from the chemical solute diffusion and viceversa.

When the solute mass concentration of the mud changes, it is clear that the pore pressure distribution depends on the solute concentration gradient between the mud and the formation. If the concentration in the mud is smaller than the formation, pore pressure increases reach a maximum and decreases, converging towards the initial pore pressure. At early times, this peak is bigger than at long times, and meets the initial pore pressure just a few centimeters behind the borehole wall. At long times this maximum is smaller, but the perturbation radius highly increases. Here, it can also be seen that the ion transfer causes the chemical-osmosis effect to be time-dependent.

The pore pressure behaves like the anisotropic case when the reflection coefficient is changed, with the difference, that here, the minima are much more pronounced as the reflection coefficient increases; high negative values of pore pressure are obtained, may be for the reasons explained before. In the case of the mud pressure variation at early and long times, the pore pressure distribution follows the same pattern explained before and the level depends of the gradient of pressure between the mud and the formation.

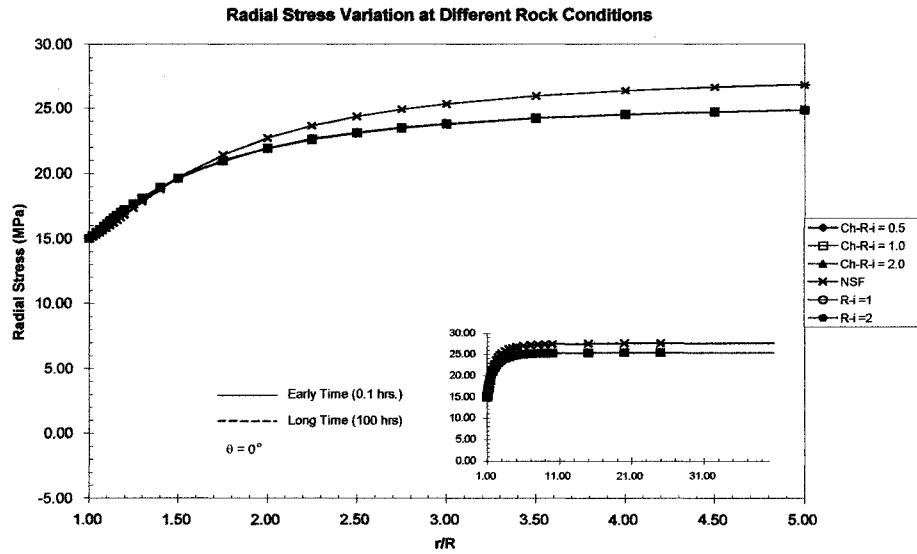


Figure 5.5: Radial stress variation along of radial ($\theta = 0$) direction for different rock conditions.

5.4.3 Total Stresses

Eventhough the total stresses are not as important as the effective ones in wellbore stability studies, they are presented here for completeness.

5.4.3.1 Radial Stress

The radial stress shows a monotonic increase from the wellbore pressure to a value in the far-field of 25.4 MPa in the radial direction and for a polar angle of 0^0 ; and 22.3 MPa when the polar angle was 90^0 . When the stress field was changed, the radial stress reached values of 27.7 MPa and 21.3 MPa for angles of 0^0 and 90^0 , respectively. The radial stress keeps the same pattern, no matter what changes were introduced (see Figures J.3, P.2, and 5.5).

5.4.3.2 Tangential Stress

The tangential stress shows a monotonic decrease along the radial direction for $\theta = 90^0$, converging to 25.4 MPa in all the cases (see Figures G.3; H.4; I.3; J.4;

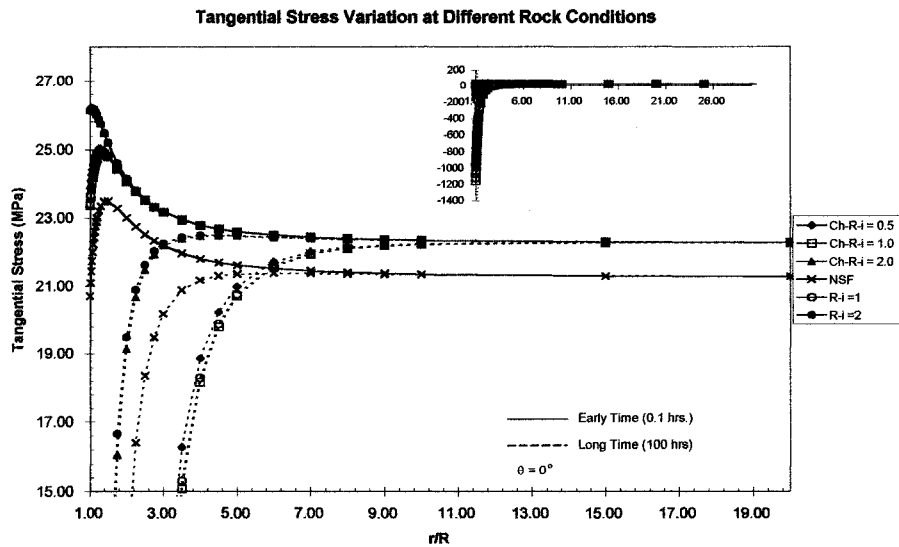


Figure 5.6: Tangential stress variation along the radial direction ($\theta = 0$) for different rock conditions, with and without chemical effects.

K.4; L.4; M.4; N.4; O.4; and P.3). As time increases, the value of the stress at the wellbore wall increases from 39 MPa, to 1,190 MPa for early and long times, respectively. However, at $\theta = 0^\circ$ for long times, the tangential stress profile increases monotonically from negative values at the borehole wall to 22.3 MPa. In addition, at early times, a smooth curve passing through a maximum and converging to the aforementioned value can be seen. From these figures and Figure 5.6, one can say that anisotropy of the material and time are the parameters that most affect the stress value at the borehole wall.

From these figures one can also observe that the chemical effects in the tangential stress profile are negligible.

5.4.3.3 Axial stress

The axial stress profile along the radial direction at both polar angles ($\theta = 0^\circ$ and $\theta = 90^\circ$) follows patterns similar to the tangential stress. However, the axial stress is more sensible to changes in rock and fluid properties. Here, the characteristics of

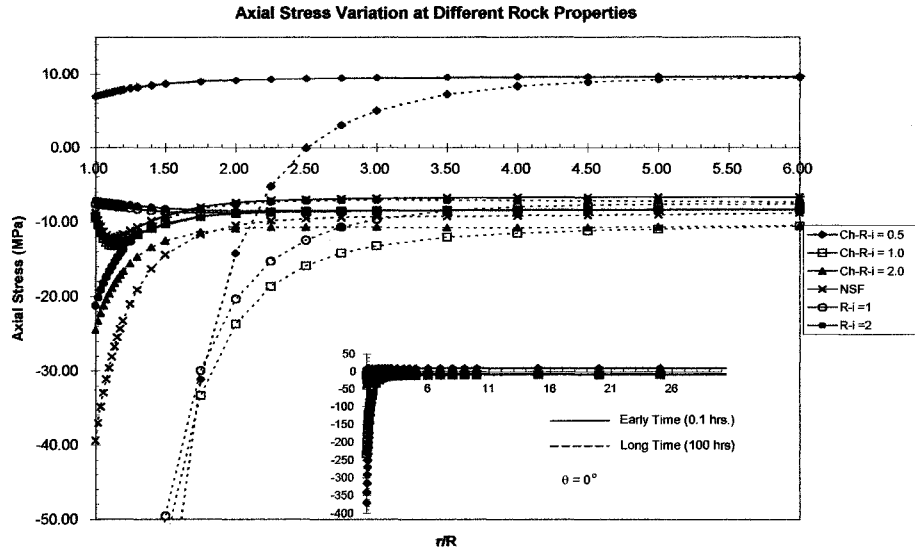


Figure 5.7: Axial stress distribution along the radial direction ($\theta = 0$) of the borehole at early and long times for different rock conditions.

the porous media, as well as the fluid (chemical properties) not only affect the axial stress profile, but also affect the magnitude of the stresses at the borehole wall, as can be seen from Figures (5.7); (G.4); (H.5); (I.4); (J.5); (K.5); (L.5); (M.5); (N.5); (O.5); and (P.4)

5.4.4 Effective Stresses

The effective stresses are the most important parameters in wellbore stability studies due to the fact that they couple the chemical and pore pressure effects in most failure criteria. In this dissertation we considered an effective stress like Terzaghi's modified effective law which is calculated according to Equation 5.1, using $\mathcal{B} = 1^2$ in order to be more conservative for the case of tensile and shear failure.

$$\sigma'_{ij} = \sigma_{ij} - \mathcal{B}p\delta_{ij} + \chi \left(C^S - \frac{b}{a^S} \right) \delta_{ij} \quad (5.1)$$

²The effective stresses are smaller, due to the fact that the magnitude of the pore pressure is subtracted completely from the total stress.

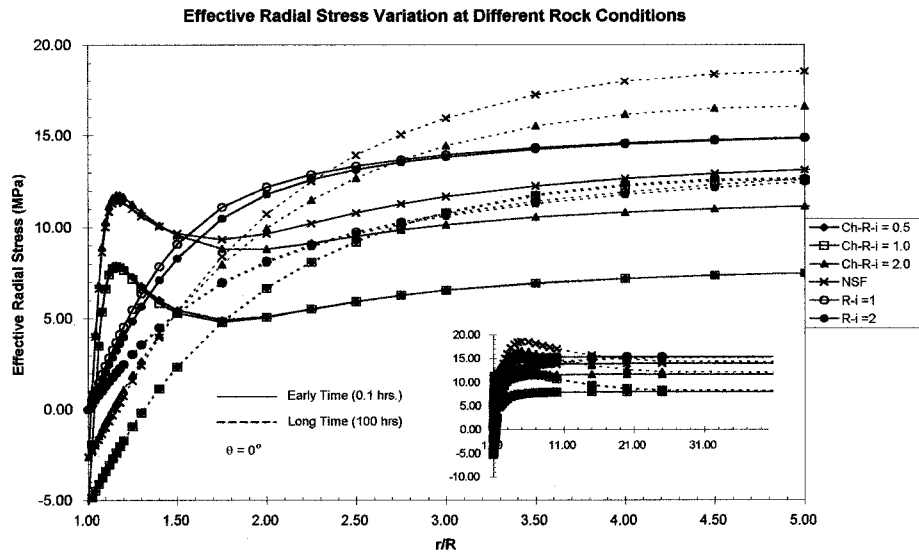


Figure 5.8: Effective radial stress distribution along the radial direction ($\theta = 0$) at early and long times for different rock properties.

5.4.4.1 Radial Stress

The effective radial stress distribution along the radial direction, when no chemical effects are taken into account, always increases monotonically from zero to 15.4 MPa and 12.3 MPa for $\theta = 0^\circ$ and $\theta = 90^\circ$, respectively. The only difference with time is the slope at which the curve increases, which decreases as time increases, resulting in a bigger perturbation in the stress field. Here, the anisotropy effect is only noticeable at early times and disappears at long times, as can be seen from Figures (G.5), and (I.5).

If the chemical effect is taken into account, the effective radial stress profile shows a non-monotonic increase with a peak nearest to the wellbore wall at early times. Also, the maximum slightly increases with time, but it is also located farther away from the borehole wall as a result of the decreasing slope, which means deeper perturbation of the stress field.

The effect of anisotropy, when chemical effects are considered, is more clear when the ratio of anisotropy is double, affecting only the magnitude of the stresses

but not the profile, as one can see from Figures (H.6), (J.6), and (K.6). Although, the wellbore is supported by a mud pressure of 15 MPa, the rock experiences a tensile effective radial stress in the borehole wall of 3 to 5 MPa, in accordance with the degree of anisotropy. The tensile effective radial stress becomes lower as one uses lower solute mass concentrations in the mud (L.6), and becomes critical³ when the solute mass fraction in the mud is lower than the solute mass fraction in the formation. This induced tensile stress is due to the solute invasion into the formation.

The value of the swelling coefficient is an other critical parameter that induces higher tensile effective radial stresses (Figure M.6) due to the fact that the magnitude of the solute invasion into the formation depends largely on this parameter. The effect of other parameters like mud pressure also modifies in some way moderately the profile (see Figure O.6). However, the reflection coefficient changes significantly the magnitude of the maximum of both at early and long times (Figure N.6). Finally, changes in the stress field do not produce significant changes in the effective stress profile (Figure P.5).

5.4.4.2 Tangential Stress

The effective tangential stress distribution along the radial direction has different profiles (increasing or decreasing) depending of the polar angle. When no chemical effects are considered, the profiles at different times are monotonic in both the isotropic and anisotropic cases (Figures G.6, and I.6); with the exception of some smooth and slight maximum for the early times along $\theta = 0^\circ$. However, in this direction, especially at long times, a highly tensile effective tangential stress is developed, diminishing as the anisotropy arises. If chemical effects are taken into account (Figures H.7, J.7, and K.7), the profile in both directions exhibit sensible

³At lower values of solute mass fraction in the mud (fresh water), the effective tensile radial stress at early time reaches -35 MPa just behind the borehole well. At long times, the effective tensile radial stress reaches -15 MPa; however, the size of the perturbation zone increases more than 12 times.

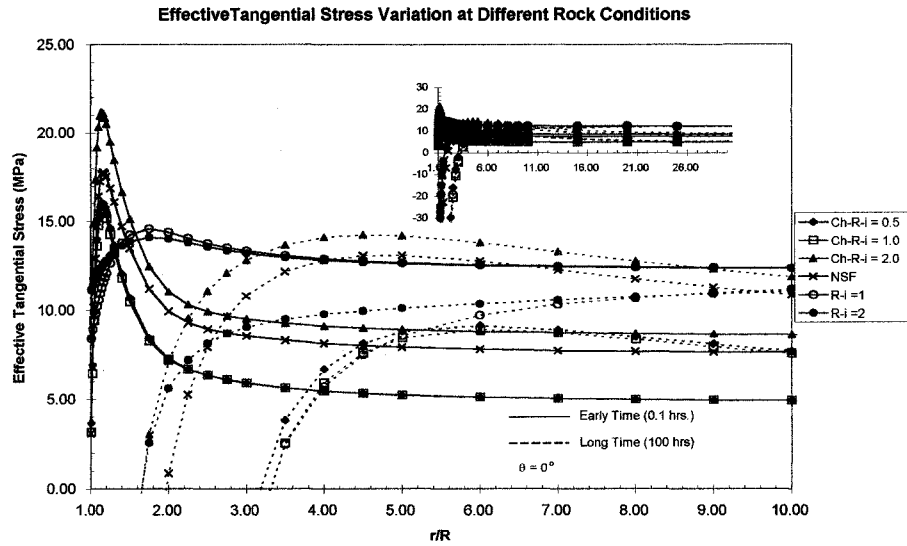


Figure 5.9: Effective stress distribution profile along the radial direction ($\theta = 0^{\circ}$) at early and long times for different rock properties

changes and present a maximum almost at all time intervals, except for long times along the $\theta = 90^{\circ}$ -direction. For $\theta = 0^{\circ}$, the maximum decreases as time increases. Also their location is further away from the borehole wall as the time increases. From these figures it is clear that the profile changes as the anisotropy changes, decreasing the tensile effective stress as the anisotropy increases as well as the size of the perturbed zone (see Figure 5.9).

Changing the solute mass concentration in the mud also has a large effect (see Figure L.7), mainly when the solute mass concentration in the mud is lower than the formation, creating a large zone subjected to tensile effective tangential stresses. Also notice that, at long times, just behind of the wellbore wall, a large tensile effective stress field is created which decreases as the mud solute concentration increases. It is well-known that the increase in tangential effective stress enhances the potential for shear failure inside the formation.

The mud pressure effect is shown in Figure (O.7). From this figure one can see that, at early times, no tensile effective stress is generated at any pressure and the

maximum effective tangential stress increases as the pressure decreases. However, at long times, high tensile effective tangential stresses appear a few centimeters from the borehole wall; this zone decreases as the mud pressure decreases. The reflection coefficient (Figure N.7) presents a similar profile to the mud pressure but in the reverse way; the maximum increases as the reflection coefficient increases and the tensile effective tangential stress generated at long times near to the wellbore wall increases as the reflection coefficient decreases.

For large values of the swelling coefficient tensile effective tangential stresses are generated in both early and long times. However, at longer times a large tensile effective tangential stress is always induced for all values of the swelling coefficient (Figure M.7). From this figure one can observe a peak near the wellbore wall at early times and a smaller smooth maximum reached at long times, implying a deeper perturbation of the stress field into the formation.

The effect of the stress field in the effective tangential stress is shown in Figure P.6; it slightly increases the tendency to generate a tensile effective tangential stress near the wellbore wall.

5.4.4.3 Axial stress

The effective axial stress distribution along the radial direction is shown in Figures (G.7) and (I.7), when no chemical effects are considered. From these figures it is clear that anisotropy affect the profiles but not the magnitude of the stresses at early times. However, it is clear that when anisotropy exists, the size of the perturbation zone decreases and concentrates closer to the wellbore. In addition, at very long times, the tensile effective stress decreases dramatically as the anisotropy increases.

When chemical effects are taken into account, the distribution and the values of the tensile effective axial stress along the radial direction changes with the anisotropy of the medium (see Figures H.8, J.8, and K.8). As discussed before, the chemical effect introduces a non-monotonic distribution of the stresses which always presents a maximum near the wellbore wall and moves away as the time

increases. Here, the higher values of tensile effective axial stress is obtained in the isotropic case, which also produces a deeper perturbation zone.

As one expects, the tensile effective axial stress increases as the concentration of the solute in the mud decreases. However, tensile effective axial stresses were obtained for all values of salinity, as can be seen in Figure (L.8). When mud salinity values below the solute mass concentration of the formation were used, the perturbation zone was larger. It is also observed that the behavior of the effective tangential stress is similar to the pore pressure when the salinity was changed, which is an indication that osmosis works in a similar way as stresses.

The variation of the mud pressure (Figure O.8) has a similar profile than the tangential stress, with the difference that, in this case, all the values of mud pressure generated tensile effective axial stresses. Nevertheless, at long times, the negative values are smaller than in the case of the tangential stresses. Figure (N.8) shows the results obtained by changing the reflection coefficient which give a similar profile than the effective tangential stress with some differences which were already pointed out before for the mud pressure. Also, the swelling coefficient (Figure M.8) presents similar profiles to the ones discussed in the case of the effective tangential stress, but with similar limitations. The magnitudes of the tensile effective stresses are more pronounced than in the case of the effective tangential stress.

As a result it is clear that the stresses and the pore pressure are influenced by the anisotropy, reflection, swelling and chemical properties of the material. From these results one can conclude that the ion transfer and chemical osmosis significantly modifies the loading conditions of the formation near the borehole wall as the exposed time increases.

5.5 Failure analysis

It is well-known, that boreholes fail either by exceeding the tensile strength, the compressive strength or the shear strength of the rock formation by the effective

stress concentration prevailing around the wellbore due to the far-field stresses and borehole relative orientation. Also, the wellbore failure is controlled by the effective stress concept, which in our case were calculated following Terzaghi's modified effective stress concept.

In this study one will consider the more common failure criteria: compressive failure, tensile failure, and Mohr-Coulomb failure.

5.5.1 Compressive failure

The compressive failure criterion used in wellbore stability analyses establishes that the Terzaghi's modified effective compressive tangential stress at the borehole wall equals the uniaxial compressive strength of the rock formation, i.e:

$$\sigma'_\theta = \sigma_\theta - p + \chi \left(C^S - \frac{b}{a^S} \right) = \sigma_c \quad (5.2)$$

Thus, from Equation (5.2) the effective compressive failure stress can be defined as:

$$\sigma_{ecfs} = \sigma_c - \sigma'_\theta \quad (5.3)$$

Where σ_{ecfs} is the effective compressive failure stress. When the value of this stress is negative, compressive failure occurs (which means $\sigma'_\theta > \sigma_c$).

Applying this criterion to the results already presented, assuming a compressive strength $\sigma_c = 40$ MPa (average compressive strength of shale in the Sen field located in the southeast of Mexico), compressive failure is likely to occur along the radial direction at $\theta = 90^\circ$ after a period of interaction time either in the isotropic or anisotropic cases. However, as the anisotropy increases, the risk of failure diminishes.

When the mud solute mass fraction, swelling coefficient, reflection coefficient, mud pressure or the stress field are changed, no risk of compression failure occurs at $\theta = 0^\circ$. However, the most risky factor is reached for high reflection coefficient

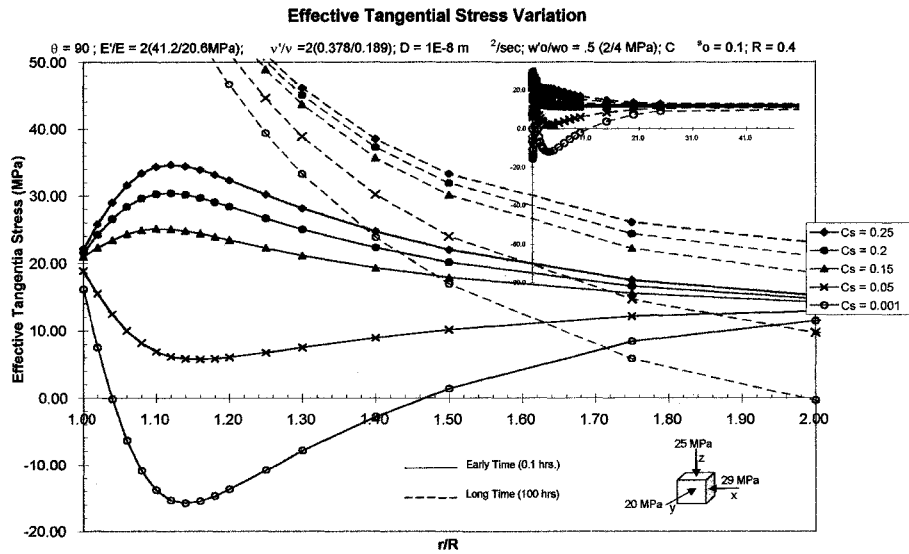


Figure 5.10: Effective tangential stress distribution along the radial direction ($\theta = 90^\circ$) for different mud salinities

values. At $\theta = 90^\circ$ there are more risks of failure due to the fact that, for extended times, the effective tangential stress increases in all cases. It is clear that the zone of induced effective compressive failure stress expands as the time increases, but it does not extend far into the rock.

From Figures (5.10), (5.11), (5.12), and (5.13), one can observe that, for long periods of time, the effective tangential stress increases beyond 40 MPa for all values of solute mass fraction in the mud, mud pressure, reflection coefficient and swelling coefficient, respectively. From the results of the solute mass fraction variation in the mud, it is observed that, as the concentration increases, the limit value of the effective compressive failure stress is located deeper into the formation (between 1.25 and 1.4 times the radius of the well). However, at early times, all values are below this stress limit. In the case of the mud pressure variation, the crossing of the stress limit is located between 1.32 to 1.56 times the borehole radius, but the tendency is reversed; the smaller the mud pressure, the deeper the location of the crossing of the stress limit. For this, at early times the peak of the smaller pressure

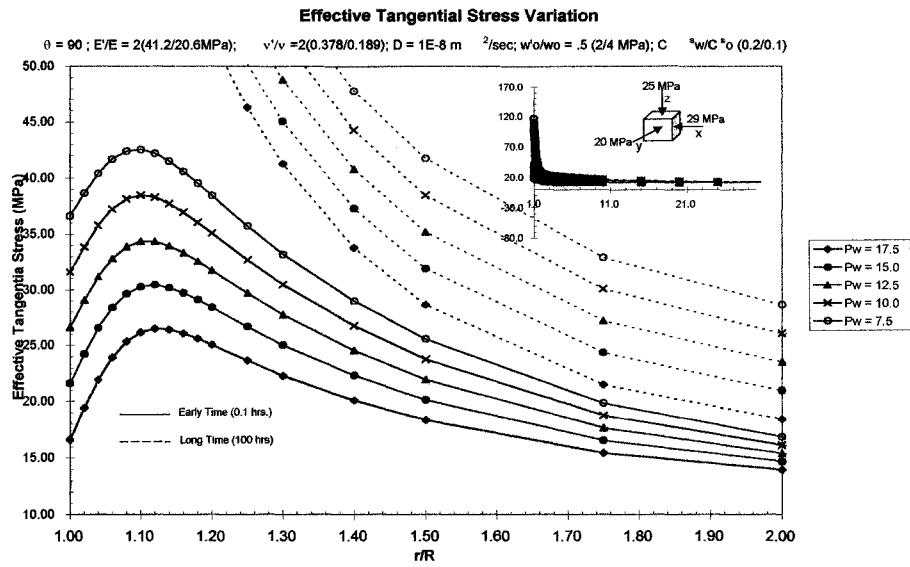


Figure 5.11: Effective tangential stress distribution along the radial direction ($\theta = 90^\circ$) for different mud pressures.

goes beyond the effective compressive failure stress very near the borehole wall.

The results of the reflection coefficient variation for long times, shows that the crossing of the stress limit is located between 1.34 to 1.42 times the wellbore radius, following the same tendency as the solute mass concentration; the bigger the reflection coefficient, the deeper the location of crossing of the stress limit. However, for early times the peak, of two values of the reflection coefficient (1.0 and 0.75) goes beyond the effective compressive failure stress. The swelling coefficient variation leads only to failure after an extended time period, crossing the stress limit at 1.16 to 1.40 times the wellbore radius, which shows the same tendency than with mud pressure; the smaller the reflection coefficient, the deeper the location of the crossing of the stress limit.

5.5.2 Tensile failure

In tensile failure there are two possible modes: one is due to fracturing the borehole wall because of increasing mud pressure which induces tensile stresses, resulting in

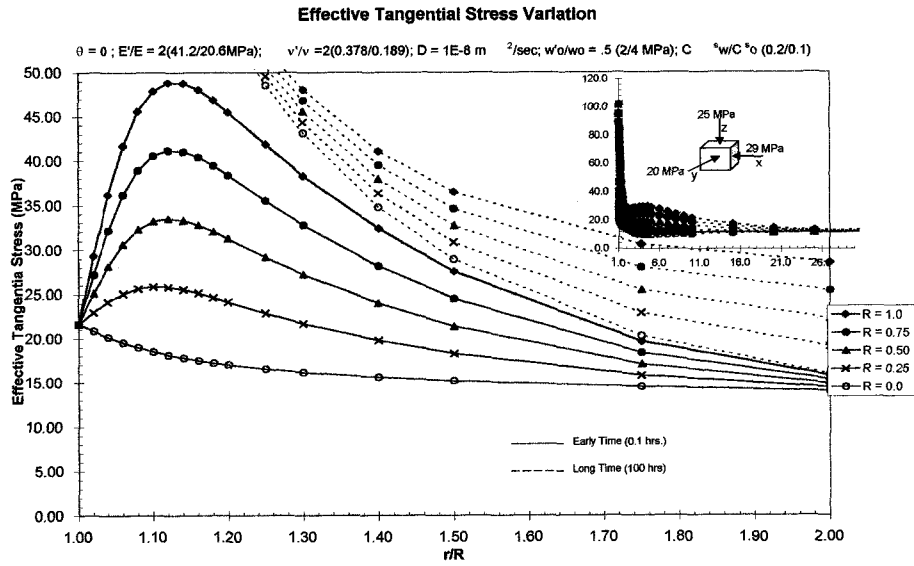


Figure 5.12: Effective tangential stress distribution along the radial direction ($\theta = 90^\circ$) for different reflection coefficients.

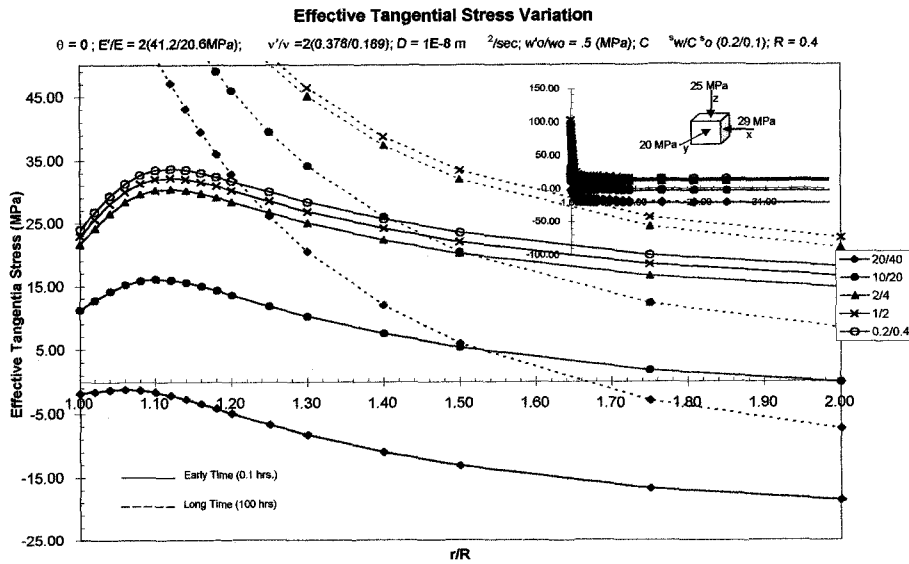


Figure 5.13: Effective tangential stress distribution along the radial direction ($\theta = 90^\circ$) for different swelling coefficients.

fracturing the rock and lost circulation problems; the second one is referred as an outburst failure or spalling, which is due to a tensile effective radial stress caused by decreasing in the mud pressure or a very rapid depressurizing borehole (Cheng et al., 1993).

5.5.2.1 Fracturing Failure

The failure criterion for fracturing establishes that the effective principal tensile stress (i.e., minor principal stress) at the borehole wall equals the formation tensile strength, such that:

$$\sigma'_3 = T \quad (5.4)$$

where, σ'_3 is the effective principal tensile stress (note that σ'_3 is a negative value). Thus, from Equation (5.4) one can define the effective fracturing stress as:

$$\sigma_{frac} = \sigma'_3 + T$$

where, σ_{frac} , is the effective fracturing stress, so that when its value is below zero fracturing will occur.

During drilling operations, when high mud density is used for well control, lost circulation could be induced. Also, this mechanism is used in hydraulic fracturing to improve oil and gas production.

5.5.2.2 Spalling Failure

The failure criterion for spalling establishes that the effective radial tensile stress in the borehole equals the formation tensile strength such that:

$$\sigma'_r = \sigma_r - p + \chi \left(C^S - \frac{b}{a^S} \right) = T \quad (5.5)$$

where σ_r is the total radial stress and p the pore pressure and σ'_r the effective radial stress.

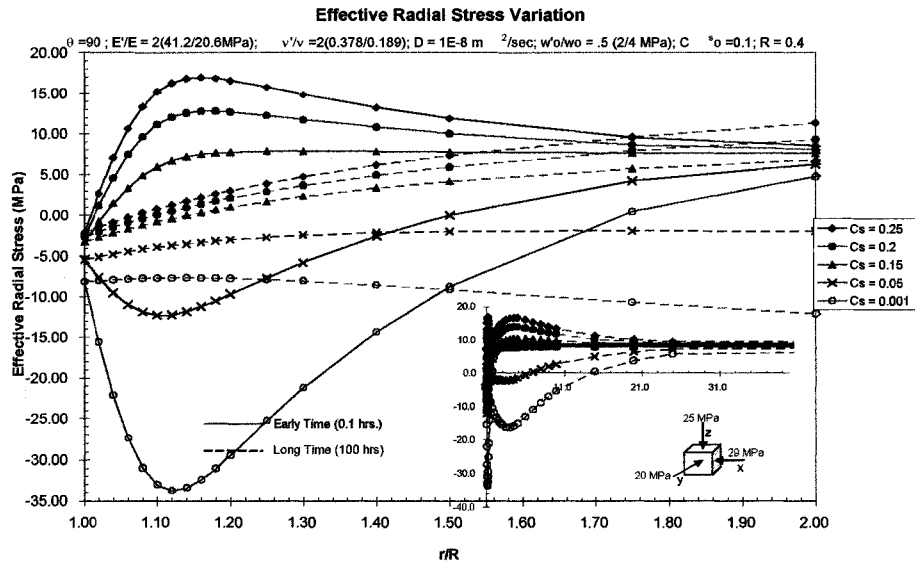


Figure 5.14: Effective radial stress distribution along the radial direction ($\theta = 90^\circ$) for different mud salinities.

From Equation (5.5) one can define the effective spalling stress, as:

$$\sigma_{spall} = T + \sigma'_r \quad (5.6)$$

It should be noted that σ'_r is negative.

Thus, from Equation (5.6), the failure criterion shows that the borehole wall will burst out when the effective tensile radial stress is larger than the rock mass tensile strength. Commonly, the tensile strength of the formation is very small and it is usual to consider it to be equal to zero. In our case, the assumed tensile strength value was 0.689 MPa (Chenevert et al., 1993). Applying this criterion to the results already presented, an induced radial tensile stress (spalling failure) only occurs when chemical effects are considered (Figures H.6, J.6, and K.6), either at $\theta = 0^\circ$ or $\theta = 90^\circ$. From these figures one can observe that the zone of induced tensile radial stress expands as time increases but it is located very near the borehole wall. It is also observed that the anisotropy reduces the extend of the failure zone.

Figures (L.6), and (5.14) show a large induced tensile radial stress when the mud

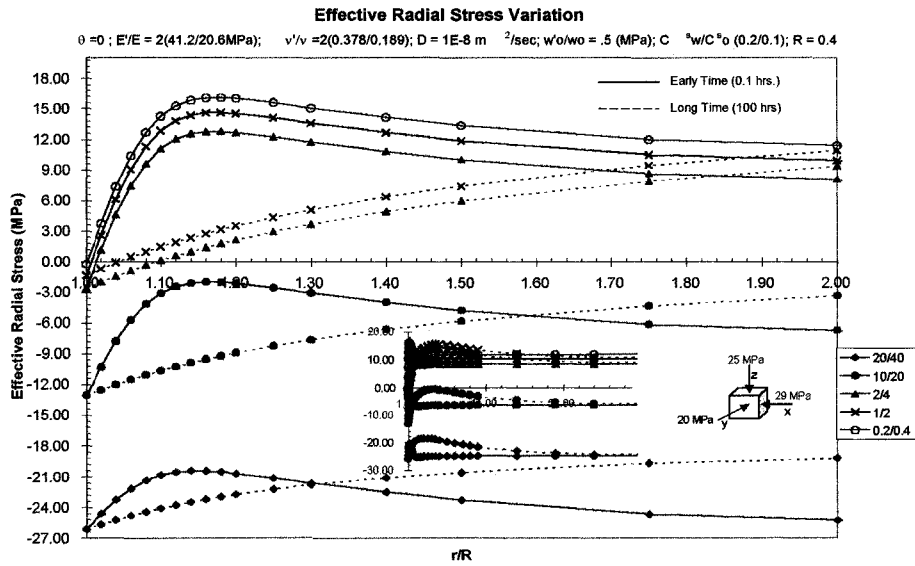


Figure 5.15: Effective radial stress distribution along the radial direction ($\theta = 90^\circ$) for different swelling coefficients.

salinity is smaller than the formation in both radial directions ($\theta = 0^\circ$ and $\theta = 90^\circ$), respectively. At early times the peak is bigger than for long times, but the induced zone of failure is smaller at early times. From Figures (M.6) and (5.15) one can observe a large induced effective tensile radial stress when the swelling coefficient is large in both radial directions ($\theta = 0^\circ$ and $\theta = 90^\circ$). For smaller values of the swelling coefficient, a smaller failed zone is produced. It is also observed that at $\theta = 90^\circ$ a slightly larger failure zone is induced.

The variation of the reflection coefficient in both radial directions ($\theta = 0^\circ$ and $\theta = 90^\circ$) induces a small failure zone, which expands as the reflection coefficient decreases (see Figures N.6 and 5.16). Also, the mud pressure variation in both radial directions ($\theta = 0^\circ$ and $\theta = 90^\circ$) induces a small failure zone, which expands as the mud pressure increases (see Figures O.6 and 5.17).

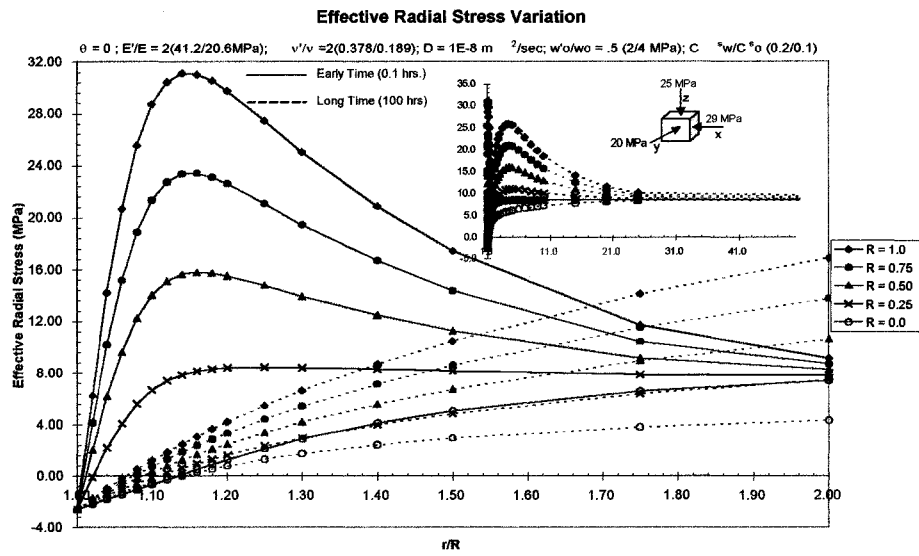


Figure 5.16: Effective radial stress distribution along the radial direction ($\theta = 90^\circ$) for different reflection coefficients.

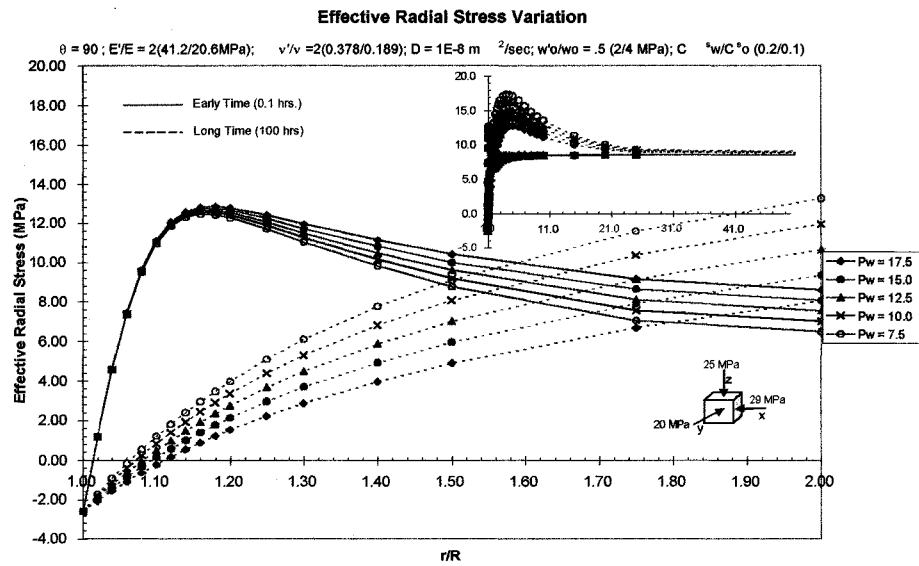


Figure 5.17: Effective radial stress distribution along the radial direction ($\theta = 90^\circ$) for different mud pressures.

5.5.3 Shear failure

The more common shear failure is the Mohr-Coulomb failure criterion, which establishes that shear failure may occur around the borehole when the shear strength of the formation is exceeded. Away from the wall of the borehole, the radial stress produces an increase in confinement; and shear failure is more probable to occur. According to Fjær, (1992) the Mohr-Coulomb failure criterion in cylindrical coordinates⁴ can be expressed as:

When $\sigma_\theta > \sigma_z > \sigma_r$

$$\sigma_\theta = C_0 + \sigma_r \tan^2 \beta \quad (5.7)$$

and

$$\sigma_r = C_0 + \sigma_\theta \tan^2 \beta \quad (5.8)$$

when $\sigma_r > \sigma_z > \sigma_\theta$

where C_0 is the uniaxial compressive strength, $\beta = \frac{\pi+2\phi}{4}$, and ϕ is the angle of internal friction.

For sake of simplicity one can use the difference between the effective radial stress and the effective tangential stress as a measure for the shear stress experienced by the formation (Heidug and Wong, 1996). Figures (5.18), (5.19), and (5.20), show that the difference between the effective radial stress and tangential stress increases monotonically with time near to the borehole wall along the radial direction at $\theta = 0^\circ$, when the swelling coefficient, reflection coefficient, and solute mass fraction in the mud are changed, respectively. From these figures one can observe that changes in these parameters lead to the same profile and the same level of magnitude. However, when the mud pressure changed, a slight difference in the profiles can be observed (see Figure 5.21).

Figure (5.22) depicts that the chemical effect does not have a significant impact

⁴Shear failure was only considered in the $(r - \theta)$ plane, but that other planes should, theoretically, also be considered.

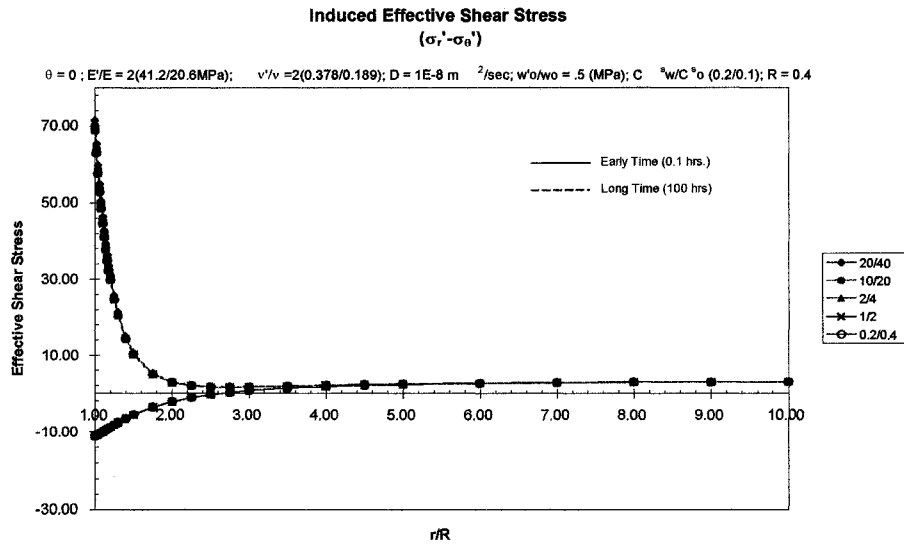


Figure 5.18: Differential stress distribution along the radial direction at $\theta = 0^\circ$ for different swelling coefficients.

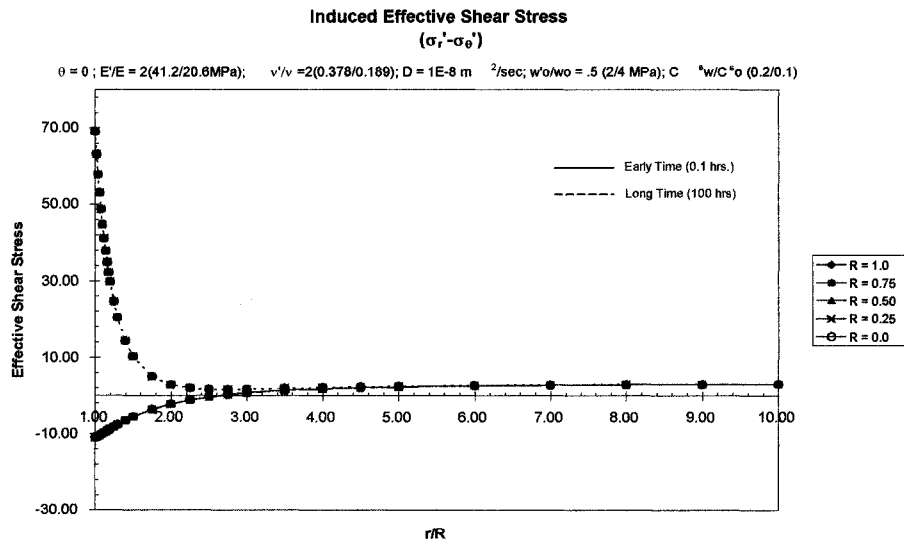


Figure 5.19: Differential stress distribution along the radial direction at $\theta = 0^\circ$ for different reflection coefficients.

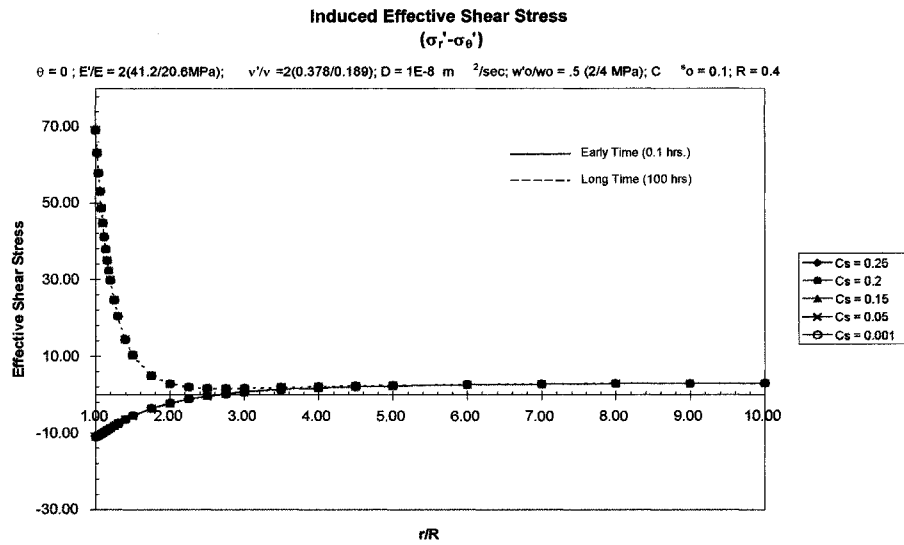


Figure 5.20: Differential stress distribution along the radial direction at $\theta = 0^0$ for different solute mass fractions in the mud.

in inducing shear stress. From this figure, it is clear that the major effect is obtained when the isotropic properties of the medium changes. Thus, the isotropic case has the major impact of inducing shear stresses along the radial direction at $\theta = 0^0$. Changes in the stress field also have an impact on the differential stress distribution.

The relevance of this observation lies in the fact that, according to the Mohr-Coulomb criterion, a high value of $(\sigma'_{rr} - \sigma'_{\theta\theta})$ promotes shear failure.

Finally, when Equations (5.7) and (5.8) were used and compared with the result presented so far, no shear failure was induced at any conditions.

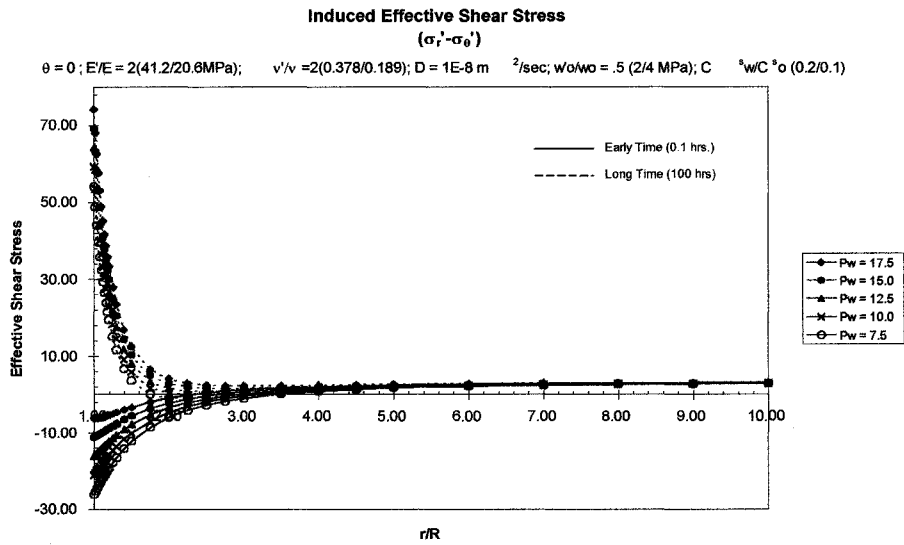


Figure 5.21: Differential stress distribution along the radial direction at $\theta = 0^\circ$ for different mud pressures.

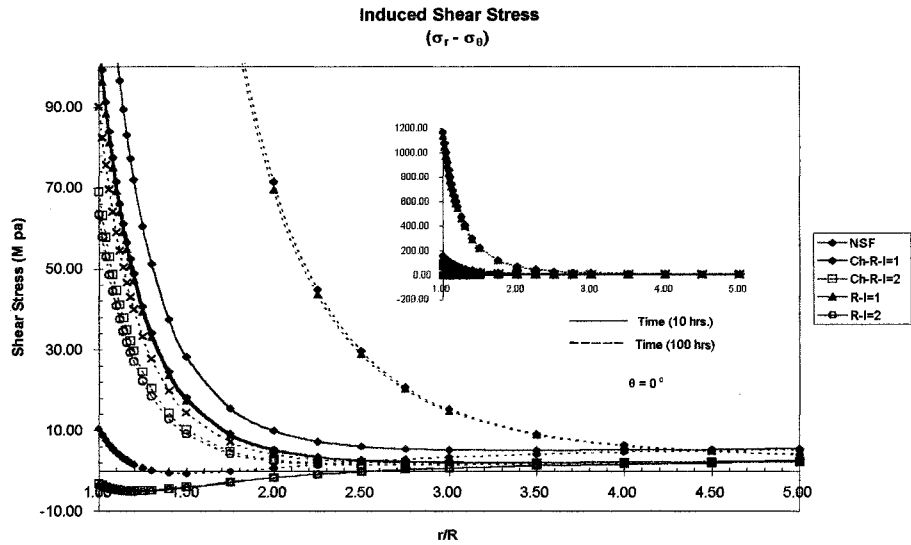


Figure 5.22: Differential stress distribution along the radial direction $\theta = 0^\circ$ for different anisotropic conditions (porous media and stress field).

6 Conclusions and Recommendations

1. Biot's theory was extended to fluid saturated poroelastic media that are chemical active and transversely isotropic.
2. The developed model is based on non-equilibrium thermodynamics, satisfying: i) the first and second laws of thermodynamics; and ii) Gibbs-Duhem's relation. It also employs Onsager's transport phenomenology to express hydraulic conduction, chemical osmosis, and solute diffusion.
3. The rock constitutive equations are derived from a state function that describes the manner in which the free energy of the wetted clay matrix per referential volume of the porous medium changes with respect to time. These equations describe the constitutive response of the rock to mechanical and chemical loading. They express the temporal evolutions of the total stresses and the variation of the fluid content in terms of the solid strains, pore pressure, and solute and diluent chemical potentials.
4. The phenomenological relations that couple the influx and efflux of fluid and solute to their driving forces are derived from the definition of the dissipation function and its associated generalized forces.
5. Field equations were developed for the linear chemical loading in terms of five independent variables; namely, the three displacements u_i , the pore pressure p , and the solute mass fraction C^S . These equations were obtained by requiring the constitutive models to satisfy the momentum, fluid mass, and solute mass balance equations.

6. In addition to the material parameters in standard poroelasticity, the theory predicts at least one chemical swelling parameter for isotropic media and two for transversely isotropic media.
7. A number of plausible assumptions were adopted to simplify the theory, among them: i) the pore fluid is compressible and consists of an ideal and sufficiently diluted solution; ii) the rock has very low permeability; iii) the clay matrix deforms elastically, iv) the hydration reaction rates are fast in comparison to the rates at which macroscopic changes of hydraulic and chemical states are communicated through the rock, i.e. local physical and chemical equilibria are maintained; v) the chemical potential of the fluid component in the pore fluid is equal to the one associated with the bound water (this assumption preserves the local chemical equilibrium); vi) the solute chemical potential is solely a function of one variable, the solute mass fraction; vii) there are no body forces, or volume fluid sources; and, viii) the anisotropic thermodynamic response or material coefficients are characterized using micromechanical assumptions.
8. The analytical solution is used to demonstrate the impact of the physico-chemical processes on the pore pressure and the stress fields around a borehole drilled in anisotropic shale.
9. The results show that the stresses and the pore pressure are influenced by the anisotropic, solute reflection, swelling and chemical properties of the shale: i) chemical osmosis alters the pore pressure and the total and effective stresses around the borehole; however, ii) solute diffusion reduces the effect of osmosis with time and impacts hole stability by inducing tensile stresses; iii) although the osmotically-induced reduction in the pore pressure tends to stabilize the borehole, solute diffusion can cause the formation to fail in tension or compression. Hence, its contribution to borehole failure is significant and should be considered in the process of optimizing the mud properties, such as salt

concentration and mud chemistry.

10. This work can be used to optimize the well trajectory, mud density, and mud chemistry to achieve borehole stability.
11. The linearized theory is most useful for field applications, for gaining a fundamental understanding of the physical phenomena, and for validating numerical solutions. The nonlinear version of the theory assuming a nonlinear chemical loading can be solved only numerically.
12. An interesting direction for future works would be to relax the local chemical equilibrium to explicitly express the hydration reaction of the clay matrix, introducing the electrochemical potential associated with charged ions, the electric double layer in a two-scales theory, nano-fast and macro-slow linked by statistical mechanics.

References

- [1] Aadnøy, B.S. (1987); "Continuum mechanics analysis of the stability of inclined boreholes in anisotropic rock formation". Ph.D. Dissertation Institutt for Gruvedrift Norges Tekniske Høgskole Universitetet I Trondheim.
- [2] Aadnøy, B.S. and Chenevert, M.E. (1987); "Stability of Highly inclined boreholes". Paper presented at the SPE/IADC Conference held in New Orleans LA March 15-18 1987. SPE/IADC 16052 pp 25-42.
- [3] Anderson, E.M. (1951); "The dynamics of faulting and Dyke formation"; Ed. Oliver and Boyd, London 2nd Ed., pp 206.
- [4] Aydin, A. and Johnson, A.M. (1978); "Development of faults as zones of deformation bands and as slip surfaces in sandstone". Pure and Applied Geophysics, 116: pp 931-42
- [5] Ballard T. J., Beare S. P., and Lawless T. A., (1992): "Fundamentals of Shale Stabilization: Water Transport Through Shales": SPE 24974.
- [6] Barbour S. L., and Fredlund D. G. (1989): "Mechanisms of Osmotic Flow and Volume Change in Clay Soils": Can. Geotech. Journal, Vol 26.
- [7] Bear, J. (1972); "Dynamics of fluid in porous media" American Elsevier Publishing Company Inc. 1972.
- [8] Biot, M.A.,(1941); "General theory of three-dimensional consolidation"; Journal of Applied Physics, Vol.12, February, pp.155-164
- [9] Biot, M.A.,(1955); "Theory of elasticity and consolidation for a porous anisotropic solid";Journal of Applied Physics, Vol.26, No.2, pp.182-185
- [10] Bleam, W. F. (1990a); "Electrostatic potential at the basal (001) surface of talc and pyrophyllite as related to tetrahedral sheet distortions": Clays & Clay Minerals 38, 522-526.
- [11] Bol G. M., Wong S. W., Davidson C. J., and Woodland D. C. (1992): "Borehole Stability in Shale": SPE 24975 Nov.

- [12] Bradley, W.B. (1979); "Failure of inclined boreholes". J. Energy Res. Tech. Trans. ASME, Vol. 101 Dec. 1979, 232-239.
- [13] Brady, B.H.G. and Brown, E.T. (1985); "Rock Mechanics for underground mining"; ed George Allen & Unwin, London pp.161-206.
- [14] Casimir, H.B.G., (1945); "On Onsager's principle of microscopic reversibility" Rev. mod. Phys. 17 (1945) 343.
- [15] Charlez P. A. (1997); "Rock Mechanics" Vol. 2 Petroleum applications. Ed. T editions Technip, Paris, pp 110-125.
- [16] Chenevert M. E. (1970); "Shale Control with Balanced-Activity Oil Continuous Muds": JPT Oct.
- [17] Chenevert M.E., and Sharma A. K., (1991); "Permeability and Effective Pore Pressure of Shales": SPE 21918.
- [18] Cheng A.H-D., Abousleiman, Y., and Roegiers, J.-C. (1993); "Review of some poroelastic effects in rock mechanics" Int. J. Rock Mech. Min. Sci. 30 pp. 1119-1126.
- [19] Cheng A.H-D., (1997); "Material coefficients of anisotropic poroelasticity" Int. J. Rock Mech. Min. Sci. 34(2) pp. 199-205.
- [20] Coulomb, C.A. (1773); "Sur une application des règles de Maximis et Minims a quelques problèmes de statique relatifs à l'Architecture", Acad. Roy. des Sciences Memories de math. et de physique par divers savans, 7,343-82.
- [21] Cui L., Cheng A.H-D., and Abousleiman, Y., (1997); "Poroelastic solution of an inclined borehole" J. Appl. Mech., ASME 64: pp. 32-38.
- [22] Cundall, P.A. (1971); "A computer model for simulating progressive large-scale movements in blocky rock system". In: Procc. Symp. Int. Soc.of Rock Mech. Nancy France, Vol. 1, paper No. II-8.
- [23] Dejaguin, B.V., Churaev, N.V., and Muller, V.M. (1987); "Surface Forces" Plenum Publishing Corporation, New York.
- [24] Detournay, E. and Cheng, A.H-D. (1988); "Poroelastic Response of a borehole in a non-hydrostatic stress field" Int. J. Rock Mech. Min. Sci. & Geomech. Abstr., Vol. 25, No. 3, pp. 171-182.
- [25] Detournay, E. and Cheng, A.H-D. (1993); "Comprehensive Rock Engineering: Principles, Practice & Projects Vol. II, Analysis and Design Methods" Chapter 5: Fundamental of Poroelasticity, pp. 113-171, Pergamon Press.

- [26] Díaz, A., (2000): "Shale Characterization and Properties" Master Thesis The University of Oklahoma, Norman, OK, June, 2000.
- [27] Diek A., Germanovich, L.N., and Ring, L.M. (1994) : "Environmental effects on rocks properties and fracture" Rock Mechanic Research Center report RMRC-94-09, Rock Mechanics Institute, The University of Oklahoma.
- [28] Diek A., and Santos, H., (1996) : "Surface forces in clay/electrolyte interactions and their effects on shale behavior" Rock Mechanic Research Center report RMRC-96-04, Rock Mechanics Institute, The University of Oklahoma
- [29] Diek, A., and Ghassemi, A.(2002); "Anisotropic chemo-poroelasticity with ion transfer" ASCE 15th Engineering Mechanics Conference, Columbia Univ. New York, June 2-5.
- [30] Drücker, D.C. and Prager, W.,(1952); "Soil mechanics and plastic analysis or limit design"; *Quat. of Appl. Math.*, Vol. 10, pp. 157-165.
- [31] Ekbote, S., Abousleiman, Y. and Zaman M.M., (2000); "Porothermoelastic solution for an inclined borehole in transversely isotropic porous media" in Girard, Liebman, Breeds and Does (Eds.), *Pacific Rocks 2000*, Balkema, Rotterdam.
- [32] Everett, D. H. (1988); "Basic Principles of Colloid Science": Royal Soc. Chem., V. C. Herts, 243 pp.
- [33] Fairhust, C. (1968); "Methods of determining in situ rock stress at depths". Mo. River Div. Corps. Eng. Omaha, NE, Techn. Rep., TRI-68.
- [34] Fairhust, C. and Lorig, L. (1999); "Improved design in rock and soil engineering with numerical modeling". In: *Distinct element modelling in geomechanics*. Ed. V.M., Sharma, K.R. Saxena and R.D. Woods. AA Balkema Rotterdam Brookfield pp.28-45.
- [35] Fritz S. J., and Marine I. W., (1983): "Experimental Support for a Predictive Osmotic Model of Clay Membrans": *Geochim. Cosmochim. Acta* 47, 1515-1522.
- [36] Ghassemi, A., Diek, A., Wolfe, A. C., and Roegiers, J.-C., (1999); "A chemomechanical model for borehole stability analyses" *Vail Rocks' 99*, 37th U.S. Rock Mechanics Symposium: pp 239-246.
- [37] Ghassemi, A., and Diek, A., (2002); "Poro-thermoelasticity for swelling shales" *J.pet. Sci. Eng.* 34, pp 123-135.
- [38] Griffith, A.A., (1921); "The phenomena of rupture and flow in solids"; *Phil. Trans. Roy. Soc., London*, A 221, 163-98.
- [39] Haase, R., (1990); "Thermodynamics of Irreversible Processes" Dover, New york.

- [40] Hale, A.H., Mody, F.K. and Salisbury, D.P., (1993); "The influence of chemical potential on wellbore stability"; SPE Drilling & Completion, September, pp. 207-216.
- [41] Heidung W. K., and Wong S. W., (1996): Hydration Swelling of Water-Absorbing Rocks: a Constitutive Model: International Journal of Numerical and Analytical Methods in Geomechanics, Vol. 20. 403-430.
- [42] Hendricks, S. B., Nelson, R. A., and Alexander, L. T. (1940) Hydration mechanism of the clay mineral montmorillonite saturated with various cations: J. Amer. Chem. Soc. 62, 1457-1464.
- [43] Hoek, E. and Brown, E.T. (1980); "Under ground scavation in rock". Inst. Min. Metal., London 527 pp.
- [44] Hunter, R. J. (1987) Foundations of Colloid Science, vol 1: Oxford University Press, Oxford, 688 pp.
- [45] Israelachvili, J.N., (1991); "Intermolecular and surface forces" 2nd ed., Academic Press, New York
- [46] Jeager, J.C. and Cook, N.G. (1969); Fundamentals of Rock Mechanics; Ed.. Methuen & Co. LTD, London.
- [47] Joshi, S.D. (1991); "Overview and application of horizontal wells"; Ed.. R.O. Fritz, M.K. Horn and S.D.Joshi. Geological Aspects of Horizontal Drilling. Am.Assoc. Pet. Geol. Cont. Educ. Course Note Ser., 33: 51-64.
- [48] Kahr, G., Krachenbuchl, F., Stoeckli, H. F., and Müller-von Moos (1990) Study of the water-bentonite system by vapor adsorption, immersion calorimetry and x-ray techniques: II. Heats of immersion, swelling pressures and thermodynamic properties: Clay Minerals 25,499-506.
- [49] Krachenbuchl, F., Stoeckli, H.F., Brummer, F., Kahr, G. and Müller-von Moos (1987) Study of the water-bentonite system by vapor adsorption, immersion calorimetry and x-ray techniques: I. Micropore volumes and internal surface areas, following Dubinin's theory: Clay Minerals 22, 1-10
- [50] Last, N.C. and McLean, M.R. (1996); "Assessing the impact of trajectory on wells drilled in overthrust region" Soc. Pet. Eng. Annual Tech.Conf.and Exhib., Dallas, TX October 22-25, pp 620-26.
- [51] Li, X. (1998); "Thermoporomechanical modelling of inclined borehole" Ph.D. Dissertation, The University of Oklahoma, Norman OK.
- [52] Low, F. P. and Anderson, D.M. (1958); "Osmotic pressure equation for determining thermodynamics properties of soil water": Soil Science, Vol. 86, No. 5, November, pp 251-253.

- [53] MacEwan, D. M. C., and Wilson, M. J., 1980, Interlayer and Intercalation Complexes of Clay Minerals, in *Crystal Structures of Clay Minerals and Their X-Ray Identification*, Brindley, G. W., and Brown, G. (eds.), Mineralogical Society, London, p. 495.
- [54] Maury, V. and Zurdo, C. (1996); "Drilling-induced lateral shifts along pre-existing fractures: A common cause of drilling problems" *Soc. Pet. Eng. Drilling and Completion*. SPE 27492. March 1996 pp.17-23.
- [55] Maury, V. (1994); "Rock failure mechanisms identification: A key for wellbore stability and reservoir behavior problem" Paper presented at Eurock' 94 Balkema, Rotterdam ISBN 90 5410502X, pp 175-182.
- [56] McLean, M.R. and addis, M.A., (1990b); "Wellbore stability: The effect of strength criteria on mud weight recommendations"; SPE 20405 65th Annual SPE Technical Conference and Exhibition, New Orleans, LA, September 23-26.
- [57] Moos, D., Zoback, M.D. and Bailey, L. (1999); "Feasibility study of the stability of open hole multilaterals, Cook Inlet, Alaska" *Soc. Pet. Eng. Mid-Continent Op. Symp.* SPE52186, Oklahoma, Ok, 28-31 March, 1999.
- [58] Morita, N., Black A.D. and Fuh G.F. (1990); "Theory of lost circulation pressure" *Soc. Pet. Eng. 65th annual Tech.Conf.* SPE 20409, Dallas, TX.
- [59] Mody F. K., and Hale A. H., (1993): *A Borehole Stability Model to Couple the Mechanics and Chemistry of Drilling Fluid Shale Interaction*: SPE 25728 Feb.
- [60] Mooney R. W., Kennan A. G., and Wood, L. A. (1952a) Adsorption of water vapor by montmorillonite. I. Heat of adsorption and application of BET theory: *J. Amer. Chem. Soc.* 74, 1367-1371.
- [61] Mooney R. W., Kennan A. G. and Wood, L. A. (1952b) Adsorption of water vapor by montmorillonite. II. Effect of exchangeable ions and lattice swelling as measured by X-ray diffraction: *J. Amer. Chem. Soc.* 74, 1371-1374.
- [62] Mulla, D. J., Cushman, J. H., and Low, P. H. (1984) Molecular dynamics and statistical mechanics of water near an uncharged silicate surface: *Water Resources Research* 20, 619-628.
- [63] Norrish, K. (1954) The swelling of montmorillonite: *Discuss. Faraday Soc.* 18, 120-133.
- [64] Onsager L., (1931); "Reciprocal relations in irreversible processes" I & II, *Phys. Rev.* 37 pp. 405 and 38 pp. 2265.
- [65] Pashley, R. M. and Israelachvili, J. N. (1984a) DLVO and hydration forces between mica surfaces in Mg²⁺, Ca²⁺, Si²⁺, and Ba²⁺ chloride solutions: *J. Colloid Interface Sci.* 97, 446-455.

- [66] Pashley, R. M. and Israelachvili, J. N. (1984b) Molecular layering of water in their films between mica surfaces and its relation to hydration forces: *J. Colloid Interface Sci.* 101,501-523.
- [67] Pashley, R. M. and Quirk, J. P. (1989) Ion exchange and interparticle forces between clay surfaces: *J. Soil Sci. Soc. Amer.* 53, 1660-1667.
- [68] Rice, J.R. and Cleary, M.P., (1976); "Some basic stress diffusion solutions for fluid-saturated elastic porous media with compressible constituents"; *Reviews of Geophysics and Space Physics*, Vol. 14, No. 2, pp 227-241.
- [69] Roegiers, J-C. (1990); "Stability and failure of circular openings". In: V. Maury and D. Fourmaintraux (editors), *Rock at Great Depth*. Balkema, Rotterdam, pp 1115.
- [70] Roegiers, J-C. (1998); "Chapter 6 Strength and failure criteria" In: *Advanced Rock Mechanics Lecture's notes given at The University of Oklahoma*. Spring 98, Norman, Ok.
- [71] Refson, K., Skipper, N., and McConnell, D. (1991) Molecular dynamics simulation of water mobility in smectites: *Mineral Mag.*
- [72] Skopec, R.A. (1991); "Rock Characterization in Reservoirs Targeted for horizontal drilling". *Soc. Pet. Eng. 66th annual Tech.Conf.*. Dallas TX Oct.6-9 1991. pp 503-513.
- [73] Steiger, R.P. and Leung, P.K. (1988); "Quantitative determination of the mechanical properties of shales". *SPE Annual Tech. Conf. Exhib.*, October 2-5, Houston, TX.
- [74] Steiger, R.P. and Leung, P.K. (1989); "Prediction of wellbore stability in shale formation at great depth". In: V. Maury and D. Fourmaintraux (editors), *Rock at Great Depth*. Balkema, Rotterdam, pp 1209-1218.
- [75] Santarelli F. J., and Carminati S.,(1995): *Do Shell Swell? A Critical Review of Available Evidence: SPE 29421 March.*
- [76] Santos H., Diek A., Roegiers J. C., and Fontura S., (1996): *Can Shale Swelling be (Easily) Controlled?: Presented at Eurock'96, The Netherlands.*
- [77] Sherwood, J.D., (1993); "Biot poroelasticity of chemically active shale"; *Proc. R. Soc. Lond. A.*, Vol 440, pp. 365-377.
- [78] Sherwood, J.D., and Bailey, L. (1994); "Swelling of shale around a cylindrical wellbore"; *Proc. R. Soc. Lond. A.*, Vol 444, pp. 161-184.
- [79] Skipper, N. T., Refson, K., and McConnell, J. D. C. (1991a) Computer simulation of interlayer water in 2:1 clays: *J. Chem. Phys.* 94, 7434 - 7445

- [80] Skipper, N. T., Refson, K., and McConnell, J. D. C. (1991b) Monte Carlo simulations of Mg- and Na-smectites: *Mineral Mag.*, (in press).
- [81] Sposito G. and Prost R. (1982) Structure of water adsorbed in smectites: *Chem. Rev.* 82, 553-573.
- [82] Stehfest, H., (1970); "Numerical Inversion of Laplace Transform" *Comm. ACM.*, 13, pp 47-49 and pp 624.
- [83] Suquet, H., de la Calle, C. and Pezerat, H. (1975) Swelling and structural organization of saponite: *Clays & Clay Minerals* 23, 1-9.
- [84] Suquet, H. and Pezerat, H. (1987) Parameters influencing layer stacking types in saponite and vermiculite: a review: *Clays & Clay Minerals* 35, 353-362.
- [85] Terzaghi, K. and Peck, R.B.,(1948); "Soil Mechanics in Engineering Practice" John Wiley & Sons, New York.
- [86] Thomson, M., and Willis, J.R. (1991); "A reformulation of the equations of anisotropic poroelasticity" *J. Appl. Mech.*, ASME 58, pp. 612-616.
- [87] van Olphen, H. (1965) Thermodynamics of interlayer adsorption of water in clays. I. Sodium vermiculite: *J. Colloid Sci.* 20, 822-837.
- [88] van Olphen, H. (1969) Thermodynamics of interlayer adsorption of water in clays. II. Magnesian vermiculite: in *Proc. Int. Clay Conf. Tokyo*, Israel University Press, Jerusalem, 1: 649-657.
- [89] van Oort, E., Hale, A. H., Mody, F. K., and Roy, S. (1996); "Transport in Shales and the design of improved water-based shale drilling fluids" *SPE Drilling & Completion*, September, pp. 137-146.
- [90] van Oort, (1997); "Physico-chemical stabilization of shales" SPE 37263, SPE International Symposium on Oilfield Chemistry, Houston, TX, 18-21 February, pp. 523-538.
- [91] Woodland, D. C. (1990); "Borehole instability in the Western Canadian Overthrust Belt". *Soc. Pet. Eng. Drill. Eng. March*: 27-30.
- [92] Wiebols, G.A. and Cook, N.G.W. (1968); "An energy criterion for the strength of rock in polyaxial compression". *Int. Rock Mech. Min. Sci.*, 5: 529-549.
- [93] Wilson, S.M., Last, N.C., Zoback, M.D. and Moos, D. (1999); "Drilling in South America: A wellbore stability approach for complex geologic conditions" *Soc. Pet. Eng. Latin American and Caribbean Conf. Caracas, Ven.*, 21-23 April 1999.

- [94] Zhou, S., Hillis, R. and Sandiford M. (1994); "A study of the design of inclined wellbore with regard to both mechanical stability and fracture intersection, and its application to the Australian North West Shelf" *J. of Applied Geophys.* 32: (1994), pp 293-304.
- [95] Zoback, M.L., Moos, D., Mastin, L. and Anderson, R.N. (1985). "Wellbore break-outs and insitu stress". *J Geophys. Res.*, 90: 5523-5530.

Appendix A: Free Energy of Fluid-saturated Porous Media

Under isothermal conditions, the fluid saturated porous medium is open to fluid mass exchanges with the surroundings. The localized internal energy balance equation can be obtained from the first law of thermodynamics. The material time derivative of the internal energy of an arbitrary region R of volume V is equal to the sum of the rate at which work is done by surface traction to deform the boundary ∂R and the rate at which the external energy is supplied through the boundary ∂R due to the transfer of all fluid component masses (Heidug and Wong, 1996); i.e.

$$\left(\int_R \varepsilon(\mathbf{x}, t) dV \right)^{\bullet} = \int_{\partial R} (\boldsymbol{\sigma} \mathbf{n} \cdot \mathbf{v}_s) da - \int_{\partial R} \left(\sum_{\beta} \mu^{\beta} \mathbf{I}^{\beta} \cdot \mathbf{n} \right) da \quad (\text{A.1})$$

where ε is the internal energy density in the current configuration, $\boldsymbol{\sigma} \mathbf{n}$ is the traction vector, \mathbf{v}_s is the solid velocity, and the dot accent on the left side indicates the material time derivative following the motion of the solid with local velocity \mathbf{v}_s :

$$\left(\int_R \varepsilon(\mathbf{x}, t) dV \right)^{\bullet} = \frac{\partial}{\partial t} \left(\int_R \varepsilon(\mathbf{x}, t) dV \right) + \mathbf{v}_s \cdot \nabla \left(\int_R \varepsilon(\mathbf{x}, t) dV \right) \quad (\text{A.2a})$$

The localized version of Equation (A.1) is obtained by applying Reynolds transport theorem (J. Bear, 1972; Heidug and Wong, 1996). Let $\mathfrak{E}(\mathbf{X}, t)$ be the internal energy per volume element dV_0 in the reference configuration corresponding to $\varepsilon(\mathbf{x}, t)$ the internal energy per volume element dV in the current configuration, such that:

$$\mathfrak{E}(\mathbf{X}, t) = \mathcal{J}\varepsilon(\mathbf{x}, t); \quad \text{where } \mathcal{J} = \frac{dV}{dV_0}; \quad \text{and } \dot{\mathcal{J}} = \mathcal{J}(\nabla \cdot \mathbf{v}_s) \quad (\text{A.3})$$

The time evolution of the internal energy per referential volume is then given by¹:

$$\dot{\mathfrak{E}} = \nabla \cdot (\sigma \mathbf{v}_s) - \nabla \cdot \left(\sum_{\beta} \mu^{\beta} \mathbf{I}^{\beta} \right) \quad (\text{A.4})$$

$$\dot{\mathfrak{E}} = \sigma_{ij} \frac{\partial \dot{u}_i}{\partial x_j} - \sum_{\beta} \mu^{\beta} (\nabla \cdot \mathbf{I}^{\beta}) - \sum_{\beta} \mathbf{I}^{\beta} \cdot \nabla \mu^{\beta} \quad (\text{A.5})$$

where the mechanical equilibrium condition (3.110) was used.

The localized entropy balance equation can be obtained from the second law of thermodynamics. Under isothermal conditions, the material time derivative of the entropy of all matter, contained in an arbitrary region R , is equal to the rate at which the internal entropy is produced relative to the matter present in R ; i.e.

$$\left(\int_R S dV \right)^{\bullet} = \int_S \vartheta dV \quad (\text{A.6})$$

The rate of internal entropy production per unit volume is denoted by ϑ . The localized version of (A.6) is obtained by defining $\mathfrak{S} = \mathcal{J}S$ as the entropy per

¹If \mathbf{X} defines a position in an arbitrary reference configuration, which corresponds to x at time t , then a measure of the rock's deformation state is provided by the Green strain tensor; i.e.

$$\mathbf{E} = \frac{1}{2} (\mathbf{F}^T \mathbf{F} - \mathbf{1}); \quad \mathbf{F} = \frac{\partial x}{\partial \mathbf{X}} (\mathbf{X}, t)$$

where ^T refers to the transposed matrix. The second Piola-Kirshoff stress tensor:

$$\mathbf{T} = \mathcal{J} \mathbf{F}^{-1} \sigma \mathbf{F}^{-T}$$

relates the Cauchy stress σ acting in the current configuration to the stress state in the reference configuration. For small strains, one could approximate:

$$\varepsilon_{ij} \approx E_{ij} \quad \sigma_{ij} \approx T_{ij}$$

The Green strain tensor E_{ij} and the Piola-Kirshoff stress tensor T_{ij} can be replaced by the infinitesimal strain tensor ε_{ij} and the Cauchy stress tensor σ_{ij} ; respectively.

volume element in the reference configuration and by applying Reynolds' transport theorem. The time evolution of the entropy per referential volume is then given by:

$$\dot{\eta} = \vartheta \quad (\text{A.7})$$

where the local entropy production rate ϑ is given by (3.8):

$$\vartheta = - \sum_{\beta} \mathbf{I}^{\beta} \cdot \nabla \mu^{\beta} \quad (\text{A.8})$$

Note that the rate of entropy production is due to the relative motions between the fluid components and the solid. Therefore, according to the second law of thermodynamics, the time evolution of the energy $T \dot{\eta}$ per referential volume satisfies the following equation:

$$T \dot{\eta} = - \sum_{\beta} (\mathbf{I}^{\beta} \cdot \nabla \mu^{\beta}) \quad (\text{A.9})$$

The time evolution of the free energy $\dot{\mathfrak{F}} = \dot{\mathfrak{E}} - T \dot{\eta}$ is then given by (A.5) and (A.9):

$$\dot{\mathfrak{F}} = \dot{\mathfrak{E}} - T \dot{\eta} = \sigma_{ij} \frac{\partial \dot{u}_i}{\partial x_j} - \sum_{\beta} \mu^{\beta} (\nabla \cdot \mathbf{I}^{\beta}) \quad (\text{A.10})$$

$$\dot{\mathfrak{F}} = \sigma_{ij} \dot{\epsilon}_{ij} + \sum_{\beta} \mu^{\beta} \dot{m}^{\beta} \quad (\text{A.11})$$

Equation (A.11) is obtained from (A.10) using the relation between the strain rate and solid velocity:

$$\dot{\epsilon}_{ij} = \frac{1}{2} \left(\frac{\partial \dot{u}_i}{\partial x_j} + \frac{\partial \dot{u}_j}{\partial x_i} \right) \quad (\text{A.12})$$

and the mass balance of the fluid component (see Appendix D):

$$\dot{m}^{\beta} + \nabla \cdot \mathbf{I}^{\beta} = 0 \quad (\text{A.13})$$

Appendix B: Isotropic Thermodynamic Response Coefficients

The isotropic thermodynamic response coefficients or material parameters α , Q , and B^β in the fundamental rock constitutive equations can be characterized in terms of more meaningful physical parameters: the rock's bulk modulus, K ; the bulk modulus of the solid matrix, K_s ; the chemical swelling parameters, ω^β ; and the porosity, ϕ . The relations between these coefficients are obtained assuming that the solid constituent of the rock deforms elastically. Consider the following isotropic constitutive equations for the time evolutions of the total stress σ_{ij} and pore volume fraction v (Heidug and Wong, 1996):

$$\dot{\sigma}_{ij} = \left(K - \frac{2G}{3} \right) \dot{\epsilon}_{kk} \delta_{ij} + 2G \dot{\epsilon}_{ij} - \alpha \dot{p} \delta_{ij} + \sum_{\beta} \omega^{\beta} \dot{\mu}^{\beta} \delta_{ij} \quad (\text{B.1})$$

$$\dot{v} = \alpha \dot{\epsilon}_{kk} + Q \dot{p} + \sum_{\beta} B^{\beta} \dot{\mu}^{\beta} \quad (\text{B.2})$$

B.1 Mechanical Loading

At constant chemical potentials $\dot{\mu}^{\beta} = 0$, the mechanical loading increment $\dot{\sigma}_{ij} = -\dot{p} \delta_{ij}$ produces a local stress change $\dot{p} \delta_{ij}$ at each point in the poroelastic medium, accompanied by a strain rate $\dot{\epsilon}_{ij} = -\left(\frac{\dot{p}}{3K_s} \right) \delta_{ij}$, and a volume change $\dot{v} = -\frac{\phi \dot{p}}{K_s}$. Substituting these values in Equations (B.1) and (B.2), and solving for α and Q , respectively; one gets:

$$\alpha = 1 - \frac{K}{K_s} \quad \text{and} \quad Q = \frac{(\alpha - \phi)}{K_s} \quad (\text{B.3})$$

B.2 Chemical Loading

At constant total stress $\dot{\sigma}_{ij} = 0$, and pore pressure $\dot{p} = 0$, one could assume that to a first approximation, a chemical loading increment $\dot{\mu}^\beta$ (change of the fluid chemical composition) produces a volumetric strain rate $\dot{\epsilon}_{kk}$ (swelling), accompanied by an equal change in the pore volume fraction \dot{v} , i.e., $\dot{\epsilon}_{kk} = \dot{v}$. Solving for the strain rate in Equation (B.1) one gets:

$$\dot{\epsilon}_{kk} = -\frac{1}{K} \sum_{\beta} \omega^{\beta} \dot{\mu}^{\beta} \quad (\text{B.4})$$

Substituting (B.4) into (B.2) with $\dot{\epsilon}_{kk} = \dot{v}$, and solving for B^β , one gets:

$$B^\beta = \frac{(\alpha - 1)}{K} \omega^\beta = -\frac{\omega^\beta}{K_s} \quad (\text{B.5})$$

Appendix C: Anisotropic Thermodynamic Response Coefficients

The thermodynamic response coefficients or material parameters α_{ij} , Q , and B^β , in the fundamental rock constitutive equations can be characterized in terms of more meaningful physical parameters: the drained elastic moduli, L_{ij} ; the bulk modulus of the solid matrix, K_s ; the chemical swelling parameters, ω^β ; and the porosity, ϕ . The relations between these coefficients are obtained using the assumptions of micro-homogeneity and micro-isotropy (Cheng, 1997). The skeleton of the porous rock is homogeneous and isotropic at the pore or granular scale. However, at the macroscopic scale, the rock is heterogeneous and anisotropic due to the structural arrangements of the grains and pores. Consider the constitutive equations for the time evolutions of total stress, σ_{ij} ; and pore volume fraction, v :

$$\dot{\sigma}_{ij} = L_{ijkl}\dot{\epsilon}_{kl} - \alpha_{ij}\dot{p} + \omega_{ij}^S\dot{\mu}^S + \omega_{ij}^D\dot{\mu}^D \quad (\text{C.1})$$

where,

$$\begin{Bmatrix} \dot{\sigma}_{11} \\ \dot{\sigma}_{22} \\ \dot{\sigma}_{33} \end{Bmatrix} = \begin{bmatrix} L_{11} & L_{12} & L_{13} \\ L_{12} & L_{11} & L_{13} \\ L_{13} & L_{13} & L_{33} \end{bmatrix} \begin{Bmatrix} \dot{\epsilon}_{11} \\ \dot{\epsilon}_{22} \\ \dot{\epsilon}_{33} \end{Bmatrix} - \begin{bmatrix} \alpha \\ \alpha \\ \alpha' \end{bmatrix} \dot{p} + \sum_{\beta=S,D} \begin{bmatrix} \omega^\beta \\ \omega^\beta \\ \omega'^\beta \end{bmatrix} \dot{\mu}^\beta \quad (\text{C.2})$$

and,

$$\dot{v} = \alpha(\dot{\epsilon}_{11} + \dot{\epsilon}_{22}) + \alpha'\dot{\epsilon}_{33} + Q\dot{p} + B^S\dot{\mu}^S + B^D\dot{\mu}^D \quad (\text{C.3})$$

C.1 Mechanical Loading

At constant chemical potentials $\dot{\mu}^\beta = 0$, the mechanical loading increment $\dot{\sigma}_{ij} = -\dot{p}\delta_{ij}$ produces a local stress change $-\dot{p}\delta_{ij}$ at each point in the poroelastic medium, accompanied by a strain rate $\dot{\epsilon}_{ij} = -\left(\frac{\dot{p}}{3K_s}\right)\delta_{ij}$, and a volume change $\dot{v} = -\frac{\phi\dot{p}}{K_s}$. Substituting these values in Equation (C.2) and solving for α and α' , one gets:

$$\alpha = 1 - \frac{(L_{11} + L_{12} + L_{13})}{3K_s}; \quad \alpha' = 1 - \frac{(2L_{13} + L_{33})}{3K_s} \quad (\text{C.4})$$

Substituting these values in (C.3), and solving for Q , one gets:

$$Q = \frac{(1 - \phi)}{K_s} - \frac{(2L_{11} + L_{33} + 2L_{12} + 4L_{13})}{9K_s^2} \quad (\text{C.5})$$

C.2 Chemical Loading

At constant total stress $\dot{\sigma}_{ij} = 0$, and pore pressure $\dot{p} = 0$, one could assume that a chemical loading increment $\dot{\mu}^\beta$ produces a volumetric strain rate $\dot{\epsilon}_{kk}$, accompanied by an equal change in the pore volume fraction \dot{v} , i.e., $\dot{\epsilon}_{kk} = \dot{v}$. Solving for the strain rate in Equation (C.2) one gets:

$$\dot{\epsilon}_{11} = \dot{\epsilon}_{22} = \sum_{\beta} \frac{(-L_{33}\omega^\beta + L_{13}\omega'^\beta)}{(L_{11}L_{33} - 2L_{13}^2 + L_{12}L_{33})} \dot{\mu}^\beta \quad (\text{C.6})$$

$$\dot{\epsilon}_{33} = \sum_{\beta} \frac{[2L_{13}\omega^\beta - (L_{11} + L_{12})\omega'^\beta]}{(L_{11}L_{33} - 2L_{13}^2 + L_{12}L_{33})} \dot{\mu}^\beta \quad (\text{C.7a})$$

Substituting Equations (C.6) and (C.7a) into (C.3) with the condition $\dot{\epsilon}_{kk} = \dot{v}$, and solving for B^β , one gets:

$$B^\beta = -\frac{1}{3} \left(\frac{2\omega^\beta + \omega'^\beta}{K_s} \right) \quad (\text{C.8})$$

after expressing α and α' in terms of L_{ij} .

Appendix D: Mass Balance

The balance equation of the fluid mass component contained in a region R which is open to fluid mass exchange with the surroundings is given by:

$$\left(\int_R \rho^\beta dV \right)^\bullet = - \int_{\partial R} (\mathbf{I}^\beta \cdot \mathbf{n}) da \quad (\text{D.1})$$

where ρ^β and \mathbf{I}^β are the mass density per unit volume in the current configuration and mass flux of the β^{th} fluid component, respectively. The localized version of (D.1) is obtained by defining $m^\beta = \mathcal{J} \rho^\beta$ as the component mass per volume in the reference configuration and by applying the Reynolds transport theorem (see J. Bear, 1972; Heidug and Wong, 1996). The time evolution of the component mass per referential volume is then given by:

$$\dot{m}^\beta + \nabla \cdot \mathbf{I}^\beta = 0 \quad (\text{D.2})$$

The total fluid mass m_f per referential volume is defined by:

$$m_f = \sum_{\beta} m^\beta = \sum_{\beta} \mathcal{J} \rho^\beta = \mathcal{J} \rho_f = \mathcal{J} \phi \check{\rho}_f = v \check{\rho}_f \quad (\text{D.3})$$

The variation of the fluid content, ζ , is related to the difference between the fluid mass densities in the current configuration m_f and the reference configuration m_{fo} by:

$$\zeta = \frac{(m_f - m_{fo})}{\check{\rho}_{fo}} = v \frac{\check{\rho}_f}{\check{\rho}_{fo}} - \phi \quad (\text{D.4})$$

The component fluid mass density m^β is given by:

$$m^\beta = C^\beta m_f = C^\beta v \check{\rho}_f = C^\beta \check{\rho}_{fo} (\zeta + \phi) \quad (\text{D.5})$$

One starts by substituting the definition of the fluid component masses in Equation (D.5) and the definition of the fluxes, \mathbf{I}^β , which measure the mass flow of the β^{th} fluid component relative to the solid matrix:

$$\mathbf{I}^\beta = \mathbf{J}^\beta + \check{\rho}^\beta \dot{\mathbf{w}} \quad (\text{D.6})$$

into the mass balance of the fluid component (D.2), one gets:

$$\check{\rho}_{fo} \dot{C}^\beta (\zeta + \phi) + \check{\rho}_{fo} C^\beta \dot{\zeta} + \nabla \cdot \mathbf{J}^\beta + \check{\rho}^\beta (\nabla \cdot \dot{\mathbf{w}}) + (\dot{\mathbf{w}} \cdot \nabla \check{\rho}^\beta) = 0 \quad (\text{D.7})$$

Next, choose as reference the configuration at any instant. For this selection $\mathfrak{J} = 1$, but $\dot{\mathfrak{J}} \neq 0$, $\check{\rho}^\beta = C^\beta \check{\rho}_{fo}$, and $\zeta = 0$, but $\dot{\zeta} \neq 0$; therefore, Equation (D.7) becomes:

$$\check{\rho}_{fo} \dot{C}^\beta \phi + \check{\rho}_{fo} C^\beta (\dot{\zeta} + \nabla \cdot \dot{\mathbf{w}}) + \nabla \cdot \mathbf{J}^\beta + \check{\rho}_{fo} (\dot{\mathbf{w}} \cdot \nabla C^\beta) = 0 \quad (\text{D.8})$$

Since $\sum_\beta C^\beta = 1$ and $\sum_\beta \mathbf{J}^\beta = 0$, and assuming over all fluid components leads to:

$$\dot{\zeta} + \nabla \cdot \dot{\mathbf{w}} = 0 \quad (\text{D.9})$$

the balance equation (D.9) dictates the mass conservation of the fluid as a whole. Inserting this equation into (D.8), one gets the mass conservation for the components of the fluid in terms of the mass fractions C^β :

$$\check{\rho}_{fo} \dot{C}^\beta \phi + \nabla \cdot \mathbf{J}^\beta + \check{\rho}_{fo} (\dot{\mathbf{w}} \cdot \nabla C^\beta) = 0 \quad (\text{D.10})$$

Appendix E: Solution for Loading Mode 2

E.1 Solute Mass Fraction

The diffusion field equation in cylindrical coordinates for solute mass fraction, neglecting the pressure solute diffusion coefficient is given by Equation (4.28):

$$\frac{\partial^2 C^S}{\partial r^2} + \frac{1}{r} \frac{\partial C^S}{\partial r} = \frac{1}{\lambda_{CS}^S} \frac{\partial C^S}{\partial t} \quad (\text{E.1})$$

where the coefficient λ_{CS}^S reduces to $\frac{D^S}{\phi}$. The equation is decoupled from the pore pressure and displacement field and can be solved with the following boundary and initial conditions:

$$r = a \quad C^S = H(t) (C_m^S - C_o^S) \quad (\text{E.2})$$

$$r = \infty \quad C^S = 0 \quad (\text{E.3})$$

Transforming equations (E.1) to (E.3) into the Laplace domain:

$$\frac{\partial^2 \tilde{C}^S}{\partial r^2} + \frac{1}{r} \frac{\partial \tilde{C}^S}{\partial r} - \lambda^2 \tilde{C}^S = 0 \quad (\text{E.4})$$

$$\tilde{C}^S = \frac{(\tilde{C}_m^S - \tilde{C}_o^S) H(t)}{s} \quad \text{at } r = a \text{ and } t > 0 \quad (\text{E.5})$$

$$\tilde{C}^S = 0 \quad \text{at } r = \infty \text{ or } t \leq 0 \quad (\text{E.6})$$

where $\lambda = \sqrt{\frac{s}{\lambda_{CS}^S}}$

Equation (E.4) is an homogeneous second order differential equation (modified Bessel equation of order zero), which has the solution:

$$\tilde{C}^S = \frac{(\tilde{C}_m^S - \tilde{C}_o^S) H(t) K_0(\lambda r)}{s K_0(\lambda a)} \quad (\text{E.7})$$

where K_0 is the modified Bessel function of the second kind of order zero.

E.2 Pore Pressure

The diffusion field equation in cylindrical coordinates, for pore pressure is given by Equation (4.27):

$$\frac{\partial^2 p}{\partial r^2} + \frac{1}{r} \frac{\partial p}{\partial r} = \frac{1}{\lambda_p^f} \frac{\partial p}{\partial t} + \frac{\lambda_p^S}{\lambda_p^f} \frac{\partial C^S}{\partial t} \quad (\text{E.8})$$

For a given solute mass fraction distribution, the pore pressure induced by both excavation and mud pressure can be obtained by solving the non-homogeneous pore pressure diffusivity equations with the following boundary and initial conditions:

$$p = (p_m - p_0) H(t) \quad \text{at} \quad r = a \quad (\text{E.9})$$

$$p = 0 \quad \text{at} \quad r = \infty \quad (\text{E.10})$$

Transforming equations (E.8) to (E.10) into the Laplace domain:

$$\frac{\partial^2 \tilde{p}}{\partial r^2} + \frac{1}{r} \frac{\partial \tilde{p}}{\partial r} - \xi_1^2 \tilde{p} = \xi_2^2 \tilde{C}^S \quad (\text{E.11})$$

where $\xi_1 = \sqrt{\frac{s}{\lambda_p^f}}$ and $\xi_2 = \sqrt{\frac{s\lambda_p^S}{\lambda_p^f}}$

$$\tilde{p} = \frac{(p_m - p_0) H(t)}{s} \quad \text{at} \quad r = a \quad \text{and} \quad t > 0 \quad (\text{E.12})$$

$$\tilde{p} = 0 \quad \text{at} \quad r = \infty \quad \text{and} \quad t \leq 0 \quad (\text{E.13})$$

The solution of Equation (E.11) has two parts; the solution of homogeneous equations and a particular solution for the non-homogeneous part, such that:

$$\tilde{p} = \tilde{p}_h + \tilde{p}_p \quad (\text{E.14})$$

The first is similar to the solution of Equation (E.4):

$$\tilde{p}_h = \frac{H(t)(p_m - p_0)}{s} \frac{K_0(\xi_1 r)}{K_0(\xi_1 a)} \quad (\text{E.15})$$

and the particular solution given by:

$$\tilde{p}_p = \frac{\lambda_p^s}{1 - \frac{\lambda_p^f}{\lambda_c^s}} \frac{(\tilde{C}_m^s - \tilde{C}_o^s) H(t) K_0(\lambda r)}{s K_0(\lambda a)} \quad (\text{E.16})$$

Substituting Equations (E.15) and (E.16) into (E.14) one gets:

$$\tilde{p} = \frac{H(t)}{s} \left[(p_m - p_0) - \frac{\lambda_p^s (\tilde{C}_m^s - \tilde{C}_o^s)}{1 - \frac{\lambda_p^f}{\lambda_c^s}} \right] \frac{K_0(\xi_1 r)}{K_0(\xi_1 a)} + \frac{\lambda_p^s (\tilde{C}_m^s - \tilde{C}_o^s) H(t) K_0(\lambda r)}{s K_0(\lambda a)} \quad (\text{E.17})$$

E.3 Stresses

Solving Equation (3.115), in radial coordinates one can obtain the radial displacement, u_r , after substituting this value into the constitutive Equation (3.72). Applying then the proper boundary conditions for mode 2, Laplace transforming the resulting equations and substituting Equations E.7 and E.17 one can get the stress field:

$$s\tilde{\sigma}_{rr}^{(2)} = \frac{(1-2\nu)\alpha'}{(1-\nu)} \left\{ \left[(p_m - p_0) - \frac{\lambda_p^s (\tilde{C}_m^s - \tilde{C}_o^s)}{1 - \frac{\lambda_p^f}{\lambda_c^s}} \right] \left[\frac{K_1(\xi_1 r)}{r\xi_1 K_0(\xi_1 a)} - \frac{aK_1(\xi_1 a)}{r^2\xi_1 K_0(\xi_1 a)} \right] + \frac{\lambda_p^s (\tilde{C}_m^s - \tilde{C}_o^s)}{1 - \frac{\lambda_p^f}{\lambda_c^s}} \left[\frac{K_1(\lambda r)}{r\lambda K_0(\lambda a)} - \frac{aK_1(\lambda a)}{r^2\lambda K_0(\lambda a)} \right] \right\}$$

$$\begin{aligned}
& + \frac{2G\beta(1+\nu)}{3(1-\nu)} (\tilde{C}_m^S - \tilde{C}_o^S) \left[\frac{K_1(\lambda r)}{r\lambda K_0(\lambda a)} - \frac{aK_1(\lambda a)}{r^2\lambda K_0(\lambda a)} \right] \\
s\tilde{\sigma}_{\theta\theta}^{(2)} = & - \frac{(1-2\nu)\alpha'}{(1-\nu)} \left\{ \left[(p_m - p_0) - \frac{\lambda_p^S(\tilde{C}_m^S - \tilde{C}_o^S)}{1 - \frac{\lambda_p^f}{\lambda_C^S}} \right] \left[\frac{K_1(\xi_1 r)}{r\xi_1 K_0(\xi_1 a)} - \frac{aK_1(\xi_1 a)}{r^2\xi_1 K_0(\xi_1 a)} + \frac{K_0(\xi_1 r)}{K_0(\xi_1 a)} \right] \right. \\
& \left. + \frac{\lambda_p^S(\tilde{C}_m^S - \tilde{C}_o^S)}{1 - \frac{\lambda_p^f}{\lambda_C^S}} \left[\frac{K_1(\lambda r)}{r\lambda K_0(\lambda a)} - \frac{aK_1(\lambda a)}{r^2\lambda K_0(\lambda a)} + \frac{K_0(\lambda r)}{K_0(\lambda a)} \right] \right\} \\
& - \frac{2G\beta(1+\nu)}{3(1-\nu)} (\tilde{C}_m^S - \tilde{C}_o^S) \left[\frac{K_1(\lambda r)}{r\lambda K_0(\lambda a)} - \frac{aK_1(\lambda a)}{r^2\lambda K_0(\lambda a)} + \frac{K_0(\lambda r)}{K_0(\lambda a)} \right]
\end{aligned}$$

Appendix F: Nomenclature

C^S	Solute mass fraction	
C^D	Diluent mass fraction	
$\overline{C^S}$	Mean value of the solute mass fraction	
$\overline{C^D}$	Mean value of the diluent mass fraction	
D	Rayleigh's dissipation function	$(J/m^3 \cdot s)$
D^S	Solute Diffusion coefficient	(m^2/s)
E	Drained Young's modulus	(Pa)
\mathfrak{E}	Internal energy density of the fluid saturated porous medium (per referential volume)	(J/m^3)
\mathfrak{F}	Free energy density of the fluid saturated porous medium (per referential volume)	(J/m^3)
\mathfrak{F}_{wm}	Free energy of the wett. clay matrix cont. bound water per unit vol. of the porous medium	(J/m^3)
\mathfrak{F}_{pore}	Pore fluid free energy per unit volume of the porous medium	(J/m^3)
f_{pore}^β	specific free energy of β th fluid component in the pore fluid	(J/kg)
G	Shear modulus	(Pa)
\mathbf{I}^β	Mass flux of the β th fluid component relative to the solid velocity	$(kg/m^2 \cdot s)$
\mathbf{J}^β	Mass flux of the β th fluid component relative to the mixture's barycentric velocity	$(kg/m^2 \cdot s)$
\mathbf{J}^f	Fluid mass flux vector	$(kg/m^2 \cdot s)$
\mathbf{J}^S	Solute mass flux vector	$(kg/m^2 \cdot s)$
k	Permeability	$(Darcy)$
K	Total bulk modulus of the porous medium	(Pa)

K_f	Fluid bulk modulus	(Pa)
K_s	Solid bulk modulus	(Pa)
L_{ij}	Drained elastic moduli	(Pa)
\mathcal{L}^{ab}	General phenomenological transport coefficients	(kg · s/m ³)
L_p	Pressure solute diffusion coefficient	(m ³ · s/kg)
m^β	Fluid mass per referential volume of the β th fluid component	(kg/m ³)
m_{pore}^β	Mass per referential volume of the β th fluid component in the pore fluid	(kg/m ³)
m_{bound}^β	Mass per referential volume of the β th fluid component in the bound water	(kg/m ³)
m_f	Total fluid mass per referential volume of the porous medium	(kg/m ³)
M	Biot Modulus	(Pa)
M^S	Molar mass of solute	(kg/mole)
N	Total number of fluid components	
p	Pore pressure	(Pa)
P_0	Hydrostatic stress	(Pa)
R	Universal gas constant	(J/°K · m ³ · mole)
\mathfrak{R}	Reflection coefficient	
$S_{x'}, S_{y'}, S_z$	In-situ principal stresses	(Pa)
T	Absolute Temperature	(°K)
\mathbf{u}	Solid displacement vector	(m)
v	Pore volume fraction	
\mathbf{v}^β	Velocity of the β th fluid component	(m/s)
\mathbf{v}_f	Fluid mixture's barycentric velocity	(m/s)
\mathbf{v}_s	Velocity of the solid	(m/s)
$\dot{\mathbf{w}}$	Darcy's filter velocity	(m/s)
\mathcal{W}	Dual potential of the wetted clay minerals	(J/m ³)
\mathbf{X}^f	Conjugate force of the fluid mass flux	(N/kg)

\mathbf{X}^S	Conjugate force of the solute mass flux	(N/kg)
\mathfrak{H}	Entropy per volume element in the reference configuration	$(J/^\circ K \cdot m^3)$
α_{ij}	Biot effective stress coefficients	
ε_{ij}	Components of the strain tensor	
η	Fluid viscosity	$(Pa \cdot s)$
ϕ	porosity	
ζ	Variation of the fluid content	
μ^β	Chemical potential (specific) of the β th fluid component	(J/kg)
μ^S	Solute chemical potential	(J/kg)
μ^D	Diluent chemical potential	(J/kg)
$\tilde{\mu}^b$	Electrochemical potential of the b th ionic specie	(J/kg)
ν	Drained Poisson's ratio	
ν_u	Undrained Poisson's ratio	
ω_{ij}^β	Chemical swelling parameters of the β th fluid component	
ω_{ij}^S	Components of chemical swelling parameter tensor of the solute	(kg/m^3)
ω_{ij}^D	Components of chemical swelling parameter tensor of the diluent	(kg/m^3)
ρ^β	Mass density of the β th fluid component (per unit volume of the porous medium)	(kg/m^3)
$\check{\rho}^\beta$	Mass density of the β th fluid component (per unit volume of fluid)	(kg/m^3)
$\check{\rho}^S$	Solute mass density (per unit volume of fluid)	(kg/m^3)
$\check{\rho}^D$	Diluent mass density (per unit volume of fluid)	(kg/m^3)
$\check{\rho}_f$	Fluid mass density (per unit volume of fluid)	(kg/m^3)
ρ_s	Mass density of the solid	(kg/m^3)
σ_{ij}	Components of the total stress tensor	(Pa)
S_0	Deviatoric part acting in a plane normal to the hola axis	(Pa)

Appendix G: Isotropic Porous Media Without Chemical Effect

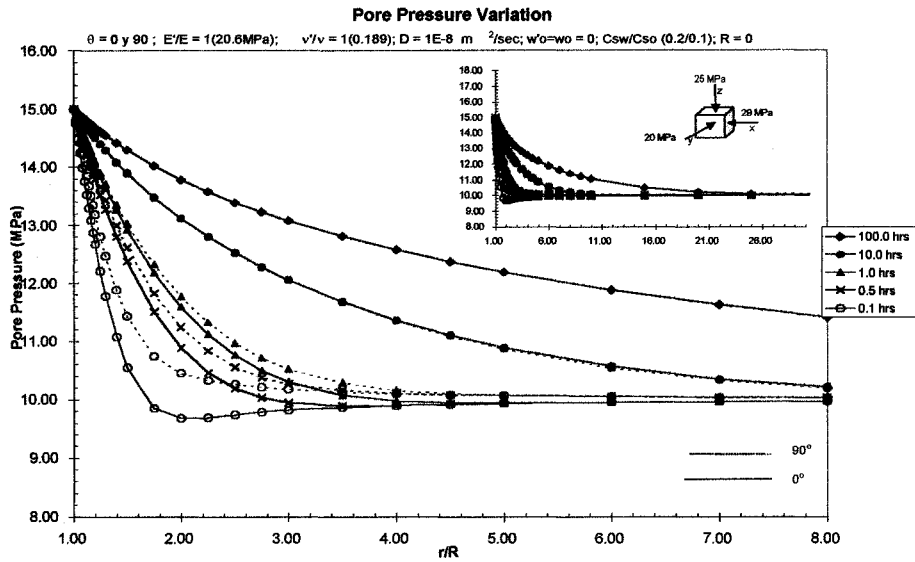


Figure G.1: Pore pressure variation with the radial distance for different times in an isotropic saturated porous media (anisotropy ratio equal to one). No chemical effect is considered.

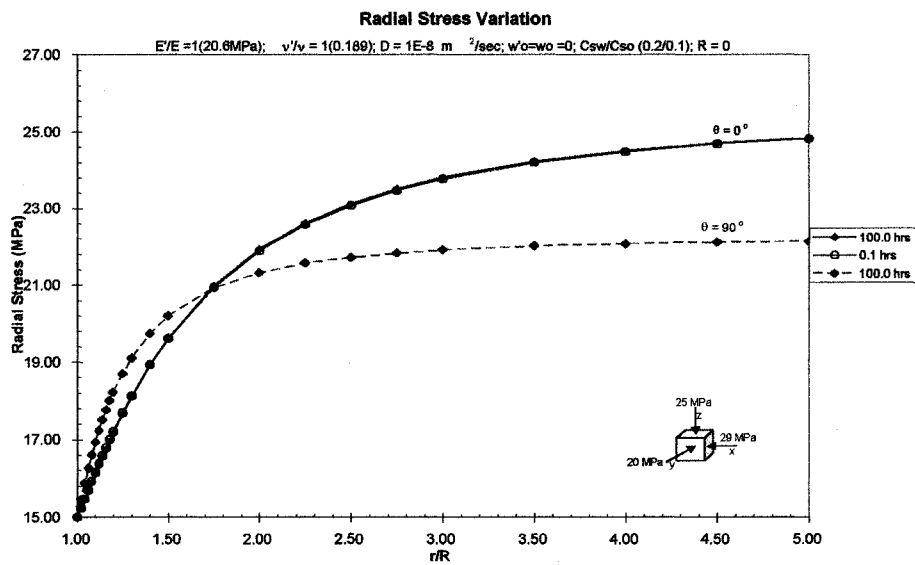


Figure G.2: Radial stress variation with the radial distance for different times in an isotropic saturated porous media (anisotropy ratio equal to one). No chemical effect is considered.

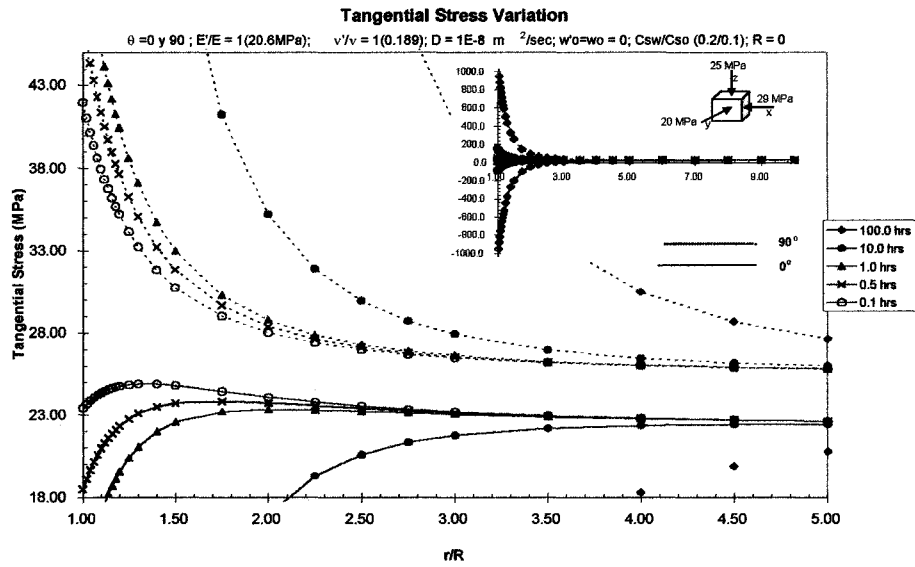


Figure G.3: Tangential stress variation with the radial distance for different times in an isotropic saturated porous media (anisotropy ratio equal to one). No chemical effect is considered.

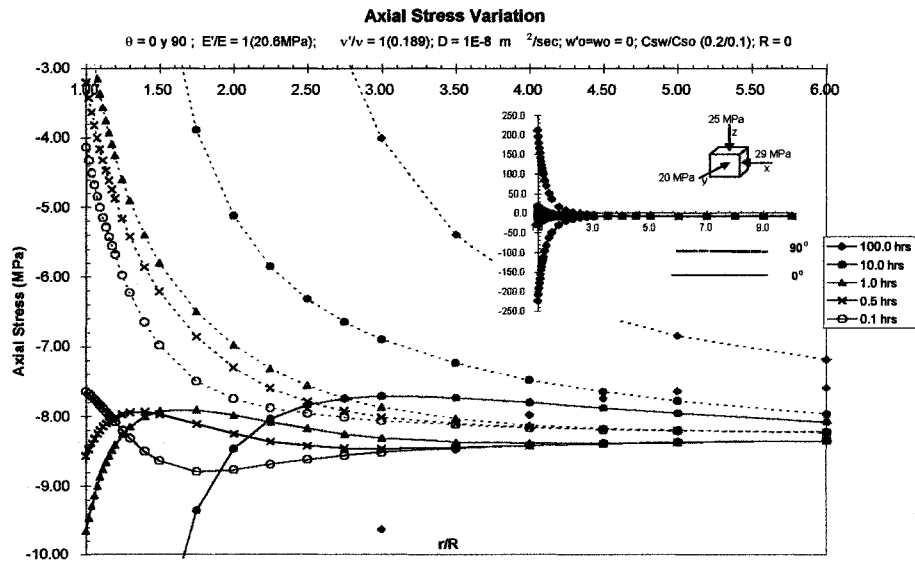


Figure G.4: Axial stress variation with the radial distance for different times in an isotropic saturated porous media (anisotropy ratio equal to one). No chemical effect is considered.

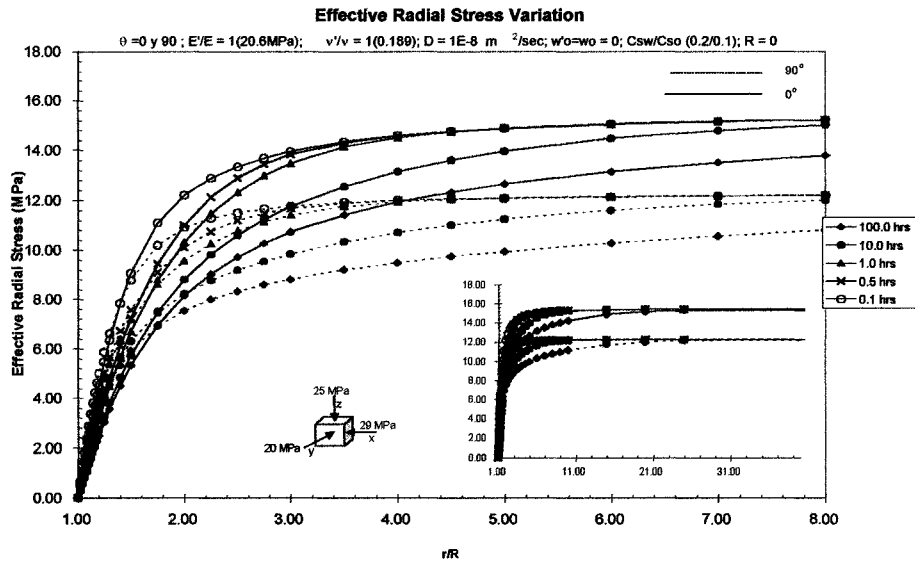


Figure G.5: Effective radial stress variation with the radial distance for different times in an isotropic saturated porous media (anisotropy ratio equal to one). No chemical effect is considered.

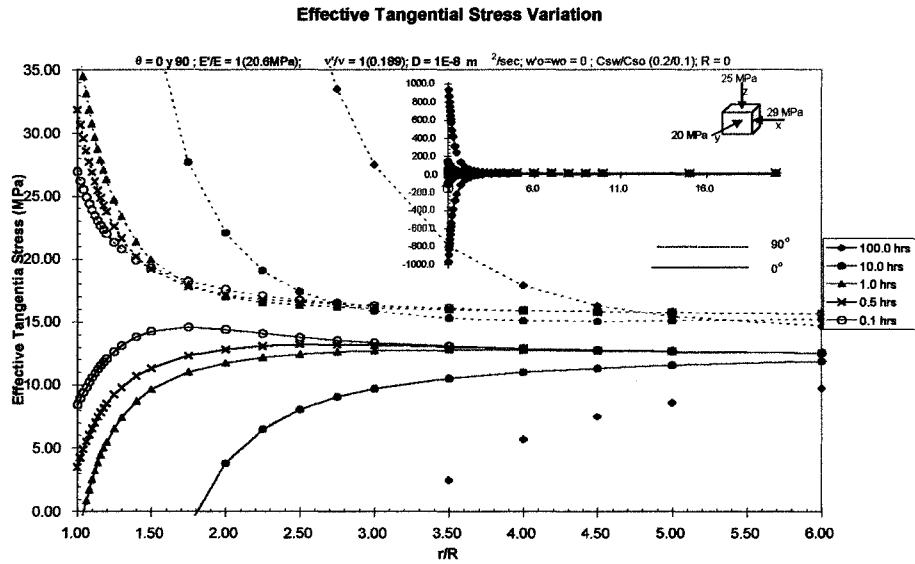


Figure G.6: Effective tangential stress variation with the radial distance for different times in an isotropic saturated porous media (anisotropy ratio equal to one). No chemical effect is considered.

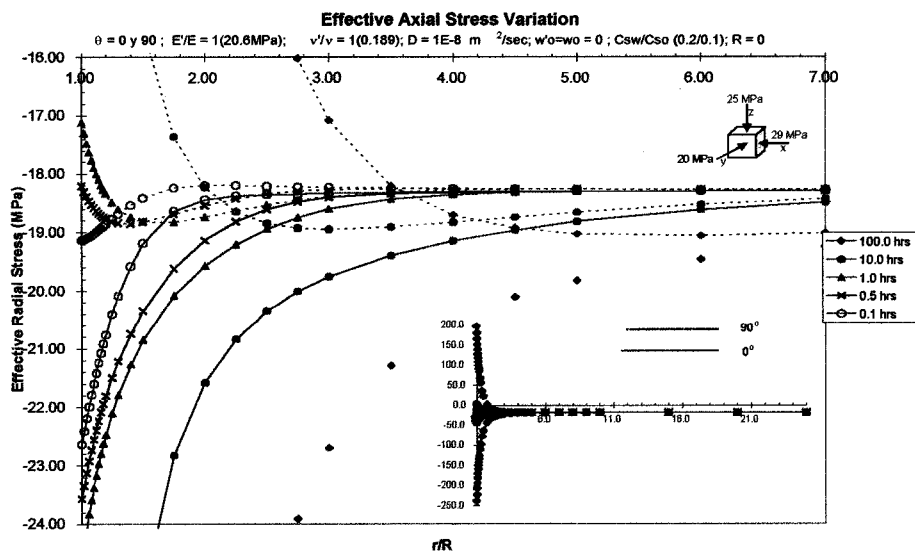


Figure G.7: Effective axial stress variation with the radial distance for different times in an isotropic saturated porous media (anisotropy ratio equal to one). No chemical effect is considered.

Appendix H: Isotropic Porous Media With Chemical Effect

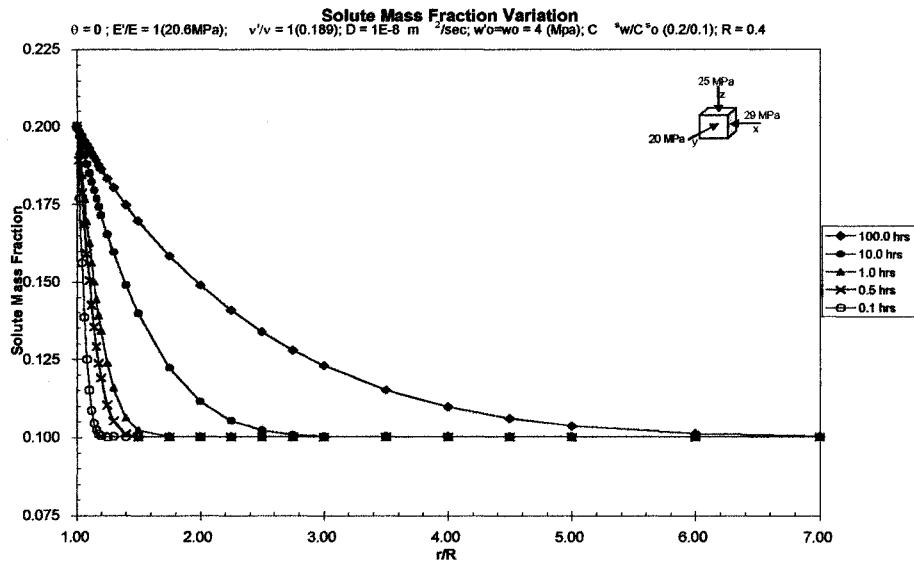


Figure H.1: Solute mass fraction variation with the radial distance for different times in an isotropic saturated porous media (anisotropy ratio equal to one) and considering chemical effect.

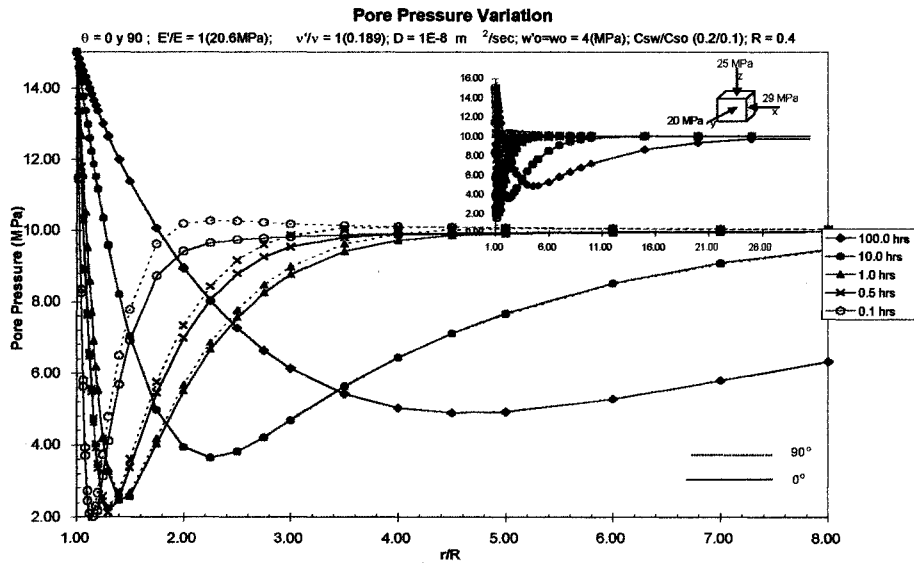


Figure H.2: Pore Pressure variation with the radial distance for different times in an isotropic saturated porous media (anisotropy ratio equal to one) and considering chemical effect.

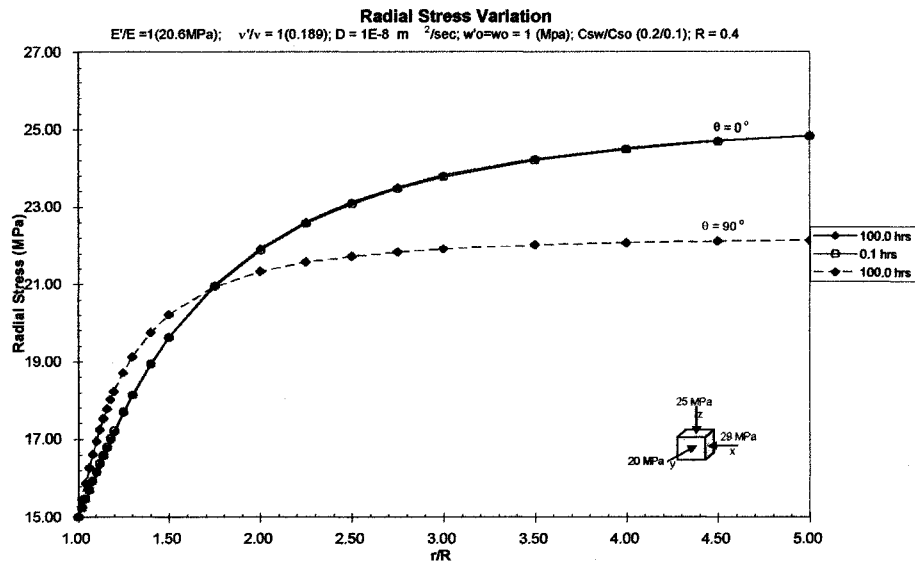


Figure H.3: Radial stress variation with the radial distance for different times in an isotropic saturated porous media (anisotropy ratio equal to one) and considering chemical effect.

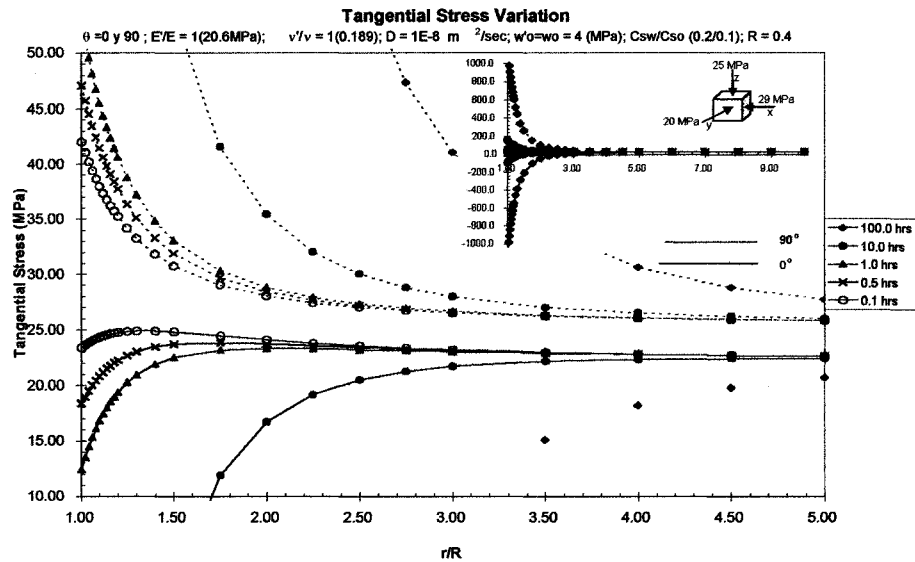


Figure H.4: Tangential stress variation with the radial distance for different times in an isotropic saturated porous media (anisotropy ratio equal to one) and considering chemical effect.

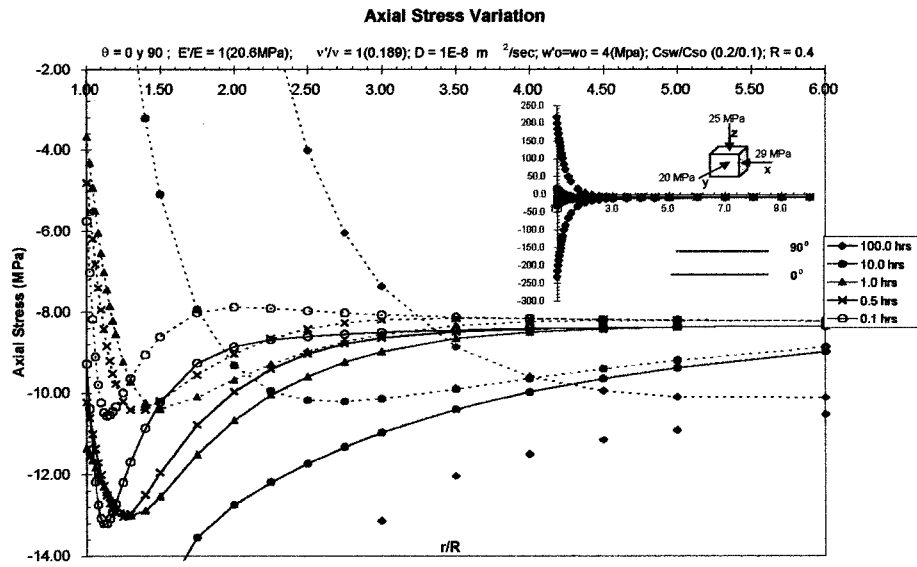


Figure H.5: Axial stress variation with the radial distance for different times in an isotropic saturated porous media (anisotropy ratio equal to one) and considering chemical effect.

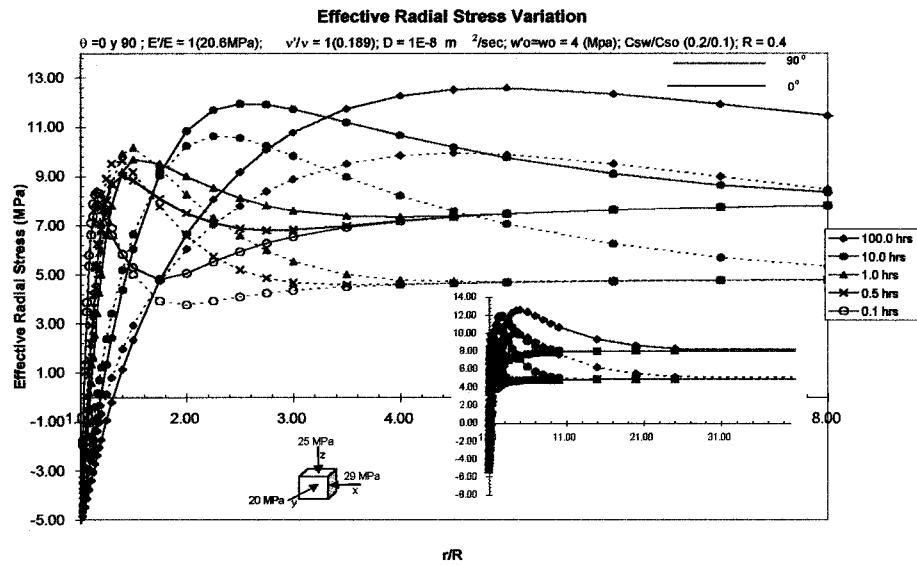


Figure H.6: Effective radial stress variation with the radial distance for different times in an isotropic saturated porous media (anisotropy ratio equal to one) and considering chemical effect.

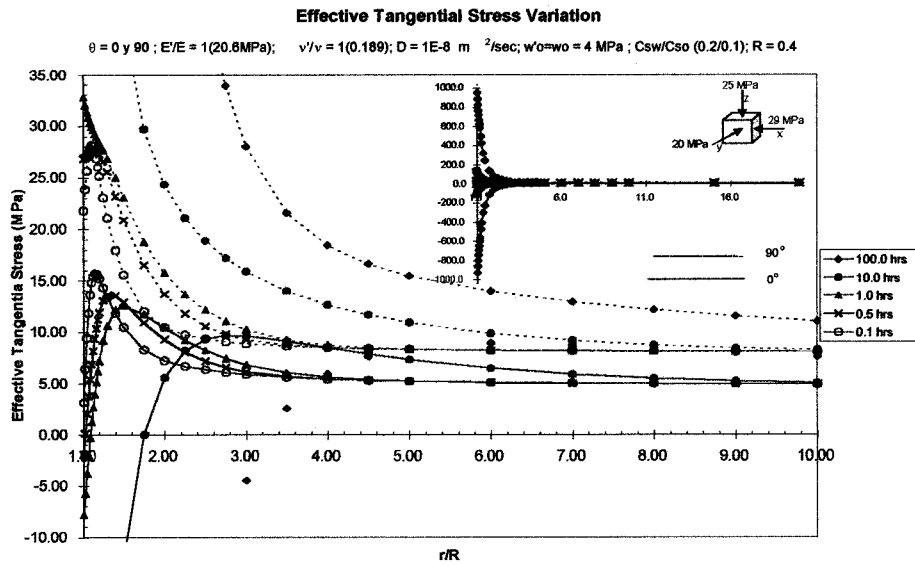


Figure H.7: Effective tangential stress variation with the radial distance for different times in an isotropic saturated porous media (anisotropy ratio equal to one) and considering chemical effect.

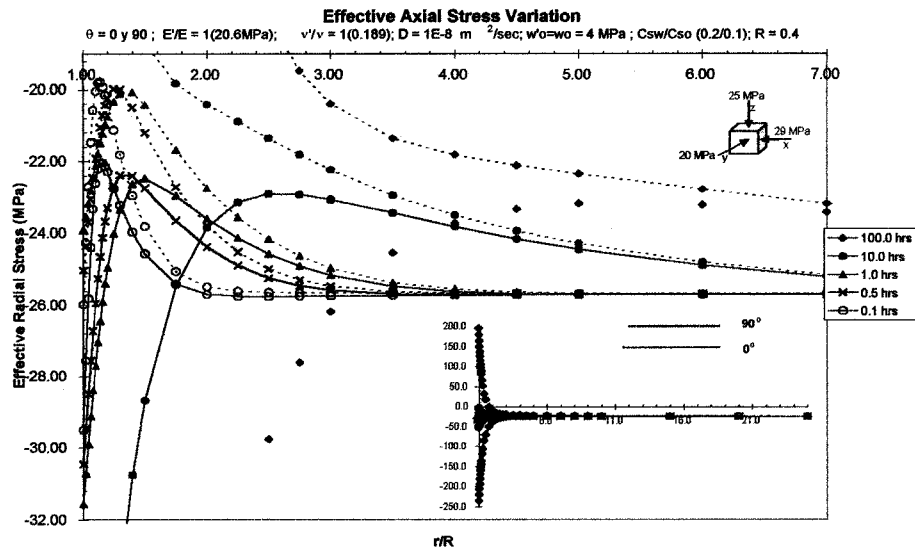


Figure H.8: Effective axial stress variation with the radial distance for different times in an isotropic saturated porous media (anisotropy ratio equal to one) and considering chemical effect.

**Appendix I: Transversely Isotropic
Porous Media Without Cemical Effect
(Anisotropic Factor Equal to two).**

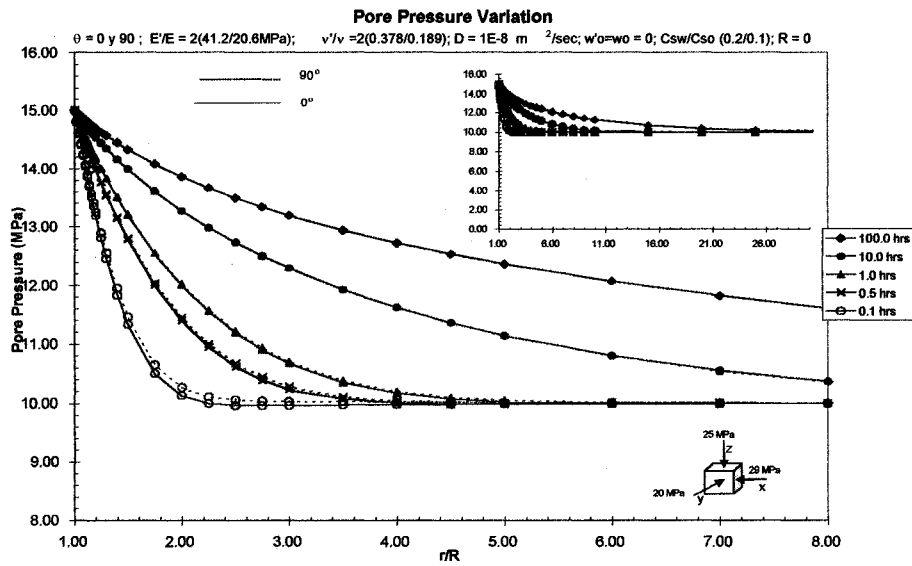


Figure I.1: Pore pressure variation with the radial distance for different times in a transversely isotropic saturated porous media (anisotropy ratio equal to two). No chemical effect is considered.

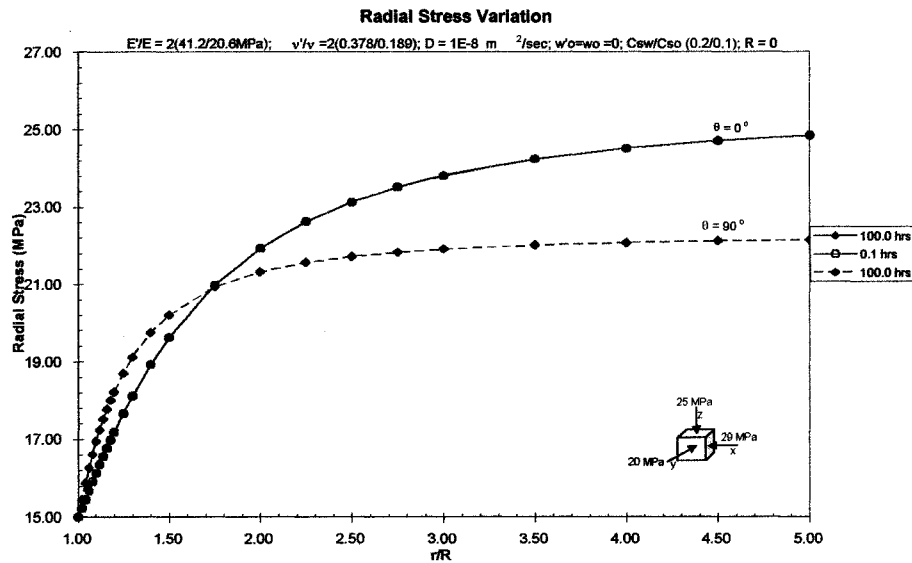


Figure I.2: Radial stress variation with the radial distance for different times in a transversely isotropic saturated porous media (anisotropy ratio equal to two). No chemical effect is considered.

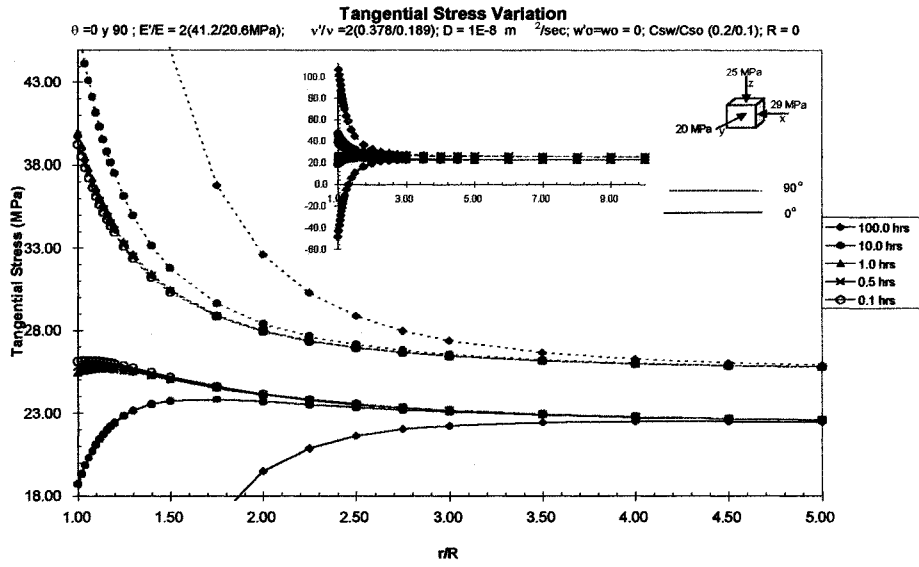


Figure I.3: Tangential stress variation with the radial distance for different times in a transversely isotropic saturated porous media (anisotropy ratio equal to two). No chemical effect is considered.

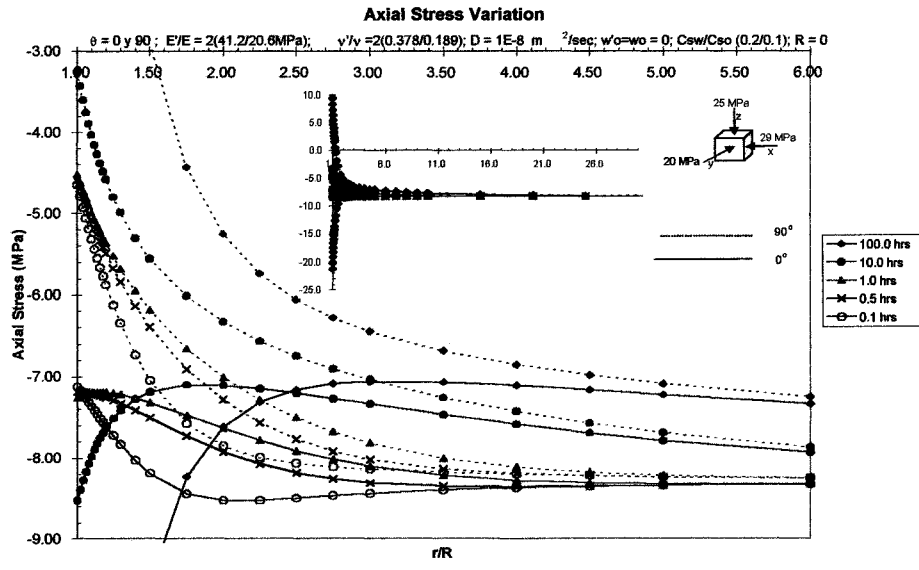


Figure I.4: Axial stress variation with the radial distance for different times in a transversely isotropic saturated porous media (anisotropy ratio equal to two). No chemical effect is considered.

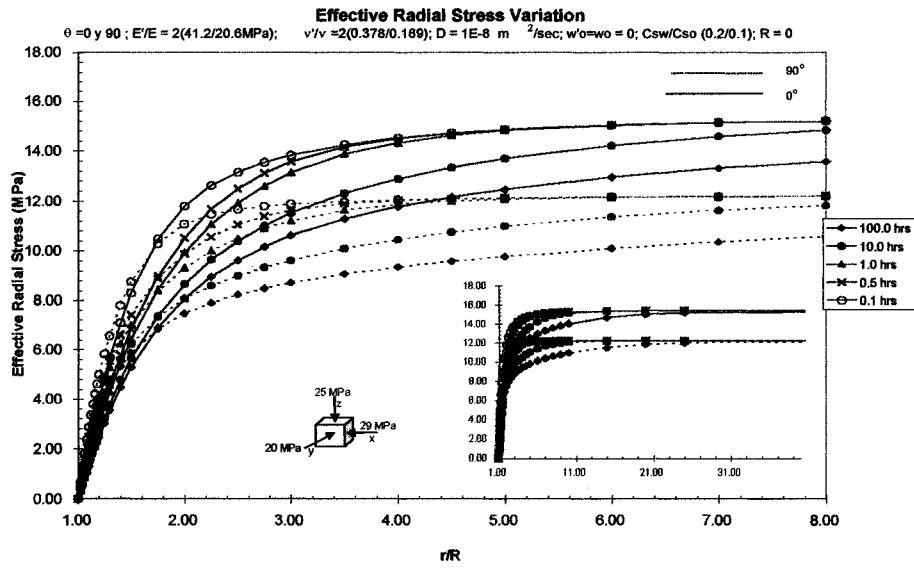


Figure I.5: Effective radial stress variation with the radial distance for different times in a transversely isotropic saturated porous media (anisotropy ratio equal to two). No chemical effect is considered.

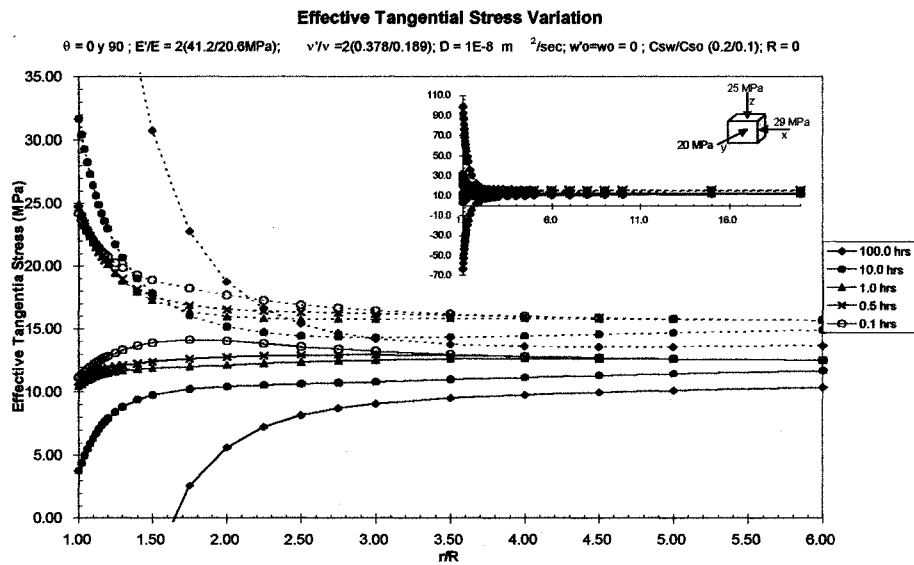


Figure I.6: Effective tangential stress variation with the radial distance for different times in a transversely isotropic saturated porous media (anisotropy ratio equal to two). No chemical effect is considered.

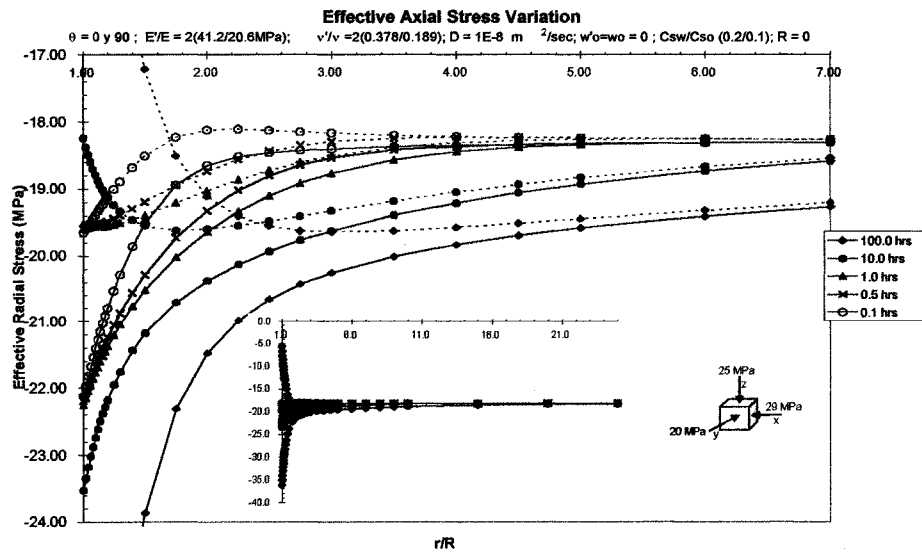


Figure I.7: Effective axial stress variation with the radial distance for different times in a transversely isotropic saturated porous media (anisotropy ratio equal to two). No chemical effect is considered.

**Appendix J: Transversely Isotropic
Porous Media With Cemical Effect
(Anisotropic Factor Equal to 1/2).**

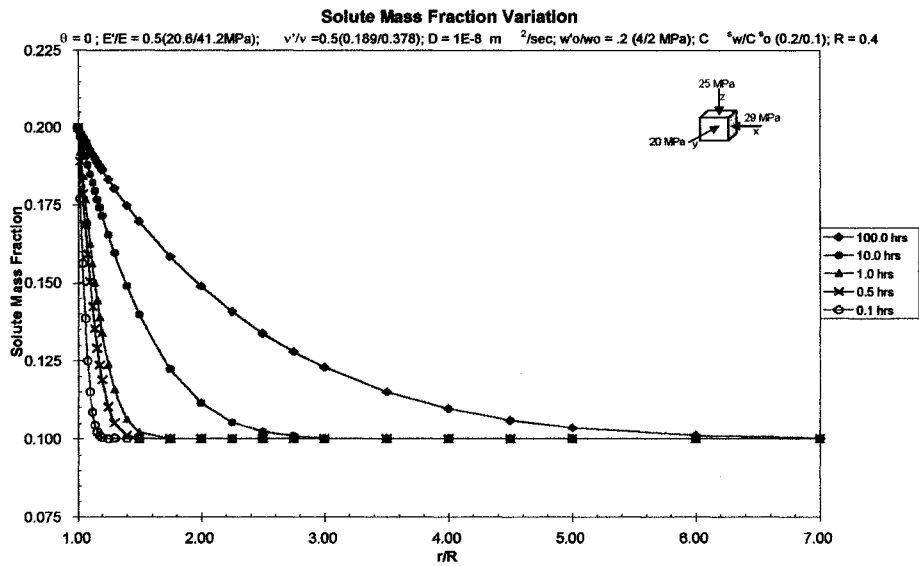


Figure J.1: Solute mass fraction variation with radial distance for different times in a transversely isotropic saturated porous media (anisotropy ratio equal to 0.5). Chemical effect is considered.

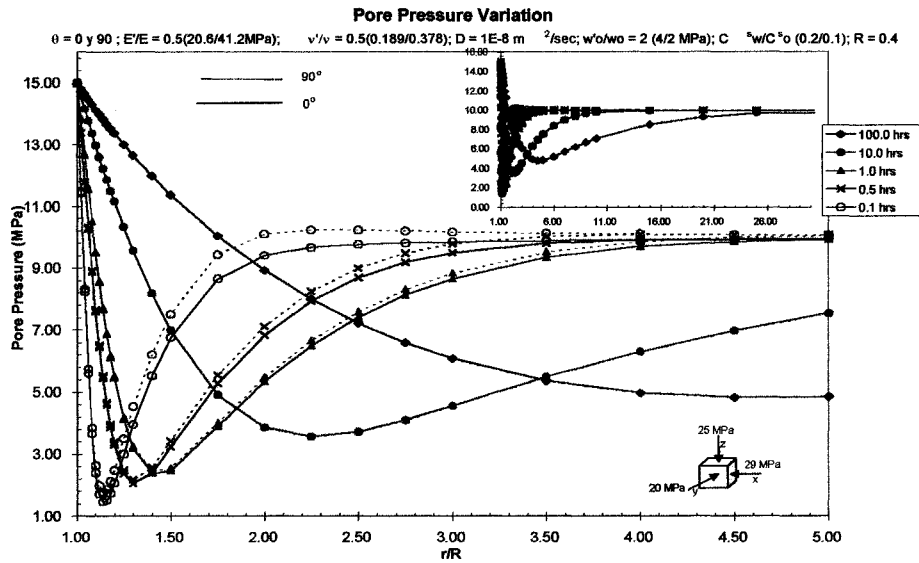


Figure J.2: Pore Pressure variation with radial distance for different times in a transversely isotropic saturated porous media (anisotropy ratio equal to 0.5). Chemical effect is considered.

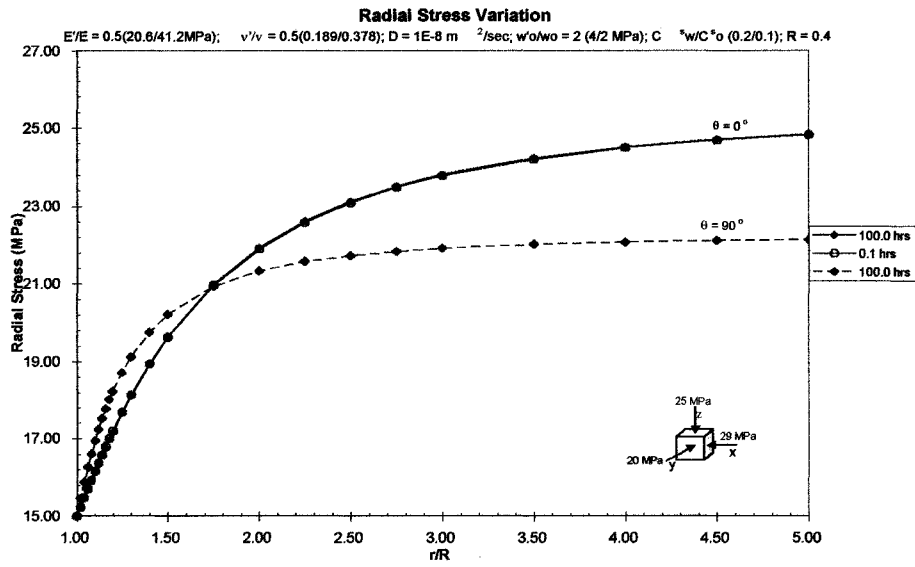


Figure J.3: Radial stress variation with radial distance for different times in a transversely isotropic saturated porous media (anisotropy ratio equal to 0.5). Chemical effect is considered.

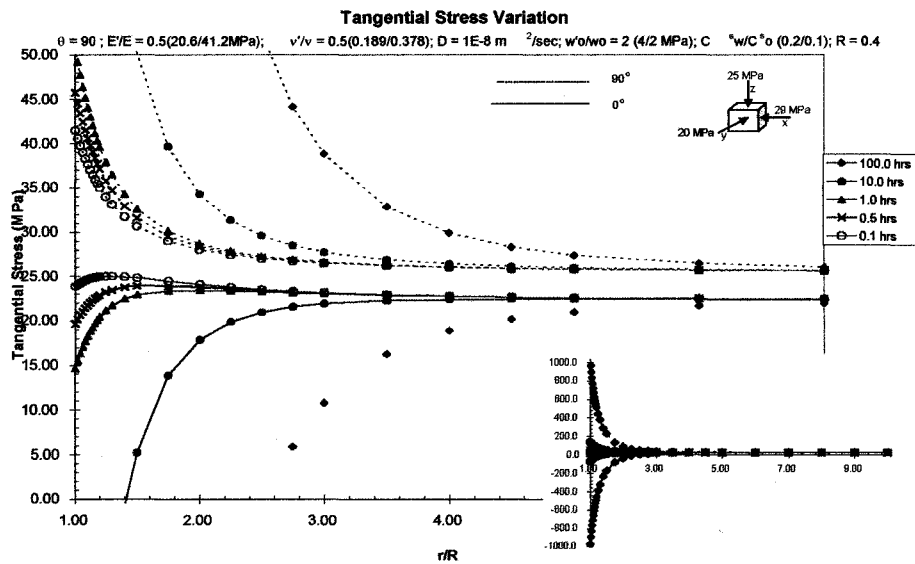


Figure J.4: Tangential stress variation with radial distance for different times in a transversely isotropic saturated porous media (anisotropy ratio equal to 0.5). Chemical effect is considered.

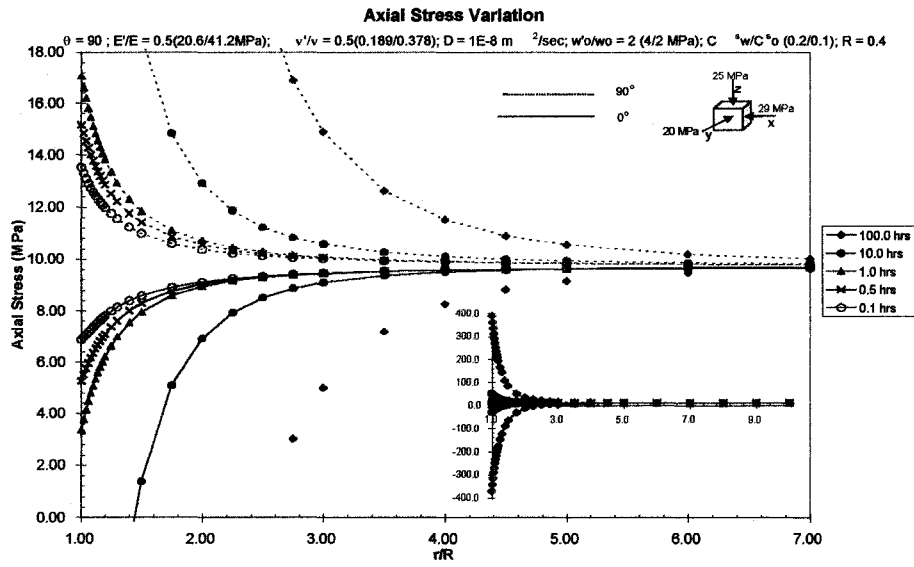


Figure J.5: Axial stress variation with radial distance for different times in a transversely isotropic saturated porous media (anisotropy ratio equal to 0.5). Chemical effect is considered.

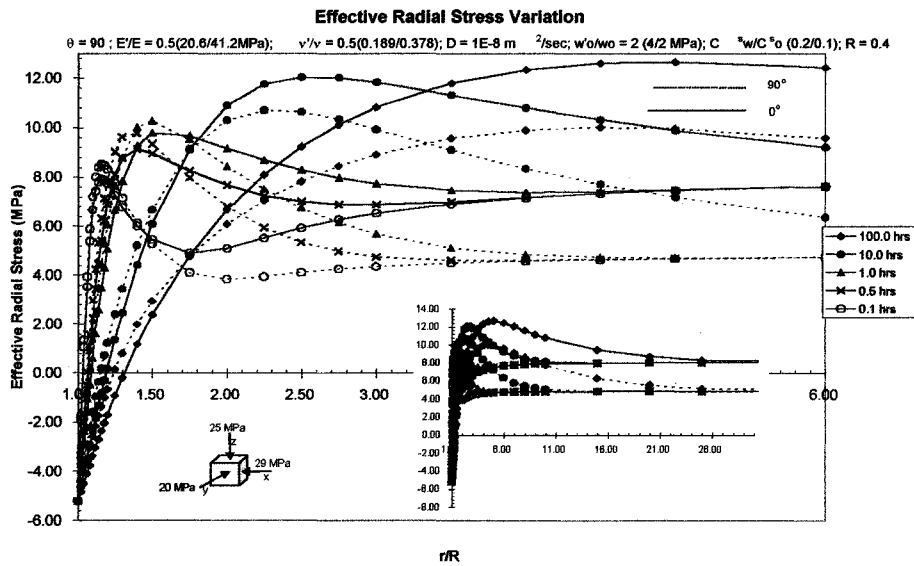


Figure J.6: Effective radial stress variation with radial distance for different times in a transversely isotropic saturated porous media (anisotropy ratio equal to 0.5). Chemical effect is considered.

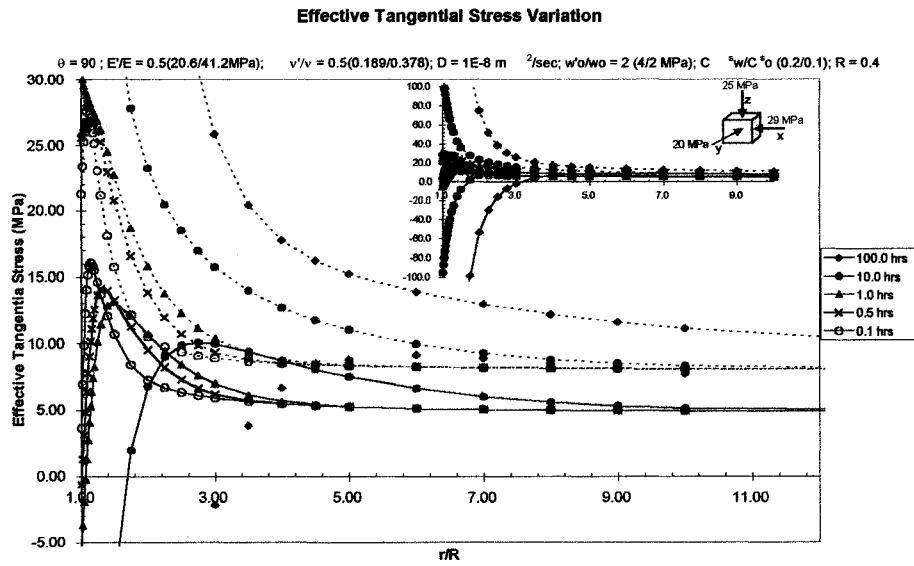


Figure J.7: Effective tangential stress variation with radial distance for different times in a transversely isotropic saturated porous media (anisotropy ratio equal to 0.5). Chemical effect is considered.

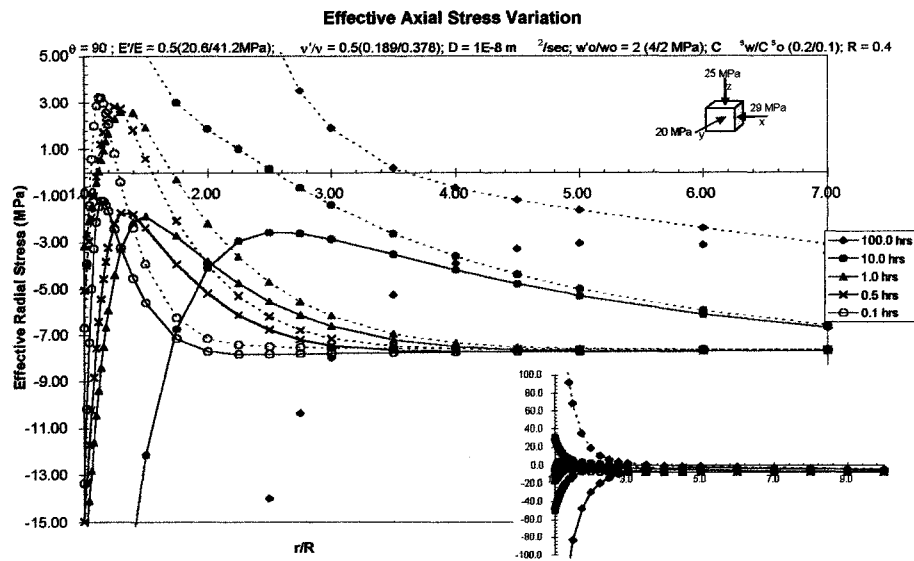
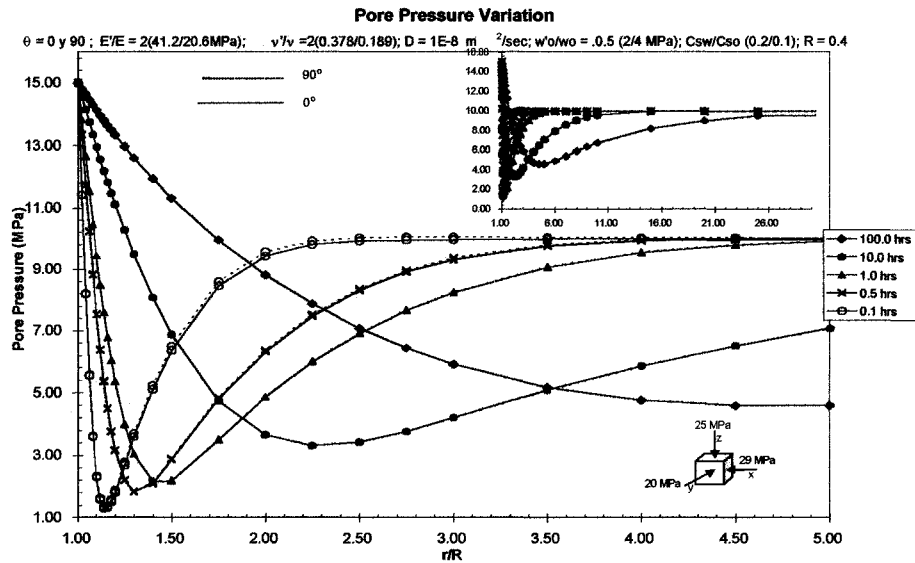
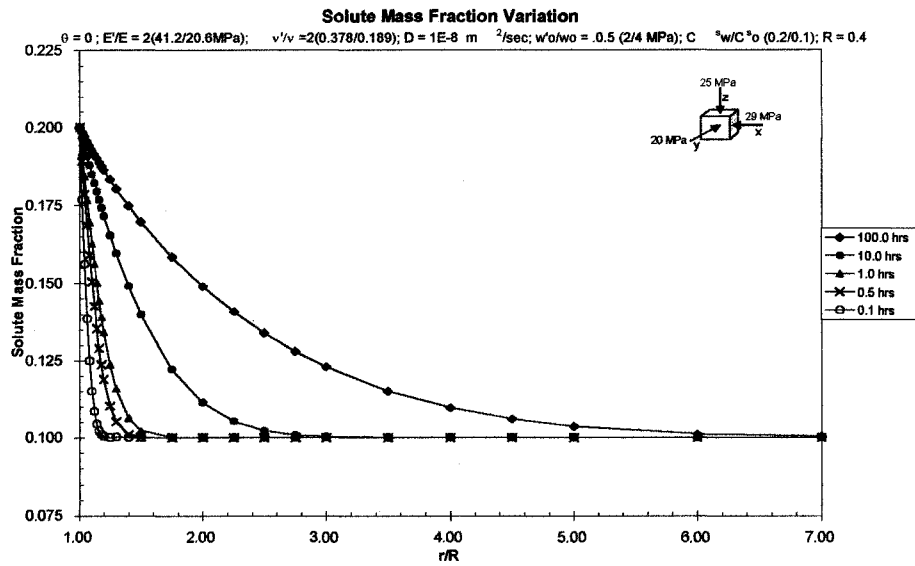


Figure J.8: Effective axial stress variation with radial distance for different times in a transversely isotropic saturated porous media (anisotropy ratio equal to 0.5). Chemical effect is considered.

**Appendix K: Transversely Isotropic
Porous Media With Cemical Effect
(Anisotropic Factor Equal to two).**



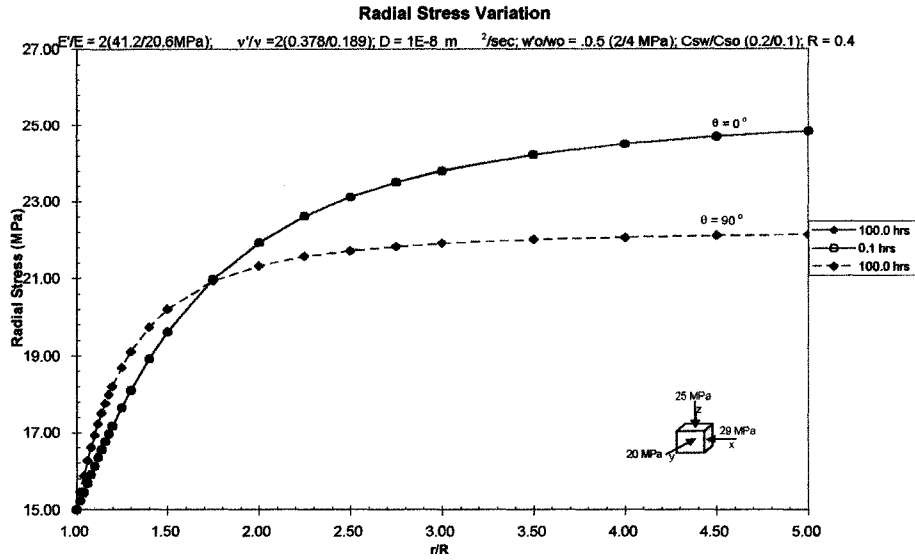


Figure K.3: Radial stress behavior with radial distance for different times in a transversely isotropic saturated porous media (anisotropy ratio equal to two) and taking into account the chemical effect.

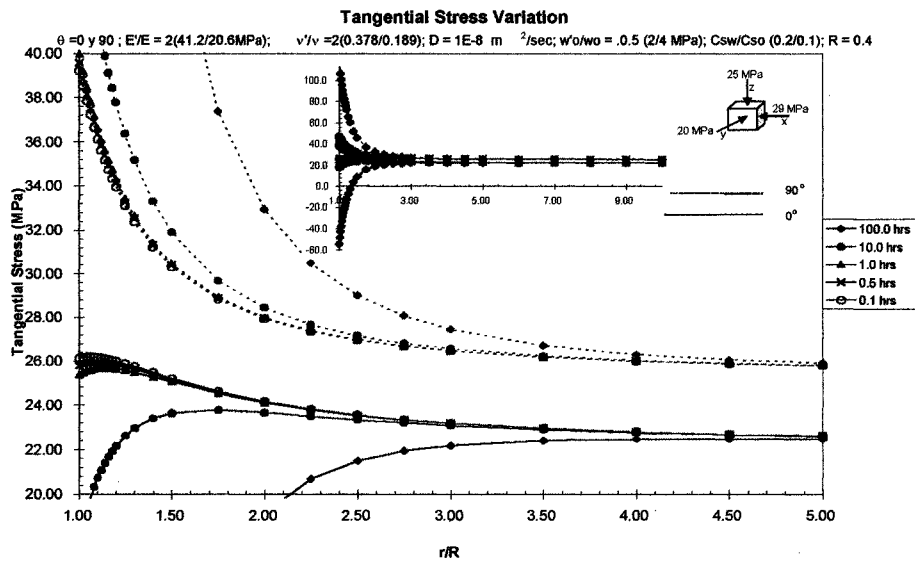


Figure K.4: Tangential stress variation with radial distance for different times in a transversely isotropic saturated porous media (anisotropy ratio equal to two) and taking into account the chemical effect.

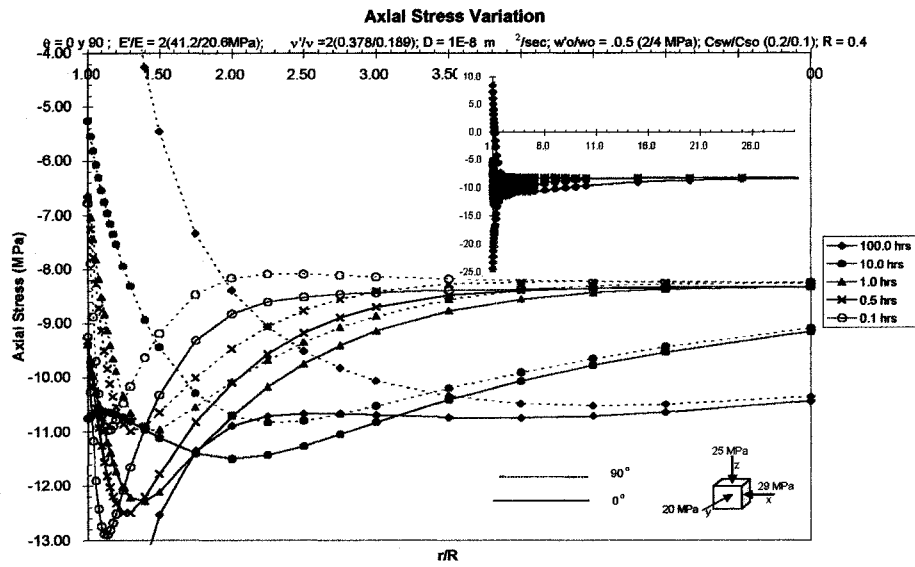


Figure K.5: Axial stress variation with radial distance for different times in a transversely isotropic saturated porous media (anisotropy ratio equal to two) and taking into account the chemical effect.

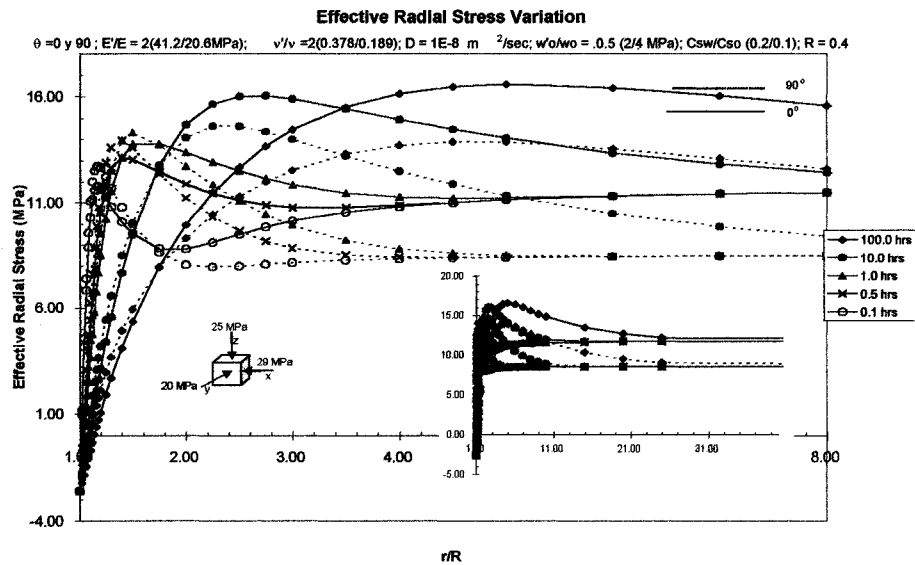


Figure K.6: Effective radial stress variation with radial distance for different times in a transversely isotropic saturated porous media (anisotropy ratio equal to two) and taking into account the chemical effect.

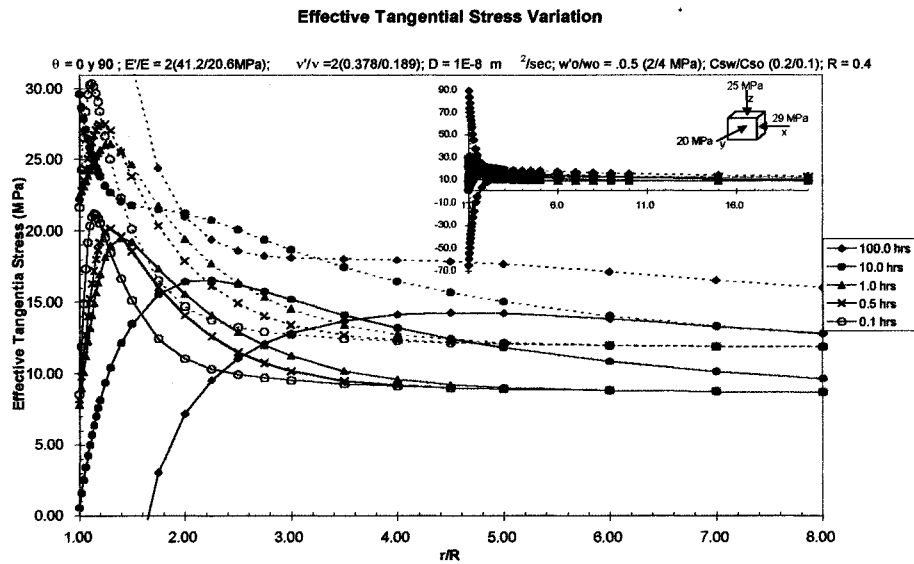


Figure K.7: Effective tangential stress variation with radial distance for different times in a transversely isotropic saturated porous media (anisotropy ratio equal to two) and taking into account the chemical effect.

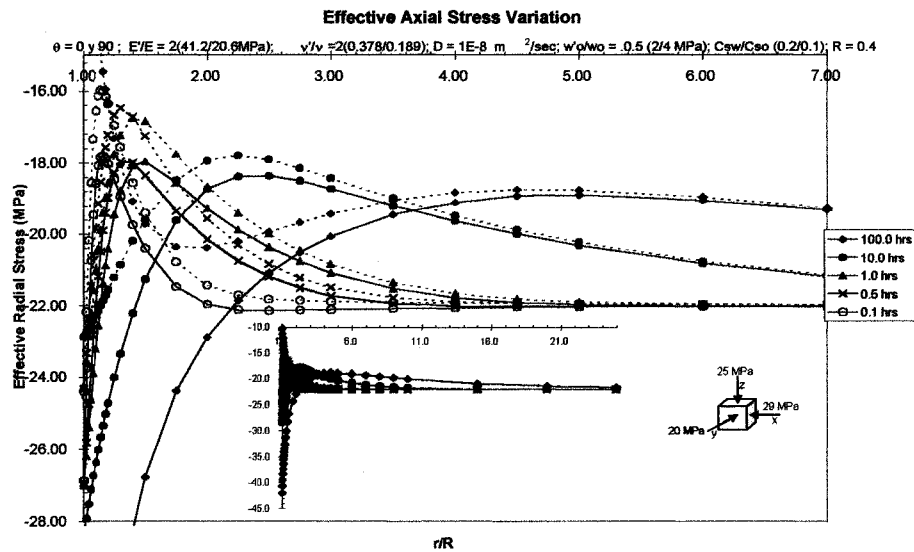


Figure K.8: Effective axial stress variation with radial distance for different times in a transversely isotropic saturated porous media (anisotropy ratio equal to two) and taking into account the chemical effect.

**Appendix L: Effect of the Mud's Solute
Mass Fraction (Anisotropic Factor Equal
to two).**

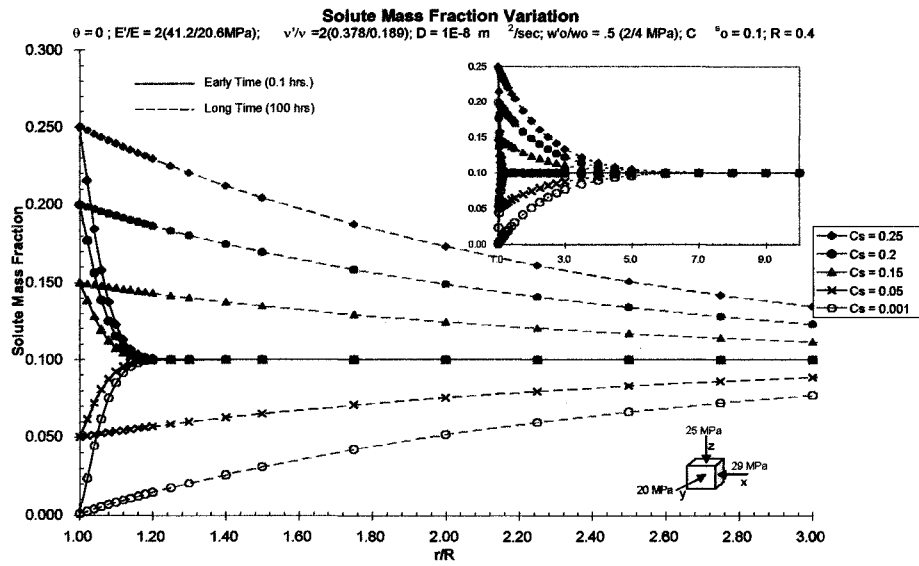


Figure L.1: Solute mass fraction variation for different mud's solute mass fraction at early and long times, in a transversely isotropic saturated porous media (AF=2). Chemical effects are also considered.

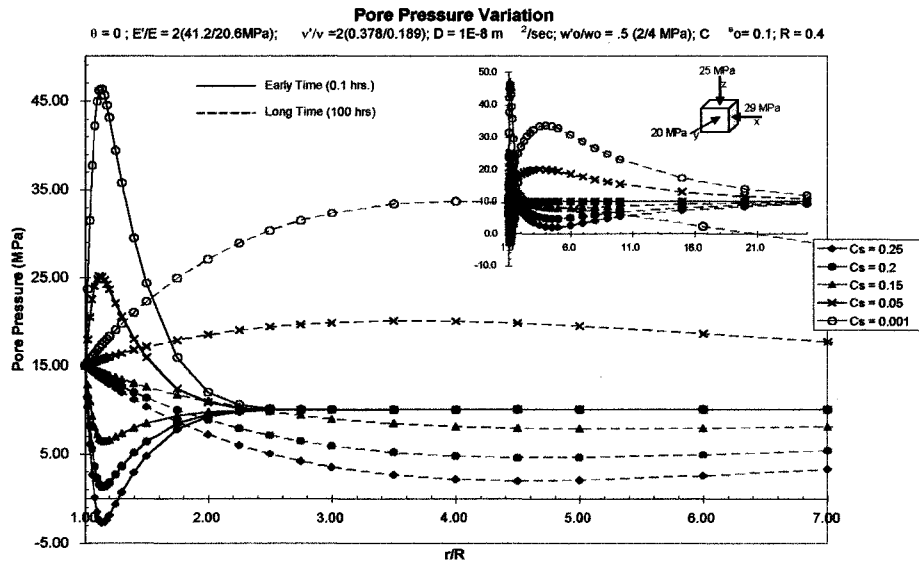


Figure L.2: Pore pressure variation for different mud's solute mass fraction at early and long times, in a transversely isotropic saturated porous media (AF=2). Chemical effects are also considered.

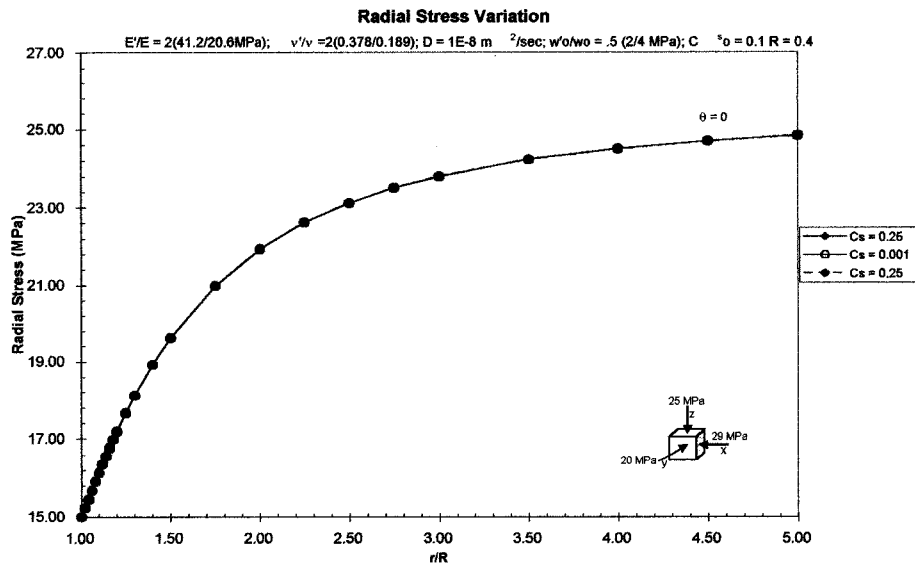


Figure L.3: Radial stress variation for different mud's solute mass fraction at early and long times, in a transversely isotropic saturated porous media (AF=2). Chemical effects are also considered.

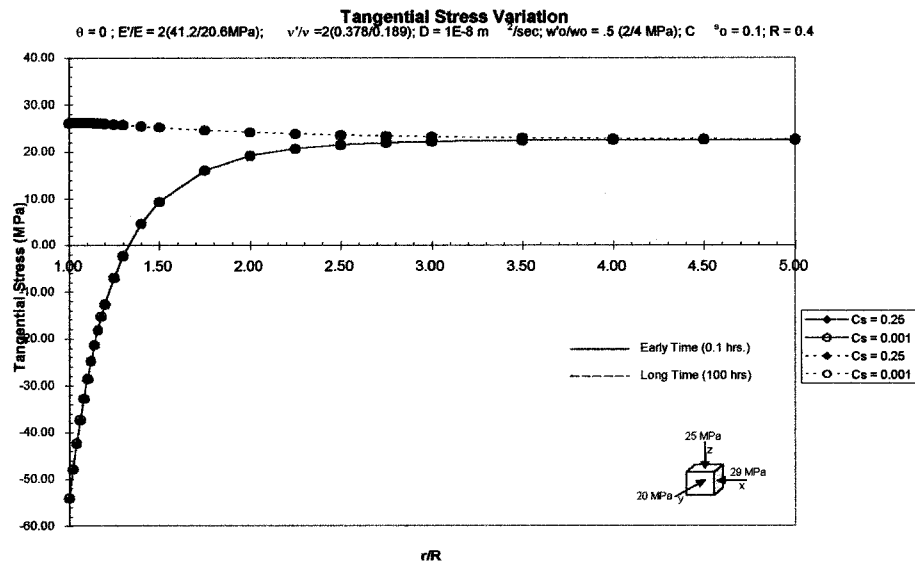


Figure L.4: Tangential stress variation for different mud's solute mass fraction at early and long times, in a transversely isotropic saturated porous media (AF=2). Chemical effects are also considered.

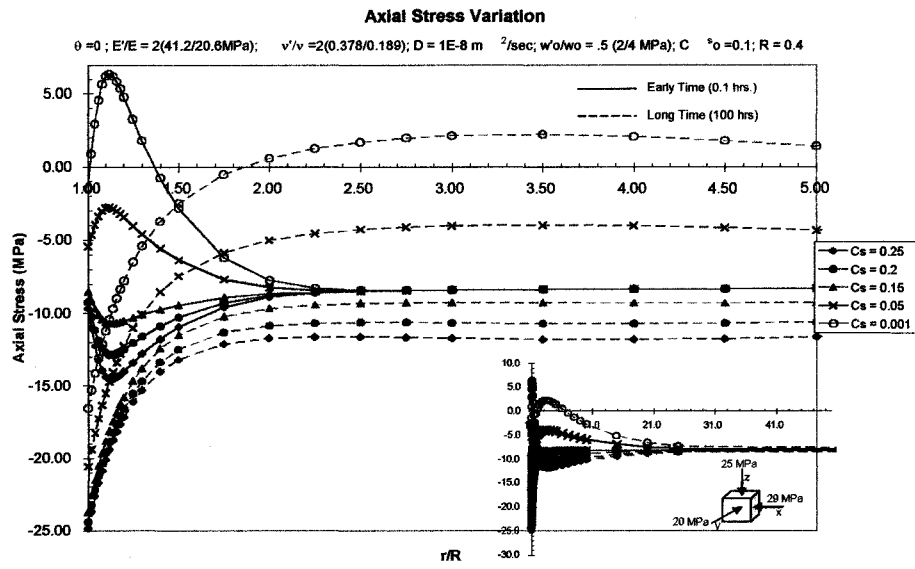


Figure L.5: Axial stress variation for different mud's solute mass fraction at early and long times, in a transversely isotropic saturated porous media (AF=2). Chemical effects are also considered.

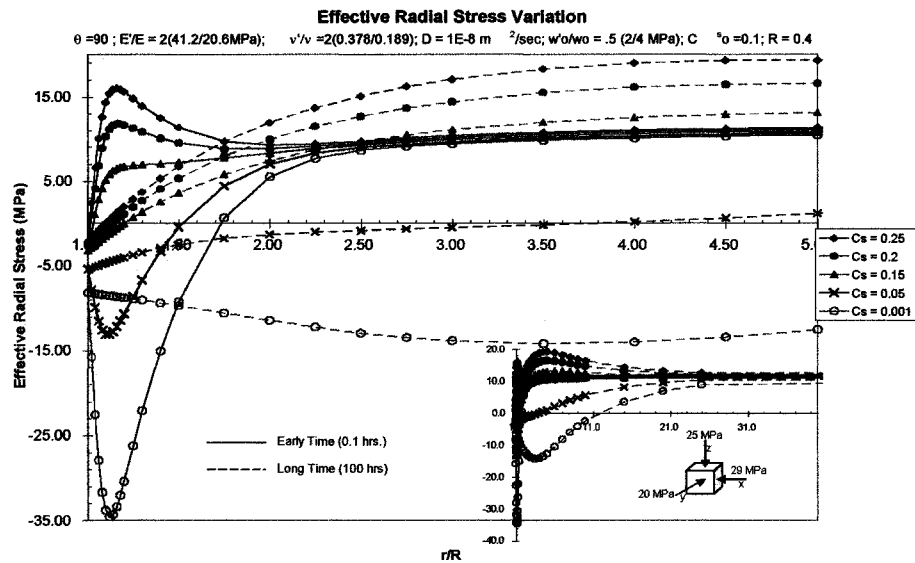


Figure L.6: Effective radial stress variation for different mud's solute mass fraction at early and long times, in a transversely isotropic saturated porous media (AF=2). Chemical effects are also considered.

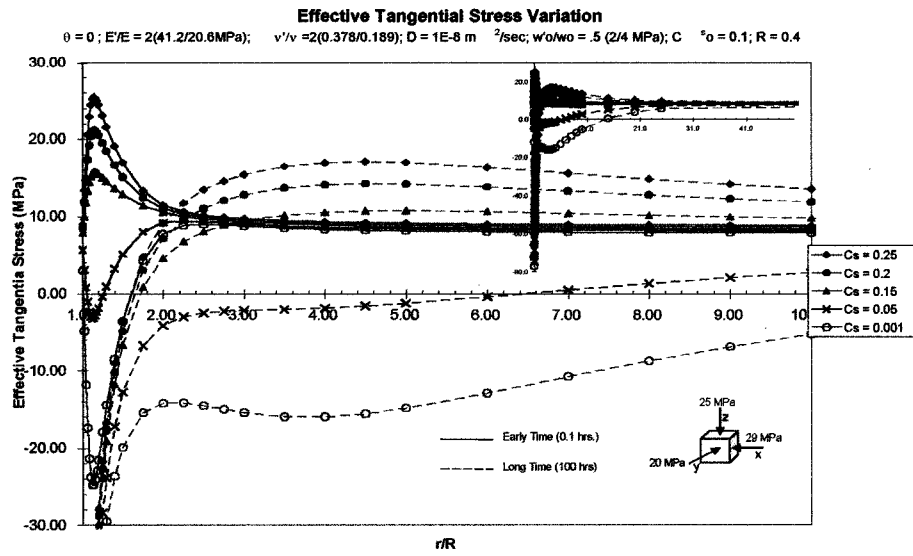


Figure L.7: Effective tangential stress variation for different mud's solute mass fraction at early and long times, in a transversely isotropic saturated porous media (AF=2). Chemical effects are also considered.

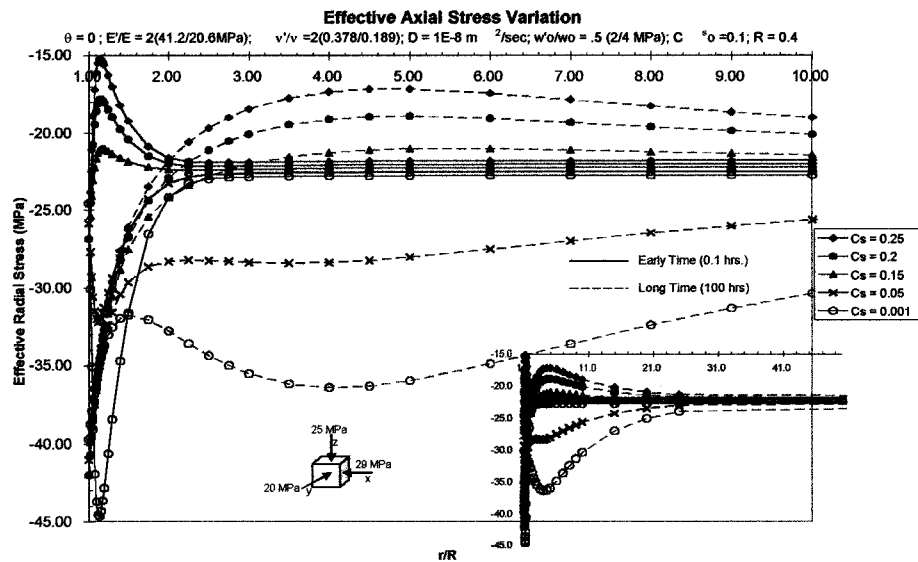


Figure L.8: Effective axial stress variation for different mud's solute mass fraction at early and long times, in a transversely isotropic saturated porous media (AF=2). Chemical effects are also considered.

**Appendix M: Effect of the Swelling
Coefficient of the Shale (Anisotropic
Factor Equal to two).**

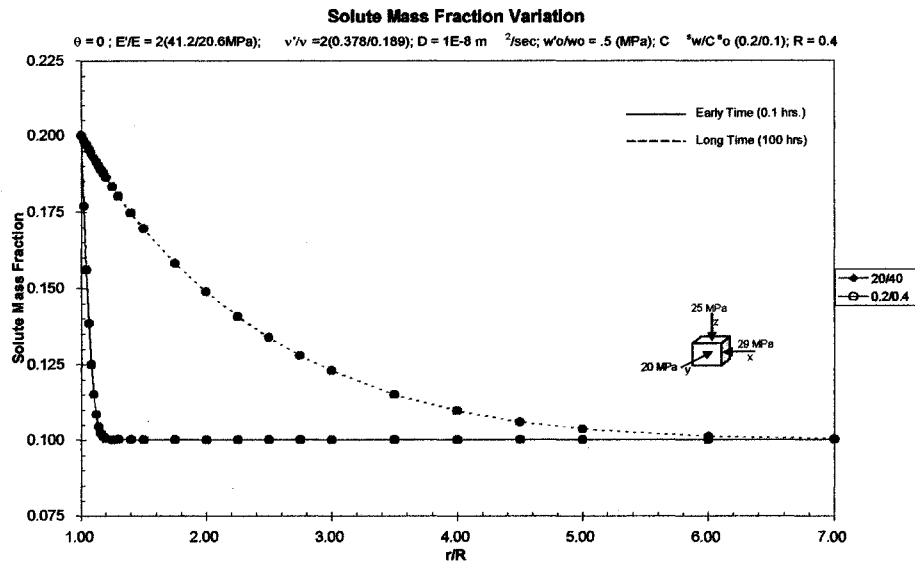


Figure M.1: Solute mass fraction variation with radial distance at early and long times, for different swelling coefficients in a transversely isotropic saturated porous media (anisotropy factor equal to two).

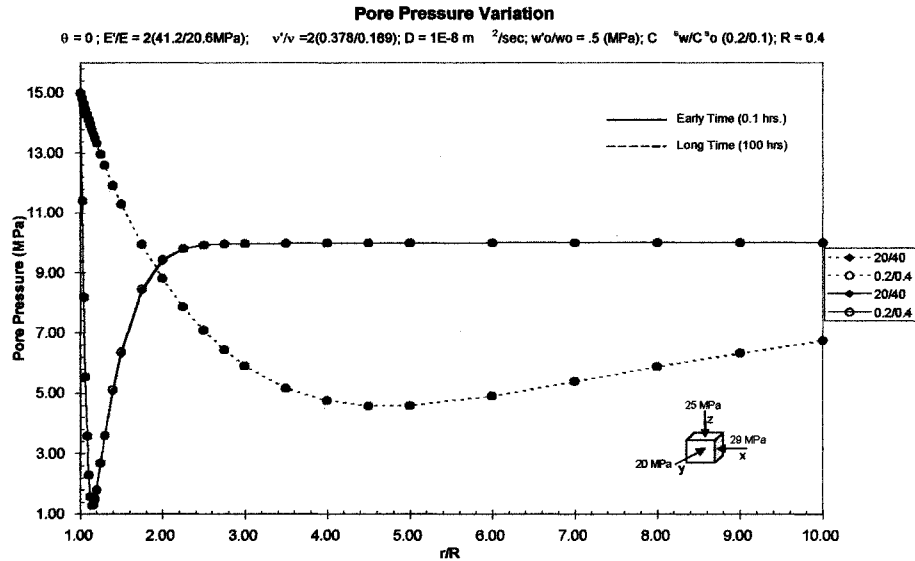


Figure M.2: Pore pressure variation with radial distance at early and long time, for different swelling coefficients in a transversely isotropic saturated porous media (anisotropy factor equal to two).

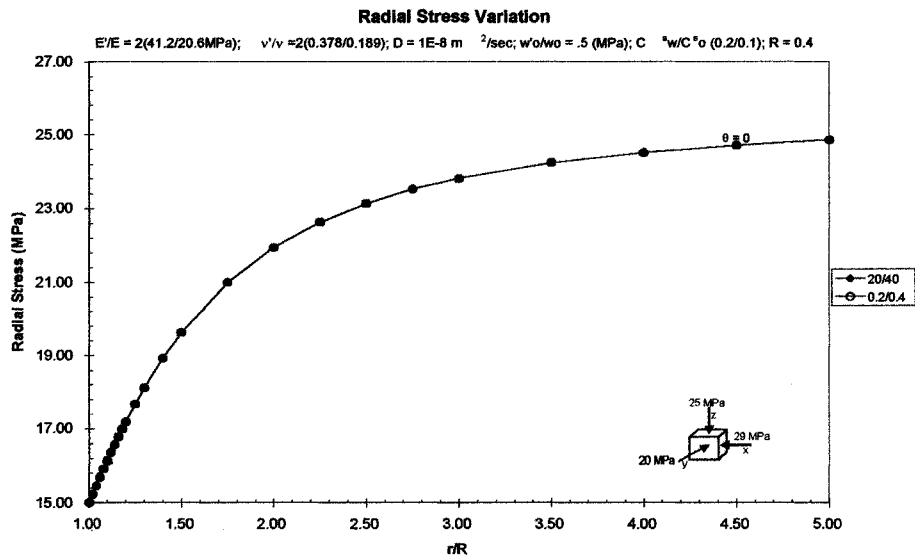


Figure M.3: Radial stress variation with radial distance at early and long times, for different swelling coefficients in a transversely isotropic saturated porous media (anisotropy factor equal to two).

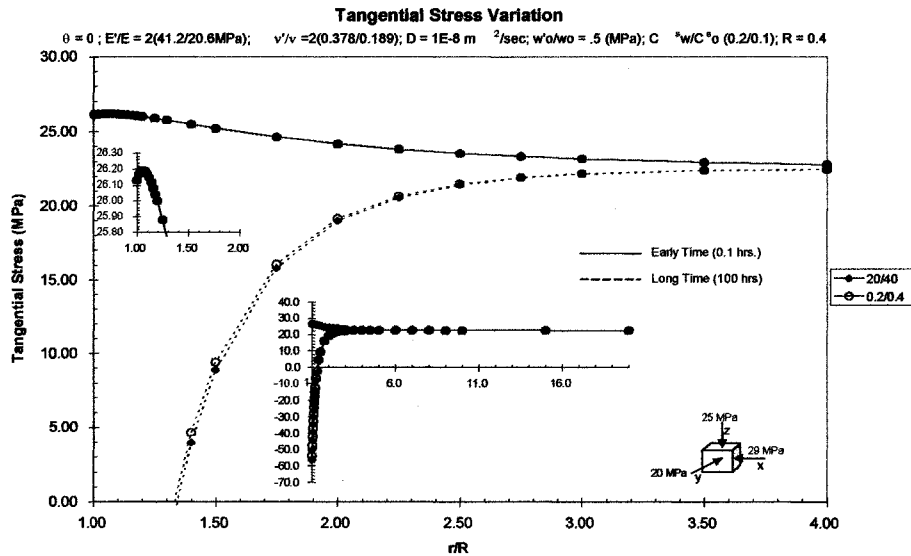


Figure M.4: Tangential stress variation with radial distance at early and long times, for different swelling coefficients in a transversely isotropic saturated porous media (anisotropy factor equal to two).

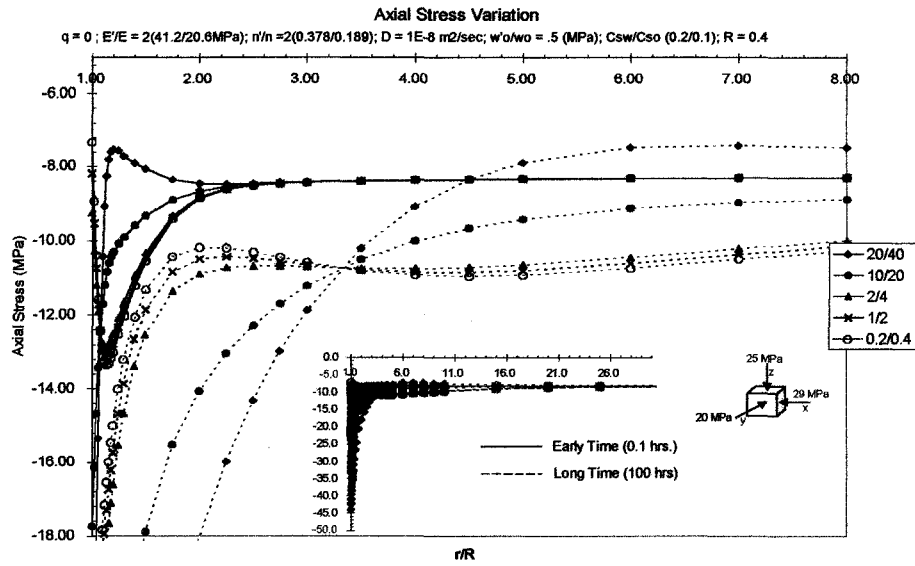


Figure M.5: Axial stress variation with radial distance at early and long times, for different swelling coefficients in a transversely isotropic saturated porous media (anisotropy factor equal to two).

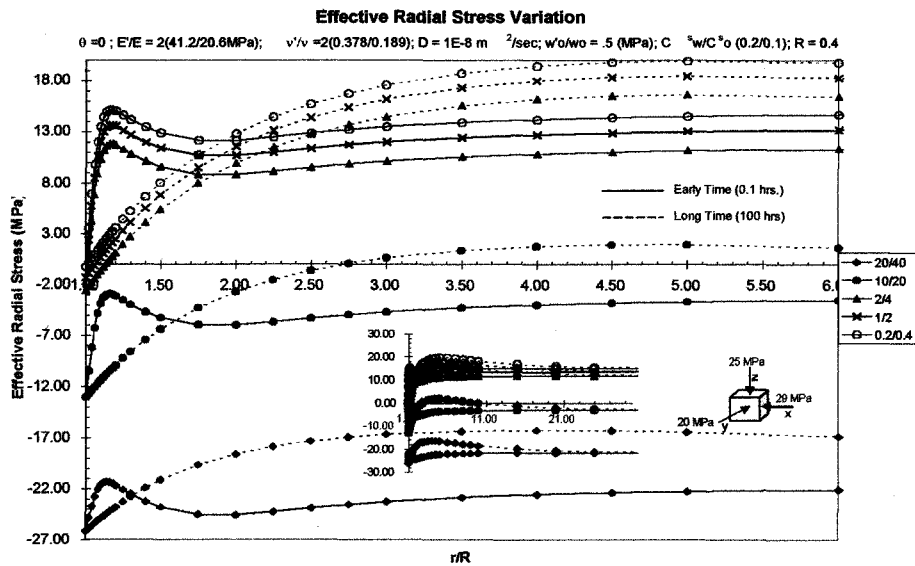


Figure M.6: Effective radial stress variation with radial distance at early and long times, for different swelling coefficients in a transversely isotropic saturated porous media (anisotropy factor equal to two).

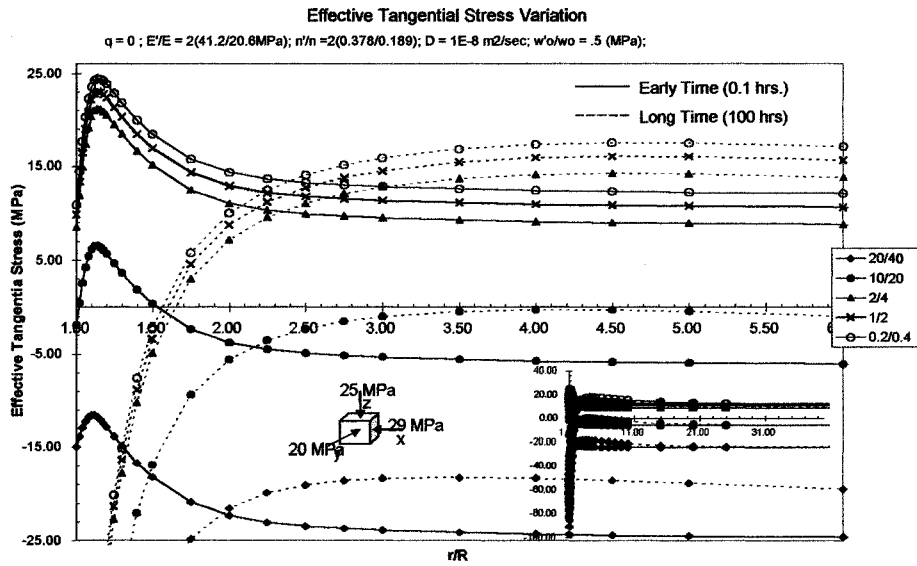


Figure M.7: Effective tangential stress variation with radial distance at early and long times, for different swelling coefficients in a transversely isotropic saturated porous media (anisotropy factor equal to two).

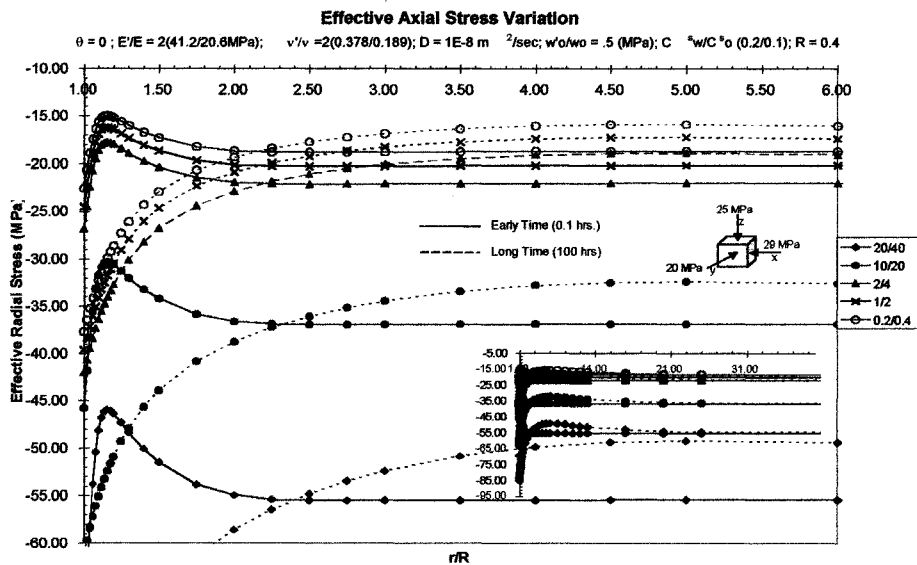


Figure M.8: Effective axial stress variation with radial distance at early and long times, for different swelling coefficients in a transversely isotropic saturated porous media (anisotropy factor equal to two).

**Appendix N: Effect of the Shale's
Reflection Coefficient (Anisotropic
Factor Equal to two)**

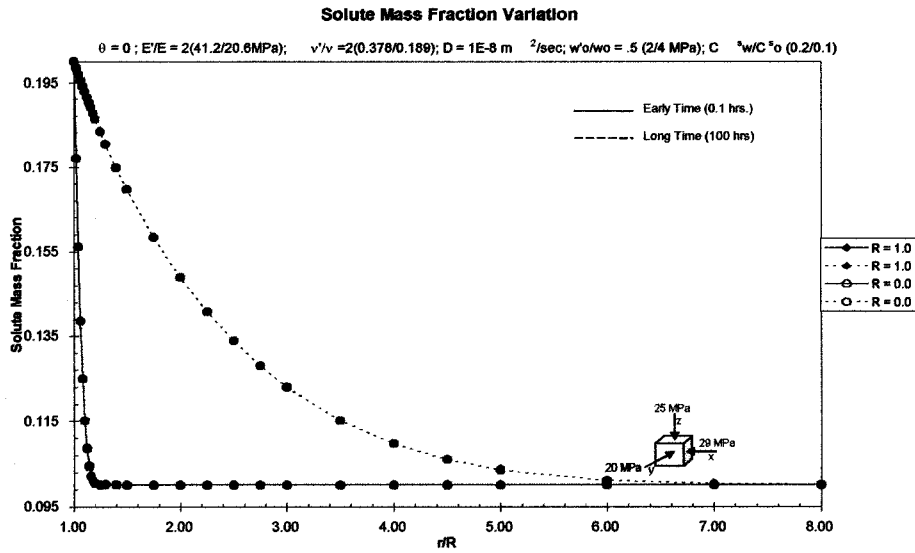


Figure N.1: Solute mass fraction variation with radial distance at early and long times, for different reflection coefficients in a transversely isotropic saturated porous media (anisotropy factor equal to two).

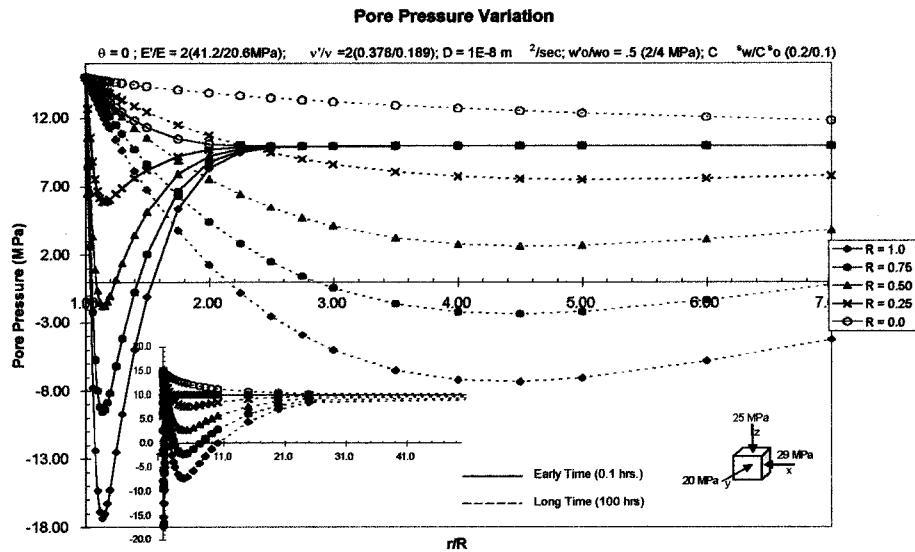


Figure N.2: Pore pressure variation with radial distance at early and long times, for different reflection coefficients in a transversely isotropic saturated porous media (anisotropy factor equal to two).

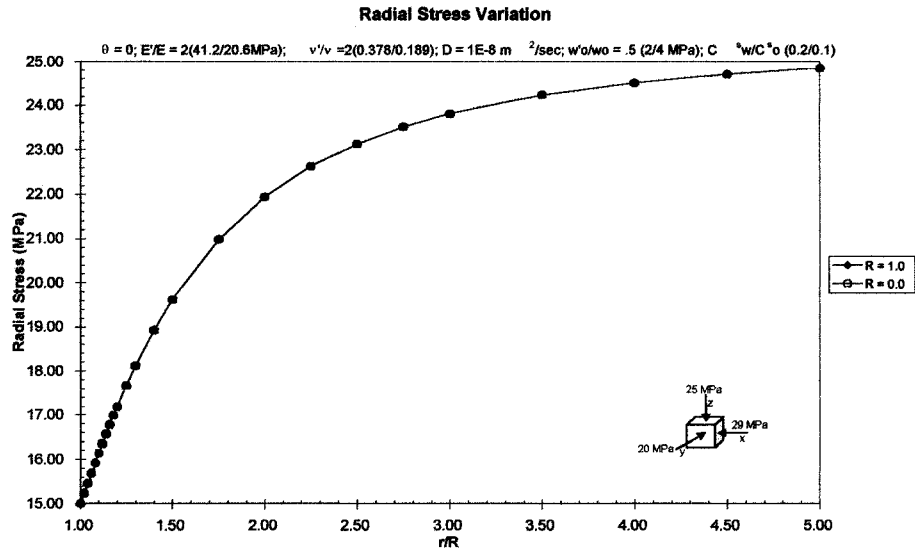


Figure N.3: Radial stress variation with radial distance at early and long times, for different reflection coefficients in a transversely isotropic saturated porous media (anisotropy factor equal to two).

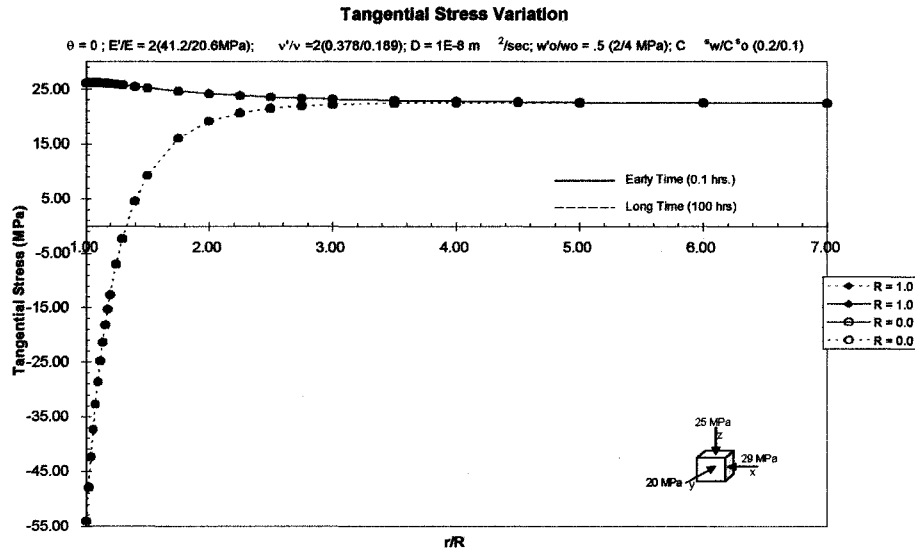


Figure N.4: Tangential stress variation with radial distance at early and long times, for different reflection coefficients in a transversely isotropic saturated porous media (anisotropy factor equal to two).

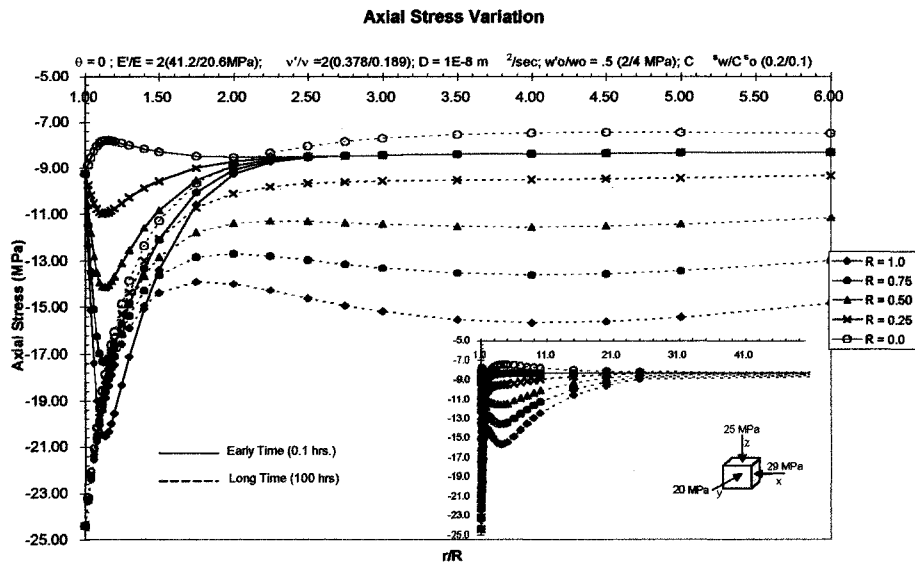


Figure N.5: Axial stress variation with radial distance at early and long times, for different reflection coefficients in a transversely isotropic saturated porous media (anisotropy factor equal to two).

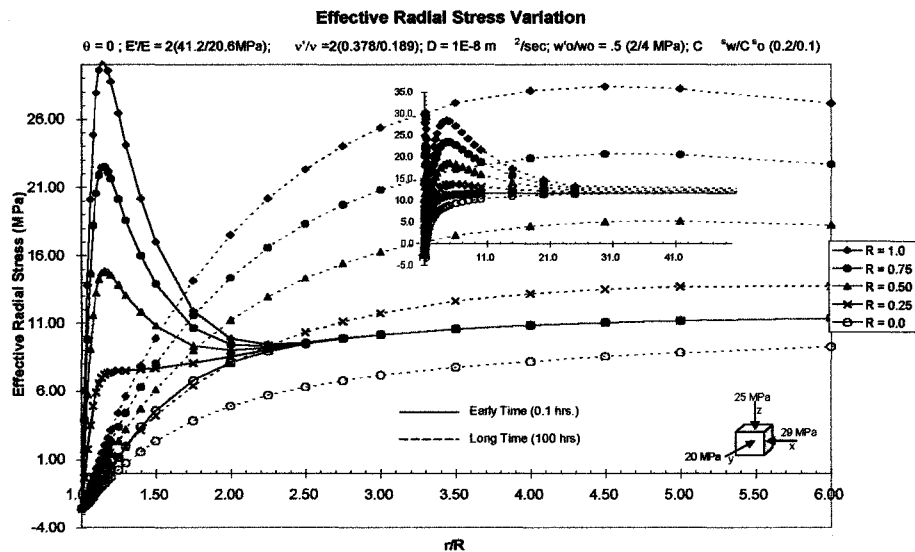


Figure N.6: Effective radial stress variation with radial distance at early and long times, for different reflection coefficients in a transversely isotropic saturated porous media (anisotropy factor equal to two).

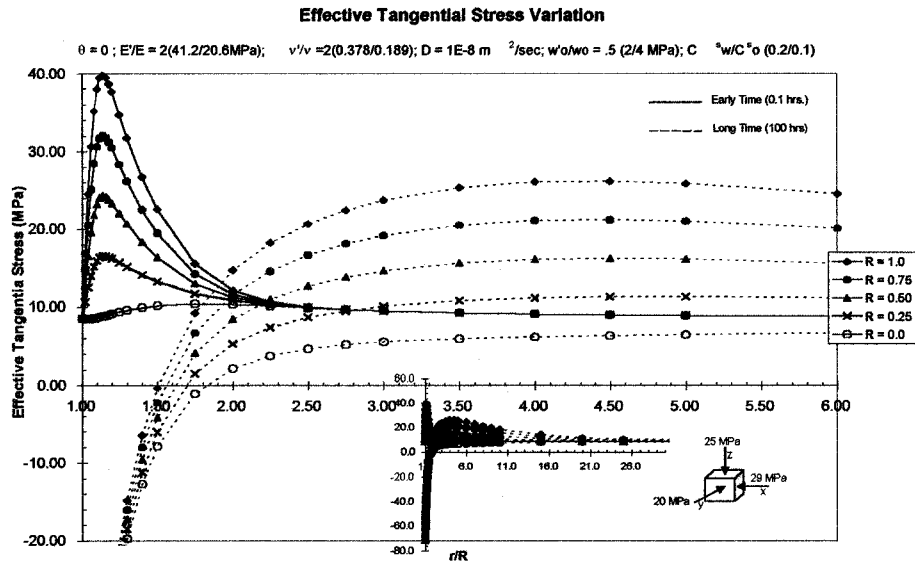


Figure N.7: Effective tangential stress variation with radial distance at early and long times, for different reflection coefficients in a transversely isotropic saturated porous media (anisotropy factor equal to two).

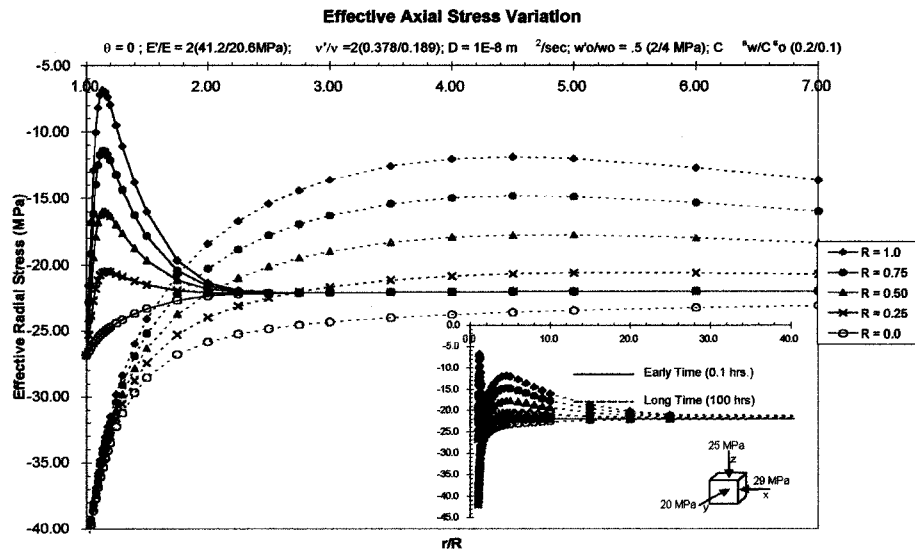


Figure N.8: Effective axial stress variation with radial distance at early and long times, for different reflection coefficients in a transversely isotropic saturated porous media (anisotropy factor equal to two).

**Appendix O: Effect of the Mud
Pressure (Anisotropic Factor Equal to
two)**

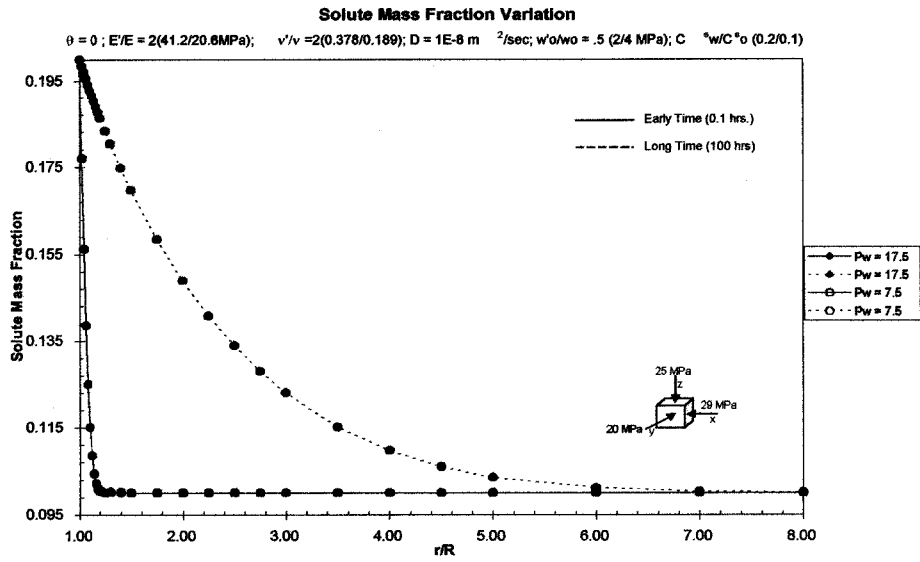


Figure O.1: Solute mass fraction variation with radial distance, for different mud pressures in a trasversely isotropic saturated porous media (anisotropy ratio equal to two)

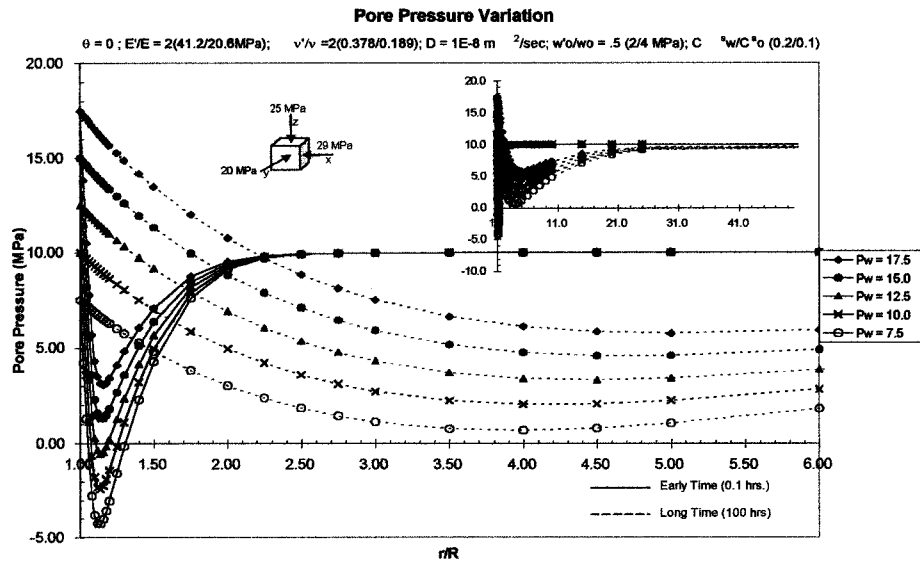


Figure O.2: Pore pressure variation with radial distance, for different mud pressures in a trasversely isotropic saturated porous media (anisotropy ratio equal to two)

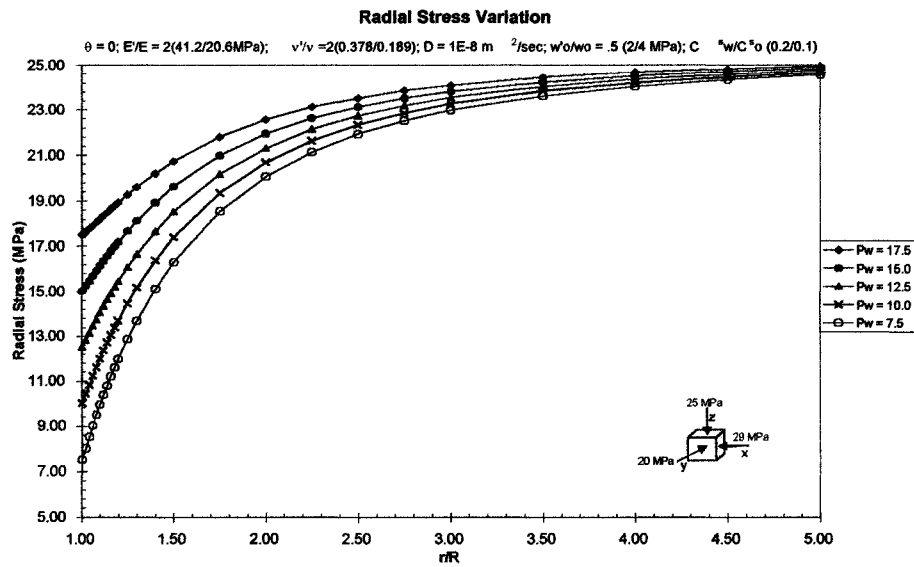


Figure O.3: Radial stress variation with radial distance, for different mud pressures in a transversely isotropic saturated porous media (anisotropy ratio equal to two)

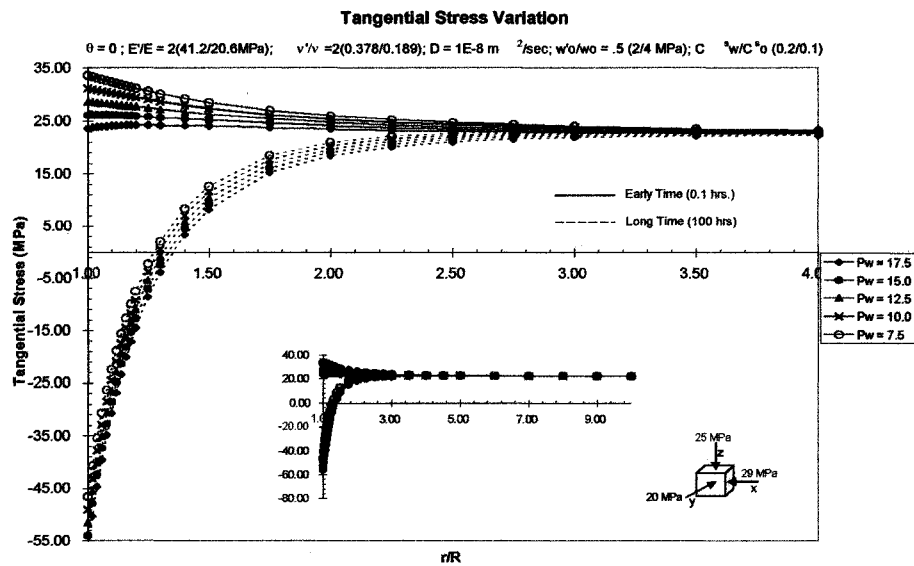


Figure O.4: Tangential stress variation with radial distance, for different mud pressures in a transversely isotropic saturated porous media (anisotropy ratio equal to two)

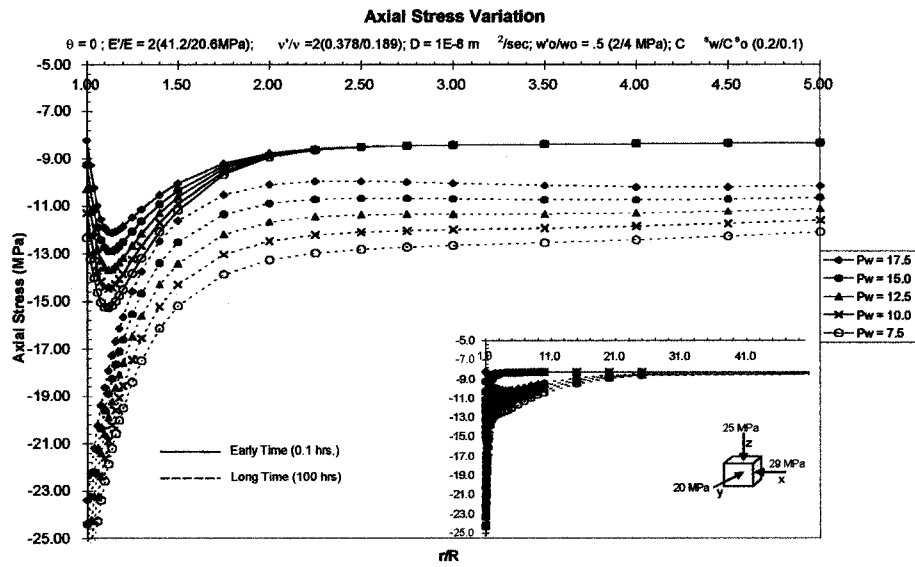


Figure O.5: Axial stress variation with radial distance, for different mud pressures in a trasversely isotropic saturated porous media (anisotropy ratio equal to two)

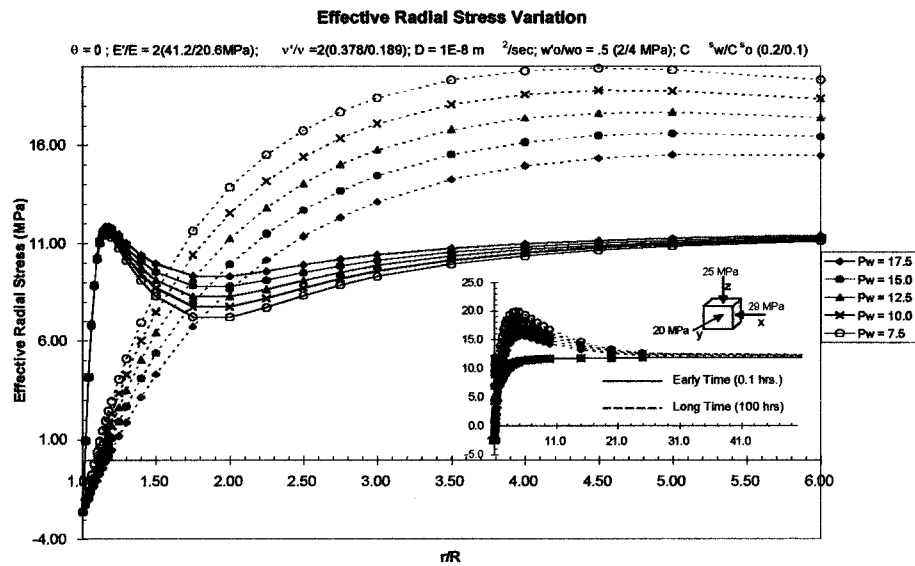


Figure O.6: Effective radial stress variation with radial distance, for different mud pressures in a trasversely isotropic saturated porous media (anisotropy ratio equal to two)

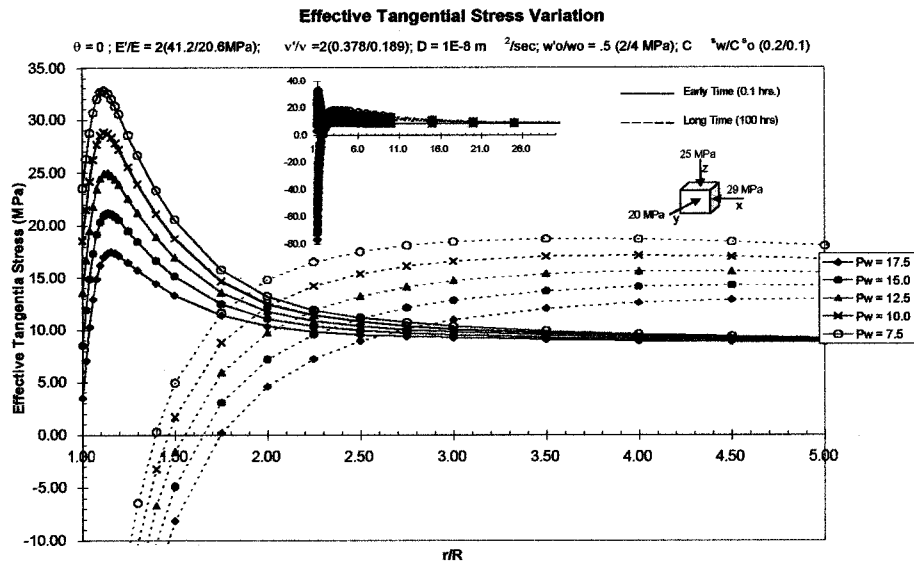


Figure O.7: Effective tangential stress variation with radial distance, for different mud pressures in a trasversely isotropic saturated porous media (anisotropy ratio equal to two)

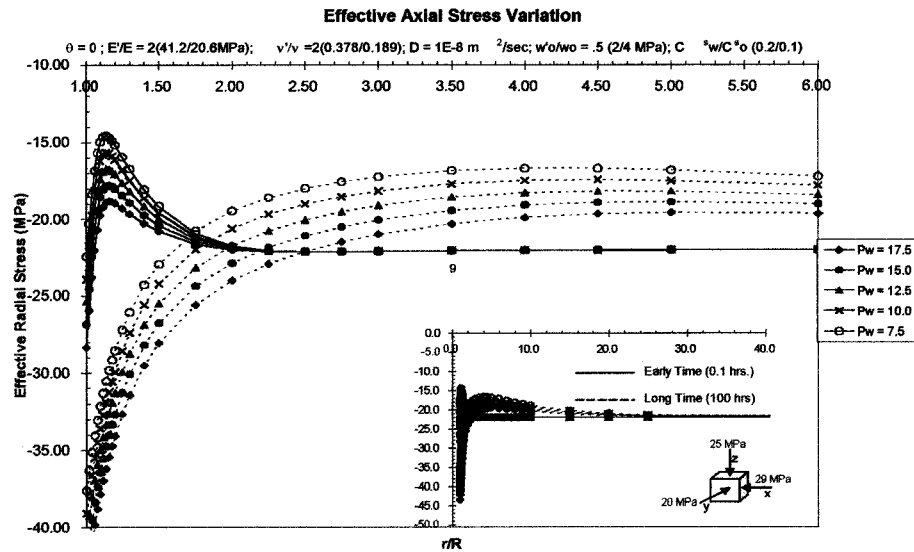


Figure O.8: Effective axial stress variation with radial distance, for different mud pressures in a trasversely isotropic saturated porous media (anisotropy ratio equal to two)

**Appendix P: Effect of the Normal
Stress Field (Anisotropic Factor Equal to
two)**

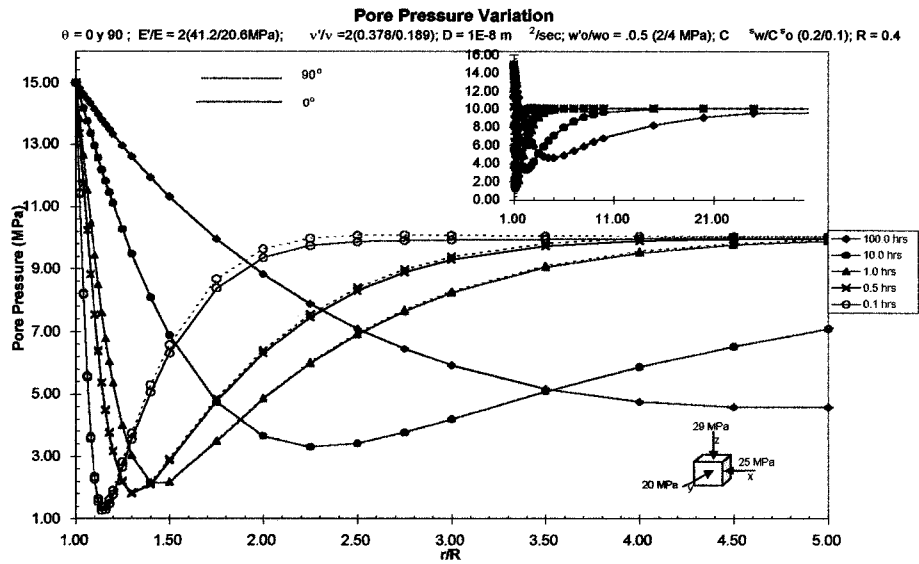


Figure P.1: Pore pressure variation with radial distance, for different times in a transversely isotropic saturated porous media (anisotropy factor equal to two) at normal stress field.

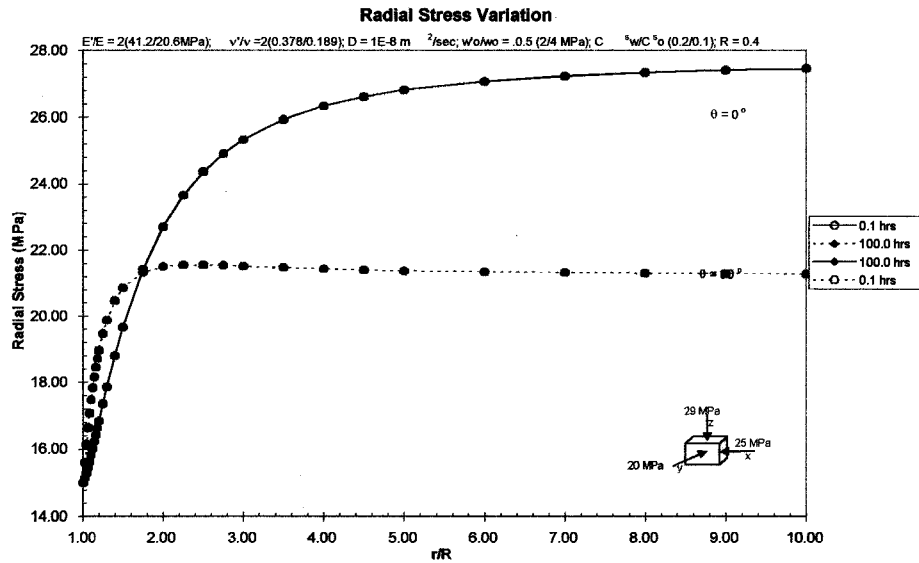


Figure P.2: Radial stress variation with radial distance, for different times in a transversely isotropic saturated porous media (anisotropy factor equal to two) at normal stress field.

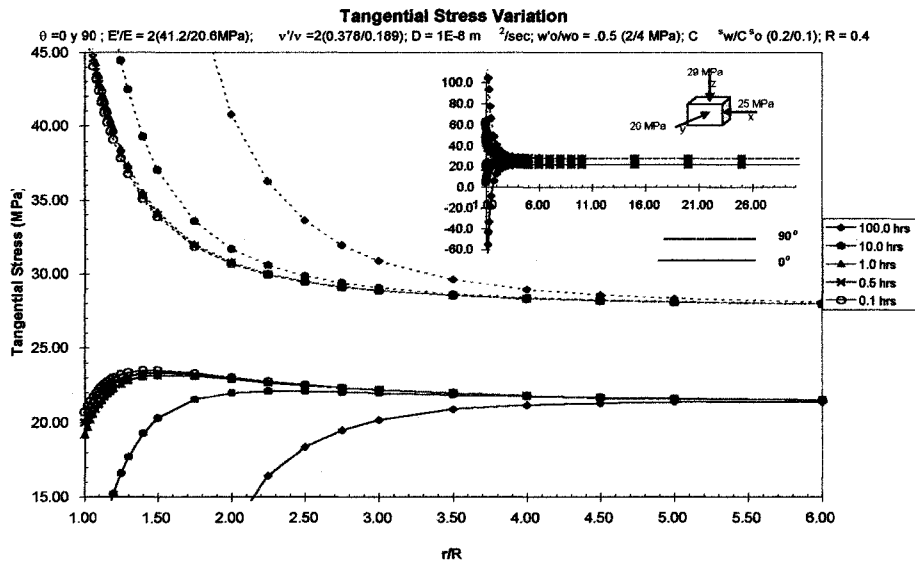


Figure P.3: Tangential stress variation with radial distance, for different times in a transversely isotropic saturated porous media (anisotropy factor equal to two) at normal stress field.

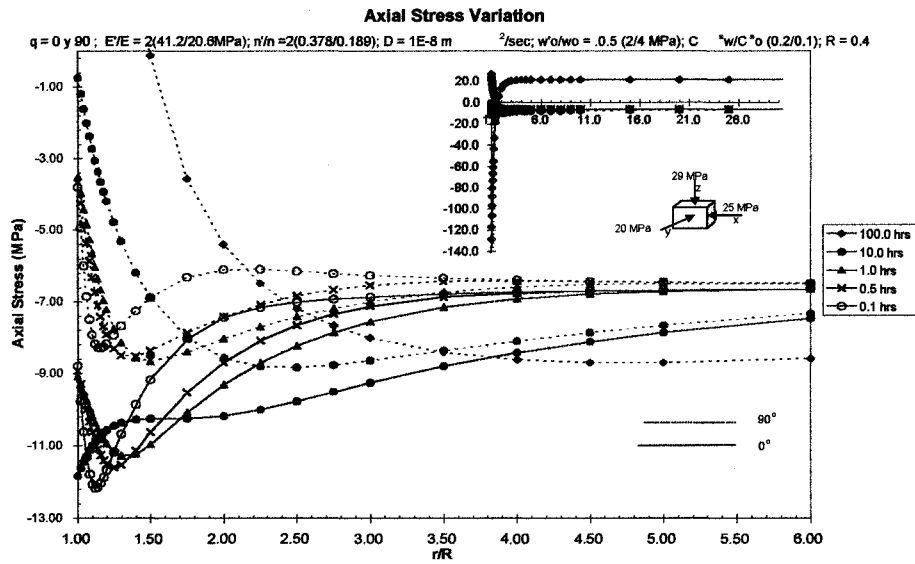


Figure P.4: Axial stress variation with radial distance, for different times in a transversely isotropic saturated porous media (anisotropy factor equal to two) at normal stress field.

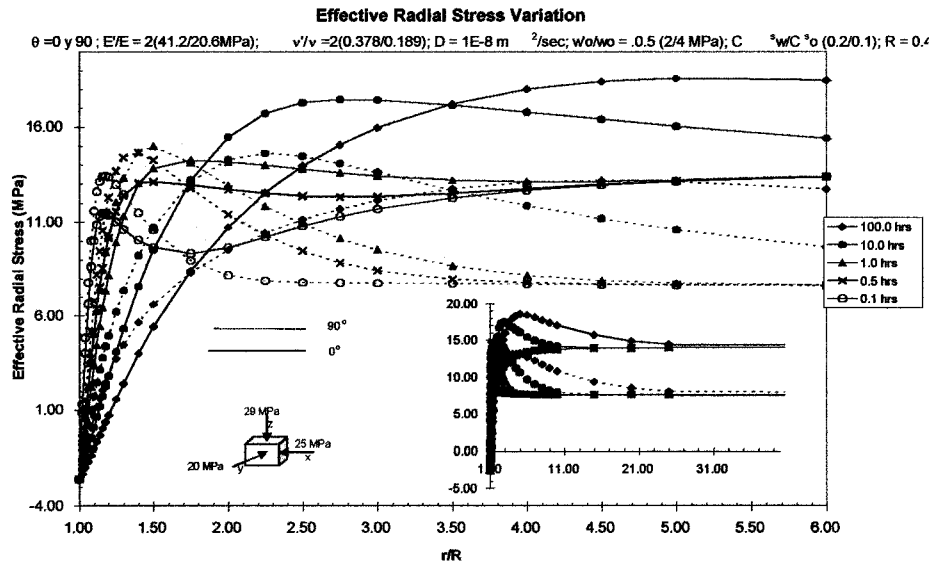


Figure P.5: Effective radial stress variation with radial distance, for different times in a transversely isotropic saturated porous media (anisotropy factor equal to two) at normal stress field.

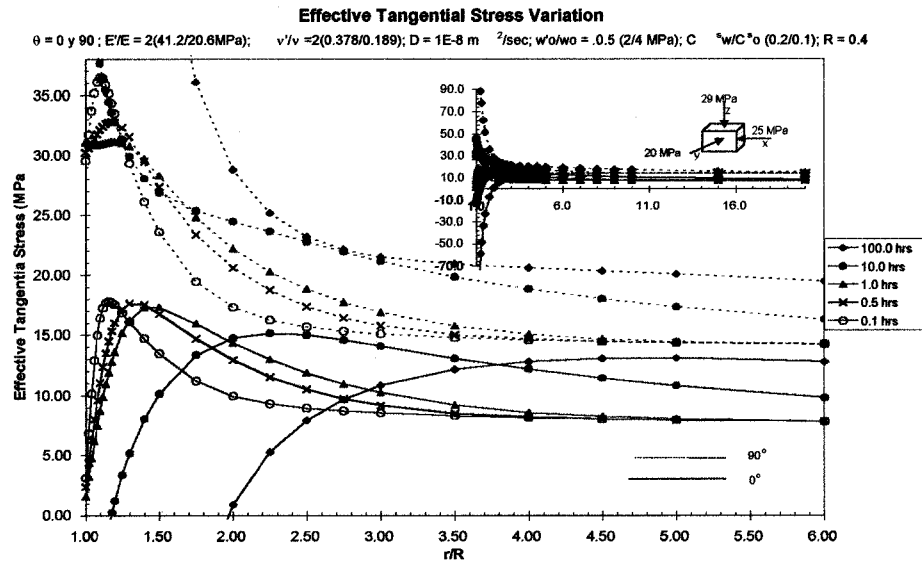


Figure P.6: Effective tangential stress variation with radial distance, for different times in a transversely isotropic saturated porous media (anisotropy factor equal to two) at normal stress field.

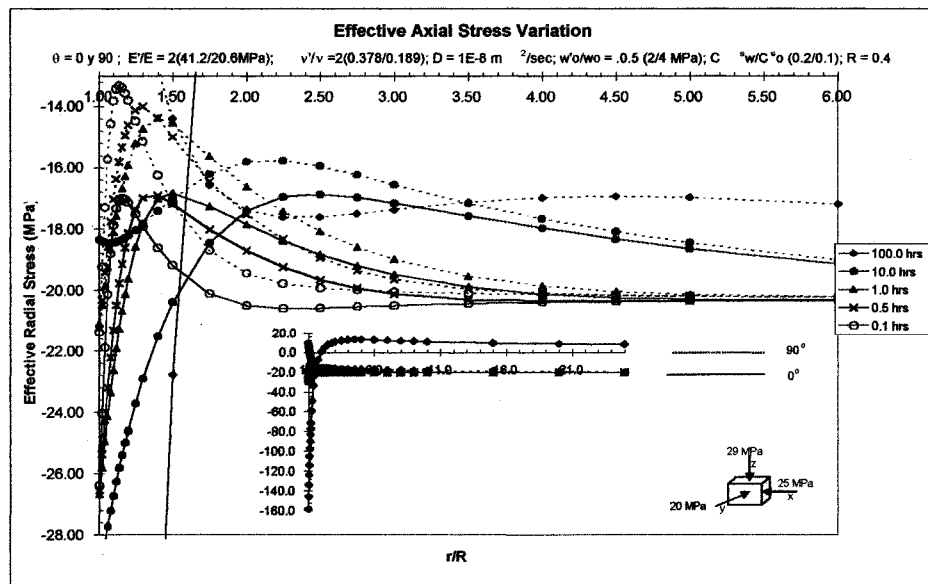


Figure P.7: Effective axial stress variation with radial distance, for different times in a transversely isotropic saturated porous media (anisotropy factor equal to two) at normal stress field.